VNIVERSITAT DE VALÈNCIA

TESI DOCTORAL

PROGRAMA DE DOCTORAT EN FÍSICA - 3126

Super-weakly coupled particles: phenomenology and neutrino mass models

Rebeca Beltrán Lloría

Director: Dr. Martin Hirsch

Tutor: Dr. Avelino Vicente Montesinos

IFIC (CSIC - Universitat de València)
Departament de Física Teòrica

València, juny 2025

Dr. Martin Hirsch, investigador científico del Consejo Superior de Investigaciones Científicas (CSIC), y Avelino Vicente Montesinos, Profesor Permanente Laboral Ppl de la Universitat de València, en título de tutor,

CERTIFICAN:

Que la presente memoria "Super-weakly coupled particles: phenomenology and neutrino mass models" ha sido realizada bajo su dirección en el Instituto de Física Corpuscular, centro mixto del CSIC y de la Universitat de València, por Rebeca Beltrán Llorìa y constituye su Tesis para optar al grado de Doctora en Física.

Y para que así conste, en cumplimiento de la legislación vigente, presenta en el Departament de Física Teòrica de la Universitat de València la referida Tesis Doctoral, y firma el presente certificado.

València, junio 2025

Dr. Martin Hirsch   Dr. Avelino Vicente Montesinos

Acknowledgements

Llevo posponiendo escribir esta sección de la tesis mucho tiempo por miedo a no escribir algo a la altura de las circunstancias. Han sido muchas las personas que han hecho que hoy puedas estar leyendo esto, seguramente tú seas una de ellas, pero si no encuentras tu nombre en estas líneas, lo siento, aunque te lo agradezco también.

La primera persona a la que quiero dar las gracias es a mi director, Martin Hirsch. Ha sido un placer trabajar y aprender a su lado durante 5 años. Y el simple hecho de que la puerta del despacho estuviera siempre abierta no tiene precio. Creo que no he podido tener mejor mentor para esta etapa y la forma en que he aprendido a ver la física se la debo a él. Gracias Martin, por tu paciencia y tus consejos.

También ha sido vital formar parte del grupo *Astroparticle and High Energy Physics*, que es más bien una familia. Gracias a los seniors, Mariam, Sergio, Avelino, José, Valentina, por haber creado este entorno y estar siempre dispuestos a ayudarnos. Gracias a los niños, Ana, Pablo, Agnese, Antonio, Javi y Adrián, por haber amenizado estos años dentro y fuera del despacho. No me olvido de los niños que ya no lo son tanto, Salva, los Pablos y Omar. En especial, gracias Omar por haber sido el mejor compañero de despacho y por todas esas charlas sobre física y sobre la vida. I would also like to thank *all* the other current and former *local AHEPians*. Thank you Chandan for your help and guidance in the last two years. Gracias Victor y Gonzalo por los buenos momentos. And thanks Jack for your words of encouragement.

This thesis could have not been possible either without my collaborators. It has been a pleasure to work with such great physicists. From our collaboration across 12 time zones, special thanks to Arsenii, for all the discussions we had, to Simon, for all your help and being always available, and to Giovanna, for your kindness and support. Thank you Frank, for your time and support since my stay at UCL. Thanks also to Patrick, Ricardo, Julian and Juan Carlos.

Otra de las cosas que me llevo de esta estapa son las amistades que he hecho durante estos años en el IFIC y en congresos y escuelas. Thanks Baibhab for all the deep conversations at IATA, I hope the IFIC sitcom still gets new interesting characters and episodes next season. Thanks Naseem for always being so cheerful and passing by our office so often. Mención especial a las personas del TAE, ellas saben quiénes son, Benasque se ha quedado para siempre en mi memoria. Beneït aquell congrés a Bilbao que em va fer conèixer Toni, espere que seguisques divulgant la física amb tanta passió allà on vages.

De un modo u otro, la física ha puesto en mi camino a personas increíbles desde hace 9 años y a ellas también les debo que hoy esté aquí. Quién nos iba a decir cuando entramos por la puerta de la facultad que estaríamos en proceso de ser doctores. Carlos y Gorka, ha sido un placer haber recorrido junto a vosotros este maratón desde el minuto uno. Ana, no tengo palabras suficientes para describir el orgullo que siento de conocer a la mejor física del mundo. Gracias Carlos por tu amistad todo este tiempo, incluso en la distancia, sabes que siempre podrás visitarme en el país en el que esté. No me olvido del resto de fisiquillos, Raúl, Pablet, Jorge, Alicia, Dani, gracias por todos los momentos en familia dentro y fuera de la facultad. Gracias Diego, por haberme descubierto el Palau y ser el mejor crítico de conciertos.

Y aunque no lo parezca hay vida más allá de la física. Gracias a las personas que más tiempo han tenido que aguantarme, es decir, a todos los miembros del team Menendez Pelayo en estos cinco años. Alicia, te toca doble agradecimiento, pero las noches en el sofá juntas escribiendo código hasta las tantas merecían estar aquí. Sandra y Álvaro, los mejores compañeros de piso, literalmente, según el duende. Espero que no hayamos sido una mala influencia con esto del doctorado para ti, Sandra, te deseo todo lo mejor en esta etapa, y ánimo Álvaro, que al final de esto se sale. Teresa, gracias por darme ánimos en estos últimos meses de escritura y por distraerme con tus episodios de BSS. Mucha suerte en todas las aventuras que te esperan.

Hay amistades que también son familia y merecen estar aquí. Victoria, que sepas que las cenas, paseos y meriendas de estos últimos años me han dado la vida y espero poder seguir descubriendo cafeterías en Chipre solo para que vayamos juntas algún día. Gracias Carla por abrirme las puertas de tu casa cada año y enseñarme lo bonitas que son las islas, que suerte tienen Gran Canaria y Tenerife de teneros a ti y a Sara. Isabel, lo que la música y la ciencia unió, que no lo separe nada, mucha suerte en esta recta final, aunque confío plenamente en que vas a ser la mejor neuro100tífica del país en el que estés, ya sea en Australia o en España.

Para terminar, quiero dar las gracias a toda mi familia, que aún sin saber qué son los neutrinos, confían en mí y en mi trabajo. A mi hermana, por su apoyo incondicional aún cuando he sido de lo más insufrible. Y sobre todo, a mis padres, por haberme inculcado el pensamiento científico y la disciplina en el estudio y en la vida, y por haberme apoyado en todas y cada una de las decisiones que he ido tomando a lo largo de los años. Gracias a vosotros habrá otra doctora en la familia.

Esta tesis ha sido financiada por: ACIF/2021/052, CIBEFP/2022/62 y todos los proyectos que me han llevado de congresos por el mundo.

Y a ti, que has leído hasta aquí, gracias.

Resumen

Esta tesis investiga cómo el origen de la masa de los neutrinos puede guiar la búsqueda de nuevas partículas débilmente acopladas más allá del Modelo Estándar (SM), centrándose en los leptones neutros pesados (HNLs), también conocidos como neutrinos estériles. Los HNLs aparecen de manera natural en varios mecanismos de generación de masa de los neutrinos con acoplamientos débiles, por lo que suelen presentar vidas medias largas. Ello los convierte en candidatos ideales para búsquedas de partículas de larga vida (LLPs) en colisionadores. Para estudiarlos de manera independiente, sin referencia a modelo específico, esta tesis emplea la Teoría de Campos Efectiva (EFT) del SM extendida con neutrinos estériles (N_RSMEFT), un marco teórico que captura posibles efectos de nueva física mediante una expansión sistemática de operadores de dimensión superior. Al combinar este enfoque EFT con las búsquedas de LLPs en el LHC, este trabajo propone una estrategia prometedora para descubrir nuevas partículas relacionadas con la física de neutrinos.

La tesis se estructura en tres partes. La Parte I proporciona la motivación teórica y experimental. Tras una breve revisión de las implicaciones teóricas de las masas y mezclas de neutrinos, se discuten modelos populares de masa de neutrinos que involucran neutrinos estériles. A continuación, se motiva la existencia de nueva física débilmente acoplada y se presentan las señales características de LLPs, así como el programa experimental de búsquedas de LLPs y detectores especializados en el LHC. Esta sección concluye con un resumen de las restricciones experimentales actuales sobre el modelo más minimalista de HNLs, en el que los neutrinos estériles interactúan únicamente a través de la mezcla con los neutrinos del SM.

La Parte II presenta el marco teórico empleado en esta tesis: N_RSMEFT y la versión a baja energía, N_RLEFT. Ambos marcos describen nuevas interacciones de neutrinos estériles a escala electrodébil mediante operadores de dimensión superior. Se clasifican los operadores relevantes hasta dimensión seis en N_RLEFT y hasta dimensión siete en N_RSMEFT. Esta sección también presenta un trabajo original: una descomposición completa a nivel árbol de los operadores de N_RSMEFT de dimensión seis y siete. Dicha clasificación identifica el conjunto completo de extensiones del SM con una o dos partículas nuevas que generan los operadores EFT a nivel árbol, proporcionando un diccionario EFT-UV exhaustivo. Además, se analiza el papel de la violación del número leptónico en N_RSMEFT y su conexión con masas de tipo Majorana para los neutrinos del SM.

Finalmente, la Parte III estudia la fenomenología en colisionadores de HNLs a escala electrodébil utilizando los marcos EFT presentados en la Parte II, haciendo énfasis en las posibles señales de LLPs que pueden originar en el LHC. Se presentan cuatro estudios originales, cada uno en un capítulo específico. El primer estudio se centra en operadores de cuatro fermiones en N_RLEFT que involucran dos HNLs o un HNL y un neutrino, junto con dos quarks ligeros. Estos operadores inducen desintegraciones raras de mesones en HNLs, los cuales pueden decaer posteriormente con un desplazamiento medible, generando señales de LLPs en detectores lejanos del LHC. El segundo estudio analiza operadores de N_RSMEFT y N_RLEFT que generan momentos magnéticos de los neutrinos estériles. Estos conducen a señales exóticas en los detectores principales, como fotones que no apuntan al vértice de colisión, a causa de la via media larga de los HNLs con masas del orden del GeV. El tercer trabajo estudia operadores de cuatro fermiones en N_RSMEFT que involucran un único HNL y quarks de primera o segunda generación, los cuales pueden gobernar tanto la producción como la desintegración de HNLs, incluso cuando se desprecia la mezcla con los neutrinos activos. Estas interacciones pueden ser exploradas en el LHC, ya que producen vértices desplazados en detectores como ATLAS. El último estudio considera operadores similares, pero involucrando quarks de tercera generación (quarks top), lo que da lugar a mecanismos novedosos de producción y señales distintivas de la desintegración de los HNLs.

Los análisis fenomenológicos realizados combinan cálculos analíticos de anchuras de desintegración de HNLs en los marcos de EFT con simulaciones Monte Carlo siguiendo una cadena basada en Feynrules, MadGraph5, MadSpin y Pythia8, junto con código personalizado que implementa las estrategias de búsqueda de LLPs. Cada estudio presenta estimaciones de sensibilidad para búsquedas de LLPs en ATLAS o en detectores lejanos propuestos en el LHC, como MATHUSLA y ANUBIS, mostrando cómo estos pueden explorar regiones del espacio de parámetros aún inexploradas y probar escenarios fuera del alcance de búsquedas tradicionales.

En resumen, esta tesis demuestra cómo las EFTs y las búsquedas de LLPs pueden, en conjunto, ofrecer estrategias potentes e independientes del modelo existente a altas energías para explorar nueva física motivada por el sector de neutrinos. Los leptones neutros pesados emergen como un objetivo bien motivado y accesible experimentalmente. Al conectar modelos en el ultravioleta, marcos de EFT y fenomenología en colisionadores, este trabajo contribuye a ampliar el conjunto de herramientas para descubrir partículas super-débilmente acopladas en experimentos actuales y futuros.

Resum

Aquesta tesi investiga com l'origen de la massa dels neutrins pot orientar la recerca de noves partícules feblement acoblades més enllà del Model Estàndard (SM), centrant-se en els leptons neutres pesats (HNLs), també coneguts com a neutrins estèrils. Els HNLs apareixen de manera natural en diversos mecanismes de generació de massa de neutrins amb acoblaments febles, per la qual cosa sovint presenten vides mitjanes llargues. Això els converteix en candidats ideals per a la recerca de partícules de llarga vida (LLPs) en col·lisionadors. Per estudiar-los de manera independent, sense referència a un model específic, aquesta tesi empra la Teoria de Camps Efectiva (EFT) del SM estesa amb neutrins estèrils (N_RSMEFT), un marc teòric que recull possibles efectes de nova física mitjançant una expansió sistemàtica d'operadors de dimensió superior. En combinar aquest enfocament de la EFT amb la recerca de LLPs al LHC, aquest treball proposa una estratègia prometedora per descobrir noves partícules relacionades amb la física dels neutrins.

La tesi s'estructura en tres parts. La Part I proporciona la motivació teòrica i experimental. Després d'una breu revisió de les implicacions teòriques de les masses i mescles de neutrins, es discuteixen models populars de generació de massa de neutrins que involucren neutrins estèrils. A continuació, es motiva l'existència de nova física feblement acoblada i es presenten els senyals característics de LLPs, així com el programa experimental de recerca de LLPs i detectors especialitzats al LHC. Aquesta secció conclou amb un resum de les restriccions experimentals actuals sobre el model més minimalista d'HNLs, en què els neutrins estèrils interactuen únicament mitjançant la mescla amb els neutrins del SM.

La Part II presenta el marc teòric emprat en aquesta tesi: N_RSMEFT i la seva versió a baixa energia, N_RLEFT. Tots dos marcs descriuen noves interaccions dels neutrins estèrils a escala electrodèbil mitjançant operadors de dimensió superior. Es classifiquen els operadors rellevants fins a dimensió sis en N_RLEFT i fins a dimensió set en N_RSMEFT. Aquesta secció també presenta un treball original: una descomposició completa a nivell arbre dels operadors de N_RSMEFT de dimensió sis i set. Aquesta classificació identifica el conjunt complet d'extensions del SM amb una o dues partícules noves que generen els operadors EFT a nivell arbre, proporcionant un diccionari EFT-UV exhaustiu. A més, s'analitza el paper de la violació del nombre leptònic en N_RSMEFT i la seva connexió amb masses de tipus Majorana per als neutrins del SM.

Finalment, la Part III estudia la fenomenologia en col·lisionadors dels HNLs a escala electrodèbil utilitzant els marcs EFT presentats a la Part II, amb èmfasi en els possibles senyals de LLPs que poden aparèixer al LHC. Es presenten quatre estudis originals, cadascun en un capítol específic. El primer estudi se centra en operadors de quatre fermions en N_RLEFT que involucren dos HNLs o un HNL i un neutrí, juntament amb dos quarks lleugers. Aquests operadors indueixen desintegracions rares de mesons en HNLs, els quals poden desintegrar-se posteriorment amb un desplaçament mesurable, generant senyals de LLPs en detectors allunyats del punt de col·lisió al LHC. El segon estudi analitza operadors en N_RSMEFT i N_RLEFT que generen moments magnètics dels neutrins estèrils. Aquests donen lloc a senyals exòtiques en els detectors principals, com fotons que no apunten al vèrtex de col·lisió, a causa de la llarga vida mitjana dels HNLs amb masses de l'ordre del GeV. El tercer treball estudia operadors de quatre fermions en N_RSMEFT que involucren un únic HNL i quarks de primera o segona generació, els quals poden controlar tant la producció com la desintegració dels HNLs, fins i tot en absència de mescla amb els neutrins actius. Aquestes interaccions poden ser explorades al LHC, ja que donen lloc a vèrtexs desplaçats en detectors com ATLAS. L'últim estudi considera operadors similars, però que involucren quarks de tercera generació (quarks top), cosa que dona lloc a mecanismes nous de producció i senyals distintives en la desintegració dels HNLs.

Les anàlisis fenomenològiques realitzades combinen càlculs analítics de les amplades de desintegració dels HNLs en els marcs EFT amb simulacions de Monte Carlo utilitzant una cadena basada en Feynrules, MadGraph5, MadSpin i Pythia8, juntament amb codi personalitzat que implementa les estratègies de recerca de LLPs. Cada estudi presenta estimacions de sensibilitat per a la recerca de LLPs a ATLAS o en detectors allunyats proposats per al LHC, com MATHUSLA i ANUBIS, mostrant com poden explorar regions encara inaccessibles de l'espai de paràmetres i posar a prova escenaris fora de l'abast de les recerques tradicionals.

En resum, aquesta tesi demostra com les EFTs i la recerca de LLPs poden, conjuntament, oferir estratègies potents i independents del model per explorar nova física motivada pel sector dels neutrins. Els leptons neutres pesats emergeixen com un objectiu ben motivat i accessible experimentalment. En connectar models ultraviolats, marcs d'EFT i fenomenologia de col·lisionadors, aquest treball contribueix a ampliar les eines per descobrir partícules super-feblement acoblades en els experiments actuals i futurs.

Abstract

This thesis investigates how the origin of neutrino mass can guide the search for new, weakly interacting particles beyond the Standard Model (SM), focusing on heavy neutral leptons (HNLs), also known as sterile neutrinos. HNLs naturally arise in many neutrino mass mechanisms with weak couplings and, thus, often exhibit long lifetimes. This makes them ideal candidates for long-lived particle (LLP) searches at colliders. To study them in a model-agnostic way, the thesis employs the Effective Field Theory (EFT) of the SM extended with sterile neutrinos (N_RSMEFT), a framework that captures possible new physics effects through a systematic expansion of higher-dimensional operators. By combining this EFT approach with LLP searches at the LHC, this work provides a promising strategy to uncover new particles connected to neutrino physics.

The thesis is structured in three parts. Part I provides the theoretical and experimental motivation for this work. After a brief review of the theoretical implications of neutrino masses and mixing, it discusses popular neutrino mass models involving sterile neutrinos. Then, it motivates weakly coupled new physics and discusses LLP signatures and the growing experimental program of LLP searches and dedicated detectors at the LHC. There is a final summary of current experimental constraints on minimal HNL models, where sterile neutrinos interact only through their mixing with SM neutrinos.

Part II discusses the theoretical framework used in the thesis: N_RSMEFT and its low-energy limit, N_RLEFT. Both frameworks encode new interactions of electroweak-scale sterile neutrinos in higher-dimensional operators. The relevant operators are classified up to dimension six in N_RLEFT and dimension seven in N_RSMEFT. This part also presents original work: a complete tree level decomposition of N_RSMEFT operators at dimension six and seven. This classification identifies the full set of one- and two-particle SM extensions that generate the EFT operators at tree level, providing a comprehensive EFT-UV dictionary. The analysis also explores the role of lepton number violation in N_RSMEFT and its connection to Majorana masses of SM neutrinos.

Finally, Part III investigates the collider phenomenology of electroweak scale HNLs using the EFT frameworks described in Part II, with a focus on LLP signatures at the LHC. It presents four original studies, each in a dedicated chapter. The first study focuses on four-fermion operators in N_RLEFT involving two HNLs or an HNL and a neutrino, and two light quarks. These operators trigger rare meson decays into HNLs, which can subsequently decay with a measurable displacement, yielding LLP

signatures in far detector experiments at the LHC. The next study turns to magnetic moment operators in N_RSMEFT and N_RLEFT. These lead to exotic signals at the main detectors such as non-pointing photons arising from GeV-scale HNL displaced decays. The third work analyzes four-fermion operators in N_RSMEFT involving a single HNL and first- and second-generation quarks, which can govern production and decay of HNLs, even in the absence of neutrino mixing. These interactions can be probed at the LHC as they lead to displaced vertices in the main detectors such as ATLAS. The last study considers similar operators, but involving third-generation quarks (top quarks) leading to novel production mechanisms and decay signatures of HNLs.

The phenomenological analyses performed in these studies combine analytical computations of HNL decay widths in the EFT frameworks with Monte Carlo simulations using a pipeline based on Feynrules, MadGraph5, MadSpin, and Pythia8, along with custom code implementing the LLP search strategies. Each study provides sensitivity estimates for LLP searches at ATLAS or proposed far detectors at the LHC, such as MATHUSLA and ANUBIS, showing how these setups can probe unexplored regions of parameter space and test scenarios that remain inaccessible in traditional searches.

In summary, this thesis demonstrates how EFTs and LLP searches can together provide powerful, model-independent strategies to explore new physics motivated by the neutrino sector. Heavy neutral leptons emerge as a well-motivated and experimentally accessible target. By bridging UV models, EFT frameworks, and collider phenomenology, this work contributes to expanding the toolkit for discovering superweakly coupled particles at current and future experiments.

List of Publications

This doctoral thesis is based on the following scientific publications, ordered according to the content of the manuscript:

1) **Tree-level UV completions for N_RSMEFT $d = 6$ and $d = 7$ operators**
   R. Beltrán, R. Cepedello, M. Hirsch
   JHEP 08 (2023) 166 • ePrint: 2306.12578 [hep-ph]

2) **Long-lived heavy neutral leptons from mesons in effective field theory**
   R. Beltrán, G. Cottin, J. C. Helo, M. Hirsch, A. Titov, Z. S. Wang
   JHEP 01 (2023) 015 • ePrint: 2210.02461 [hep-ph]

3) **Probing Heavy Neutrino Magnetic Moments at the LHC using Long-Lived Particle Searches**
   R. Beltrán, P. D. Bolton, F. F. Deppisch, C. Hati, M. Hirsch
   JHEP 07 (2024) 153 • ePrint: 2405.08877 [hep-ph]

4) **Long-lived heavy neutral leptons at the LHC: four-fermion single-N_R operators**
   R. Beltrán, G. Cottin, J. C. Helo, M. Hirsch, A. Titov, Z. S. Wang
   JHEP 01 (2022) 044 • ePrint: 2110.15096 [hep-ph]

5) **Heavy neutral leptons and top quarks in effective field theory**
   R. Beltrán, G. Cottin, J. Günther, M. Hirsch, A. Titov, Z.S. Wang
   JHEP 05 (2025) 238 • ePrint: 2501.09065 [hep-ph]

Other scientific publications not included in this doctoral thesis:

1) **Heavy neutral leptons from kaons in effective field theory**
   R. Beltrán, J. Günther, M. Hirsch, A.Titov, Z. S. Wang
   Phys. Rev. D. 109 (2024) 11, 115014 • ePrint: 2309.11546 [hep-ph]

2) **Reinterpretation of searches for long-lived particles from meson decays**
   R. Beltrán, G. Cottin, M. Hirsch, A. Titov, Z. S. Wang
   JHEP 05 (2023) 031 • ePrint: 2302.03216 [hep-ph]

Contents

List of Abbreviations

BNV	Baryon Number Violation
BSM	Beyond the Standard Model
C.L.	Confidence Level
cLFV	charged Lepton Flavor Violation
DV	Displaced Vertex
ECAL	Electromagnetic calorimeter
EFT	Effective Field Theory
EWSB	Electroweak Symmetry Breaking
HNL	Heavy Neutral Lepton
HL-LHC	High-Luminosity LHC
IP	Interaction Point
LHC	Large Hadron Collider
LEFT	Low-Energy Effective Field Theory
LFV	Lepton Flavor Violation
LLP	Long-Lived Particle
LNC	Lepton Number Conservation
LNV	Lepton Number Violation
NP	New Physics
$\boldsymbol{N_R}$**LEFT**	Right-handed neutrino extension of LEFT
$\boldsymbol{N_R}$**SMEFT**	Right-handed neutrino extension of SMEFT
RGE	Renormalization Group Equations
SM	Standard Model
SMEFT	Standard Model Effective Field Theory
UV	Ultraviolet
VEV	Vacuum Expectation Value

Introduction

The Standard Model (SM) of particle physics, though remarkably successful, is incomplete. It provides no mechanism for neutrino masses, does not account for the nature of dark matter, and lacks an explanation for the observed baryon asymmetry of the universe. These puzzles strongly motivate the search for physics beyond the SM.

Over the last few decades, both theoretical and experimental efforts have aimed to uncover new physics. The Large Hadron Collider (LHC), as the most energetic collider to date, has led the experimetal search in the energy frontier. Yet, despite more than a decade of operation, no direct sign of new particles, interactions or symmetries has emerged. This persistent null result has prompted two main hypotheses: perhaps new physics lies at energy scales too high to be directly probed, or perhaps it is already within reach but so weakly coupled to the SM that it has evaded detection so far.

The first possibility is well captured by Effective Field Theories (EFTs), which allow us to describe the low-energy effects of heavy new particles without specifying their ultraviolet (UV) origin. The second scenario, involving *super-weakly* coupled particles, leads naturally to long-lived particle (LLP) signatures, exotic signals that cannot be mimicked by the SM particle content. The challenge of detecting such signatures has driven the development of novel experimental strategies and inspired the proposal of dedicated LLP detectors.

Among the best-motivated candidates for this type of new physics are sterile neutrinos, also referred to as heavy neutral leptons (HNLs). These appear in a variety of neutrino mass models and interact with the SM primarily through small mixings with active neutrinos, which make them prime examples of weakly coupled particles. Therefore, their potential for having long lifetimes and exotic decay signatures places them at the forefront of LLP search programs. This interplay between neutrino mass generation, weak couplings, and LLP signatures makes sterile neutrinos an especially compelling subject of study and exploring their properties, interactions, and experimental manifestations offers a powerful window into physics beyond the SM.

This thesis is framed along this line. It presents a comprehensive study of sterile neutrinos, focusing on their theoretical motivations, their connection to neutrino mass mechanisms and their collider phenomenology. It compiles the research I have conducted over the past four years and is structured in three parts, the latter two containing results from five original works.

Part I motivates neutrino physics as a gateway to weakly coupled particles: Chapter 1 reviews key theoretical implications of nonzero neutrino masses, including lepton number violation and neutrino electromagnetic properties; Chapter 2 discusses several well-established neutrino mass models that introduce sterile neutrinos as weakly coupled new states; and Chapter 3 motivates the study of long-lived particles, discussing the experimental signatures and the current landscape of LLP searches at the LHC and future experiments.

Part II explores sterile neutrinos in broader theoretical frameworks, both at low and high energies: Chapter 4 introduces two EFT frameworks to describe generalized sterile neutrino interactions at experimentally accessible energies, namely N_RSMEFT, the EFT of the SM extended with sterile neutrinos, and its low-energy counterpart, N_RLEFT; while Chapter 5 investigates possible UV completions of these EFTs and provides the first comprehensive tree level UV-EFT dictionary for N_RSMEFT.

Part III investigates the collider phenomenology of HNLs within these effective frameworks, with a focus on distinctive LLP signatures and detection prospects at the LHC. It presents four original studies, each in a dedicated chapter: Chapter 6 analyzes sub-GeV HNLs produced in meson decays; Chapter 7 considers GeV-scale sterile neutrinos with sizable magnetic dipole moments; Chapter 8 studies HNLs with GeV masses produced through interactions with first- and second-generation quarks; and Chapter 9 explores electroweak-scale HNLs interacting preferentially with top quarks. All four studies evaluate the potential of LLP searches at the LHC to probe long-lived HNLs across different mass ranges and with different interaction types.

The thesis concludes with some reflections on the broader implications of this research for neutrino physics and the search for hidden new physics at colliders.

Part I

Neutrinos as a window into weakly coupled new physics

Chapter 1

Neutrino physics: observations and theoretical implications

The discovery of neutrino oscillations over 25 years ago provided the first direct evidence that neutrinos have nonzero masses, marking a major breakthrough in our understanding of particle physics. This discovery challenged the SM, which originally assumed neutrinos to be massless, necessitating the introduction of new physics beyond its framework.

The confirmation that neutrinos have mass raises several fundamental theoretical questions. What is the mechanism responsible for their masses? Are neutrinos Dirac or Majorana particles? What is the absolute mass scale of neutrinos, and how are their masses ordered? Addressing these open questions is critical for constructing a more complete theory of fundamental interactions.

This chapter provides an overview of key aspects of neutrino physics that are central to these discussions. We begin in Section 1.1 with a summary of the neutrino oscillation paradigm, which established the need for nonzero neutrino masses. We then explore in Section 1.2 different theoretical perspectives on the origin of neutrino mass, including Dirac and Majorana possibilities, before discussing in Section 1.3 the connection between Majorana neutrinos and lepton number violation. Finally, we examine additional properties of massive neutrinos, such as neutrino magnetic moments and its connection to charged lepton flavor violation.

Throughout this discussion, we motivate sterile neutrinos, which naturally arise in neutrino mass mechanisms, and highlight how they fit into various aspects of neutrino physics, setting the stage for the more detailed theoretical treatment in Chapter 2.

1.1 Neutrino mixing and oscillations

Neutrinos are produced and detected via weak interactions as flavor eigenstates, denoted as ν_α ($\alpha = e, \mu, \tau$), but they propagate as mass eigenstates, ν_i ($i = 1, 2, 3$). This mismatch between the flavor and mass bases leads to the phenomenon of neutrino oscillations, where a neutrino produced in one flavor state can be detected as a different flavor after propagation. The relation between these two bases is given by [1]

$$\nu_\alpha = \sum_{i=1}^{3} U_{\alpha i}\, \nu_i, \tag{1.1}$$

where U is the lepton mixing matrix. As a consequence, the SM electroweak currents mediated by the W and Z gauge bosons can be rewritten in terms of the neutrino mass eigenstates as [1]

$$\mathcal{L}_{\text{CC}}^{\text{lepton}} = -\frac{g}{\sqrt{2}} U_{\alpha i} \left(\overline{\ell_\alpha} \gamma^\mu P_L \nu_i\right) W_\mu + \text{h.c.}, \tag{1.2}$$

$$\mathcal{L}_{\text{NC}}^{\text{lepton}} = -\frac{g}{2\cos\theta_W} U_{\alpha i} U^*_{\alpha j} \left(\overline{\nu_j} \gamma^\mu P_L \nu_i\right) Z_\mu, \tag{1.3}$$

where we implicitly sum over the mass (i, j) and flavor (α) indices. Here, g is the $SU(2)$ gauge coupling, θ_W is the Weinberg angle, P_L is the left-handed chirality projector and ℓ_α denotes a charged lepton of flavor $\alpha = e, \mu, \tau$. The matrix U in Eq. (1.2) corresponds to the PMNS matrix (named after Pontecorvo-Maki-Nakagawa-Sakata), which is conventionally expressed as [2]

$$U_{\text{PMNS}} = \begin{pmatrix} c_{12}c_{13} & s_{12}c_{13} & s_{13}e^{-i\delta_{CP}} \\ -s_{12}c_{23} - c_{12}s_{13}s_{23}e^{i\delta_{CP}} & c_{12}c_{23} - s_{12}s_{13}s_{23}e^{i\delta_{CP}} & c_{13}s_{23} \\ s_{12}s_{23} - c_{12}s_{13}c_{23}e^{i\delta_{CP}} & -c_{12}s_{23} - s_{12}s_{13}c_{23}e^{i\delta_{CP}} & c_{13}c_{23} \end{pmatrix}, \tag{1.4}$$

where we define $c_{ij} \equiv \cos\theta_{ij}$, $s_{ij} \equiv \sin\theta_{ij}$ and $\delta_{CP} \in [0, 2\pi]$. The phase δ_{CP} governs Charge-Parity (CP) violation in neutrino oscillations, affecting the asymmetry between neutrino and antineutrino conversion probabilities. The mixing angles θ_{12}, θ_{13} and θ_{23} are known as the solar, reactor and atmospheric mixing angles, respectively, named after the sources producing the neutrinos used to measure them.

If neutrinos are Majorana particles (see discussions in Sections 1.2 and 1.3), the PMNS matrix contains two additional CP-violating phases, $\eta_1, \eta_2 \in [0, 2\pi]$, leading to the extended form

$$\tilde{U}_{\text{PMNS}} = U(\theta_{12}, \theta_{13}, \theta_{23}, \delta_{CP}) \begin{pmatrix} e^{i\eta_1} & 0 & 0 \\ 0 & e^{i\eta_2} & 0 \\ 0 & 0 & 1 \end{pmatrix}, \tag{1.5}$$

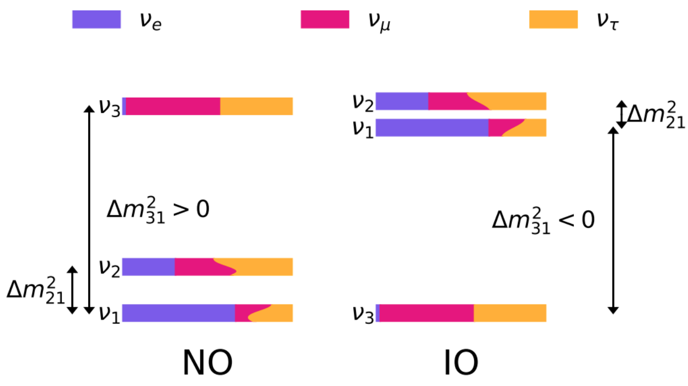

FIGURE 1.1: Two possible orderings for the neutrino mass eigenstates according to the sign of Δm^2_{31}: normal (NO) and inverted (IO). Image from [3].

where U is the same unitary matrix as in Eq. (1.4). Unlike δ_{CP}, the Majorana phases η_1 and η_2 do not affect neutrino oscillations and can only be probed through lepton number violating processes, such as neutrinoless double beta decay.

Besides the mixing angles, neutrino oscillations are also characterized by two independent mass-squared differences, denoted as Δm^2_{21} and Δm^2_{31}, known as the solar and atmospheric mass splittings, respectively. The sign of the latter remains undetermined, though, leading to the two possible neutrino mass orderings depicted in Fig. 1.1. We refer to normal ordering (NO) when $\Delta m^2_{31} > 0$, i.e., the lightest neutrino is the one with the largest electron component. In contrast, the inverted ordering (IO) corresponds to $\Delta m^2_{31} < 0$, where the lightest neutrino has the least amount of electron component. Although there is a mild preference for NO [4], the statistical significance remains limited to the 2σ level, leaving the issue unresolved. Future experiments, such as JUNO and Hyper-Kamiokande, aim to answer this question [5, 6]. The best fit values (68.4% C.L.) for the mass-squared differences derived from a global fit to observations of neutrino oscillations are [4]

$$\Delta m^2_{21} = \left(7.5^{+0.22}_{-0.20}\right) \times 10^{-5}\,\mathrm{eV}^2\,, \tag{1.6}$$

$$|\Delta m^2_{31}| = \begin{cases} \left(2.55^{+0.02}_{-0.03}\right) \times 10^{-3}\,\mathrm{eV}^2\ (\mathrm{NO})\,, \\ \left(2.45^{+0.02}_{-0.03}\right) \times 10^{-3}\,\mathrm{eV}^2\ (\mathrm{IO})\,. \end{cases} \tag{1.7}$$

For a state-of-the-art global fit of all the neutrino oscillation parameters, we refer the reader to Ref. [4] (see also Ref. [7]).

The observation of two distinct mass-squared differences establishes that at least two neutrinos must have nonzero mass, but the absolute neutrino mass scale remains unknown. Oscillation experiments, by their nature, are only sensitive to mass differences and cannot determine the absolute mass of any individual neutrino. To address this limitation, direct kinematic measurements from beta decay experiments provide a complementary approach. By analyzing the kinematics of electron emission in tritium decay, the KATRIN experiment has set an upper bound of $m_\nu < 0.45$ eV at 90% C.L. on the effective electron neutrino mass [8]. However, a direct measurement of the neutrino mass is still lacking. Cosmological observations provide additional, albeit model-dependent, constraints at the sub-eV level [9].

While the discovery of neutrino oscillations provided clear evidence of neutrino mass, it brought several puzzles that remain unresolved, strongly motivating the study of new physics scenarios addressing these open questions, such as the origin of neutrino mass or the nature of neutrinos. In the following sections we discuss these and other aspects of massive neutrinos.

1.2 Origin of neutrino mass

In its minimal formulation, the SM does not accommodate neutrino masses. Contrary to charged fermions, neutrinos lack right-handed counterparts, preventing a Yukawa interaction with the Higgs field. Additionally, a Majorana mass term involving only left-handed neutrinos cannot be written explicitly as it is not gauge invariant [10]. Consequently, the existence of neutrino masses necessarily implies the presence of BSM physics. When discussing neutrino mass generation mechanisms, one can classify them depending on the resulting Dirac or Majorana nature of neutrinos. In this section, we outline the primary approaches to both possibilites.

Dirac neutrino masses

A straightforward way to generate neutrino masses is to introduce right-handed neutrino fields, ν_R, which are singlets under the SM gauge group $G_{\text{SM}} = SU(3)_C \times SU(2)_L \times U(1)_Y$. This allows the construction of a Yukawa interaction analogous to that of the other SM fermions,

$$\mathcal{L}_{\text{Yuk}} = -\overline{L}\tilde{H}Y_\nu \nu_R + \text{h.c.}, \tag{1.8}$$

where L and H are the SM lepton and Higgs doublets and $\tilde{H} = i\sigma_2 H^*$. Here, Y_ν denotes the neutrino Yukawa matrix. After electroweak symmetry breaking (EWSB), the Higgs acquires a vacuum expectation value (VEV), $\langle H \rangle = v/\sqrt{2}$, leading to a Dirac mass for neutrinos,

$$m_\nu^D = Y_\nu \frac{v}{\sqrt{2}}. \tag{1.9}$$

Since experimental constraints require neutrino masses to be at most $\mathcal{O}$(eV), this scenario would necessitate Yukawa couplings $\mathcal{O}(10^{-11})$. This extreme suppression stands in contrast with the scale of other fermion Yukawa couplings,[1] raising the question of whether an additional mechanism is responsible for the smallness of Y_ν.

While this minimal setup suffices to generate Dirac neutrino masses, other possibilities exist that avoid the need for unnaturally small Yukawa couplings. One such possibility involves extending the Higgs sector. For example, introducing additional Higgs doublets or singlets can modify the neutrino mass structure [11, 12]. Another class of scenarios postulates new symmetries, such as discrete lepton number symmetries, which forbid neutrino masses at tree level but allow them to arise through symmetry breaking [13, 14]. These constructions provide a compelling alternative to the minimal Dirac mass scenario and can be embedded in larger frameworks that also address dark matter or other open questions in particle physics.

Majorana neutrinos and the Weinberg operator

A fundamental difference between neutrinos and other SM fermions is their lack of electric charge, allowing them to be Majorana particles, that is, identical to their own antiparticles. This opens an alternative route to generating neutrino masses. The minimal extension of the SM accounting for Majorana neutrino masses is the dimension 5 ($d = 5$) operator known as the Weinberg operator [15],

$$\mathcal{O}_{\text{Weinberg}} = (\overline{L^c_\alpha}\tilde{H}^*)(\tilde{H}^\dagger L_\beta), \tag{1.10}$$

where $L^c \equiv \mathcal{C}\bar{L}^T$, with $\mathcal{C}$ being the charge conjugation matrix. Being a dimension 5 operator, in the Lagrangian it appears with a prefactor $c_{\alpha\beta}/\Lambda$,[2] where Λ denotes a new physics energy scale and $c_{\alpha\beta}$ is a Wilson coefficient in flavor space. After EWSB, this operator induces a Majorana mass term proportional to $m_\nu^M \sim v^2/\Lambda$.

Since the observed neutrino masses are below the eV scale, this implies that Λ should be significantly larger than the electroweak scale, around 10^{14} GeV assuming $\mathcal{O}(1)$ Wilson coefficients. This suggests the presence of new physics at or near the scale of grand unification, which lies far beyond the sensitivity of any terrestrial experiment.

[1]The Yukawa couplings for the charged fermions range from $\mathcal{O}(10^{-6})$, as for the electron, to $\mathcal{O}(1)$, as for the top quark.

[2]This higher-dimensional operator approach lies within the framework of effective field theories, which are discussed in detail in Chapter 4.

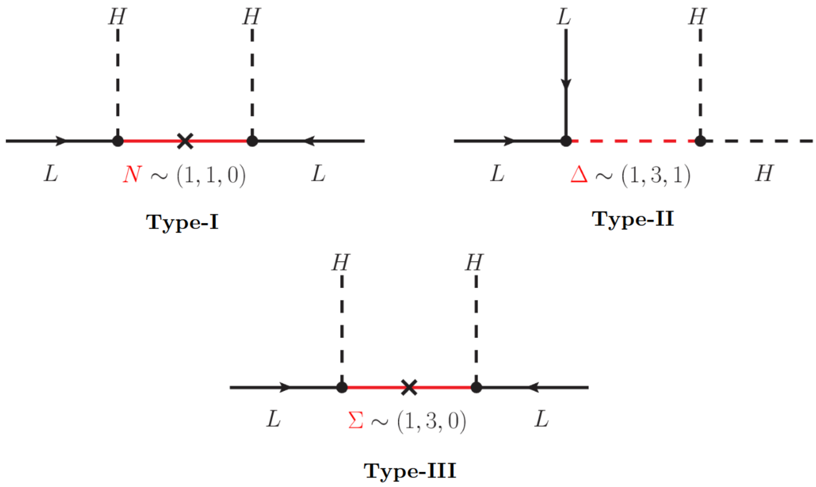

FIGURE 1.2: Tree level openings of the Weinberg operator corresponding to the three seesaw mechanisms. Each mechanism adds a new field to the SM particle content: a singlet fermion (type-I), a triplet scalar (type-II) or a triplet fermion (type-III).

However, the scale at which this operator is generated might be much lower if the Wilson coefficients are suppressed, giving rise to observable phenomena at experiments. We discuss this issue affecting neutrino mass mechanisms in Chapter 2.

Crucially, this operator explicitly violates lepton number by two units, providing a direct link between neutrino masses and Lepton Number Violation (LNV). This connection has profound phenomenological implications, which we discuss in the following section.

The Weinberg operator represents an effective description of neutrino masses at low energies but does not specify the underlying high-energy completion responsible for its generation. At tree level, the Weinberg operator can be generated in exactly three distinct ways by introducing new heavy particles, as illustrated in Fig. 1.2. They introduce either a singlet fermion $N \sim (\mathbf{1}, \mathbf{1}, 0)$, triplet scalar $\Delta \sim (\mathbf{1}, \mathbf{3}, 1)$ or triplet fermion $\Sigma \sim (\mathbf{1}, \mathbf{3}, 0)$, corresponding to the Type-I [16, 17], Type-II [18, 19, 20], and Type-III [21] seesaw mechanisms, respectively.

Among these mechanisms, the Type-I seesaw is the simplest and most widely studied as it extends the SM only by incorporating singlet fermions or sterile neutrinos. Beyond this minimal realization, sterile neutrinos also appear in a variety of neutrino mass models and broader extensions of the SM, such as Left-Right Symmetric models [22, 23]. For this reason, we separately discuss the role of sterile neutrinos in neutrino mass models in Chapter 2.

Beyond tree level and the Weinberg Operator

While the Weinberg operator and its tree level realizations provide the simplest extensions of the SM to accommodate neutrino masses,[3] other mechanisms may be at play. For instance, radiative neutrino mass models. Instead of being generated at tree level, neutrino masses can arise at loop level, leading to additional suppression factors that naturally explain their smallness. Well-known examples include the Zee model [24], which introduces charged scalars in one-loop diagrams, and the Scotogenic model [25], where neutrino masses are generated via a dark sector. Such scenarios are particularly attractive because they can relate neutrino mass generation to dark matter.

Another possibility is that Majorana neutrino masses originate from LNV higher-dimensional operators beyond the Weinberg term. Although the Weinberg operator is the leading contribution in an effective field theory expansion, it may be absent in certain UV completions, making higher-dimensional terms ($d = 7$ or higher) dominant. These operators introduce novel LNV interactions and have been systematically classified within the Standard Model Effective Field Theory (SMEFT) framework up to $d = 11$ [26].

Such alternative pathways to neutrino mass generation are actively explored in the literature, and recent efforts have focused on classifying all possible tree level and loop level realizations of the LNV higher-dimensional operators [27, 28, 29, 30, 31, 32]. These approaches not only provide insights into the structure of neutrino masses but also establish connections with other BSM phenomena, including lepton flavor violation and dark matter.

1.3 Lepton number violation and Majorana neutrinos

LNV is deeply linked to the Majorana nature of neutrinos. A Majorana mass term inherently violates lepton number by two units ($\Delta L = 2$), opening the door to BSM processes such as neutrinoless double beta decay ($0\nu\beta\beta$). This hypothetical process, in which a nucleus undergoes double beta decay without emitting neutrinos, is the most sensitive experimental probe of Majorana neutrinos. The observation of $0\nu\beta\beta$ would provide unambiguous evidence that at least one neutrino mass eigenstate has a Majorana component, independent of the specific underlying mechanism. This result follows from the so-called black box theorem [33], which states that if $0\nu\beta\beta$ is

[3] If neutrinos were Dirac fermions, analogous seesaw realizations to generate neutrino masses can also be invoked.

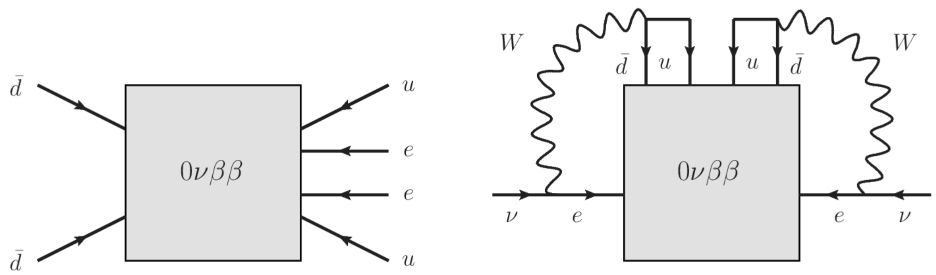

FIGURE 1.3: Black box theorem of $0\nu\beta\beta$ decay graphically: whatever is the underlying mechanism generating a nonzero neutrinoless double beta decay amplitude (left diagram), will also generate a Majorana mass term for at least one of the SM neutrinos (right diagram).

observed, a Majorana mass term for neutrinos is necessarily generated at some order in perturbation theory. This is illustrated in Fig. 1.3. The diagram on the left is a schematic representation of $0\nu\beta\beta$, where the box includes all possible mechanisms contributing to the process. Only the external lines of the quarks and the two final electrons are visible. The diagram on the right shows how the same external lines can be joined via SM weak interactions to neutrino lines in order to generate a Majorana mass entry.

Note that, while $0\nu\beta\beta$ establishes the existence of Majorana mass terms, the induced contribution to the observed neutrino masses is expected to be orders of magnitude smaller than the mass splittings measured in neutrino oscillations [34], implying that $0\nu\beta\beta$ alone is not the dominant mechanism for neutrino mass generation.

The opposite statement is also true: the main contribution to the $0\nu\beta\beta$ decay does not necessarily come from the exchange of Majorana massive neutrinos, but the mass mechanism is guaranteed to give a contribution. Assuming that the primary contribution to $0\nu\beta\beta$ comes from the exchange of light Majorana neutrinos, corresponding to the diagram in Fig. 1.4, and no other new physics is involved, the amplitude of the process is proportional to the effective Majorana mass parameter defined as

$$m_{\beta\beta} = \left| \sum_{i=1}^{3} U_{ei}^2 m_i \right|, \tag{1.11}$$

where U_{ei} are the first-row elements of the Majorana PMNS mixing matrix, cf. Eq. (1.5), and m_i are the neutrino mass eigenvalues. Note that this process is sensitive to the Majorana phases of the lepton mixing matrix. In addition, depending on the neutrino mass ordering, the value of $m_{\beta\beta}$ differs significantly. For IO, the contribution

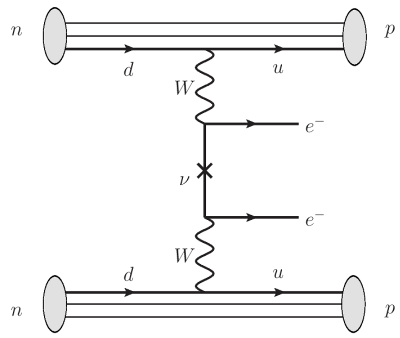

FIGURE 1.4: Contribution from light Majorana neutrino exchange to $0\nu\beta\beta$ decay.

is typically large, leading to $0\nu\beta\beta$ rates that should be within experimental reach if neutrinos are Majorana. In contrast, for NO a strong suppression is possible due to destructive interference between terms in the sum. In extreme cases, this could render $0\nu\beta\beta$ effectively unobservable, even if neutrinos are Majorana particles [35].

Current experimental efforts, such as GERDA, KamLAND-Zen, LEGEND-200 and CUORE, are searching for $0\nu\beta\beta$ and setting stringent limits on $m_{\beta\beta}$, with sensitivities reaching the range of $60 - 300$ meV [36, 37, 38]. Future projects like nEXO, DARWIN and LEGEND-1000 aim to push these limits further, potentially probing IO [39, 40, 41].

While light neutrino exchange provides the minimal interpretation, new physics can contribute to $0\nu\beta\beta$ via mechanisms that do not rely on the standard seesaw Majorana masses. For instance, supersymmetric models with R-parity violation [42, 43], scalar leptoquarks [44, 45] or Left-Right Symmetric models [46]. In general, the contributions to the $0\nu\beta\beta$ can be divided into a long-range [47] and short-range [48] part. The former refers to the cases where a light virtual neutrino is exchanged between two nucleons, while the latter includes all possible heavy particle exchanges, usually encoded by an effective high-dimensional operator.

We finally comment that, beyond neutrinoless double beta decay, LNV could also manifest in other processes, such as rare meson decays, providing complementary experimental tests of Majorana neutrinos. These processes are particularly interesting in scenarios where Majorana sterile neutrinos exist at the GeV scale. The potential relation between sterile neutrinos and LNV will be further discussed in Part II and LNV rare meson decays involving sterile neutrinos will be revisited in Part III.

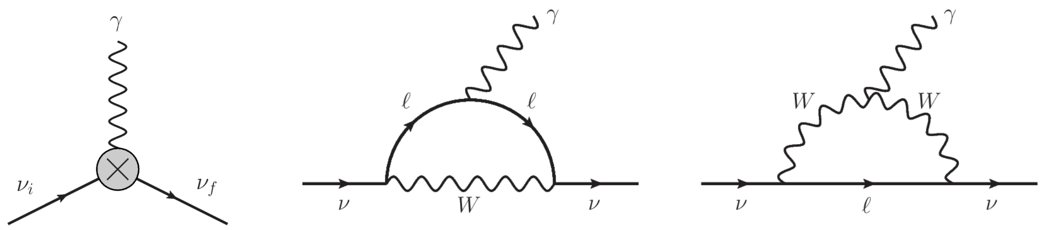

(a) (b)

FIGURE 1.5: a) Effective interaction vertex describing neutrino magnetic moments. b) One-loop diagrams in the SM contributing to the magnetic moment.

1.4 Neutrino magnetic moments

Massive neutrinos present further properties beyond oscillations and mixing. For instance, they show effective electromagnetic interactions with photons as depicted in Fig. 1.5a. In this section, we focus on neutrino magnetic moment interactions, which at low energies can be described by the effective lagrangian

$$\mathcal{L}_{\text{eff}} \propto \frac{\mu_{fi}}{2}\left(\overline{\nu_f}\sigma^{\mu\nu}\nu_i\right)F_{\mu\nu}\,, \tag{1.12}$$

where $F_{\mu\nu}$ is the photon field strength tensor, $\sigma^{\mu\nu} \equiv \frac{i}{2}\left[\gamma^\mu, \gamma^\nu\right]$, and μ_{fi} is the neutrino magnetic moment. If neutrinos are Dirac particles, both diagonal (μ_{ii}) and transition (μ_{fi}, with $f \neq i$) magnetic moments exist. However, if neutrinos are Majorana, only transition moments are present, as the diagonal terms vanish exactly due to symmetry arguments.

In the SM, extended to include nonzero neutrino masses, neutrinos acquire a magnetic moment through one-loop diagrams as those shown in Fig. 1.5b. In the Dirac case, the complete calculation leads to the result [49]

$$\mu^D_{fi} \simeq \frac{3eG_F}{8\sqrt{2}\pi^2}(m_f + m_i)\left(\delta_{fi} - \sum_{\alpha=e,\mu,\tau} U^*_{\alpha f}U_{\alpha i}\frac{m^2_\alpha}{m^2_W}\right)\,, \tag{1.13}$$

where G_F is the Fermi constant and e is the electron charge. The result depends on the neutrino mass eigenvalues $m_{f,i}$, the W boson mass and the mass of the charged lepton ($\alpha = e, \mu, \tau$) running in the loop (see Fig. 1.5b). Since the mass ratio is small, $m^2_\alpha/m^2_W \leq m^2_\tau/m^2_W \approx 5 \times 10^{-4}$, the previous expression can be expanded in a Taylor series of m^2_α/m^2_W. The diagonal magnetic moments ($f = i$) can be then approximated at leading order to

$$\mu^D_{ii} \approx \frac{3eG_F}{8\sqrt{2}\pi^2}m_i = 3 \times 10^{-19}\mu_B\left(\frac{m_i}{\text{eV}}\right)\,, \tag{1.14}$$

where $\mu_B = 2e/m_e$ is the Bohr magneton. Assuming neutrino masses below the eV scale, this numerical estimation is well below the sensitivity of current experiments. The Dirac transition magnetic moments ($f \neq i$) are further suppressed relative to the diagonal moment μ_{ii}^D by an additional factor of m_α^2/m_W^2, leading to values of order $10^{-23}\mu_B$ or smaller.

For Majorana neutrinos, only transition moments are present, and in the limit of small m_α^2/m_W^2, the leading contribution is

$$\mu_{fi}^M \approx -\frac{3ieG_F}{8\sqrt{2}\pi^2}(m_f + m_i) \sum_{\alpha=e,\mu,\tau} \mathrm{Im}\left(U_{\alpha f}^* U_{\alpha i}\right) \frac{m_\alpha^2}{m_W^2} \,. \tag{1.15}$$

This result cannot be directly compared to the Dirac one as the mixing matrices are different in the two cases. Nevertheless, the Majorana transition dipole moments are also suppressed by m_α^2/m_W^2 and so they are expected to be no larger than $10^{-23}\mu_B$.

Experimental searches for neutrino magnetic moments at reactor experiments, such as GEMMA, have set upper bounds of approximately $\mu_\nu < 2.9\times10^{-11}\mu_B$ at 90% C.L. [50]. Astrophysical limits, derived from stellar cooling processes, are even more stringent, placing constraints at the level of $\mu_\nu < 10^{-12}\mu_B$ [51]. Future experiments probing coherent neutrino-nucleus scattering aim to further improve these bounds [52, 53].

Many BSM models predict enhanced neutrino magnetic moments through additional loop corrections involving new particles charged under the SM. Such new physics contributions can significantly modify the active neutrino magnetic moments, potentially bringing them within experimental reach. More interestingly, scenarios with sterile neutrinos introduce the possibility of new transition magnetic moments between active and sterile states, as well as purely sterile-sterile magnetic moments. These interactions are also experimentally testable and have been explored in laboratory searches [54, 55, 56] and astrophysical observations [57, 58]. In Chapter 7, we will come back to this topic and analyze a scenario where such active-sterile and sterile-sterile dipole moments arise and discuss their phenomenological implications.

1.5 Charged Lepton Flavor Violation

In the SM extended with only left-handed neutrino masses, charged Lepton Flavor Violation (cLFV) is mediated by neutrino mixing although it is highly suppressed due to the tiny neutrino masses. For instance, the decay $\mu \to e\gamma$ can proceed via the one-loop process shown in Fig. 1.6, as a consequence of the flavor changing interactions in Eq. (1.2). The decay rate of this process can be computed in the R_ξ gauge, taking

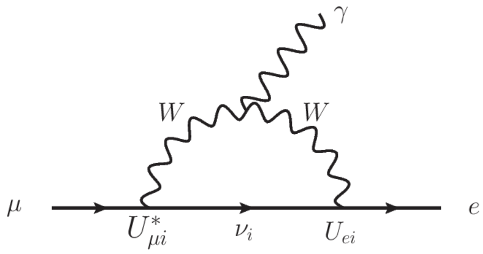

FIGURE 1.6: Contribution from light neutrino mixing to the cLFV decay $\mu \to e\gamma$.

into account additional diagrams. Finally, dividing by the dominant lepton flavor conserving rate $\Gamma(\mu \to e\nu\bar{\nu})$, the resulting branching ratio yields [59]

$$\mathcal{B}(\mu \to e\gamma) = \frac{3\alpha_e}{32\pi}\left|\sum_i U^*_{ei}U_{\mu i}\frac{m_i^2}{m_W^2}\right|^2 , \tag{1.16}$$

where α_e is the fine structure constant and the sum runs over the light neutrino mass eigenstates. Substituting the best-fit numerical values of the oscillation parameters leads to an estimated branching ratio of $\mathcal{B}(\mu \to e\gamma) \sim 10^{-54} - 10^{-55}$. This is vastly below the current and foreseeable experimental sensitivity, making the detection of this decay impossible.

In the presence of new physics, cLFV rates can be significantly enhanced, making these processes powerful probes of BSM physics. Many well-motivated scenarios, including supersymmetry or two-Higgs doublet models, predict sizable contributions to cLFV observables [60, 61, 62]. Importantly, a direct connection exists between neutrino mass models and cLFV phenomenology [63, 64]. Of special relevance for us are those mass mechanisms featuring heavy sterile neutrinos. If sterile neutrinos mix significantly with the active neutrino sector, they can mediate the processes $\ell_\alpha \to \ell_\beta\gamma$ and $\ell_\alpha \to \ell_\beta\ell_\sigma\ell_\sigma$ at observable rates [65]. The strength of these effects depends on the sterile neutrino mass scale and their couplings to SM leptons, providing a complementary probe of the mechanism behind neutrino mass generation.

The experimental search for cLFV rare processes is an essential part of the broader effort to uncover new physics. Dedicated experiments have set increasingly stringent limits on these decays, especially in muon and tau decays. Table 1.1 summarizes the current experimental bounds on some cLFV observables and the future sensitivity of upcoming experiments to these processes. A positive signal in any of these channels would be a clear indication of BSM physics, offering valuable insights into the flavor structure of new interactions and potentially shedding light on the mechanism

cLFV observable	Current bound	Future sensitivity
$\mathcal{B}(\mu \to e\gamma)$	4.2×10^{-13} (MEG [66])	6×10^{-14} (MEG II [67])
$\mathcal{B}(\tau \to e\gamma)$	3.3×10^{-8} (BaBar [68])	3×10^{-9} (Belle II [69])
$\mathcal{B}(\tau \to \mu\gamma)$	4.2×10^{-8} (Belle [70])	10^{-9} (Belle II [69])
$\mathcal{B}(\mu \to 3e)$	1.0×10^{-12} (SINDRUM [71])	$10^{-15(-16)}$ (Mu3e [72])
$\mathcal{B}(\tau \to 3e)$	2.7×10^{-8} (Belle [73])	5×10^{-10} (Belle II [69])
$\mathcal{B}(\tau \to 3\mu)$	1.9×10^{-8} (Belle II [74])	5×10^{-10} (Belle II [69])

TABLE 1.1: Current bounds and future sensitvity to cLFV observables. Quoted limits correspond to 90% C.L.

responsible for neutrino mass generation.

Interestingly, cLFV processes and neutrino magnetic properties are often related in BSM scenarios, as they both arise from new sources of lepton flavor violation. However, this connection is model-dependent. In some frameworks, new physics contributions to neutrino magnetic moments may be enhanced without significantly affecting cLFV rates, while in others, both effects stem from the same underlying interactions. In Chapter 7, we will explore a specific BSM model where a common UV origin gives rise to both sizable neutrino magnetic moments and enhanced cLFV rates, offering a testable link between these two observables.

To conclude this chapter, we have shown how the existence of nonzero neutrino masses points unambiguously to physics beyond the SM. We briefly reviewed some of the most relevant consequences, including lepton number violation, neutrino electromagnetic properties, and charged lepton flavor violation, and discussed their connection to new physics scenarios. While the exact mechanism responsible for neutrino mass generation remains unknown, all viable models require extending the SM with new ingredients. Among the most compelling possibilities is the introduction of sterile neutrinos. In the following chapter, we explore a range of neutrino mass models featuring sterile neutrinos and highlight their potential for experimental discovery.

Chapter 2

Neutrino mass models and sterile neutrinos

Since the 1980s, a wide variety of theoretical models has been proposed to explain the small but nonzero masses of neutrinos. While these models can be classified from different perspectives — by the loop order at which neutrino masses arise or by whether neutrinos are Dirac or Majorana particles — they all share the common feature of extending the SM with new fields, interactions, or symmetries. Identifying experimental signatures of these extensions could provide crucial insights into the underlying neutrino mass mechanism.

In Chapter 1, we briefly reviewed the current experimental status and theoretical implications of massive neutrinos, emphasizing the need for new physics. One particularly well-motivated scenario involves the introduction of sterile neutrinos: gauge-singlet fermions that do not couple directly to the SM gauge interactions. In this chapter, we focus on neutrino mass models in which sterile neutrinos play a central role. These frameworks not only explain the smallness of active neutrino masses but also predict heavy Majorana or pseudo-Dirac states that may be within reach of current or future high-energy experiments. This connection between the neutrino mass mechanism and testable signatures provides strong motivation for their study.

To illustrate these ideas, Section 2.1 introduces the Type-I seesaw mechanism, the simplest and most widely studied framework involving sterile neutrinos. Section 2.2 explores two low-scale seesaw variations: the inverse seesaw and the linear seesaw. Finally, Section 2.3 presents the Scotogenic model, in which sterile neutrinos generate neutrino masses radiatively at one loop.

2.1 Type-I Seesaw mechanism

The Type-I seesaw [16, 17] constitutes the minimal extension of the SM that allows for neutrino mass generation. It introduces n generations of right-handed neutrinos,[1] denoted as N_R, which are singlets under the SM gauge group and therefore often referred to as sterile neutrinos. The general Type-I seesaw Lagrangian is given by

$$\mathcal{L}_{\text{type-I}} = i\overline{N_R}\partial\!\!\!/ N_R - \left(\overline{L}\tilde{H}Y_\nu N_R + \frac{1}{2}\overline{N_R^c}M_R N_R + \text{h.c.}\right) \tag{2.1}$$

where $N_R^c \equiv \mathcal{C}\overline{N_R}^T$, with $\mathcal{C}$ being the charge conjugation matrix, Y_ν is the $3 \times n$ neutrino Yukawa coupling matrix and M_R is a symmetric $n \times n$ Majorana mass matrix for the sterile neutrinos. If we assign lepton number $L(N_R) = 1$, then all terms in the Lagrangian conserve lepton number except for the Majorana mass term, which explicitly violates lepton number by two units ($\Delta L = 2$). The sterile neutrinos interact with the SM exclusively through their Yukawa interactions.

After Electroweak Symmetry Breaking (EWSB), the Higgs acquires a Vacuum Expectation Value (VEV), $\langle H \rangle = v/\sqrt{2}$, leading to the following mass terms in the neutral lepton sector [1]

$$\mathcal{L}_{\text{type-I}}^{\text{mass}} \supset -\frac{1}{2}\begin{pmatrix}\overline{\nu_L} & \overline{N_R^c}\end{pmatrix}\mathcal{M}_\nu\begin{pmatrix}\nu_L^c \\ N_R\end{pmatrix} + \text{h.c.}\,; \quad \mathcal{M}_\nu = \begin{pmatrix} 0 & \frac{vY_\nu}{\sqrt{2}} \\ \frac{vY_\nu^T}{\sqrt{2}} & M_R\end{pmatrix}. \tag{2.2}$$

To move to the mass basis, we perform a unitary transformation to block-diagonalize $\mathcal{M}_\nu$. Assuming the Majorana mass scale is much larger than the electroweak scale, $|M_R| \gg v$, an expansion in vM_R^{-1} leads to the well-known seesaw expressions for the light and heavy neutrino masses [1]

$$m_\nu \approx -\frac{v^2}{2}\left(Y_\nu M_R^{-1} Y_\nu^T\right), \qquad M_N \approx M_R\,, \tag{2.3}$$

where the heavy scale M_R is expected to highly suppress m_ν. The resulting Majorana mass eigenstates consist of three light neutrinos, $\nu_i\,(i = 1, 2, 3)$, which are predominantly SM-like, and n heavy neutrinos, $N_j\,(j = 1, \ldots, n)$, which are mostly sterile.[2]

[1] At least two sterile neutrinos are needed to reproduce the neutrino oscillation data.

[2] The diagonalization procedure further requires an additional rotation to express the mass eigenstates in terms of the flavor basis. In particular, the light neutrino mass is given by

$$\hat{m}_\nu = U^\dagger m_\nu U\,,$$

where U is the PMNS matrix for Majorana neutrinos introduced in Chapter 1. Without loss of generality, M_R can be chosen to be diagonal.

As a byproduct of the diagonalization process, there is an induced mixing between the active SM neutrinos and the sterile neutrinos, which, at first order in the seesaw expansion, is given by

$$V_{\alpha N_i} \approx \frac{v}{\sqrt{2}} \left(Y_\nu M_R^{-1} \right)_{\alpha i} , \tag{2.4}$$

where α denotes a flavor index and i refers to the sterile neutrino generation index. As a consequence, the heavy (nearly) sterile states inherit the electroweak interactions of SM neutrinos, although suppressed by this mixing parameter. The charged and neutral current interactions for the sterile states read [1]

$$\mathcal{L}_{\rm CC}^{\rm sterile} = -\frac{g}{\sqrt{2}} V_{\alpha N_i} \left(\overline{\ell_\alpha} \gamma^\mu P_L N_i \right) W_\mu + \text{h.c.}, \tag{2.5}$$

$$\mathcal{L}_{\rm NC}^{\rm sterile} = -\frac{g}{2\cos\theta_W} \left\{ U_{\alpha k} V^*_{\alpha N_i} \left(\overline{N_i} \gamma^\mu P_L \nu_k \right) + V_{\alpha N_j} V^*_{\alpha N_i} \left(\overline{N_i} \gamma^\mu P_L N_j \right) \right\} Z_\mu, \tag{2.6}$$

where we implicitly sum over the flavor (α) and generation (i, j, k) indices. Importantly, these interactions can lead to observable effects as the N can be produced and decay to different final states in collider experiments. However, the observability ultimately depends on the interaction strength governed by the mixing parameter.

To reproduce the observed light neutrino masses via Eq. (2.3), one can assume Dirac Yukawa couplings $Y_\nu \sim 1$, requiring a Majorana mass scale $M_R \sim 10^{14}$ GeV. In this limit of such high scales, one can integrate out the heavy sterile neutrinos from the Lagrangian, effectively generating the Weinberg operator in Eq. (1.10). Alternatively, if the Dirac Yukawas are highly suppressed, say $Y_\nu \sim 10^{-6}$ (as for the electron Yukawa), then a much lower Majorana mass, $M_R \sim 100$ GeV, is necessary to obtain the correct neutrino masses. This latter possibility is preferred from the phenomenology point of view since such a heavy sterile neutrino could be probed at terrestrial experiments. Nevertheless, the active-sterile neutrino mixing is extremely small, even for not so heavy sterile neutrino masses: a naive estimation using Eq. (2.4) and assuming there are no cancellations among the different terms contributing to m_ν leads to $V \sim 10^{-13}$ for $M_R \sim 10^{14}$ GeV and $V \sim 10^{-7}$ for $M_R \sim 100$ GeV.

In summary, although it is a very elegant solution to the neutrino mass problem, the Type-I seesaw is challenging to probe. If the Majorana mass scale is too high, the heavy neutrinos lie outside experimental reach. On the other hand, even if M_R is within experimental reach, the active-sterile mixing is typically too small to be observed in current or near-future experiments. This motivates exploring alternative seesaw realizations with enhanced experimental signatures, which we discuss next.

2.2 Inverse and linear seesaw mechanisms

The inverse [75, 76, 77] and linear [78, 79, 80] seesaw variants extend the SM particle content by introducing n and m generations of two types of sterile neutrinos, denoted as N_R and S_L, respectively. The most general Lagrangian governing their interactions is then given by [1, 81]

$$\begin{aligned}
-\mathcal{L} \supset\ & \overline{L}\tilde{H}Y_\nu N_R + \overline{S_L}M_{NS}N_R \\
& + \overline{L}\tilde{H}\epsilon Y_S S_L^c + \frac{1}{2}\mu_N \overline{N_R^c}N_R + \frac{1}{2}\mu_S \overline{S_L}S_L^c + \text{h.c.}\,,
\end{aligned} \tag{2.7}$$

where Y_ν and ϵY_S are $3 \times n$ and $3 \times m$ Dirac Yukawa matrices coupling the sterile neutrinos to the Higgs, while M_{NS} is a $n \times m$ mass matrix connecting N_R and S_L. The parameters μ_N and μ_S are Majorana mass matrices for the sterile neutrinos. If we make the lepton number assignment $L(N_R) = L(S_L) = L(L)$, then the terms in the first row conserve lepton number, whereas those in the second one violate it. The three quantities in the interaction terms of the second row, ϵY_S, μ_N and μ_S, are therefore expected to be small in the 't Hooft sense [82], as lepton number symmetry is restored in the limit $\epsilon, \mu_{N,S} \to 0$.

After EWSB, the mass matrix of the neutral fermions, in the $(\nu_L^c\,, N_R\,, S_L^c)^T$ basis, takes the form

$$\mathcal{M}_\nu = \begin{pmatrix} 0 & m_{\nu N} & \epsilon\, m_{\nu S} \\ m_{\nu N}^T & \mu_N & M_{NS} \\ \epsilon\, m_{\nu S}^T & M_{NS}^T & \mu_S \end{pmatrix}, \tag{2.8}$$

where we have defined the Dirac mass terms as $(m_{\nu N}, m_{\nu S}) \equiv (vY_\nu/\sqrt{2}, vY_S/\sqrt{2})$. Depending on the underlying symmetries, some LNV parameters may be absent. Here, we study two possible textures of the mass matrix, corresponding to two seesaw realizations: the inverse seesaw, obtained in the limit $\epsilon = \mu_N = 0$ with $\mu_S \ll M_{NS}$; and the linear seesaw, which arises when $\mu_N = \mu_S = 0$ and $\epsilon m_{\nu S} \ll M_{NS}$.

In both cases, diagonalizing the mass matrix leads to a light neutrino sector and a heavy sterile neutrino sector. Analogously to the Type-I seesaw, one can perform an expansion in the small quantities μ_S/M_{NS} and $\epsilon m_{\nu S}/M_{NS}$, leading to the light neutrino mass matrix

$$m_\nu \simeq -m_{\nu N}\frac{1}{M_{NS}^T}\mu_S\frac{1}{M_{NS}}m_{\nu N}^T - \epsilon\left(m_{\nu S}\frac{1}{M_{NS}}m_{\nu N}^T + m_{\nu N}\frac{1}{M_{NS}^T}m_{\nu S}^T\right). \tag{2.9}$$

The expression for the inverse (linear) seesaw can be then obtained by taking $\epsilon \to 0$ ($\mu_S \to 0$). Notice that, to lowest order, the Majorana mass μ_N does not contribute

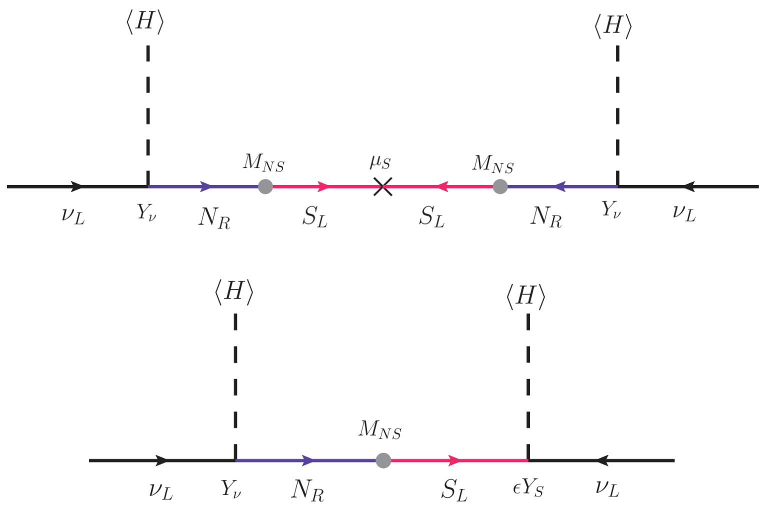

FIGURE 2.1: Tree level contributions to neutrino mass in the gauge basis in the inverse (top) and linear (bottom) seesaw models.

to m_ν. However, it contributes to finite 1-loop corrections of m_ν, which can even be sizable for non-negligible values of μ_N [83]. We illustrate the light neutrino mass generation mechanism for the two seesaw variants in Fig. 2.1.

Unlike in the Type-I seesaw, where neutrino masses are suppressed by an inverse power of a large Majorana mass, the expression in Eq. (2.9) reveals that light neutrino masses are further suppressed by either μ_S (in the inverse seesaw) or by ϵ (in the linear seesaw). This means the scale M_{NS} (the analogue to M_R in the Type-I) does not need to be as large as in the canonical seesaw. A rough numerical estimate assuming $m_{\nu N} \sim \mathcal{O}$(GeV) and $\mu_S \sim \mathcal{O}$(keV) in the inverse seesaw limit (or $\epsilon m_{\nu S} \sim \mathcal{O}(10\,\text{eV})$ in the linear seesaw limit) suggests that neutrino masses can be correctly reproduced with $M_{NS} \sim \mathcal{O}$(TeV). This manifests the low-energy character of these seesaw variants.

As regards the heavy sterile eigenstates, in both seesaw variants they present similar phenomenology. Therefore, for illustrative purposes, let us discuss only the inverse seesaw scenario ($\epsilon = \mu_N = 0$ and $\mu_S \neq 0$). In this case, the heavy neutrinos, with masses at the M_{NS} scale, form quasi-degenerate pairs (usually referred to as quasi-Dirac states [84, 85]) with a mass splitting proportional to μ_S. In the exact $\mu_S \to 0$ limit, they become degenerate forming a Dirac pair. As a consequence, LNV processes involving the heavy neutrinos are absent in this limit, in contrast to the Type-I seesaw. Although this limiting case is not completely realistic, since light neutrino masses would vanish exactly, it provides a natural way to suppress LNV observables.

Field	Irrep	Spin	Multiplicity	$\mathbb{Z}_2$
η	$\left(\mathbf{1},\mathbf{2},\frac{1}{2}\right)$	0	1	–
N	$(\mathbf{1},\mathbf{1},0)$	$\frac{1}{2}$	3	–

TABLE 2.1: New particle content of the Scotogenic model and their corresponding quantum numbers under the SM gauge symmetry. Both fields are odd under the discrete $\mathbb{Z}_2$ symmetry.

Another key feature of the inverse seesaw is the enhanced active-sterile mixing compared to the Type-I seesaw. The mixing parameter scales as $V \sim m_{\nu N}/M_{NS} \sim \sqrt{m_\nu/\mu_S}$. Since μ_S is pressumably small, this allows for sizable active-sterile mixing without requiring extremely suppressed Yukawa couplings. This makes the inverse seesaw (and low-energy seesaw variants in general) particularly appealing for experimental searches, as the heavy neutrinos could be within collider energy reach and simultaneously have large enough mixings to be produced and detected at experiments, while still satisfying light neutrino mass constraints.

2.3 Scotogenic model

So far, we have discussed tree level contributions to neutrino mass. However, these might be absent, due to an underlying symmetry, or be simply subdominant compared to higher-order corrections in perturbation theory. In this case, radiative neutrino mass models become relevant. The loop corrections naturally suppress their contributions, making them an appealing framework to explain the smallness of neutrino masses. Among these models, the Scotogenic model [86, 25] (also known as radiative seesaw model) stands out as one of the most minimal and well-motivated. It not only accounts for neutrino masses but also introduces a viable dark matter (DM) candidate, making it a compelling extension of the SM.

The Scotogenic model extends the SM particle content by introducing a second scalar doublet, $\eta = (\eta^+, \eta^0)^T$, and three singlet fermions, N_i ($i = 1, 2, 3$). A key feature of this model is the presence of an exact $\mathbb{Z}_2$ symmetry under which the new fields are odd while the SM fields remain even. The new particles and their transformation properties under the SM gauge symmetry and $\mathbb{Z}_2$ are summarized in Table 2.1.

The presence of $\mathbb{Z}_2$ prevents the usual Yukawa interaction between the Higgs doublet and the new singlet neutrinos, as seen in the transformation

$$\overline{L}\tilde{H}N_R \quad \xrightarrow{\mathbb{Z}_2} \quad -\overline{L}\tilde{H}N_R\,. \tag{2.10}$$

As a result, neutrino masses do not receive tree level contributions. Instead, they are generated radiatively via a one-loop mechanism, with the relevant interactions given by

$$\mathcal{L} \supset V + \frac{1}{2}\overline{N^c} M_N N + \eta \overline{N} Y'_N L + \text{h.c.} \tag{2.11}$$

Here, M_N is a Majorana mass term for the fermion singlets, Y'_N is a 3×3 Yukawa matrix between the new scalar and fermion, and V represents the scalar potential, given by

$$\begin{aligned} V =& - m_H^2 H^\dagger H + m_\eta^2 \eta^\dagger \eta + \frac{1}{2}\lambda_H (H^\dagger H)^2 + \frac{1}{2}\lambda_\eta (\eta^\dagger \eta)^2 \\ &+ \lambda_3 (H^\dagger H)(\eta^\dagger \eta) + \lambda_4 (H^\dagger \eta)(\eta^\dagger H) + \frac{1}{2}\lambda_5 \left[(H^\dagger \eta)^2 + (\eta^\dagger H)^2 \right] . \end{aligned} \tag{2.12}$$

After EWSB, Majorana masses for the light neutrinos arise at the one-loop level, mediated by the exchange of the new scalar η and the singlet fermions N_i, as depicted in Fig. 2.2. The resulting neutrino mass matrix is given by [25, 87]

$$[\mathcal{M}_\nu]_{ij} = \sum_k \frac{[Y'_N]_{ki}[Y'_N]_{kj}}{32\pi^2} M_{N_k} \left[\frac{m_R^2}{m_R^2 - M_{N_k}^2} \log\left(\frac{m_R^2}{M_{N_k}^2} \right) - \frac{m_I^2}{m_I^2 - M_{N_k}^2} \log\left(\frac{m_I^2}{M_{N_k}^2} \right) \right] , \tag{2.13}$$

where the masses of the scalar and pseudoscalar components of $\eta^0 = (\eta_R + i\eta_I)/\sqrt{2}$ are given by

$$m_{R,I}^2 = m_\eta^2 + \frac{1}{2}(\lambda_3 + \lambda_4 \pm \lambda_5) v^2 . \tag{2.14}$$

A simplified expression can be obtained in the almost degenerate limit $m_R \approx m_I \equiv m_0$ (i.e., $\lambda_5 \ll 1$) and for $m_0^2 \simeq M_{N_k}^2$. In this case, the mass matrix simplifies to

$$[\mathcal{M}_\nu]_{ij} \simeq \frac{\lambda_5 v^2}{16\pi^2} \sum_k \frac{[Y'_N]_{ki}[Y'_N]_{kj}}{M_{N_k}} . \tag{2.15}$$

This expression highlights the radiative suppression of neutrino masses: compared to the Type-I seesaw, the effective scale for M_N is reduced by a factor of $\lambda_5/(16\pi^2)$, allowing for the sterile neutrinos to reside at lower scales. For neutrino masses to be nonzero, the simultaneous presence of λ_5, Y'_N, and M_N is required, as Eq. (2.15) shows. If any of these vanish, the radiative mechanism fails.

A remarkable feature of the Scotogenic model is that it also provides a natural dark matter candidate. Due to the unbroken $\mathbb{Z}_2$ symmetry, the lightest odd particle is stable. This could be either: 1) the lightest singlet fermion, N_1, which behaves as a sterile neutrino DM candidate if it has the right relic abundance; 2) the lightest neutral scalar, either $\text{Re}(\eta^0)$ or $\text{Im}(\eta^0)$, which could act as a scalar DM candidate. Both scenarios

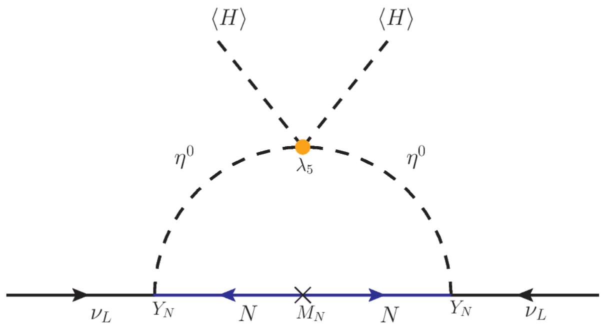

FIGURE 2.2: One-loop contribution to neutrino mass in the gauge basis in the Scotogenic model. The simultaneous presence of λ_5, M_N and Y_N' is required to draw the diagram.

lead to distinct experimental signatures, including potential signals in indirect and direct detection, and even collider searches. Additionally, due to the loop-suppressed neutrino mass generation, the Yukawa couplings Y_N' can remain sizable, potentially leading to observable effects in lepton flavor violating processes [64].

The Scotogenic model reveals a neutrino mass mechanism where sterile neutrinos do not directly mix with SM neutrinos but present additional interactions involving other BSM fields. This exemplifies a broader theme explored in Part II: sterile neutrinos interacting with hidden sectors or other BSM fields at high energies. In Chapter 4 we will adopt an effective field theory framework to study these general sterile neutrino interactions at collider energies, offering a model-agnostic approach to describe the associated phenomenology. Then, in Chapter 5, we will explore which BSM heavy fields could give rise to these effective operators.

More generally, the new particles introduced in neutrino mass models are naturally weakly coupled to the SM. As we have seen, sterile neutrinos in seesaw-type scenarios often interact only via small mixing angles, which can result in macroscopic decay lengths. This makes them promising candidates for long-lived particles, which are the focus of the next chapter. While sterile neutrinos provide a motivated benchmark, they are just one example within a wider class of weakly interacting new particles. The next chapter explores this broader landscape, highlighting the theoretical motivation and experimental strategies for long-lived particle searches across a range of BSM scenarios.

Chapter 3

Introduction to weakly coupled particles

Weakly coupled new physics is naturally associated with long-lived particles (LLPs), since *weakly* interacting particles often present macroscopic lifetimes. Beyond their strong theoretical motivation in various extensions of the SM, LLPs have attracted growing experimental attention over the past decade, particularly at the LHC. This interest has led to the development of dedicated search strategies at general-purpose detectors and inspired proposals for far detectors designed to enhance the sensitivity to LLPs.

Beyond the LHC, LLP searches have also been embraced by intensity-frontier experiments and future collider proposals, recognizing their potential to uncover new physics that may evade prompt searches. In light of the persistent absence of signals in traditional searches, LLPs offer a compelling avenue to explore previously inaccessible regions of parameter space.

This chapter provides an overview of the theoretical motivation and experimental signatures of LLPs, with a particular focus on heavy neutral leptons (HNLs) — singlet fermions that can be identified with sterile neutrinos appearing in neutrino mass models. The HNLs are prime LLP candidates and constitute the central focus of this thesis.

The chapter is structured as follows. Section 3.1 outlines the theoretical motivation for LLPs, while Section 3.2 describes their distinctive experimental signatures. Section 3.3 reviews the current status of LLP searches at the LHC. Finally, Section 3.4 summarizes experimental constraints on minimal HNLs from both collider and intensity-frontier experiments.

3.1 Theoretical motivation

The SM provides a remarkably successful framework for describing fundamental interactions, yet it leaves several key questions unanswered. The origin of neutrino masses, the nature of dark matter, and the matter-antimatter asymmetry all point toward the existence of BSM physics. Many theoretical extensions introduce new particles, but their non-observation in collider experiments suggests that either these states are too heavy to be produced at current energies, or they interact too feebly with SM particles that have been missed by standard searches. Here, we focus on the latter possibility.

The proper lifetime, τ, (or proper decay length, $c\tau$) of a particle is related to the decay width, Γ, via $\tau \propto \Gamma^{-1}$. Thus, in order to be long-lived, a particle must have a suppressed decay rate. This suppression can arise due to limited phase space, or result from a small matrix element governing the decay. The latter situation can occur when an approximate symmetry forbids certain decay modes, or when the particle interacts too weakly, with effectively small couplings. We broadly distinguish two types of such couplings: 1) small dimensionless constants, and 2) small dimensionful couplings that are inversely proportional to a high energy scale, as it occurs with higher-dimensional operators.[1] Many theoretical models naturally predict LLPs due to one or both of these mechanisms and, for illustrative purposes, we outline a few examples below involving LLPs:

- **Right-handed neutrino theories**: As discussed in the previous chapter, the seesaw mechanisms predict heavy sterile neutrinos with small couplings to active neutrinos. If these states have masses in the GeV–TeV range, they can have long lifetimes and are natural LLP candidates. Their collider phenomenology is rich, as they can be produced through different mechanisms and lead to displaced vertex signatures or other LLP signals. UV-complete models that feature right-handed (sterile) neutrinos include the νMSM [88] and Left-Right Symmetric Models [22, 23].
- **Supersymmetry (SUSY)**: In SUSY scenarios with R-parity violation (RPV) [89], long-lived neutralinos may arise due to suppressed RPV couplings. Alternatively, in gauge-mediated SUSY breaking models, the next-to-lightest supersymmetric particle (LSP), often a neutralino, can be metastable, decaying with a macroscopic lifetime.

[1] We discuss higher-dimensional operators within EFTs in Chapter 4.

- **Higgs and gauge portals**: Neutral BSM states can couple to the SM via renormalizable "portal" interactions. The Higgs portal allows for feebly interacting scalars that mix with the SM Higgs boson, potentially leading to LLPs from exotic Higgs decays. Similarly, in dark photon models, where a hidden-sector gauge boson kinetically mixes with the SM photon, displaced decay signatures can naturally arise [90].
- **Dark matter and hidden sector models**: A variety of dark matter scenarios predict LLP signatures. In freeze-in mechanisms [91], the dark matter production is governed by extremely weak interactions, often implying that the mediators involved are long-lived. In strongly coupled dark sectors, dark glueballs or dark mesons can be long-lived due to limited decay channels.

These examples highlight that LLPs are a common and generic feature across many well-motivated extensions of the SM. However, their detection requires dedicated experimental strategies targetting the distinctive LLP signatures, as we discuss in the following section.

3.2 Long-lived particles and experimental signatures

LLPs represent both a challenge and an opportunity for new physics searches at colliders. Unlike heavy, promptly decaying particles, which can be reconstructed close to the primary interaction point, LLPs travel a measurable distance before decaying, leading to distinctive experimental signatures that often fall outside the scope of conventional search strategies. The features of these signatures depend on the nature of the LLP (its quantum numbers, such as charge and color) as well as that of its decaying products.

While LLPs are often associated with BSM physics, the SM itself contains several long-lived states. Examples include muons, kaons, and B-mesons, which have decay lengths of $\mathcal{O}(\mu\mathrm{m})$ or larger. Their signatures are well understood and incorporated into the SM background models. In contrast, BSM LLPs may exhibit unexpected behaviors that deviate substantially from standard expectations. Based on their properties, LLPs can be broadly classified into three categories:

- **Electrically neutral LLPs:** These states are invisible as they traverse the detector but may decay into visible particles within the detector volume. Such decays produce displaced vertices featuring charged leptons, jets, or non-pointing photons. Examples of neutral LLPs are sterile neutrinos or dark photons.

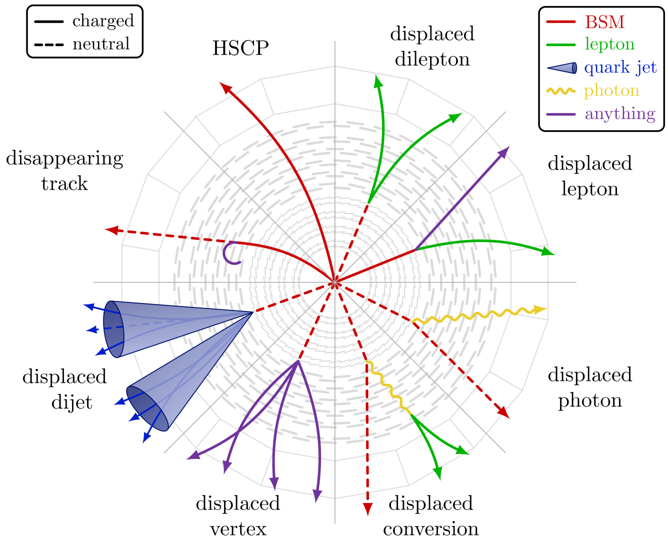

FIGURE 3.1: Schematic representation of neutral and charged LLP exotic signatures at the LHC. The image shows a transverse cut of a general-purpose LHC detector. Image from Izaak Neutelings code of TikZ [92].

- **Electrically charged LLPs:** Long-lived charged particles, such as exotic leptons or long-lived charginos, ionize the detector material along their path, leaving anomalously slow-moving charged tracks. If they are sufficiently long-lived to escape the detector without decaying, they appear as Heavy Stable Charged Particles (HSCPs).
- **Color-charged LLPs:** In SUSY models, gluinos or squarks can hadronize into exotic bound states, known as R-hadrons, which can be long-lived. These particles may scatter within the detector or be stopped in calorimeters, sometimes leading to disappearing tracks or delayed decays.

Fig. 3.1 illustrates the typical signatures associated with the different types of LLPs mentioned above. In this thesis, we focus primarily on neutral LLPs, specifically, on long-lived sterile neutrinos. Their hallmark signature in collider detectors is a displaced vertex (DV): a set of charged tracks originating from a common spatial point that is significantly separated from the primary interaction vertex. Because such events can only be mimicked by SM neutral B-mesons or kaons (whose masses are known and thus can be vetoed), DVs constitute a particularly clean and powerful probe of new physics. This exotic signature forms the core of our phenomenological analyses in Chapters 6, 8 and 9. Additionally, we investigate non-pointing photons (photons that do not point back directly to the primary vertex) arising from radiative decays of long-lived sterile neutrinos in Chapter 7.

Nonetheless, detecting LLPs presents significant experimental challenges, as most searches and detector designs have been optimized for prompt decays. Several key obstacles include: 1) reconstruction, as standard event reconstruction techniques are geared toward prompt decays, requiring dedicated displaced object reconstruction algorithms; 2) misidentification risks for cosmic-ray muons and detector noise, which can mimic LLP signatures; and 3) limited geometrical acceptance, since LLPs with longer lifetimes can decay outside the detector, there are blind spots in the coverage of main LHC detectors where LLPs might escape detection.

Despite these challenges, LLP searches benefit from an important advantage: they typically have low SM background contamination, meaning that any observed excess in displaced or anomalous signatures could point directly to new physics.

3.3 Experimental searches and dedicated detectors

As discussed in the previous section, LLPs present unique experimental challenges requiring search strategies that go beyond conventional prompt decays. At the LHC, two complementary approaches are pursued: searches within the main detectors and searches at dedicated far detector experiments, designed explicitly to extend the sensitivity reach to LLPs with very long lifetimes.

3.3.1 LLP searches at general-purpose LHC detectors

The main LHC experiments (ATLAS, CMS and LHCb) have actively developed dedicated LLP searches, adapting their detector capabilities to target displaced decays and other non-standard signatures.

ATLAS and CMS have exploited their facilities to achieve sensitive to a variety of LLP signatures. Fig. 3.2 displays the ATLAS detector layout, highlighting its key components that can be used in LLP searches: the inner detectors, the calorimeters and the muon spectrometers. Displaced charged-particle tracks and secondary vertices can be reconstructed in the inner tracking systems [94]. The electromagnetic (ECAL) and hadronic (HCAL) calorimeters enable sensitivity to LLPs decaying into photons or jets [95], while the muon systems extend coverage to LLPs that decay outside the inner detector [96]. Recent advances in trigger strategies [97, 98] have further improved sensitivity to displaced signatures, a crucial step toward maximizing the discovery potential in Run 3 and the High-Luminosity LHC (HL-LHC).

LHCb, originally designed for heavy flavor physics, offers high-precision tracking and vertexing, making it particularly sensitive to LLPs produced in heavy hadron decays

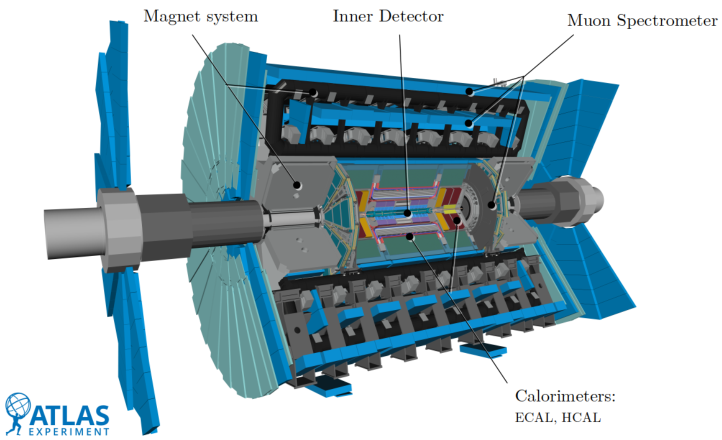

FIGURE 3.2: Schematic illustration of the ATLAS detector highlighting components relevant to LLP searches: inner detector, calorimeters, and muon spectrometers. Image from [93].

[99]. Its unique geometry, optimized for detecting particles traveling at small angles relative to the beamline, makes it well suited for low-mass LLPs arising from meson decays.

The importance of LLP searches has been increasingly recognized within the LHC community. The formation of the LHC LLP Working Group and its white paper [100] established a roadmap for Run 2 analyses and laid the foundation for future efforts. As a result, ATLAS, CMS, and LHCb have incorporated simplified LLP benchmark models into their analyses, ensuring broad theoretical coverage and enhanced reinterpretability.

3.3.2 Far detectors at the LHC

Despite the progress made in LLP searches at ATLAS, CMS, and LHCb, intrinsic limitations restrict their sensitivity to LLPs: the overwhelming background from QCD processes makes the detection of neutral LLPs particularly challenging and the trigger systems, designed primarily for prompt events, can miss displaced signals. To address these challenges, several proposals have been put forward for far detectors, placed tens to hundreds of meters away from the LHC interaction points. These detectors benefit from low-background environments and significantly extend the LHC reach to LLPs with longer lifetimes.

Proposed far detectors can be broadly categorized by their orientation with respect to the beamline. Detectors such as MATHUSLA [102, 103, 104], ANUBIS [105], MoEDAL-MAPP [106, 107], and CODEX-b [108] would be located transversely to the interaction point, being more sensitive to LLPs with large transverse momenta. In contrast,

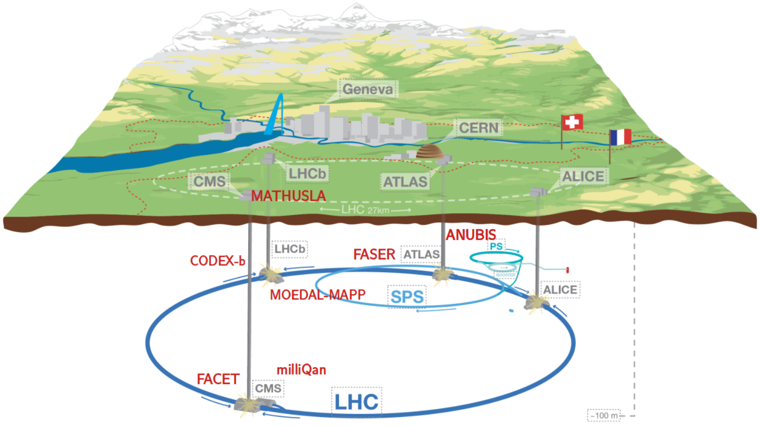

FIGURE 3.3: Map showing the main LHC detector locations and proposed sites for far detectors. Image reproduced from [101].

FASER [109, 110] and FACET [111] are situated downstream along the beamline, targeting highly boosted LLPs produced in forward processes. Their proposed sites at CERN are illustrated in Fig. 3.3.

Among the far detectors, MATHUSLA stands out as one of the most ambitious proposals. Planned to be installed on the surface above the CMS interaction point, it consists of a large-volume tracker designed to identify LLP decays in a background-free environment.[2] ANUBIS was originally conceived to exploit an existing service shaft above ATLAS to host a vertical detector. A revised geometry featuring tracking layers in the ceiling of the ATLAS cavern is currently under study [112].

CODEX-b is a more compact proposal near LHCb, optimized for detecting LLPs from exotic hadron decays, whereas MoEDAL-MAPP aims to probe milli-charged particles using dedicated detectors placed in underground galleries close to the LHCb interaction point.

FASER, installed 480 meters downstream of ATLAS, targets light, highly boosted LLPs. It has been approved and is currently taking data. An upgraded version, FASER2, has been proposed as part of the Forward Physics Facility (FPF) [113], which would significantly extend its physics reach. FACET, positioned closer to CMS, is designed to probe LLPs with intermediate lifetimes and energies, complementing both FASER and the main detectors.

While FASER is operational, most far detector proposals, such as MATHUSLA and ANUBIS, remain under feasibility studies for potential implementation during the

[2] The new conceptual design report [104] has been released during the writing of this thesis.

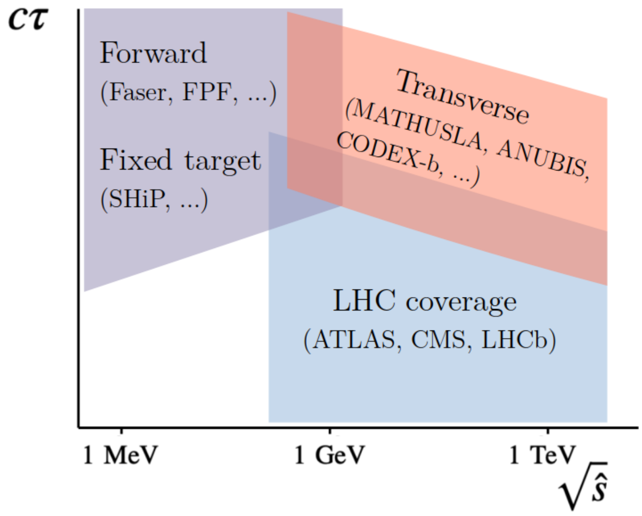

FIGURE 3.4: Schematic illustration of the sensitivity ranges of various experiments to LLP lifetimes, as a function of the partonic center-of-mass energy $\sqrt{\hat{s}}$.

HL-LHC era. If realized, they would fill crucial gaps in existing coverage and dramatically enhance the discovery prospects for weakly coupled particles. In Part III of this thesis, we present sensitivity studies for several of these far detectors to BSM scenarios with sterile neutrinos, revealing they can probe new model parameter space complementary to that explored with general-purpose detectors. This complementarity is schematically illustrated in Fig. 3.4.

3.3.3 Beyond the LHC: future and complementary searches

While the LHC covers the highest-energy frontier, complementary experiments at different energy and intensity scales provide essential sensitivity to other regions of LLP parameter space. Two particularly promising programs in this regard are SHiP at the SPS and DUNE at Fermilab.

The SHiP experiment [114, 115, 116], approved in spring 2024, is designed to explore weakly coupled new physics using the high-intensity 400 GeV proton beam at the SPS. SHiP will operate as a beam-dump experiment: proton beams are dumped on a fixed target, aiming to produce large numbers of hidden-sector particles, including LLP candidates, which may decay in a downstream, shielded decay volume. This setup will enable SHiP to probe a broad class of LLP models, especially in the MeV-GeV mass range.

In parallel, neutrino experiments are emerging as powerful tools for LLP detection. The Deep Underground Neutrino Experiment (DUNE) [117, 118, 119], currently under construction at Fermilab, is primarily focused on neutrino oscillation physics. However, its near detector complex (DUNE-ND) [120], located close to the beam source, will be exposed to an intense flux of particles from meson decays and other processes. Thanks to its precise tracking and calorimetry capabilities, DUNE-ND will be able to detect LLP decays with displaced signatures, offering complementary sensitivity to both beam-dump and collider experiments.

Together, SHiP and DUNE highlight the importance of multi-experiment approaches in the hunt for LLPs, covering parameter regions that would otherwise remain unexplored at the LHC. Their results will be crucial for guiding future searches.

3.4 Experimental constraints on minimal HNLs

Among the many candidates for weakly coupled new physics, HNLs stand out due to their close connection to the origin of neutrino masses and their potential as LLPs. Before exploring more general frameworks in Part II of this thesis, it is instructive to consider the so-called *minimal* HNL scenario.

Generally, the term heavy neutral lepton refers to a BSM electrically neutral (singlet) fermion, called heavy in contrast to the light SM neutrinos. However, there is no fixed prediction for its mass, which could lie anywhere from a few keV to several hundred TeV, nor for its nature, which could be Dirac or Majorana. A priori, HNLs do not explain light neutrino masses, but one can make a connection with neutrino mass models by identifying the sterile neutrino mass eigenstates appearing in these models as HNLs. In the seesaw-type models introduced in Chapter 2, we discussed how the heavy (nearly) sterile neutrinos interact with SM particles via a small mixing with the active neutrinos. We refer to such states, which couple to the SM solely through this mixing, as minimal HNLs.

Different neutrino mass models predict distinct values for the active-sterile mixing, which ultimately depends on the HNL mass or other model-specific parameters, as seen in Chapter 2 with the type-I and low-scale seesaw variants. However, in phenomenological studies and experimental analyses, it is common to treat the HNL mass and its mixing with each SM flavor neutrino as free, independent parameters. This opens up new parts of parameter space. Within this framework, the HNL decay width has been computed in the literature as a function of its mass and mixing, see e.g. [121, 122], which has allowed to identify the regimes where the HNLs become long-lived.

Minimal HNLs have been adopted as benchmark targets in several LLP searches at the LHC and other fixed-target experiments. The absence of a positive signal has allowed them to place constraints on the parameter space of the minimal HNL scenario. In Fig. 3.5, we summarize the current experimental bounds in the plane of squared mixing angle versus HNL mass, based on the compilation in [123]. The three panels correspond to the three scenarios in which the HNL predominantly mixes with a single active flavor: electron, muon or tau. In general, constraints for the tau-mixing case (bottom panel) are significantly weaker than those for the electron (top) or muon (middle) cases, largely due to the lower reconstruction efficiency of tau leptons.

Searches at the LHC are particularly sensitive to HNLs in the GeV mass range and currently set the most stringent bounds in this region [124, 125]. At lower masses, experiments such as CHARM and BEBC provide leading constraints down to a few hundred MeV [126, 127]. Below the kaon mass, the most stringent limits come from kaon decay experiments like T2K [128] and NA62 [129]. Constraints from cosmology [130] also apply at low HNL masses, but since they rely on assumptions about the early universe and its thermal history, they are often treated separately from laboratory bounds. At the opposite end of the spectrum, for masses above the electroweak scale, indirect constraints arise from precision electroweak observables, most notably from deviations in the unitarity of the PMNS matrix [131].

It is worth noting that this minimal scenario where the HNL couples to only one flavor is a simplification adopted for clarity and ease of interpretation. In more realistic settings, HNLs may mix with multiple active flavors with comparable strength, which can significantly modify the exclusion limits [132]. Furthermore, the presence of more than one kinematically accessible HNL can also alter the production and decay patterns, with important implications for phenomenology and experimental reach.

From a theoretical perspective, the minimal HNL scenario is only a starting point. The possibility that HNLs participate in additional BSM interactions beyond the minimal mixing paradigm opens a broader and less constrained landscape. Exploring these non-minimal interactions, how they arise in theory, and how they manifest in experiments, is the core focus of this thesis.

This concludes Part I, where we have motivated sterile neutrinos as natural candidates for weakly coupled new physics. In Part II, we discuss EFT frameworks that extend the SM with sterile neutrinos, providing a generalized way to describe their BSM interactions. In Part III, we explore the phenomenology of these interactions, focusing on their signatures at the LHC and the role of LLP searches in probing otherwise inaccessible regions of parameter space.

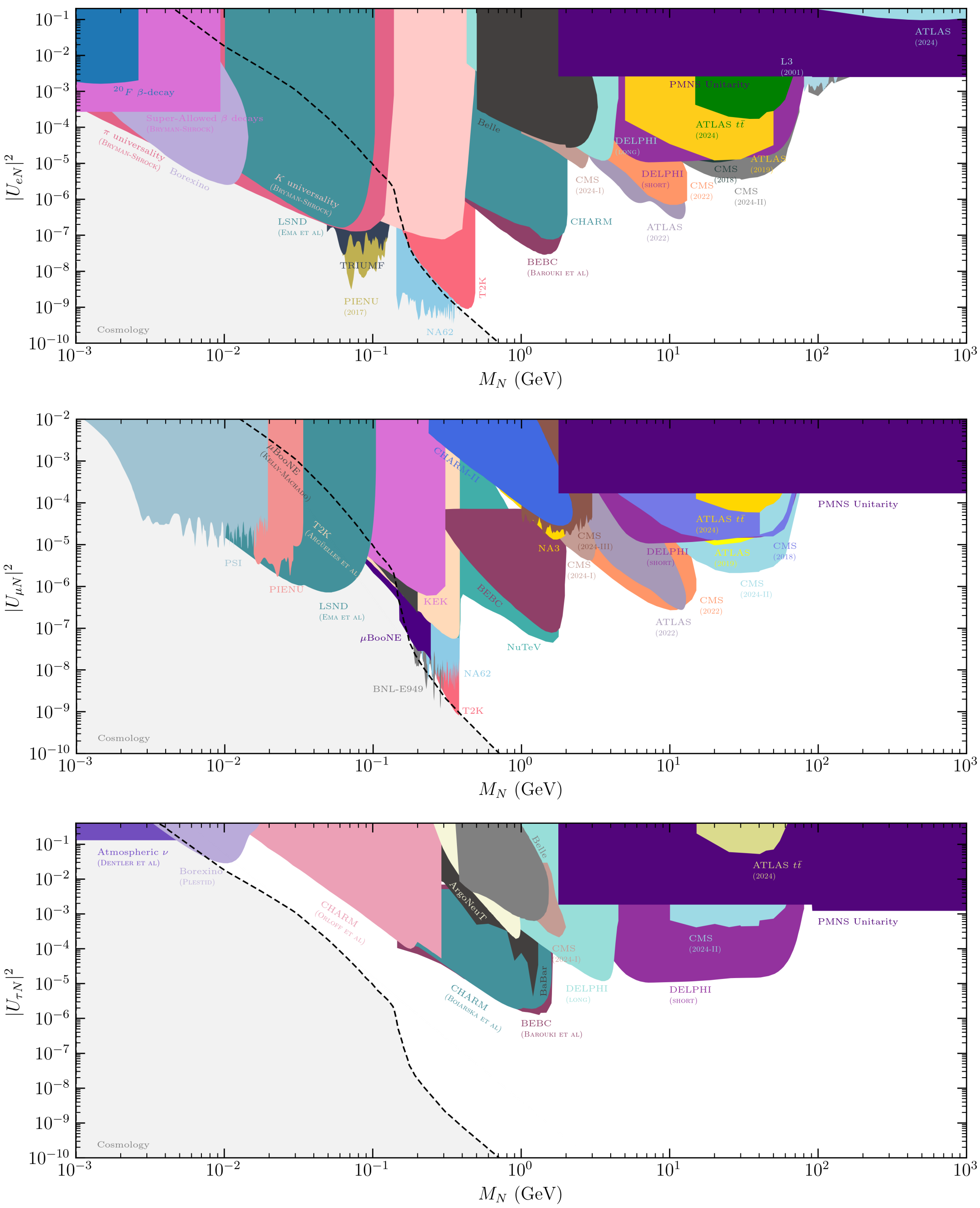

FIGURE 3.5: Present exclusion limits (90% C.L.) of HNL mixing with active neutrinos as a function of HNL mass. Plots from [123]. The HNL is assumed to be Majorana. The three panels correspond to the three flavor-dominance scenarios: electron-mixing (top), muon-mixing (middle) and tau-mixing (bottom).

Part II

Theoretical frameworks with sterile neutrinos

Chapter 4

Sterile neutrinos in Effective Field Theories

In Part I, we saw that sterile neutrinos represent one of the most minimal and well-motivated extensions of the SM, offering a natural explanation for neutrino masses and potentially contributing to the dark matter puzzle. These right-handed or sterile neutrinos, denoted by N_R, may also act as a portal to hidden sectors beyond the SM. If the sterile neutrinos have masses at or near the electroweak scale, while other new physics resides at much higher energies, their low-energy interactions can be systematically described within an effective field theory (EFT) framework. In this approach, the SM is extended to include N_R as an explicit dynamical degree of freedom, leading to the so-called N_RSMEFT, the EFT of the SM extended with right-handed neutrinos. This model-agnostic framework encodes new interactions involving sterile neutrinos at energies accessible to current and future experiments.

This chapter lays out the theoretical foundations of EFTs involving sterile neutrinos and it is structured as follows. Section 4.1 begins with a brief overview of the general EFT formalism, introducing the SMEFT and its low-energy counterpart, LEFT. In Section 4.2, we introduce the N_RSMEFT, present its operator basis up to dimension $d = 7$ and discuss the phenomenological relevance of the leading interactions. Finally, Section 4.3 covers the low-energy limit of this theory, the N_RLEFT, which is particularly relevant for low-energy observables such as meson decays and for experiments targeting GeV-scale sterile neutrinos.

4.1 EFTs in a nutshell

EFTs provide a systematic framework for describing physics at different energy scales. When the fundamental theory of nature operates at energies far beyond experimental reach, EFTs allow us to parametrize its low-energy effects, without requiring knowledge of the ultraviolet (UV) completion. By retaining only the relevant degrees of freedom and organizing interactions in an expansion in inverse powers of a new physics energy scale, denoted by Λ, EFTs encode the imprint of UV physics via higher-dimensional operators. The effective Lagrangian at low energies takes the general form [133]

$$\mathcal{L}_{\text{EFT}} = \mathcal{L}^{(4)} + \sum_{d\geq 5} \frac{1}{\Lambda^{d-4}} \sum_i c_i^{(d)} \mathcal{O}_i^{(d)} \,, \tag{4.1}$$

where $\mathcal{L}^{(4)}$ contains all renormalizable terms up to mass dimension 4, while the effective operators $\mathcal{O}_i^{(d)}$ have mass dimension $d \geq 5$. Each operator contains only light degrees of freedom of the theory, and is accompanied by a Wilson coefficient $c_i^{(d)}$ that encapsulates the effects of the heavy particles at the UV scale. The suppression by $1/\Lambda^{d-4}$ ensures that the higher the dimension of the operator, the less relevant it becomes at low energies, justifying a truncation of the expansion at a given order.

A prime example of this approach is the EFT of the SM, called SMEFT, in which the SM is regarded as the low-energy limit of a more fundamental theory [134]. The SMEFT extends the SM Lagrangian by including all possible higher-dimensional operators, constructed from the SM fields in Table 4.1 and their derivatives, which are Lorentz- and gauge-invariant under $SU(3)_C \times SU(2)_L \times U(1)_Y$. These effective operators can break, however, the accidental global symmetries of the SM, such as lepton number (L) and baryon number (B).[1]

The construction of complete and non-redundant operator bases in the SMEFT has been the subject of sustained theoretical effort since the early formulations of effective operators at $d = 5$ [15] and $d = 6$ [135]. A central challenge in this task is that many operator structures that appear independent *a priori* can, in fact, be related through field redefinitions, equations of motion, integration by parts, or Fierz identities. These relations must be carefully taken into account to eliminate redundancies and isolate a minimal set of independent operators. The first $d = 6$ operator basis, proposed in [136], was later shown to be overcomplete. It took more than two decades to construct a fully non-redundant basis at this dimension, now known as the "Warsaw basis" [137]. This work was followed by the classification of all $d = 7$ operators in [138].

[1] These violations are tightly constrained by experiment, especially in the case of B violation, but are generically expected in many UV completions.

Field	Irrep	Spin	Multiplicity
$Q = (u_L,\, d_L)^T$	$(\mathbf{3}, \mathbf{2}, 1/6)$	$1/2$	3
u_R	$(\mathbf{3}, \mathbf{1}, 2/3)$	$1/2$	3
d_R	$(\mathbf{3}, \mathbf{1}, -1/3)$	$1/2$	3
$L = (\nu_L,\, e_L)^T$	$(\mathbf{1}, \mathbf{2}, -1/2)$	$1/2$	3
e_R	$(\mathbf{1}, \mathbf{1}, -1)$	$1/2$	3
G_μ	$(\mathbf{8}, \mathbf{1}, 0)$	1	1
W_μ	$(\mathbf{1}, \mathbf{3}, 0)$	1	1
B_μ	$(\mathbf{1}, \mathbf{1}, 0)$	1	1
H	$(\mathbf{1}, \mathbf{2}, 1/2)$	0	1

TABLE 4.1: SMEFT field content. All operators are built from these fields, their conjugates and their derivatives. The last column gives the number of generations (flavors) of each field.

Since the number of independent operators grows rapidly with the mass dimension, algebraic tools such as Hilbert series techniques [139, 140] have been developed to automate the identification of redundancies. These methods have enabled the construction of operator bases in SMEFT up to $d = 15$ [141].

A key strength of the EFT framework lies in its applicability across a wide range of energy scales, provided that the relevant degrees of freedom and symmetries are correctly accounted for at each stage. At energies well below the scale of new physics Λ, the SMEFT offers a valid description under the assumption that only SM fields are present.[2] At even lower energies, specifically, below the electroweak scale, heavy SM fields such as the top quark, Higgs boson, and the W and Z bosons are no longer active degrees of freedom and should be integrated out. The resulting low-energy description is provided by the so-called LEFT, the low-energy EFT of the SM, which is constructed from the light SM fields and is invariant under the unbroken gauge group $SU(3)_c \times U(1)_{\text{em}}$.

Two additional concepts are central to the EFT approach: *matching* and *running*. Matching ensures that physical observables remain unchanged when moving between effective descriptions at different energy scales. This includes matching a UV theory onto an EFT at the scale Λ, or matching two EFTs at intermediate thresholds, for instance, matching SMEFT onto LEFT at the electroweak scale. In particular, the SMEFT Wilson

[2] A more general framework, known as Higgs EFT (HEFT), allows for non-linear realizations of electroweak symmetry breaking and may be more appropriate in scenarios where the SMEFT expansion breaks down.

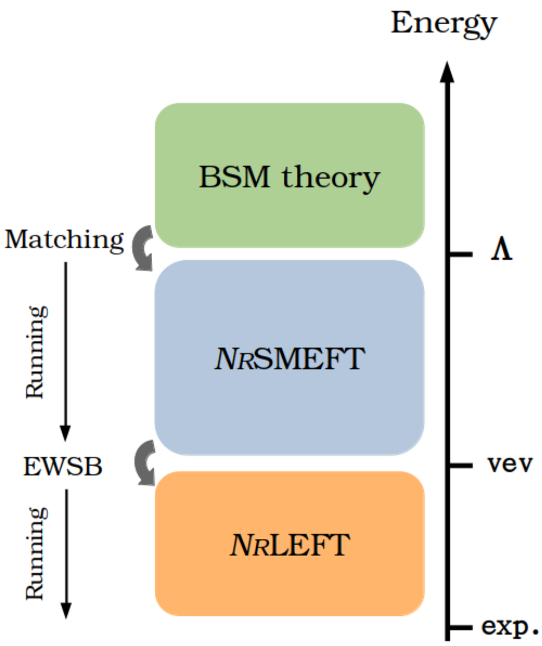

FIGURE 4.1: Different EFT descriptions at three energy scales: new physics scale Λ, electroweak scale (Higgs vev) and low-energy experiments scale.

coefficients can be related by matching to a more fundamental theory at high energies, thereby encoding the imprint of heavy new physics. This matching procedure allows EFTs to remain predictive even in the absence of full knowledge of the UV completion. Running refers to the scale dependence of the Wilson coefficients $c_i^{(d)}$, which arises from quantum corrections. Their evolution with energy is governed by renormalization group equations (RGEs), which describe how the EFT parameters "run" between different scales.

Fig. 4.1 schematically illustrates the energy regimes in which various EFTs are valid, namely SMEFT and LEFT, or their extensions with sterile neutrinos, N_RSMEFT and N_RLEFT. It also indicates where matching and running procedures become relevant. These concepts will play an important role in later chapters, particularly when connecting N_RSMEFT to its low-energy counterpart (N_RLEFT), or when exploring tree level UV completions of N_RSMEFT in Chapter 5.

In practical applications, constructing operator bases and automating matching and running is further aided by specialized computational tools. Software packages such as `Sym2Int` [142, 143] automate the classification of operators, accounting for redundancies and symmetry constraints, while `MatchMakerEFT` [144] and `Matchete` [145] can perform the matching between UV theories and EFTs. We also mention the Python packages Wilson [146] and Flavio [147], useful for running, matching, and translating Wilson coefficients beyond the SM above and below the electroweak scale. Throughout this thesis, several of these tools have been relevant for analyzing the structure of EFT operators and performing the EFT matching to UV theories.

We close this section stating that while SMEFT provides a powerful framework for probing new physics, it relies on the assumption that no new particles are present at or below the electroweak scale, hence excluding light new physics in this energy regime. Given their role in neutrino mass generation and their potential connection to hidden sectors, electroweak scale sterile neutrinos motivate an extension of this framework.

4.2 N_RSMEFT: formalism and relevant operators

If sterile neutrinos exist with masses below or around the electroweak scale, their interactions with SM fields, and with potential heavy new physics, can be described within an EFT that explicitly includes right-handed neutrinos, N_R, as dynamical fields. This leads to the so-called N_RSMEFT. In this section, we write down the N_RSMEFT Lagrangian up to dimension $d = 7$, highlighting the operators that play a leading role in phenomenology.

The general form of the N_RSMEFT Lagrangian follows Eq. (4.1). The renormalizable part contains, in addition to the SM Lagrangian, the kinetic and mass terms for N_R, as well as a Yukawa coupling to the SM Higgs doublet,

$$\mathcal{L}^{(4)}_{N_R\text{SMEFT}} = \mathcal{L}_{\text{SM}} + \overline{N_R} i\partial\!\!\!/ N_R - \left[\frac{1}{2}\overline{N_R^c} M_R N_R + \overline{L}\tilde{H} Y_\nu N_R + \text{ h.c.}\right] . \tag{4.2}$$

Here, we have assumed the sterile neutrino to be Majorana. This minimal setup hence leads to active neutrino masses via the type-I seesaw mechanism (see Section 2.1). However, one could assume a Dirac sterile neutrino, motivated by other seesaw realizations, such as the inverse seesaw, cf. Section 2.2, introduce a second Weyl fermion, S_L, and replace M_R with a Dirac mass term $M_{NS}\overline{N_R}S_L$. We distinguish between the left- and right-handed components of this particle because in the following we will consider only higher-dimensional operators involving N_R. In this sense, the Dirac scenario resembles more closely the Majorana case.

As regards the $d \geq 5$ terms, the list of SMEFT operators must be extended to include those containing SM fields and N_R. The full set of operators containing N_R was derived up to dimension $d = 7$ for the first time in Ref. [148], and extended to $d = 9$ more

$\psi^2 H^3$ (+h.c.)		ψ^4		ψ^4 (+h.c.)	
$\mathcal{O}_{LNH^3}$	$(\overline{L}N_R)\tilde{H}(H^\dagger H)$	$\mathcal{O}_{NN}$	$(\overline{N_R}\gamma^\mu N_R)(\overline{N_R}\gamma_\mu N_R)$	$\mathcal{O}_{QuNL}$	$(\overline{Q}u_R)(\overline{N_R}L)$
$\psi^2 H^2 D$ (+h.c.)		$\mathcal{O}_{eN}$	$(\overline{e}_R\gamma^\mu e_R)(\overline{N_R}\gamma_\mu N_R)$	$\mathcal{O}_{LNLe}$	$(\overline{L}N_R)\epsilon(\overline{L}e_R)$
$\mathcal{O}_{NH^2D}$	$(\overline{N_R}\gamma^\mu N_R)(H^\dagger i\overleftrightarrow{D}_\mu H)$	$\mathcal{O}_{uN}$	$(\overline{u}_R\gamma^\mu u_R)(\overline{N_R}\gamma_\mu N_R)$	$\mathcal{O}_{LNQd}$	$(\overline{L}N_R)\epsilon(\overline{Q}d_R)$
$\mathcal{O}_{NeH^2D}$	$(\overline{N_R}\gamma^\mu e_R)(\tilde{H}^\dagger iD_\mu H)$	$\mathcal{O}_{dN}$	$(\overline{d}_R\gamma^\mu d_R)(\overline{N_R}\gamma_\mu N_R)$	$\mathcal{O}_{LdQN}$	$(\overline{L}d_R)\epsilon(\overline{Q}N_R)$
$\psi^2 H^2 X$ (+h.c.)		$\mathcal{O}_{duNe}$ (+h.c.)	$(\overline{d}_R\gamma^\mu u_R)(\overline{N_R}\gamma_\mu e_R)$	$\mathcal{O}_{NNNN}$	$(\overline{N_R^c}N_R)(\overline{N_R^c}N_R)$
$\mathcal{O}_{NBH}$	$(\overline{L}\sigma^{\mu\nu}N_R)\tilde{H}B_{\mu\nu}$	$\mathcal{O}_{LN}$	$(\overline{L}\gamma^\mu L)(\overline{N_R}\gamma_\mu N_R)$	$\mathcal{O}_{QQdN}$	$\varepsilon_{ij}\left(\overline{Q_i^c}Q_j\right)\left(\overline{d_R^c}N_R\right)$
$\mathcal{O}_{NWH}$	$(\overline{L}\sigma^{\mu\nu}N_R)\tau^I\tilde{H}W^I_{\mu\nu}$	$\mathcal{O}_{QN}$	$(\overline{Q}\gamma^\mu Q)(\overline{N_R}\gamma_\mu N_R)$	$\mathcal{O}_{uddN}$	$\left(\overline{u_R^c}d_R\right)\left(\overline{d_R^c}N_R\right)$

TABLE 4.2: N_RSMEFT operator structures at $d = 6$ classified according to the field content. In the last column, the operators marked in red violate B and L in one unit, while $\mathcal{O}_{NNNN}$ violates L in four units.

recently in [149]. In what follows, we focus on the most phenomenologically relevant operators at dimensions $d = 5$, 6, and 7.

Dimension-5 operators. In addition to the well-known Weinberg operator [15] already present in SMEFT, N_RSMEFT introduces two lepton number violating (LNV) operators involving N_R, which are [150, 151]

$$\mathcal{O}_{NNH} = (H^\dagger H)\overline{N_R^c}N_R\,, \tag{4.3}$$

$$\mathcal{O}_{NNB} = \left(\overline{N_R^c}\sigma_{\mu\nu}N_R\right)B^{\mu\nu}\,. \tag{4.4}$$

The first operator contributes to the Majorana mass of sterile neutrinos while the second operator induces a sterile neutrino magnetic moment at low energies. Notably, $\mathcal{O}_{NNB}$ is antisymmetric in generation space, and thus vanishes identically for a single N_R generation. The phenomenology of the latter operator will be discussed in more detail in Chapter 7.

Dimension-6 operators. In addition to the SMEFT operators in the "Warsaw basis" [137], there exist 19 independent $d = 6$ operators[3] involving at least one N_R [148]. We list them in Table 4.2. These operators can be classified, based on their field content (namely fermions ψ, the Higgs field H, covariant derivatives D,[4] and gauge field strength tensors X), into four classes: ψ^2H^3, ψ^2H^2D, ψ^2H^2X and ψ^4. The first three classes contain five operators in total. The four-fermion class, ψ^4, includes 14 operators: 11 that conserve baryon and lepton numbers, one that violates lepton number

[3]Here, we count distinct operator types without considering flavor indices or hermitian conjugates.
[4]In the operators, we employ the convention $D_\mu = \partial_\mu + ig\tau^I W^{I\mu} + ig'YB_\mu$.

by four units ($\mathcal{O}_{NNNN}$), and two that violate both baryon and lepton number ($\mathcal{O}_{QQdN}$ and $\mathcal{O}_{uddN}$). The LNV operator $\mathcal{O}_{NNNN}$ is antisymmetric in flavor space and thus vanishes for a single N_R generation. We note that all fermion fields in the operators carry a flavor index and hence each operator structure must be expanded in flavor space, with a corresponding Wilson coefficient for each flavor configuration.

These $d = 6$ operators lead to a variety of phenomenological consequences. For example, $\mathcal{O}_{LNH^3}$ modifies the Yukawa coupling in Eq. (4.2), while $\mathcal{O}_{NH^2D^2}$ and $\mathcal{O}_{NeH^2D}$ change the neutral and charged electroweak currents, respectively. Operators like $\mathcal{O}_{NBH}$ and $\mathcal{O}_{NWH}$ generate active-sterile neutrino magnetic moments after electroweak symmetry breaking and we will study them as well in Chapter 7. The four-fermion operators can also have a profound impact on N_R phenomenology. Those containing a pair of quarks (and one or two N_R), such as $\mathcal{O}_{uN}$, $\mathcal{O}_{duNe}$ or $\mathcal{O}_{QuNL}$, are of special interest for the LHC and hadron colliders, while operators containing a pair of SM leptons, such as $\mathcal{O}_{eN}$, $\mathcal{O}_{LN}$ or $\mathcal{O}_{LNLe}$, could be probed at lepton colliders. We will explore the phenomenology at the LHC of the four-fermion operators with quarks and at least one N_R in Chapter 8 and Chapter 9.

Dimension-7 operators. While SMEFT contains 18 independent $d = 7$ operators [138, 152], the inclusion of right-handed neutrinos in N_RSMEFT expands this set to 52 new structures [148]. These operators fall into eight distinct classes: six contain two fermions plus a combination of Higgs fields, derivatives, or field strength tensors, which are $\psi^2H^2D^2$, ψ^2H^3D, ψ^2HDX, ψ^2H^2X, ψ^2X^2 and ψ^2H^4; and the other two classes are four-fermion operators that additionally include a Higgs boson (ψ^4H) or a covariant derivative (ψ^4D). The majority of the operators belong to the two latter classes: of the 52 operator structures, 21 correspond to ψ^4H and 12 to ψ^4D. In total, only 5 violate baryon number explicitly. The complete list of operators is shown in Tables 4.3 and 4.4. All $d = 7$ operators involving sterile neutrinos violate lepton or baryon number, and obey the general rule $|\Delta B - \Delta L| = 2$.

Although the effects of $d = 7$ operators are suppressed by an additional power of Λ compared to $d = 6$ operators, they can still have a non-negligible impact on phenomenology. For instance, $\Delta L = 2$ operators can give a contribution to SM neutrino masses beyond the leading seesaw terms, they can also mediate neutrinoless double beta decay or induce LNV rare meson decays. An exhaustive study of the phenomenology of $d = 7$ operators in N_RSMEFT lies beyond the scope of this thesis. Nevertheless, we will revisit some of them in Chapter 6, in particular, those contributing to LNV meson decays at low energies.

ψ^2H^3D		ψ^4H	
$\mathcal{O}_{NLH^3D}$	$\epsilon_{ij}(\overline{N_R^c}\gamma_\mu L^i)(iD^\mu H^j)(H^\dagger H)$	$\mathcal{O}_{LNLH}$	$\epsilon_{ij}(\overline{L}\gamma_\mu L)(\overline{N_R^c}\gamma^\mu L^i)H^j$
	$\epsilon_{ij}(\overline{N_R^c}\gamma_\mu L^i)H^j(H^\dagger i\overleftrightarrow{D^\mu}H)$	$\mathcal{O}_{QNLH}$	$\epsilon_{ij}(\overline{Q}\gamma_\mu Q)(\overline{N_R^c}\gamma^\mu L^i)H^j$
$\psi^2H^2D^2$			$\epsilon_{ij}(\overline{Q}\gamma_\mu Q^i)(\overline{N_R^c}\gamma^\mu L^j)H$
$\mathcal{O}_{NeH^2D^2}$	$\epsilon_{ij}(\overline{N_R^c}\overleftrightarrow{D_\mu}e_R)(H^iD^\mu H^j)$	$\mathcal{O}_{eNLH}$	$\epsilon_{ij}(\overline{e_R}\gamma_\mu e_R)(\overline{N_R^c}\gamma^\mu L^i)H^j$
$\mathcal{O}_{NH^2D^2}$	$(\overline{N_R^c}\overleftrightarrow{\partial_\mu}N_R)(H^\dagger\overleftrightarrow{D^\mu}H)$	$\mathcal{O}_{dNLH}$	$\epsilon_{ij}(\overline{d_R}\gamma_\mu d_R)(\overline{N_R^c}\gamma^\mu L^i)H^j$
	$(\overline{N_R^c}N_R)(D_\mu H)^\dagger D^\mu H$	$\mathcal{O}_{uNLH}$	$\epsilon_{ij}(\overline{u_R}\gamma_\mu u_R)(\overline{N_R^c}\gamma^\mu L^i)H^j$
ψ^2H^2X		$\mathcal{O}_{duNLH}$	$\epsilon_{ij}(\overline{d_R}\gamma_\mu u_R)(\overline{N_R^c}\gamma^\mu L^i)\tilde{H}^j$
$\mathcal{O}_{NeH^2W}$	$(\epsilon\tau^I)_{ij}(\overline{N_R^c}\sigma^{\mu\nu}e_R)(H^iH^j)W^I_{\mu\nu}$	$\mathcal{O}_{dQNeH}$	$\epsilon_{ij}(\overline{d_R}Q^i)(\overline{N_R^c}e_R)H^j$
$\mathcal{O}_{NH^2B}$	$(\overline{N_R^c}\sigma^{\mu\nu}N_R)(H^\dagger H)B_{\mu\nu}$	$\mathcal{O}_{QuNeH}$	$(\overline{Q}u_R)(\overline{N_R^c}e_R)H$
$\mathcal{O}_{NH^2W}$	$(\overline{N_R^c}\sigma^{\mu\nu}N_R)(H^\dagger\tau^IH)W^I_{\mu\nu}$		$(\overline{Q}\sigma_{\mu\nu}u_R)(\overline{N_R^c}\sigma^{\mu\nu}e_R)H$
ψ^2H^4		$\mathcal{O}_{LNeH}$	$(\overline{L}N_R)(\overline{N_R^c}e_R)H$
$\mathcal{O}_{NH^4}$	$(\overline{N_R^c}N_R)(H^\dagger H)^2$	$\mathcal{O}_{eLNH}$	$H^\dagger(\overline{e_R}L)(\overline{N_R^c}N_R)$
ψ^4H		$\mathcal{O}_{QNdH}$	$(\overline{Q}N_R)(\overline{N_R^c}d_R)H$
$(\Delta L,\Delta B)=(1,-1)$		$\mathcal{O}_{dQNH}$	$H^\dagger(\overline{d_R}Q)(\overline{N_R^c}N_R)$
$\mathcal{O}_{QNddH}$	$\epsilon_{ij}(\overline{Q^i}N_R)(\overline{d_R}d_R^c)\tilde{H}^j$	$\mathcal{O}_{QNuH}$	$(\overline{Q}N_R)(\overline{N_R^c}u_R)\tilde{H}$
$\mathcal{O}_{QNQH}$	$\epsilon_{ij}(\overline{Q_i}N_R)(\overline{Q_j}Q^c)H$	$\mathcal{O}_{uQNH}$	$\tilde{H}^\dagger(\overline{u_R}Q)(\overline{N_R^c}N_R)$
$\mathcal{O}_{QNudH}$	$(\overline{Q}N_R)(\overline{u_R}d_R^c)H$	$\mathcal{O}_{LNNH}$	$(\overline{L}N_R)(\overline{N_R^c}N)\tilde{H}$
		$\mathcal{O}_{NLNH}$	$\tilde{H}^\dagger(\overline{N_R}L)(\overline{N_R^c}N)$

TABLE 4.3: N_RSMEFT operator structures at $d=7$. Here, we list those in the classes $\psi^2H^2D^2$, ψ^2H^3D, ψ^2H^2X, ψ^2H^4 and ψ^4H. All operators are non-hermitian, (+h.c.) is implicitly assumed. For the $(\Delta L,\Delta B)=(1,-1)$ operators, the contraction of the $SU(3)$ indices requires the antisymmetric tensor $\epsilon_{\alpha\beta\sigma}$.

The presence of such a rich operator landscape naturally raises the question of its origin. In this EFT context, each operator must arise from integrating out heavy degrees of freedom in a more fundamental UV theory. Identifying viable UV completions is essential for understanding the theory underlying N_RSMEFT and for guiding experimental searches for new physics at current and future colliders. We will explore this topic in Chapter 5.

To summarize, the N_RSMEFT formalism captures sterile neutrino interactions above the electroweak scale. However, many of the experimental probes of such particles, especially meson decays or precision observables, occur at much lower energies. In this regime, the appropriate framework becomes the N_RLEFT, which we discuss next.

$\psi^2 X^2$		$\psi^4 D$	
$\mathcal{O}_{NB1}$	$(\overline{N_R^c} N_R) B_{\mu\nu} B^{\mu\nu}$	$\mathcal{O}_{eNLLD}$	$\epsilon_{ij}(\overline{e_R}\gamma_\mu N_R)(\overline{L^{i,C}} i \overleftrightarrow{D}^\mu L^j)$
$\mathcal{O}_{NB2}$	$(\overline{N_R^c} N_R) B_{\mu\nu} \tilde{B}^{\mu\nu}$	$\mathcal{O}_{duNeD}$	$(\overline{d_R}\gamma_\mu u_R)(\overline{N_R^c} i \overleftrightarrow{D}^\mu e_R)$
$\mathcal{O}_{NW1}$	$(\overline{N_R^c} N_R) W^I_{\mu\nu} W^{I\mu\nu}$	$\mathcal{O}_{QuNLD}$	$(\overline{Q} i \overleftrightarrow{D}_\mu u_R)(\overline{N_R^c}\gamma^\mu L^j)$
$\mathcal{O}_{NW2}$	$(\overline{N_R^c} N_R) W^I_{\mu\nu} \tilde{W}^{I\mu\nu}$	$\mathcal{O}_{dqNLD}$	$\epsilon_{ij}(\overline{d_R} i \overleftrightarrow{D}_\mu Q^i)(\overline{N_R^c}\gamma^\mu L)$
$\mathcal{O}_{NG1}$	$(\overline{N_R^c} N_R) G^A_{\mu\nu} G^{A\mu\nu}$	$\mathcal{O}_{LND}$	$(\overline{L}\gamma_\mu L)(\overline{N_R^c} i \overleftrightarrow{\partial}^\mu N_R)$
$\mathcal{O}_{NG2}$	$(\overline{N_R^c} N_R) G^A_{\mu\nu} \tilde{G}^{A\mu\nu}$	$\mathcal{O}_{QND}$	$(\overline{Q}\gamma_\mu Q)(\overline{N_R^c} i \overleftrightarrow{\partial}^\mu N_R)$
$\psi^2 HXD$		$\mathcal{O}_{eND}$	$(\overline{e_R}\gamma_\mu e_R)(\overline{N_R^c} i \overleftrightarrow{\partial}^\mu N_R)$
$\mathcal{O}_{NLB1}$	$\epsilon_{ij}(\overline{N_R^c}\gamma^\mu L^i)(D^\nu H^j) B_{\mu\nu}$	$\mathcal{O}_{uND}$	$(\overline{u_R}\gamma_\mu u_R)(\overline{N_R^c} i \overleftrightarrow{\partial}^\mu N_R)$
$\mathcal{O}_{NLB2}$	$\epsilon_{ij}(\overline{N_R^c}\gamma^\mu L^i)(D^\nu H^j) \tilde{B}_{\mu\nu}$	$\mathcal{O}_{dND}$	$(\overline{d_R}\gamma_\mu d_R)(\overline{N_R^c} i \overleftrightarrow{\partial}^\mu N_R)$
$\mathcal{O}_{NLW1}$	$(\epsilon\tau^I)_{ij}(\overline{N_R^c}\gamma^\mu L^i)(D^\nu H^j) W^I_{\mu\nu}$	$\mathcal{O}_{NND}$	$(\overline{N_R}\gamma_\mu N_R)(\overline{N_R^c} i \overleftrightarrow{\partial}^\mu N_R)$
$\mathcal{O}_{NLW2}$	$(\epsilon\tau^I)_{ij}(\overline{N_R^c}\gamma^\mu L^i)(D^\nu H^j) \tilde{W}^I_{\mu\nu}$	$(\Delta L, \Delta B) = (1, -1)$	
		$\mathcal{O}_{uNdD}$	$(\overline{u_R}\gamma_\mu N_R)(\overline{d_R} i \overleftrightarrow{D}^\mu d_R^c)$
		$\mathcal{O}_{dNQD}$	$\epsilon_{ij}(\overline{d_R}\gamma_\mu N_R)(\overline{Q_i} i \overleftrightarrow{D}^\mu Q_j^c)$

TABLE 4.4: Continuation of Table 4.3. N_RSMEFT operator structures at $d = 7$ belonging to the classes $\psi^2 HDX$, $\psi^2 X^2$ and $\psi^4 D$. Again, (+h.c.) is implicitly assumed, and the operators violating baryon number require the antisymmetric tensor $\epsilon_{\alpha\beta\sigma}$ for the $SU(3)$ contraction.

4.3 Going to lower energies: N_RLEFT

At energies well below the electroweak scale, $E \ll \Lambda_{\text{EW}} \simeq v = 246$ GeV, the heaviest SM fields, namely the top quark, the Higgs and the W and Z bosons, are not dynamical degrees of freedom. In this energy regime, sterile neutrino interactions must be described by an EFT where these particles are integrated out. This leads to the Low-Energy EFT of the SM extended with right-handed neutrinos, which we refer to as N_RLEFT. It respects the unbroken gauge symmetry $SU(3)_C \times U(1)_{\text{em}}$, and includes as active fields the gluons, the photon, the five light quark flavors (u, d, s, c, b), all SM leptons and an arbitrary number n_f of sterile neutrinos.

In addition to the operators built purely from SM fields, classified up to $d = 6$ in [153], the N_RLEFT introduces new terms involving N_R. The renormalizable part of the Lagrangian reads

$$\mathcal{L}^{(4)}_{N_R\text{LEFT}} = \mathcal{L}_{\text{QCD+QED}} + \overline{N_R} i \partial\!\!\!/ N_R - \left[\frac{1}{2} \overline{\nu_L} M_\nu \nu_L^c + \frac{1}{2} \overline{N_R^c} M_R N_R + \overline{\nu_L} M_D N_R + \text{h.c.} \right], \tag{4.5}$$

where $\mathcal{L}_{\text{QCD+QED}}$ is the usual QCD and QED Lagrangian containing SM leptons and light quarks (see e.g. Eq. (5.1) in [153]). The mass terms include a Majorana matrix M_ν for active neutrinos, a Majorana mass M_R for sterile neutrinos and a Dirac matrix M_D connecting the active and sterile sectors. If lepton number is conserved, the Majorana mass terms vanish.

The full N_RLEFT Lagrangian then takes the form

$$\mathcal{L}_{N_R\text{LEFT}} = \mathcal{L}^{(4)} + \sum_{d\geq 5}\sum_i c_i^{(d)}\mathcal{O}_i^{(d)} , \tag{4.6}$$

where we have introduced *dimensionful* Wilson coefficients $c_i^{(d)}$, scaling as $1/\Lambda^{d-4}$. One typically identifies $\Lambda \equiv \Lambda_{\text{EW}}$, and then assumes that N_RLEFT originitates from N_RSMEFT, hence matching the two theories at Λ_{EW}.[5] Analogously to our discussion of N_RSMEFT, we now list the relevant operators at lowest dimension.

Dimension-5 operators. There are two non-hermitian operators involving N_R [154]

$$\mathcal{O}_{NN\gamma} = \overline{N_R^c}\sigma^{\mu\nu}N_R F_{\mu\nu} , \tag{4.7}$$

$$\mathcal{O}_{\nu N\gamma} = \overline{\nu_L}\sigma^{\mu\nu}N_R F_{\mu\nu} , \tag{4.8}$$

where $F_{\mu\nu}$ is the photon field strength tensor. The operator $\mathcal{O}_{NN\gamma}$ violates lepton number and is antisymmetric in generation space, vanishing for $n_f = 1$, whereas $\mathcal{O}_{\nu N\gamma}$ is lepton number conserving. Both operators induce electromagnetic interactions for active and sterile neutrinos. Their phenomenology is discussed in Chapter 7.

Dimension-6 operators. The N_RLEFT contains 55 four-fermion interactions with N_R: 23 conserve lepton number [155], 26 violate lepton number, and 6 violate both lepton and baryon numbers [154]. The LNC operators are summarized in Table 4.5 and the LNV and BNV operators, in Table 4.6. They have been grouped into vector, scalar and tensor current operators and we have added the corresponding superscript (V, S, T) to the operator name to differentiate operators with the same field content. In addition, we specify the chiralities (R or L) of the two bilinears that make up each four-fermion structure. As for N_RSMEFT, we omit the fermion flavor indices in the operators. Note, however, that the number of flavors for up-type quarks here is $n_u = 2$, while for down-type quarks and SM leptons, we have $n_f = 3$. In the third and sixth

[5] In this case, after performing the matching between the two EFTs, the dimensionful Wilson coefficients in N_RLEFT can have additional suppression factors in powers of $(\Lambda_{\text{EW}}/\Lambda)$, where Λ here denotes the energy scale associated to new physics in the UV.

$(\Delta L, \Delta B) = (0,0)$					
$\mathcal{O}_{duNe}^{V,RR}$	$(\overline{d_R}\gamma_\mu u_R)(\overline{N_R}\gamma^\mu e_R)$	$n_f^3 n_u$	$\mathcal{O}_{dN}^{V,RR}$	$(\overline{d_R}\gamma_\mu d_R)(\overline{N_R}\gamma^\mu N_R)$	n_f^4
$\mathcal{O}_{eN}^{V,RR}$	$(\overline{e_R}\gamma_\mu e_R)(\overline{N_R}\gamma^\mu N_R)$	n_f^4	$\mathcal{O}_{uN}^{V,RR}$	$(\overline{u_R}\gamma_\mu u_R)(\overline{N_R}\gamma^\mu N_R)$	$n_f^2 n_u^2$
$\mathcal{O}_{NN}^{V,RR}$	$(\overline{N_R}\gamma_\mu N_R)(\overline{N_R}\gamma^\mu N_R)$	$\frac{1}{4}n_f^2(n_f+1)^2$			
$\mathcal{O}_{duNe}^{V,LR}$	$(\overline{d_L}\gamma_\mu u_L)(\overline{N_R}\gamma^\mu e_R)$	$n_f^3 n_u$	$\mathcal{O}_{dN}^{V,LR}$	$(\overline{d_L}\gamma_\mu d_L)(\overline{N_R}\gamma^\mu N_R)$	n_f^4
$\mathcal{O}_{eN}^{V,LR}$	$(\overline{e_L}\gamma_\mu e_L)(\overline{N_R}\gamma^\mu N_R)$	n_f^4	$\mathcal{O}_{uN}^{V,LR}$	$(\overline{u_L}\gamma_\mu u_L)(\overline{N_R}\gamma^\mu N_R)$	$n_f^2 n_u^2$
$\mathcal{O}_{\nu N}^{V,LR}$	$(\overline{\nu_L}\gamma_\mu \nu_L)(\overline{N_R}\gamma^\mu N_R)$	n_f^4			
$\mathcal{O}_{duNe}^{S,LL}$	$(\overline{d_R}u_L)(\overline{N_R}e_L)$	$n_f^3 n_u$	$\mathcal{O}_{d\nu N}^{S,RR}$	$(\overline{d_L}d_R)(\overline{\nu_L}N_R)$	n_f^4
$\mathcal{O}_{duNe}^{T,LL}$	$(\overline{d_R}\sigma_{\mu\nu}u_L)(\overline{N_R}\sigma^{\mu\nu}e_L)$	$n_f^3 n_u$	$\mathcal{O}_{d\nu N}^{T,RR}$	$(\overline{d_L}\sigma_{\mu\nu}d_R)(\overline{\nu_L}\sigma^{\mu\nu}N_R)$	n_f^4
$\mathcal{O}_{e\nu N}^{S,RR}$	$(\overline{e_L}e_R)(\overline{\nu_L}N_R)$	n_f^4	$\mathcal{O}_{u\nu N}^{S,RR}$	$(\overline{u_L}u_R)(\overline{\nu_L}N_R)$	$n_f^2 n_u^2$
$\mathcal{O}_{e\nu N}^{T,RR}$	$(\overline{e_L}\sigma_{\mu\nu}e_R)(\overline{\nu_L}\sigma^{\mu\nu}N_R)$	n_f^4	$\mathcal{O}_{u\nu N}^{T,RR}$	$(\overline{u_L}\sigma_{\mu\nu}u_R)(\overline{\nu_L}\sigma^{\mu\nu}N_R)$	$n_f^2 n_u^2$
$\mathcal{O}_{\nu N}^{S,RR}$	$(\overline{\nu_L}N_R)(\overline{\nu_L}N_R)$	$\frac{1}{2}n_f^2(n_f^2+1)$			
$\mathcal{O}_{duNe}^{S,RL}$	$(\overline{d_L}u_R)(\overline{N_R}e_L)$	$n_f^3 n_u$	$\mathcal{O}_{d\nu N}^{S,LR}$	$(\overline{d_R}d_L)(\overline{\nu_L}N_R)$	n_f^4
$\mathcal{O}_{e\nu N}^{S,LR}$	$(\overline{e_R}e_L)(\overline{\nu_L}N_R)$	n_f^4	$\mathcal{O}_{u\nu N}^{S,LR}$	$(\overline{u_R}u_L)(\overline{\nu_L}N_R)$	$n_f^2 n_u^2$

TABLE 4.5: Lepton number conserving $d=6$ operators in N_RLEFT. All operator structures are non-hermitian except those containing a pair of N_R. Next to each operator structure we indicate the independent number of parameters when flavor is taken into account.

columns of Tables 4.5 and 4.6 we have written explicitly the independent number of parameters taking into account the fermion flavor structure, as provided in [154].

According to their field content, we can classify the four-fermion interactions into two broad categories: purely leptonic operators and lepto-quark operators (containing both leptons and quarks). The former can induce lepton flavor violating (LFV) processes, while the latter can mediate rare meson decays involving sterile neutrinos. We will discuss rare decays of B and D mesons induced by these lepto-quark operators in Chapter 6.

A notable feature is that the LNV operators appearing at $d=6$ in N_RLEFT cannot originate from the minimal set of $d=6$ operators in N_RSMEFT, which contains only one LNV structure, $\mathcal{O}_{NNNN}$, vanishing for a single N_R. Therefore, these low-energy LNV operators must arise from $d=7$ (or higher) operators in N_RSMEFT. This connection becomes manifest in the matching procedure between the two EFTs, which we also discuss in Chapter 6.

$(\Delta L, \Delta B) = (2,0)$					
$\mathcal{O}^{V,LL}_{duNe}$	$(\overline{d_L}\gamma_\mu u_L)(\overline{N_R^c}\gamma^\mu e_L)$	$n_f^3 n_u$	$\mathcal{O}^{V,RR}_{d\nu N}$	$(\overline{d_R}\gamma_\mu d_R)(\overline{\nu_L^c}\gamma^\mu N_R)$	n_f^4
$\mathcal{O}^{V,RR}_{e\nu N}$	$(\overline{e_R}\gamma_\mu e_R)(\overline{\nu_L^c}\gamma^\mu N_R)$	n_f^4	$\mathcal{O}^{V,RR}_{u\nu N}$	$(\overline{u_R}\gamma_\mu u_R)(\overline{\nu_L^c}\gamma^\mu N_R)$	$n_f^2 n_u^2$
$\mathcal{O}^{V,RR}_{N\nu N}$	$(\overline{N_R}\gamma_\mu N_R)(\overline{\nu_L^c}\gamma^\mu N_R)$	$\frac{1}{2}n_f^3(n_f+1)$			
$\mathcal{O}^{V,RL}_{duNe}$	$(\overline{d_R}\gamma_\mu u_R)(\overline{N_R^c}\gamma^\mu e_L)$	$n_f^3 n_u$	$\mathcal{O}^{V,LR}_{d\nu N}$	$(\overline{d_L}\gamma_\mu d_L)(\overline{\nu_L^c}\gamma^\mu N_R)$	n_f^4
$\mathcal{O}^{V,LR}_{e\nu N}$	$(\overline{e_L}\gamma_\mu e_L)(\overline{\nu_L^c}\gamma^\mu N_R)$	n_f^4	$\mathcal{O}^{V,LR}_{u\nu N}$	$(\overline{u_L}\gamma_\mu u_L)(\overline{\nu_L^c}\gamma^\mu N_R)$	$n_f^2 n_u^2$
$\mathcal{O}^{V,LR}_{\nu\nu N}$	$(\overline{\nu_L}\gamma_\mu \nu_L)(\overline{\nu_L^c}\gamma^\mu N_R)$	$\frac{1}{2}n_f^3(n_f+1)$			
$\mathcal{O}^{S,RR}_{duNe}$	$(\overline{d_L}u_R)(\overline{N_R^c}e_R)$	$n_f^3 n_u$	$\mathcal{O}^{S,RR}_{dN}$	$(\overline{d_L}d_R)(\overline{N_R^c}N_R)$	$\frac{1}{2}n_f^3(n_f+1)$
$\mathcal{O}^{T,RR}_{duNe}$	$(\overline{d_L}\sigma_{\mu\nu}u_R)(\overline{N_R^c}\sigma^{\mu\nu}e_R)$	$n_f^3 n_u$	$\mathcal{O}^{T,RR}_{dN}$	$(\overline{d_L}\sigma_{\mu\nu}d_R)(\overline{N_R^c}\sigma^{\mu\nu}N_R)$	$\frac{1}{2}n_f^3(n_f-1)$
$\mathcal{O}^{S,RR}_{eN}$	$(\overline{e_L}e_R)(\overline{N_R^c}N_R)$	$\frac{1}{2}n_f^3(n_f+1)$	$\mathcal{O}^{S,RR}_{uN}$	$(\overline{u_L}u_R)(\overline{N_R^c}N_R)$	$\frac{1}{2}n_f(n_f+1)n_u^2$
$\mathcal{O}^{T,RR}_{eN}$	$(\overline{e_L}\sigma_{\mu\nu}e_R)(\overline{N_R^c}\sigma^{\mu\nu}N_R)$	$\frac{1}{2}n_f^3(n_f-1)$	$\mathcal{O}^{T,RR}_{uN}$	$(\overline{u_L}\sigma_{\mu\nu}u_R)(\overline{N_R^c}\sigma^{\mu\nu}N_R)$	$\frac{1}{2}n_f(n_f-1)n_u^2$
$\mathcal{O}^{S,RR}_{\nu NN}$	$(\overline{\nu_L}N_R)(\overline{N_R^c}N_R)$	$\frac{1}{3}n_f^2(n_f^2-1)$			
$\mathcal{O}^{S,LR}_{duNe}$	$(\overline{d_R}u_L)(\overline{N_R^c}e_R)$	$n_f^3 n_u$	$\mathcal{O}^{S,LR}_{dN}$	$(\overline{d_R}d_L)(\overline{N_R^c}N_R)$	$\frac{1}{2}n_f^3(n_f+1)$
$\mathcal{O}^{S,LR}_{eN}$	$(\overline{e_R}e_L)(\overline{N_R^c}N_R)$	$\frac{1}{2}n_f^3(n_f+1)$	$\mathcal{O}^{S,LR}_{uN}$	$(\overline{u_R}u_L)(\overline{N_R^c}N_R)$	$\frac{1}{2}n_f(n_f+1)n_u^2$
$\mathcal{O}^{S,LL}_{N\nu\nu}$	$(\overline{N_R}\nu_L)(\overline{\nu_L^c}\nu_L)$	$\frac{1}{3}n_f^2(n_f^2-1)$			
$(\Delta L, \Delta B) = (4,0)$					
$\mathcal{O}^{S,LR}_{\nu N}$	$(\overline{\nu_L^c}\nu_L)(\overline{N_R^c}N_R)$	$\frac{1}{4}n_f^2(n_f+1)^2$	$\mathcal{O}^{S,RR}_{N}$	$(\overline{N_R^c}N_R)(\overline{N_R^c}N_R)$	$\frac{1}{12}n_f^2(n_f^2-1)$
$(\Delta L, \lvert\Delta B\rvert) = (1,1)$					
$\mathcal{O}^{V,RR}_{dduN}$	$(\overline{d_R}\gamma_\mu d_L^c)(\overline{u_R}\gamma^\mu N_R)$	$n_f^3 n_u$	$\mathcal{O}^{V,LR}_{dduN}$	$(\overline{d_R^c}\gamma_\mu d_L)(\overline{u_L^c}\gamma^\mu N_R)$	$n_f^3 n_u$
$\mathcal{O}^{S,LR}_{dduN1}$	$(\overline{d_R}d_R^c)(\overline{u_L}N_R)$	$\frac{1}{2}n_f^2(n_f-1)n_u$	$\mathcal{O}^{S,LR}_{dduN2}$	$(\overline{d_L^c}d_L)(\overline{u_R^c}N_R)$	$\frac{1}{2}n_f^2(n_f-1)n_u$
$\mathcal{O}^{S,RR}_{uddN1}$	$(\overline{u_L}d_L^c)(\overline{d_L}N_R)$	$n_f^3 n_u$	$\mathcal{O}^{S,RR}_{uddN2}$	$(\overline{u_R^c}d_R)(\overline{d_R^c}N_R)$	$n_f^3 n_u$

TABLE 4.6: Lepton and baryon number violating $d = 6$ operators in N_RLEFT. All operator structures are non-hermitian.

This section closes Chapter 4, where we have discussed the theoretical foundation for describing sterile neutrino interactions across a wide range of energies. From the UV scale Λ down to the GeV range, the N_RSMEFT and N_RLEFT provide EFT frameworks that encode the possible imprints of weakly coupled new physics.

In the next chapter, we will focus on the UV side of the story. We will examine how the N_RSMEFT operators discussed above can arise at tree level by integrating out heavy mediators in UV complete theories. These completions not only provide theoretical motivation for the operator structures, but also point to distinctive experimental signatures that may shed light on the nature of the sterile neutrino sector.

Chapter 5

A tree level dictionary for N_RSMEFT $d = 6$ and $d = 7$ operators

In recent years, several ultraviolet (UV) completions of N_RSMEFT operators at dimension $d = 5$ and $d = 6$ have been explored in the literature, however, a comprehensive and systematic study is still lacking. In particular, what has been missing is an exhaustive decomposition of the full set of $d = 6$ and $d = 7$ operators, that is, a complete classification of particle extensions of the SM capable of generating these operators at tree level.

The primary goal of this chapter, based on the results presented in [156], is to provide such a classification. We construct a "dictionary" of heavy fields that, when integrated out, produce the N_RSMEFT operator basis up to $d = 7$. Of relevant importance for us is Ref. [157], which catalogued all one-field extensions of the SM that generate SMEFT operators at $d = 6$. We compare our findings to this earlier dictionary, highlighting the key differences that arise when including right-handed neutrinos into the light particle content.

The structure of the chapter is as follows: in Section 5.1, we outline the diagrammatic method used to systematically decompose EFT operators into renormalizable interactions. In Section 5.2, we present the full set of tree level decompositions for $d = 6$ and $d = 7$ N_RSMEFT operators, with baryon number violating structures discussed separately. In Section 5.3, we analyze lepton number violation in N_RSMEFT, thouroughly discussing its connection to neutrino mass generation. We close with a short summary.

Name	$\mathcal{S}$	$\mathcal{S}_1$	φ	Ξ	Ξ_1
Irrep	$(1,1,0)$	$(1,1,1)$	$\left(1,2,\frac{1}{2}\right)$	$(1,3,0)$	$(1,3,1)$
$d=6$	$\circ$	$\circ$	$\circ$	$\circ$	$\circ$
Name	ω_1	ω_2	Π_1	Π_7	ζ
Irrep	$\left(3,1,-\frac{1}{3}\right)$	$\left(3,1,\frac{2}{3}\right)$	$\left(3,2,\frac{1}{6}\right)$	$\left(3,2,\frac{7}{6}\right)$	$\left(3,3,-\frac{1}{3}\right)$
$d=6$	$\circ$	$\circ$	$\circ$		

TABLE 5.1: New scalars contributing to $d=6$ and $d=7$ N_RSMEFT operators at tree level. Only fields marked with a circle contribute to $d=6$, the remaining ones appear in models for $d=7$ operators. Field names follow the conventions of [157].

Name	$\mathcal{N}$	E	Δ_1	Δ_3	Σ	Σ_1	
Irrep	$(1,1,0)$	$(1,1,-1)$	$\left(1,2,-\frac{1}{2}\right)$	$\left(1,2,-\frac{3}{2}\right)$	$(1,3,0)$	$(1,3,-1)$	
$d=6$	$\circ$		$\circ$		$\circ$	$\circ$	
Name	U	D	Q_1	Q_5	Q_7	T_1	T_2
Irrep	$\left(3,1,\frac{2}{3}\right)$	$\left(3,1,-\frac{1}{3}\right)$	$\left(3,2,\frac{1}{6}\right)$	$\left(3,2,-\frac{5}{6}\right)$	$\left(3,2,\frac{7}{6}\right)$	$\left(3,3,-\frac{1}{3}\right)$	$\left(3,3,\frac{2}{3}\right)$
$d=6$							

TABLE 5.2: New vector-like fermions contributing to $d=6,7$ N_RSMEFT operators at tree level.

Name	$\mathcal{B}$	$\mathcal{B}_1$	$\mathcal{W}$	$\mathcal{W}_1$	$\mathcal{L}_1$	$\mathcal{L}_3$
Irrep	$(1,1,0)$	$(1,1,1)$	$(1,3,0)$	$(1,3,1)$	$\left(1,2,\frac{1}{2}\right)$	$\left(1,2,-\frac{3}{2}\right)$
$d=6$	$\circ$	$\circ$			$\circ$	
Name	$\mathcal{U}_1$	$\mathcal{U}_2$	$\mathcal{Q}_1$	$\mathcal{Q}_5$	$\mathcal{X}$	
Irrep	$\left(3,1,-\frac{1}{3}\right)$	$\left(3,1,\frac{2}{3}\right)$	$\left(3,2,\frac{1}{6}\right)$	$\left(3,2,-\frac{5}{6}\right)$	$\left(3,3,\frac{2}{3}\right)$	
$d=6$	$\circ$	$\circ$	$\circ$			

TABLE 5.3: New vector bosons contributing to $d=6,7$ N_RSMEFT operators at tree level. Two fields, $\mathcal{L}_1$ and $\mathcal{U}_1$, are special cases, see text.

5.1 Diagrammatic approach

The concept of decomposing effective operators refers to the process of expanding an operator into a series of UV renormalizable interactions generating the initial operator. This can be done using a diagrammatic method, which has been used previously for studying the Weinberg operator at different loop orders in [27, 28, 30, 158] and for 1-loop openings of SMEFT four-fermion operators in [159, 160].

Here, we apply the diagrammatic method to N_RSMEFT operators which include at least one N_R at both $d = 6$ and $d = 7$. The decomposition procedure follows three main steps. First, given an effective operator involving n light fields, one constructs all possible *topologies* that can generate the operator at some loop order. Each topology defines a graph made up of n external legs connected through internal lines using only renormalizable interactions, i.e. 3- and 4-point interaction vertices. The number of internal lines depends on the topology and on loop order. In our case, we consider only tree level openings and all internal lines are identified with BSM *heavy* fields.

Next, light fields are assigned to the external legs, and Lorentz invariance is used to determine the allowed spin for the internal lines: scalars, fermions or vectors. At this stage, the output consists of a set of *diagrams* where every line has definite Lorentz nature. Finally, we impose gauge invariance at each vertex — in our case under $SU(3)_C \times SU(2)_L \times U(1)_Y$. This uniquely determines (for tree level openings) the quantum numbers of the heavy internal fields. The diagrams are then promoted to *model diagrams* and the lists of particles that can be accommodated as internal lines constitute our *models*.

In summary, the outcome of this procedure is, for each N_RSMEFT operator of a given dimension d, a set of models consisting of heavy BSM particles, each of which gives a tree level opening of the operator.

Several additional comments are in order. The entire procedure is implemented in a custom `Mathematica` code. The input for this code is the list of fields and the number of derivatives contained in the considered operator. Neither the Lorentz structure nor the field contractions have to be specified. As a consequence, in cases where the basis of operators allow more than one operator with the same field content the method yields a list of model diagrams, each of which will contribute to at least one operator in this set, but does not provide the information to which specific operator (or operators) the model will be matched. The model lists found in this way are complete, once one scans over all possible operators at a given level of d.

The code does not fix the operator list to any particular on-shell basis. In consequence, we do not consider diagrams with light *bridges* (internal propagators). Once the operator list, to which any given model is matched, is reduced to the on-shell basis, operators containing diagrams with light bridges will be automatically included. It is important to note, however, that diagrams with light bridges do not present new models, i.e. it is guaranteed that with the diagrammatic method, as discussed here, no models are lost.

With that being said, we applied the diagrammatic method to the N_RSMEFT $d = 6$ and $d = 7$ operators. All the BSM fields appearing in the output model diagrams are collected in Tables 5.1, 5.2 and 5.3, classified by spin (scalars, fermions and vector bosons, respectively). Fields contributing to $d = 6$ operators are explicitly marked, while the remaining ones appear only in $d = 7$ operator decompositions. We indicate the quantum numbers under the SM gauge symmetry and adopt the naming conventions of [157]. Most fields in our list of possible BSM particles have already appeared in that reference in a different context. We note that the scalar triplet Ξ_1 is often denoted by Δ in the neutrino literature, and we use $\mathcal{N}$ to label a heavy fermion with quantum numbers $(1, 1, 0)$ to distinguish it from the light sterile neutrino N_R. Two special cases deserve comment: the vectors $\mathcal{L}_1$ and $\mathcal{U}_1$. The latter does not appear in pure SMEFT at $d = 6$ [157], but this field is listed in [161].

The case of $\mathcal{L}_1$ is more subtle. If $\mathcal{L}_1$ is a general vector field (not necessarily a gauge boson) one can write down all renormalizable interactions allowed by Lorentz and gauge symmetry. However, if $\mathcal{L}_1$ is a gauge vector, certain interactions may be forbidden [162]. For example, in SMEFT the interaction $\mathcal{L}_{1,\mu}^{\dagger} D^{\mu} H$ must be present to generate $d = 6$ operators, but this term is not permitted if $\mathcal{L}_1$ is a true gauge boson. In N_RSMEFT, by contrast, $\mathcal{L}_1$ can still contribute to the matching even if it is forced to be a gauge vector. [1]

All heavy fermions in our list are assumed to be vector-like under the SM gauge group, even if only one chirality is needed to complete a given diagram. This is motivated by experimental constraints: the observation of a SM-like Higgs boson at the LHC [166, 167] strongly disfavors the existence of a chiral fourth generation in the minimal SM.

In the next section, we present the specific decompositions obtained for each operator at $d = 6$ and $d = 7$, with a separated discussion for those that violate baryon number.

[1] We do not give an explicit list of the gauge groups for the vector bosons, but $\mathcal{L}_1$ appears, for instance, in $SU(3)_C \times SU(3)_L \times U(1)_X$ ("331") models [163, 164, 165].

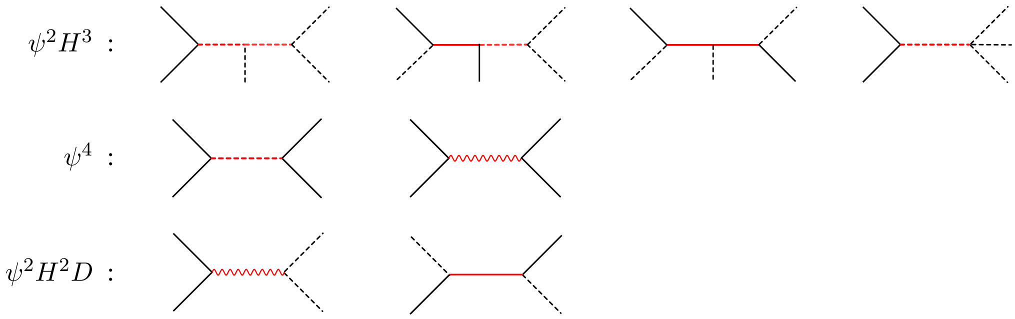

FIGURE 5.1: Operator classes at $d = 6$ and their respective tree openings at the diagram level. Solid lines correspond to fermions, dashed lines to scalars and wavy lines to vectors. Red lines are for heavy fields.

5.2 List of operator decompositions

5.2.1 Dictionary for $d = 6$

The complete basis of operators at $d = 6$ (see Table 4.2) contains four operator classes: $\psi^2 H^3$, $\psi^2 H^2 D$, ψ^4 and $\psi^2 HX$. However, not all of these can be generated at tree level using renormalizable interactions. In particular, operators in the $\psi^2 HX$ class require at least one loop to be realized [162] and thus fall outside the scope of the present analysis.

Fig. 5.1 displays the full set of tree level diagrams that generate the remaining three classes: $\psi^2 H^3$, $\psi^2 H^2 D$ and ψ^4. In these diagrams, solid, dashed, and wavy lines denote fermions (F), scalars (S), and vector bosons (V), respectively. Light SM fields are shown in black, while red lines correspond to heavy BSM mediators. The $\psi^2 H^3$ class admits two distinct topologies at tree level: one involving two heavy mediators (which can be either SS, FF or SF, see first row of Fig. 5.1) and one involving a single scalar mediator with a 4-point vertex interaction. The former topology leads in most cases to two-particle extensions of the SM, while the latter corresponds to one-particle extensions only. The four-fermion operators, ψ^4, can only be generated at tree level with a scalar or a vector heavy propagator, depending on the chirality of the external fermions. Finally, for $\psi^2 H^2 D$, there exist two diagrams involving a single heavy mediator: in one, the derivative is part of the VSS interaction vertex; in the other, it arises from the fermion propagator. Altogether, we find that all $d = 6$ operators in Table 4.2 can be generated at tree level using one-particle extensions, with two exceptions: $\mathcal{O}_{LNH^3}$ in the $\psi^2 H^3$ class requires two mediators in some openings, as discussed above, while the dipole operators in the $\psi^2 H^2 X$ class ($\mathcal{O}_{NBH}$ and $\mathcal{O}_{NWH}$) cannot be opened at tree level.

Models	Operators
$\mathcal{S}$	$\mathcal{O}_{NN}$, $\mathcal{O}_{NNNN}$
$\mathcal{S}_1$	$\mathcal{O}_{LNLe}$, $\mathcal{O}_{eN}$
φ	$\mathcal{O}_{QuNL}$, $\mathcal{O}_{LNLe}$, $\mathcal{O}_{LNQd}$, $\mathcal{O}_{LN}$, $\mathcal{O}_{LNH^3}$
ω_1	$\mathcal{O}_{LNQd}$, $\mathcal{O}_{dN}$, $\mathcal{O}_{duNe}$
ω_2	$\mathcal{O}_{uN}$
Π_1	$\mathcal{O}_{LNQd}$, $\mathcal{O}_{QN}$
Δ_1	$\mathcal{O}_{NH^2D}$, $\mathcal{O}_{NeH^2D}$
$\mathcal{B}$	$\mathcal{O}_{NH^2D}$, $\mathcal{O}_{NN}$, $\mathcal{O}_{eN}$, $\mathcal{O}_{uN}$, $\mathcal{O}_{dN}$, $\mathcal{O}_{LN}$, $\mathcal{O}_{QN}$
$\mathcal{B}_1$	$\mathcal{O}_{NeH^2D}$, $\mathcal{O}_{eN}$, $\mathcal{O}_{duNe}$
$\mathcal{L}_1$	$\mathcal{O}_{LN}$
$\mathcal{U}_1$	$\mathcal{O}_{dN}$
$\mathcal{U}_2$	$\mathcal{O}_{QuNL}$, $\mathcal{O}_{uN}$, $\mathcal{O}_{duNe}$
$\mathcal{Q}_1$	$\mathcal{O}_{QuNL}$, $\mathcal{O}_{QN}$

TABLE 5.4: One-particle decompositions for $d = 6$ N_RSMEFT operators. We separate them in scalar, fermion and vector models. The first column gives the particle (*model*), the second the corresponding operators generated at tree level.

$\psi^2 H^3$	Two-particle models	
$\mathcal{O}_{LNH^3}$	SS :	$(\mathcal{S},\varphi)$, (Ξ_1,φ), (Ξ,φ)
	FF :	$(\Delta_1,\mathcal{N})$, (Δ_1,Σ_1), (Δ_1,Σ)
	FS :	$(\mathcal{N},\mathcal{S})$, $(\Delta_1,\mathcal{S})$, (Δ_1,Ξ_1), (Σ_1,Ξ_1), (Δ_1,Ξ), (Σ,Ξ)

TABLE 5.5: Two-particle decompositions for the $d = 6$ operator $\mathcal{O}_{LNH^3}$. There are three types of models according to the possible spins of the heavy fields.

Here, our approach differs from the philosophy followed in [157], since we insist on using only renormalizable vertices, while the authors of [157], on the other hand, consider only one-particle extensions of the SM. However, already at $d = 6$ in pure SMEFT there are some operators which require two BSM fields. The list of decompositions given in [157] for pure SMEFT is nevertheless complete, since they add also non-renormalizable operator interactions at $d = 5$ to their Lagrangian.

We present in Table 5.4 the list of one-particle models found at $d = 6$ along with the operators they induce at tree level. The two-particle models generating $\mathcal{O}_{LNH^3}$ are collected separately in Table 5.5, and are classified by the spin of the mediators. Among the new fields appearing in these decompositions, the vector $\mathcal{U}_1$ contributes only to a single operator, $\mathcal{O}_{dN}$. The reason is that there is only one renormalizable term involving $\mathcal{U}_1$ and light fields; in particular, such interaction is $\mathcal{L} \propto \left(\overline{N_R}\gamma_\mu d_R\right) \mathcal{U}_1^{\mu\dagger}$.

We provide the full list of renormalizable interaction terms involving N_R and the heavy mediators in Appendix A of this thesis, as well as the renormalizable interactions for the new vector $\mathcal{U}_1$. For N_RSMEFT, we find additional renormalizable interactions of the vector $\mathcal{L}_1$, which are also presented in the appendix. Recall that the vector boson $\mathcal{L}_1$ was also included in [157] but as a non-gauge vector. Specifically, we highlight here the interaction term $\mathcal{L} \propto \left(\overline{N_R^c}\gamma_\mu L\right)\mathcal{L}_1^\mu$, which contributes to the matching of the operator $\mathcal{O}_{LN}$.

Given the complete UV Lagrangian, one could perform the tree level matching onto the set of N_RSMEFT operators. While we do not explicitly perform the matching here, this procedure can be automated using tools such as `Matchete` [145] and we provided a `Mathematica` notebook with some example models as supplementary material to our paper [156].

5.2.2 Dictionary for $d = 7$

We now turn to the UV completions of $d = 7$ N_RSMEFT operators. The complete operator basis at this dimension (see Tables 4.3 and 4.4) spans eight classes, as discussed in Chapter 4. However, not all of them can be generated at tree level using renormalizable interactions. In particular, operators with two fermions and derivatives or gauge field strength tensors have to contain, in addition, at least two scalar fields to be generated at tree level [162]. Similarly, four-fermion operators with a derivative cannot be opened at tree level, since the diagrams with four external fermion legs do not have derivatives in their interaction vertices, see Fig. 5.1.

Consequently, only five operator classes admit tree level decompositions: ψ^2H^3D, $\psi^2H^2D^2$, ψ^2H^2X, ψ^4H, and ψ^2H^4. The remaining classes, namely ψ^2HDX, ψ^4D, and ψ^2X^2, can only be generated at loop level. The subset of operators that can be generated at tree level is listed in Table 4.3, whereas the operators requiring loop level completions are listed in Table 4.4 of Chapter 4.

Fig. 5.2 illustrates the full set of diagrams used to generate the operators in Table 4.3. At $d = 7$, many of the resulting diagrams involve two or even three internal propagators. A notable exception is the $\psi^2H^2D^2$ class, for which some operators can be generated with just a single heavy mediator. Accordingly, we encounter models that require one, two, or three heavy BSM particles. The allowed spin of the mediators vary for each operator class: ψ^2H^2X requires heavy fermions only; $\psi^2H^2D^2$ and ψ^2H^4 can be opened with scalar and/or fermion mediators; and ψ^2H^3D and ψ^4H admit mixed combinations involving scalars, fermions and vectors.

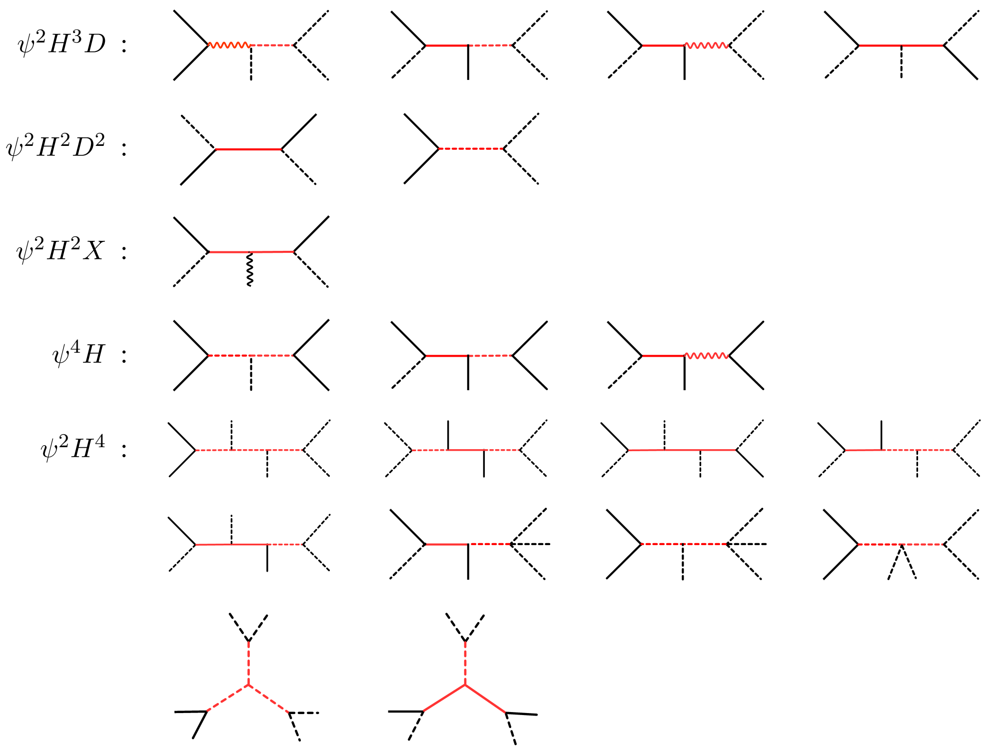

FIGURE 5.2: Diagrams generating different $d = 7$ operator classes at tree level. External light fields appear as black lines and heavy propagators are marked in red.

As the number of internal lines increases in diagrams of higher dimensional operators, so does the possible number of models. In total, we find 224 distinct UV decompositions for the $d = 7$ operators in Table 4.3. However, multiple operator decompositions often share the same particle content. After accounting for repetitions, the number of unique particle combinations is reduced to 112. We present the decomposition results for each operator in Tables 5.6 and 5.7, classifying the models by the number of BSM particles they contain (one, two or three) and by their spin.

Among these, only two operators can be generated via one-particle completions: one involving the scalar $\mathcal{S}$ and another involving the fermion Δ_1. Two-particle models account for the vast majority of completions, with a total of 102 distinct configurations. These include: 42 FS models, 45 FV models, 3 FF models, 9 SS models and 3 SV models. Notably, we do not find any completions involving two vector mediators (VV), as can be seen in Fig. 5.2. Finally, we identify 8 three-particle completions, all of which generate the operator $\mathcal{O}_{NH^4}$. It is worth emphasizing that subsets of the heavy fields in these three-particle models can also give rise to other $d = 7$ operators.

$\psi^2H^2D^2$	Models	ψ^2H^2X	Models
$\mathcal{O}_{NeH^2D^2}$	$F\ :\ \ \Delta_1$	$\mathcal{O}_{NeH^2W}$	$F\ :\ \ \Delta_1$
$\mathcal{O}_{NH^2D^2}$	$S\ :\ \ \mathcal{S}$	$\mathcal{O}_{NH^2B}$	$F\ :\ \ \Delta_1$
	$F\ :\ \ \Delta_1$	$\mathcal{O}_{NH^2W}$	$F\ :\ \ \Delta_1$

ψ^4H	Models
$\mathcal{O}_{LNLH}$	SS : $(\mathcal{S}_1,\varphi)$ (φ,Ξ_1) FS : $(E,\mathcal{S}_1)$ (Σ_1,Ξ_1) $(\Delta_1,\mathcal{S}_1)$ (Δ_1,Ξ_1) $(\mathcal{N},\varphi)$ (Σ,φ) FV : $(\mathcal{N},\mathcal{B})$ $(\Sigma,\mathcal{W})$ $(\mathcal{N},\mathcal{L}_1)$ $(\Sigma,\mathcal{L}_1)$ $(\Delta_1,\mathcal{B})$ $(\Delta_1,\mathcal{W})$ $(E,\mathcal{L}_1)$ $(\Sigma_1,\mathcal{L}_1)$
$\mathcal{O}_{QNLH}$	SS : (ω_1,Π_1) (Π_1,ζ) FS : (D,ω_1) (T_1,ζ) (Δ_1,ω_1) (Δ_1,ζ) $(\mathcal{N},\Pi_1)$ (Σ,Π_1) (U,Π_1) (T_2,Π_1) FV : $(U,\mathcal{U}_2)$ (T_2,χ) $(U,\mathcal{L}_1)$ $(T_2,\mathcal{L}_1)$ $(\mathcal{N},\mathcal{B})$ $(\Sigma,\mathcal{W})$ $(\mathcal{N},\mathcal{Q}_1)$ $(\Sigma,\mathcal{Q}_1)$ $(\Delta_1,\mathcal{U}_2)$ (Δ_1,χ) $(D,\mathcal{L}_1)$ $(T_1,\mathcal{L}_1)$ $(\Delta_1,\mathcal{B})$ $(\Delta_1,\mathcal{W})$ $(D,\mathcal{Q}_1)$ $(T_1,\mathcal{Q}_1)$
$\mathcal{O}_{eNLH}$	SS : $(\mathcal{S}_1,\varphi)$ FS : $(\mathcal{N},\mathcal{S}_1)$ (Δ_1,φ) $(\Delta_3,\mathcal{S}_1)$ FV : $(\mathcal{N},\mathcal{B})$ $(\mathcal{N},\mathcal{B}_1)$ $(\Delta_3,\mathcal{L}_3)$ $(\Delta_3,\mathcal{L}_1)$ $(\Delta_1,\mathcal{B})$ $(\Delta_1,\mathcal{B}_1)$ $(\Delta_1,\mathcal{L}_3)$ $(\Delta_1,\mathcal{L}_1)$
$\mathcal{O}_{dNLH}$	SS : (ω_1,Π_1) FS : (Q_1,Π_1) (Δ_1,Π_1) (Q_5,ω_1) $(\mathcal{N},\omega_1)$ FV : $(\mathcal{N},\mathcal{B})$ $(\mathcal{N},\mathcal{U}_1)$ $(Q_5,\mathcal{Q}_5)$ $(Q_5,\mathcal{L}_1)$ $(\Delta_1,\mathcal{B})$ $(Q_1,\mathcal{U}_1)$ $(\Delta_1,\mathcal{Q}_5)$ $(Q_1,\mathcal{L}_1)$
$\mathcal{O}_{uNLH}$	SS : (ω_2,Π_7) FS : (Q_7,Π_7) (Δ_1,Π_7) $(\mathcal{N},\omega_2)$ (Q_1,ω_2) FV : $(Q_1,\mathcal{Q}_1)$ $(Q_1,\mathcal{L}_1)$ $(\mathcal{N},\mathcal{B})$ $(\mathcal{N},\mathcal{U}_2)$ $(\Delta_1,\mathcal{Q}_1)$ $(Q_7,\mathcal{L}_1)$ $(\Delta_1,\mathcal{B})$ $(Q_7,\mathcal{U}_2)$
$\mathcal{O}_{duNLH}$	SS : (ω_2,Π_1) FS : (Q_1,Π_1) (Δ_1,Π_1) (Q_1,ω_2) (E,ω_2) FV : $(E,\mathcal{B}_1)$ $(E,\mathcal{U}_1)$ $(Q_1,\mathcal{Q}_1)$ $(Q_1,\mathcal{L}_1)$ $(\Delta_1,\mathcal{B}_1)$ $(Q_1,\mathcal{U}_1)$ $(\Delta_1,\mathcal{Q}_1)$
$\mathcal{O}_{dQNeH}$	SS : $(\mathcal{S}_1,\varphi)$ FS : (Δ_1,φ) $(Q_5,\mathcal{S}_1)$ $(U,\mathcal{S}_1)$ FV : $(U,\mathcal{U}_2)$ $(U,\mathcal{U}_1)$ $(Q_5,\mathcal{Q}_5)$ $(Q_5,\mathcal{Q}_1)$ $(\Delta_1,\mathcal{U}_2)$ $(\Delta_1,\mathcal{U}_1)$ $(\Delta_1,\mathcal{Q}_5)$ $(\Delta_1,\mathcal{Q}_1)$
$\mathcal{O}_{QuNeH}$	SS : $(\mathcal{S}_1,\varphi)$ (ω_1,Π_1) (ω_2,Π_7) FS : (Q_7,Π_7) (Δ_1,Π_7) (D,ω_1) (Δ_1,ω_1) $(D,\mathcal{S}_1)$ $(Q_7,\mathcal{S}_1)$ (Δ_1,φ) (Δ_1,Π_1) (Q_7,Π_1) (Δ_1,ω_2) (D,ω_2)

TABLE 5.6: List of models generating at tree level $d = 7$ operators belonging to the operator classes $\psi^2H^2D^2$, ψ^2H^2X and ψ^4H.

$\psi^2 H^3 D$	Models
$\mathcal{O}_{NLH^3D}$	SV : $(\mathcal{S}, \mathcal{L}_1)$ $(\Xi, \mathcal{L}_1)$ $(\Xi_1, \mathcal{L}_1)$ FS : $(\mathcal{N}, \mathcal{S})$ (Σ, Ξ) (Σ_1, Ξ_1) $(\Delta_1, \mathcal{S})$ (Δ_1, Ξ) (Δ_1, Ξ_1) FV : $(\mathcal{N}, \mathcal{B})$ $(\Sigma, \mathcal{W})$ $(\Sigma_1, \mathcal{W}_1)$ $(\Delta_1, \mathcal{B})$ $(\Delta_1, \mathcal{W})$ $(\Delta_1, \mathcal{B}_1)$ $(\Delta_1, \mathcal{W}_1)$ FF : $(\mathcal{N}, \Delta_1)$ (Δ_1, Σ) (Δ_1, Σ_1)
$\psi^2 H^4$	Models
$\mathcal{O}_{NH^4}$	S : $\mathcal{S}$ SS : $(\mathcal{S}, \varphi)$ $(\mathcal{S}, \Xi_1)$ $(\mathcal{S}, \Xi)$ FS : $(\mathcal{N}, \mathcal{S})$ (Σ, Ξ) (Σ_1, Ξ_1) $(\Delta_1, \mathcal{S})$ (Δ_1, Ξ) (Δ_1, Ξ_1) (Δ_1, φ) FF : $(\mathcal{N}, \Delta_1)$ (Δ_1, Σ) (Δ_1, Σ_1) SSS : $(\mathcal{S}, \varphi, \Xi_1)$ $(\mathcal{S}, \varphi, \Xi)$ FFS : $(\Delta_1, \Sigma_1, \Xi_1)$ $(\mathcal{N}, \Delta_1, \mathcal{S})$ (Δ_1, Σ, Ξ) FSS : $(\Delta_1, \mathcal{S}, \varphi)$ (Δ_1, φ, Ξ) $(\Delta_1, \varphi, \Xi_1)$
$\psi^4 H$	Models
$\mathcal{O}_{LNeH}$	SS : $(\mathcal{S}, \varphi)$ $(\mathcal{S}_1, \varphi)$ FS : $(E, \mathcal{S})$ $(E, \mathcal{S}_1)$ (Δ_1, φ) $(\Delta_1, \mathcal{S})$ $(\Delta_1, \mathcal{S}_1)$
$\mathcal{O}_{eLNH}$	SS : $(\mathcal{S}, \varphi)$ FS : $(\Delta_1, \mathcal{S})$ (Δ_1, φ) $(E, \mathcal{S})$ FV : $(E, \mathcal{B}_1)$ $(\Delta_1, \mathcal{L}_1)$ $(\Delta_1, \mathcal{B}_1)$
$\mathcal{O}_{QNdH}$	SS : $(\mathcal{S}, \varphi)$ (ω_1, Π_1) FS : (Δ_1, φ) $(D, \omega_1)(\Delta_1, \omega_1)$ (Q_1, Π_1) (Δ_1, Π_1) $(Q_1, \mathcal{S})$ $(D, \mathcal{S})$
$\mathcal{O}_{dQNH}$	SS : $(\mathcal{S}, \varphi)$ FS : (Δ_1, φ) $(Q_1, \mathcal{S})$ $(D, \mathcal{S})$ FV : $(\Delta_1, \mathcal{U}_1)$ $(\Delta_1, \mathcal{Q}_1)$ $(D, \mathcal{U}_1)$ $(Q_1, \mathcal{Q}_1)$
$\mathcal{O}_{QNuH}$	SS : $(\mathcal{S}, \varphi)$ (ω_2, Π_1) FS : (Q_1, Π_1), (Δ_1, Π_1), (U, ω_2), (Δ_1, ω_2), $(U, \mathcal{S})$, $(Q_1, \mathcal{S})$
$\mathcal{O}_{uQNH}$	SS : $(\mathcal{S}, \varphi)$ FS : (Δ_1, φ) $(U, \mathcal{S})$ $(Q_1, \mathcal{S})$ FV : $(Q_1, \mathcal{Q}_1)$ $(U, \mathcal{U}_2)$ $(\Delta_1, \mathcal{Q}_1)$ $(\Delta_1, \mathcal{U}_2)$
$\mathcal{O}_{LNNH}$	SS : $(\mathcal{S}, \varphi)$ FS : $(\mathcal{N}, \mathcal{S})$ $(\Delta_1, \mathcal{S})$ (Δ_1, φ)
$\mathcal{O}_{NLNH}$	SS : $(\mathcal{S}, \varphi)$ FS : $(\mathcal{N}, \mathcal{S})$ $(\Delta_1, \mathcal{S})$ (Δ_1, φ) FV : $(\mathcal{N}, \mathcal{B})$ $(\Delta_1, \mathcal{B})$ $(\Delta_1, \mathcal{L}_1)$

TABLE 5.7: Continuation of table 5.6. N_RSMEFT $d = 7$ operators in $\psi^2 H^3 D$, $\psi^2 H^4$, $\psi^4 H$ and their tree level decompositions.

$\psi^4 \quad (d=6)$	Models
$\mathcal{O}_{QQdN}$	S : ω_1 V : $\mathcal{Q}_1$
$\mathcal{O}_{uddN}$	S : ω_1, ω_2
$\psi^4 H \quad (d=7)$	Models
$\mathcal{O}_{QNddH}$	SS : (ω_2, Π_1) FS : (U, ω_2) (Δ_1, ω_2) (Q_1, Π_1) FV : $(Q_1, \mathcal{Q}_1)$ $(Q_1, \mathcal{U}_1)$ $(\Delta_1, \mathcal{Q}_1)$ $(U, \mathcal{U}_1)$
$\mathcal{O}_{QNQH}$	SS : (ω_1, Π_1) (Π_1, ζ) FS : (D, ω_1) (Δ_1, ω_1) (T_1, ζ) (Δ_1, ζ) (D, Π_1) (T_1, Π_1)
$\mathcal{O}_{QNudH}$	SS : (ω_1, Π_1) FS : (D, ω_1) (Δ_1, ω_1) (Q_5, Π_1) (Q_1, Π_1) FV : $(Q_1, \mathcal{Q}_1)$ $(Q_1, \mathcal{U}_1)$ $(Q_5, \mathcal{Q}_5)$ $(Q_5, \mathcal{U}_2)$ $(\Delta_1, \mathcal{Q}_1)$ $(D, \mathcal{U}_1)$ $(\Delta_1, \mathcal{Q}_5)$ $(D, \mathcal{U}_2)$

TABLE 5.8: Tree level decompositions for the baryon number violating operators of $d = 6$ and $d = 7$ in N_RSMEFT. Models are classified in terms of the Lorentz nature of the fields.

5.2.3 Models for BNV operators

We now turn to the discussion of BNV operators in N_RSMEFT. These operators are generally considered irrelevant for collider phenomenology due to the severe constraints from proton decay experiments, as we discuss below.

Table 5.8 lists the BNV operators at $d = 6$ and $d = 7$ that admit tree level UV completions, along with their decompositions classified by the spin of the heavy fields. At $d = 6$, there are two four-fermion BNV operators that can be opened at tree level. At $d = 7$, five BNV operators appear in the basis, but two of them belong to the $\psi^4 D$ class and thus require loop level completions; hence we do not list them here. The remaining three operators, all in the $\psi^4 H$ class, admit tree level completions via three distinct diagrams, as shown in Fig. 5.2.

For the $d = 6$ operators, we find three possible one-particle UV completions: the scalars ω_1, ω_2, and the vector boson $\mathcal{Q}_1$. The $d = 7$ BNV operators admit 22 two-particle completions, consisting of 3 SS, 10 FS, and 9 FV combinations. Of these, 17 appear also in the decomposition of other $d = 7$ N_RSMEFT operators, while the remaining five are specific to the BNV case. These are the FS models (D, Π_1), (T_1, Π_1), (Q_5, Π_1) and the FV models $(Q_5, \mathcal{U}_2)$, $(D, \mathcal{U}_2)$.

Experimental bounds on proton lifetime place extremely tight constraints on the parameters of models that permit BNV. To illustrate this, consider a simple UV completion of the $d = 6$ operator $\mathcal{O}_{uddN} = (\overline{u_R^c} d_R)(\overline{d_R^c} N_R)$ via the scalar ω_1. The relevant terms in the UV Lagrangian are

$$\begin{aligned}\mathcal{L} \propto\, & y_{ue}^{\omega_1} \left(\overline{u_R^c} e_R\right) \omega_1^\dagger + y_{Nd}^{\omega_1} \left(\overline{d_R^c} N_R\right) \omega_1^\dagger + y_{QL}^{\omega_1} \left(\overline{Q^c} L\right) \omega_1^\dagger \\ & + y_{ud}^{\omega_1} \left(\overline{u_R^c} d_R\right) \omega_1 + y_Q^{\omega_1} \left(\overline{Q^c} Q\right) \omega_1 + \text{h.c.} + \ldots \end{aligned} \tag{5.1}$$

The contribution to the operator $\mathcal{O}_{uddN}$ is given by the matching relation

$$c_{uddN} = \frac{y_{Nd}^{\omega_1} y_{ud}^{\omega_1}}{\Lambda^2}\,, \tag{5.2}$$

where we assumed $m_{\omega_1} = \Lambda$. Here, $c_{\mathcal{O}}$ denotes the dimensionful Wilson coefficient, which is inversely proportional to the new physics scale Λ. In addition, we have suppressed flavor indices.

This operator triggers the decay process $p \to \pi^+ N$, assuming $m_N < m_p - m_{\pi^+}$.[2] Current experimental limits from Super-Kamiokande and other proton decay searches [168] constrain the Wilson coefficient to

$$y_{Nd}^{\omega_1} y_{ud}^{\omega_1} \lesssim 10^{-26} \left(\frac{\Lambda}{\text{TeV}}\right)^2 . \tag{5.3}$$

Clearly, this constraint renders $\mathcal{O}_{uddN}$ unobservable for any foreseeable collider experiment. However, this does not imply that the mediator ω_1 is ruled out entirely. The BNV arises from the presence of both $y_{Nd}^{\omega_1}$ and $y_{ud}^{\omega_1}$ couplings in the UV Lagrangian. Since no baryon number assignment can make both terms in Eq. (5.1) simultaneously B-conserving, the violation results from the combination of the two. If we instead enforce baryon number conservation, only one of the two couplings must vanish, depending on the baryon number assigned to ω_1. In such scenarios, ω_1 may still contribute to the decomposition of other N_RSMEFT operators, potentially leading to observable effects at colliders.

This reasoning can be extended to $d = 7$ BNV operators, though the analysis becomes more intricate due to the larger number of couplings entering the matching relations. In general, decompositions at $d = 7$ involve three independent UV couplings. Typically, enforcing B conservation in the UV can be achieved by setting just one of these

[2] If $m_N > m_p - m_{\pi^+}$, an off-shell N_R can contribute to decays such as $p \to \pi^+\pi^0\nu$, which still puts limits on the Wilson coefficients, although these are much weaker.

couplings to zero, thus preventing proton decay while allowing the mediator fields to appear in other phenomenologically relevant operators.

Finally, we comment that the discussion above does not rely on the lepton number assignment for N_R. If we adopt the conventional choice $L(N_R) = 1$, we find that $d = 6$ BNV operators in N_RSMEFT violate $B + L$ while preserving $B - L$. By contrast, $d = 7$ operators violate $B - L$. This follows exactly the same pattern as found in SMEFT.

Just as BNV processes put tight experimental constraints on the operators, LNV interactions in N_RSMEFT could also be subject to stringent bounds, particularly if they induce observable processes or contribute to Majorana masses for the SM neutrinos. However, unlike the BNV case, the connection between LNV effective operators and neutrino masses is more subtle. The presence of LNV operators does not immediately fix the scale of neutrino mass generation. In the next section, we explore this connection in detail and how LNV arises in N_RSMEFT.

5.3 LNV operators and connection to neutrino mass

In this section we will discuss lepton number violation in N_RSMEFT and how it is connected to observable LNV processes with charged leptons at the LHC and to the Majorana masses of the SM neutrinos. Before we turn to N_RSMEFT operators, we revisit the "black box theorem" of neutrinoless double beta decay ($0\nu\beta\beta$ decay) [33]. Then, using very similar arguments, we will discuss how the observation of LNV at the LHC in processes involving a N_R and Majorana neutrino masses are related at the operator level. For N_RSMEFT at $d = 7$ we have given the possible decompositions at tree level in the previous section. At the end of this section, we examine Majorana neutrino masses in the renormalizable UV models found there.

Black box theorem

The observation of $0\nu\beta\beta$ decay will guarantee that at least one neutrino has a Majorana mass term [33]. This is known as the "black box theorem", since the mechanism (or "model") underlying the $0\nu\beta\beta$ decay amplitude needs not to be known for this conclusion to hold. $0\nu\beta\beta$ decay is a low-energy process, thus the black box diagram is usually drawn in the mass eigenstate basis, as it was done in Fig. 1.3, right. It is instructive, however, to discuss the black box theorem in terms of SMEFT operators.

As discussed in Part I, the neutrino Majorana mass matrix can be generated from the famous Weinberg operator, $\mathcal{O}_{Wbg} \propto LLHH$, while contributions to the $0\nu\beta\beta$ decay amplitude start at the $d = 9$ level. $\Delta L = 2$ operators (disregarding operators with

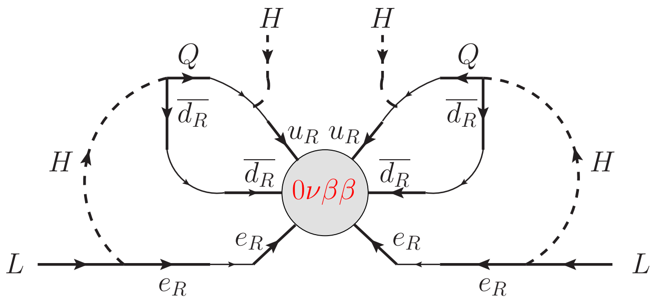

FIGURE 5.3: Example diagram of the black box theorem of $0\nu\beta\beta$ decay [33] for the operator $\mathcal{O}^9_{ude} = u_R^2 \overline{d_R}^2 e_R^2$ in the gauge basis.

derivatives or field strength tensors) have been listed up to $d = 11$ in [26]. At $d = 9$ there are six operators relevant for $0\nu\beta\beta$ decay.[3] The simplest six-fermion SMEFT operator for $0\nu\beta\beta$ decay is $\mathcal{O}^9_{u\bar{d}e} \propto u_R^2 \overline{d_R}^2 e_R^2$. The operator and its black box connection is shown in Fig. 5.3. The SM Yukawa couplings $\bar{L}e_R H$, $\bar{Q}d_R H$ and $\overline{u_R}QH$ are used to close the loops. This example results in a 4-loop diagram, the same as the black box diagram in the mass basis. The other five $d = 9$ operators will result either in 2-loop or in 3-loop black box diagrams.

Note that black box diagrams are in general divergent. Thus, one expects that neutrino masses are generated at a lower loop level than indicated by the respective black box diagram. However, at the level of effective operators it is not possible to decide at which level neutrino masses are indeed generated, for this one needs to know the underlying UV model. We will come back to this question later.

A 4-loop diagram will give only a tiny contribution to the neutrino mass [34] and, thus, the guaranteed, but minimal, contribution from the $0\nu\beta\beta$ decay black box diagram to the neutrino masses is numerically much smaller than what is required to explain neutrino oscillation data. However, given the finite number of operators at $d = 9$, one can open up the $0\nu\beta\beta$ decay operator(s) in all possible ways, say, at tree level [169]. The list of possible UV "models" found in this exercise can then be examined one by one and neutrino mass models from the tree to the 4-loop level emerge [170]. Whether any particular of these models can or can not be the *main* contribution to the neutrino masses — as required for an explanation of oscillation data — is then mainly a question of the loop level at which the neutrino masses are generated in the respective model, but in all cases a nonzero Majorana mass for the SM neutrinos is guaranteed.

[3] The mass mechanism of $0\nu\beta\beta$ decay corresponds actually to a $d = 11$ operator: $\mathcal{O}^{11}_{\bar{Q}^2 Q^2 L^2 H^2}$.

A black box for N_RSMEFT and Majorana neutrino masses

Before turning to N_RSMEFT operators, let us briefly discuss the renormalizable Lagrangian for the simplest model that adds a N_R to the SM, i.e. the minimal type-I seesaw, which contains a Yukawa term for N_R and a Majorana mass term

$$\mathcal{L}_{\text{type-I}} = -\overline{L}\tilde{H}Y_\nu N_R - \frac{1}{2}\overline{N_R^c}M_R N_R + \text{h.c.} \tag{5.4}$$

Here, the Majorana nature of the mass term is specific to the type-I seesaw. As discussed in the previous chapter, the mass term for N_R could also be of Dirac type, as in the inverse seesaw model. Then, one introduces a second Weyl fermion S_L and replaces M_R with a Dirac mass term $M_{NS}\overline{S_L}N_R$. Assigning lepton number $L(N_R) = 1$ (and $L(S_L) = 1$), both the Yukawa interaction and M_{NS} preserve lepton number, while M_R violates lepton number by $\Delta L = 2$. However, in the absence of Y_ν, one could also assign $L(N_R) = 0$, in which case M_R would be lepton number conserving. While this may seem trivial, it illustrates an important point: LNV always stems from a mismatch in the lepton number assignments between different terms in the Lagrangian. This is true in any model, and N_RSMEFT is no exception.

After EWSB, the simple model, defined by Eq. (5.4), introduces a nonzero coupling of the (mostly) singlet state, N,[4] to the gauge bosons, $gV_{\alpha N}$, where $V_{\alpha N}$ is the mixing angle between active and sterile states. At the LHC, W bosons are produced, which can then decay to $N + \ell$ via this nonzero coupling.[5] N will decay itself via an off-shell W to another lepton plus jets. For a Majorana neutrino, the probability to decay to either lepton or anti-lepton is the same (at tree level), thus the final state for the whole process will contain two leptons and two jets, leading to the ratio

$$R_{\ell\ell} = \frac{\#(\text{same-sign dilepton})}{\#(\text{opposite-sign dilepton})} = 1\,. \tag{5.5}$$

Same-sign dilepton events are obviously $\Delta L = 2$ processes, formally the same as a Majorana neutrino mass. The diagram for this LHC process is shown in Fig. 5.4 on the left. From this diagram, one can cut off the quarks and draw the 2-loop Majorana neutrino mass diagram shown on the right of Fig. 5.4.

Clearly, if the diagram on the left is present in the model, the diagram on the right must also exist. Thus, the observation of this LNV process at the LHC guarantees that neutrinos are Majorana states *for this particular model*. Several comments are in order.

[4] N_RSMEFT operators put the chirality of N_R as right-handed. In the mass eigenstate basis N has both, left- and right-handed components, so we do not add the subscript R for mass eigenstates.

[5] At the LHC $\ell = e, \mu, \tau$, in $0\nu\beta\beta$ decay only $\ell = e$, of course. We will not discuss flavor in detail.

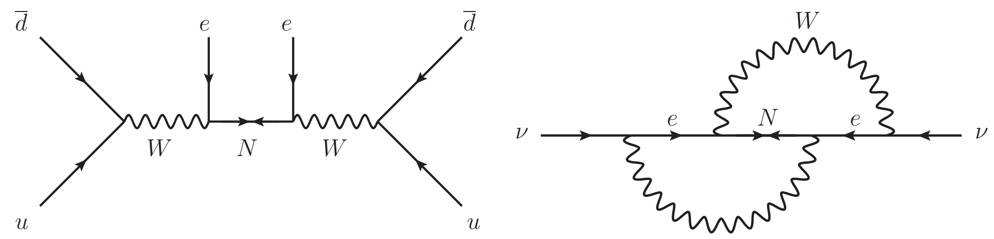

FIGURE 5.4: Lepton number violation at the LHC in a minimally extended variant of the SM (left) and a 2-loop neutrino mass diagram that will necessarily be generated at the same time.

First of all, the connection between the LHC process and Majorana neutrino masses in this particular example can be trivially understood. The model as discussed is, after all, a type-I seesaw and it of course generates Majorana neutrino masses. However, Majorana neutrino masses in the seesaw are generated at tree level, thus the 2-loop diagram in Fig. 5.4 just represents a "minimal link" between the LHC process and the existence of a Majorana neutrino mass. Numerically, it is only a very minor correction to the total neutrino mass in this model. This is very similar to the black box theorem for $0\nu\beta\beta$ decay discussed above.

However, different from the black box theorem for $0\nu\beta\beta$ decay, the discussion as presented so far is *model-dependent*, since we have assumed that the Lagrangian terms of Eq. (5.4) exist. To make statements as model-independent as possible, we should not a priori assume that N has a coupling to SM W bosons,[6] nor that the mass of the N is of Majorana type, but instead consider EFT operators.

In the mass eigenstate basis, after EWSB, the simplest purely fermionic operator one can write down for the production of a singlet fermion is either $\bar{d}u\overline{N}e$ or $\bar{d}u\overline{N^c}e$. Assigning lepton number to N as $L(N) = 1$ ($L(N) = -1$), the former (latter) operator is lepton number conserving, while the latter (former) represents a LNV object. If both types of operators are present, LNV processes will be generated — independently of the nature of the mass term of N. However, N needs to be a massive particle, its mass term could be either Dirac, i.e. lepton number conserving (LNC), or Majorana (LNV), as discussed above. Thus, overall, one can find $\Delta L = 2$ processes with two different combinations:

- Two LNC operators and a Majorana propagator (mass flip).
- One LNV and one LNC operator, along with a Dirac propagator (no mass flip).

For the discussion to be complete, we need to cover both options.

[6] We will come back to this point near the end of this subsection.

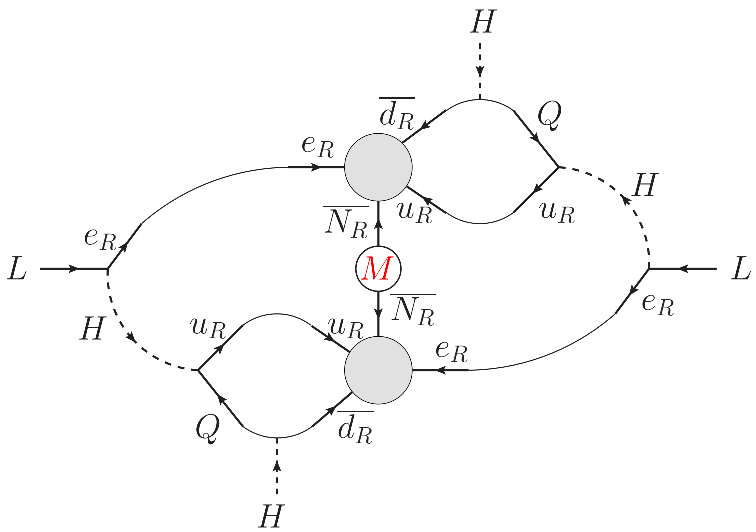

FIGURE 5.5: Lepton number violation at the LHC and a 4-loop realization of the Weinberg operator in the gauge basis, assuming the $d = 6$ operator $\mathcal{O}_{duNe}$ is nonzero. The origin of the LNV is assigned to the Majorana mass M.

Fig. 5.5 shows an example based on the simplest $d = 6$ N_RSMEFT operator, $\mathcal{O}_{duNe} = (\overline{d_R}\gamma_\mu u_R)(\overline{N_R}\gamma^\mu e_R)$, combining two insertions of the LNC operator with a LNV Majorana mass insertion in the N propagator. Here, the diagram gives actually a 4-loop realization of the Weinberg operator, $\mathcal{O}_{\rm Wbg} \propto LLHH$, which will generate the neutrino mass matrix after EWSB.

Note that, simple power counting shows that this 4-loop diagram is divergent. Clearly, a lower order diagram contributing to the neutrino mass should exist, in order to provide a counter term for this infinity, and — apart from some very fine-tuned special cases — that lower order diagram will give a larger contribution to the neutrino mass than the 4-loop diagram. However, given only the effective operator and not the full UV complete model, it is not possible to decide at which loop level Majorana masses will appear.

The LHC LNV process $pp \to \ell^+\ell^+jj$ is contained in the inside of the diagram, just cutting the diagram at the thin lines. Thus, the two observables are always either both present in the theory or none of them is, exactly as in the originally black box theorem for $0\nu\beta\beta$ decay.

In the above discussion it was assumed that the source of the LNV is the Majorana propagator of the N_R. However, the same black box connection between LNV at

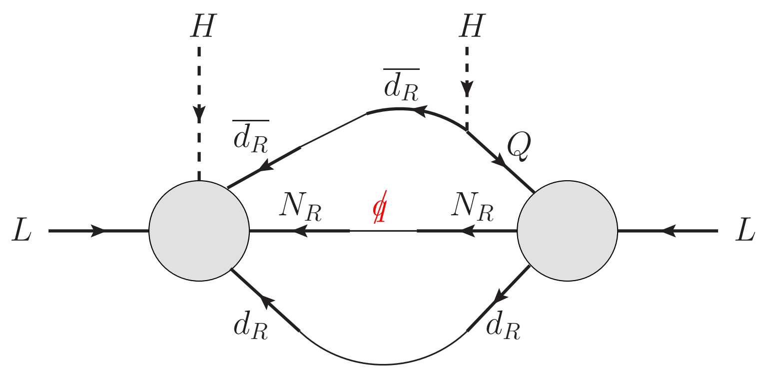

FIGURE 5.6: Lepton number violation at the LHC and a 2-loop realization of the Weinberg operator. Different from Fig. 5.5, in this diagram the origin of LNV is the $d = 7$ operator $\mathcal{O}_{dNLH}$.

the LHC and Majorana neutrino mass can be established in the case that the necessary LNV is due to a LNV operator. We choose as the LNV $d = 7$ operator the example of $\mathcal{O}_{dNLH} = \epsilon(\overline{d_R}\gamma_\mu d_R)(\overline{N_R^c}\gamma^\mu L)H$. For the LNC $d = 6$ operator we choose $\mathcal{O}_{LNQd} = (\overline{L}N_R)\epsilon(\overline{Q}d_R)$. Fig. 5.6 shows the resulting 2-loop diagram for $\mathcal{O}_{\mathrm{Wbg}}$. As before, cutting open the loops defines a LNV process for the LHC: one could, for example, produce the N via $\mathcal{O}_{LNQd}$, while the final state is produced from the decay of N via $\mathcal{O}_{dNLH}$. This decay could either contain two jets plus a Higgs (or Z^0) boson and missing momentum, or two jets plus a W and a charged lepton.[7] The additional bosons (relative to the "standard" $\ell\ell jj$ signal) could actually be used to distinguish the two possibilities (Majorana propagator versus $d = 7$ operator) *experimentally*, at least in principle.

One can easily check that the chiralities in the diagram in Fig. 5.6 are such that the momentum $\not{q}$ is picked from the neutrino propagator (no mass flip). Again, the resulting integral is divergent, indicating that a lower order contribution to the neutrino mass should exist in any UV completion generating this diagram at low energies. However, whether the neutrino mass comes at tree level or 1-loop can not be decided at the level of effective operators only. While we have concentrated here on a specific combination of operators, the same conclusions can easily be reached for all other possible combinations: the observation of LNV at the LHC guarantees the existence of Majorana neutrino masses for the SM neutrinos.

[7]Only final states *without* missing energy can be used to determine lepton number experimentally.

Neutrino masses in models derived from LNV $d = 7$ operators

Here, we will briefly discuss neutrino mass generation at the renormalizable level. The aim of this discussion is not to provide a detailed fit of neutrino masses and mixing angles to experimental data,[8] but rather to demonstrate that all models generating LNV operators with N_R also generate active neutrino masses.[9] Given this connection, one might be tempted to think that $d = 7$ operators are not observable in accelerator experiments, due to the smallness of the observed neutrino masses. However, as we will discuss now, such a conclusion holds only for a very specific subset of UV decompositions and not in general.

First of all, with N_R being a complete SM singlet, all models giving rise to single-N_R $d = 6$ operators necessarily allow to write down also a neutrino yukawa coupling, as discussed above. If, in addition, lepton number is violated, also a Majorana mass for N_R is allowed. In fact, the Majorana mass term is mandatory in this case. One can easily show that in all N_R models with LNV, M_M is generated radiatively via diagrams with divergent integrals. Thus, for consistency, all these models require also the presence of a tree level M_M as a counter term. A seesaw type-I contribution to the neutrino masses is therefore unavoidable in all models with a N_R and LNV. For the discussion in this subsection, however, this contribution to the neutrino masses is irrelevant, since it does not place any restrictions on the Wilson coefficients of the $d = 7$ operators.

As we pointed out in Section 5.2, we found 112 different models for $d = 7$ operators. We will not discuss all these models in detail, but instead focus on just four decompositions for the example operator $\mathcal{O}_{LNLH} = \epsilon(\overline{L}\gamma_\mu L)(\overline{N_R^c}\gamma^\mu L)H$, see Fig. 5.7. These four examples are sufficient to cover essentially all relevant aspects of neutrino mass generation in the 112 models. The remaining models could be discussed in much the same way, with adequate replacements for the corresponding model parameters.

In Fig. 5.7, we show in the top row two example decompositions for $\mathcal{O}_{LNLH}$ containing $\mathcal{N}$ and Ξ_1. These will give a tree level seesaw contribution of type-I and type-II to the neutrino masses (note that one can replace $\mathcal{N}$ by Σ, and obtain a decomposition with a type-III seesaw too). We note in passing that out of the 112 models (14, 8, 8) contain ($\mathcal{N}$, Ξ_1, Σ), respectively. The decompositions in the bottom row, on the other hand, will generate neutrino masses radiatively.

[8] Once a particular model is specified, neutrino fits can be easily done using the formulas in [171].
[9] To simplify the discussion below, we assume the $d = 7$ operators violate L.

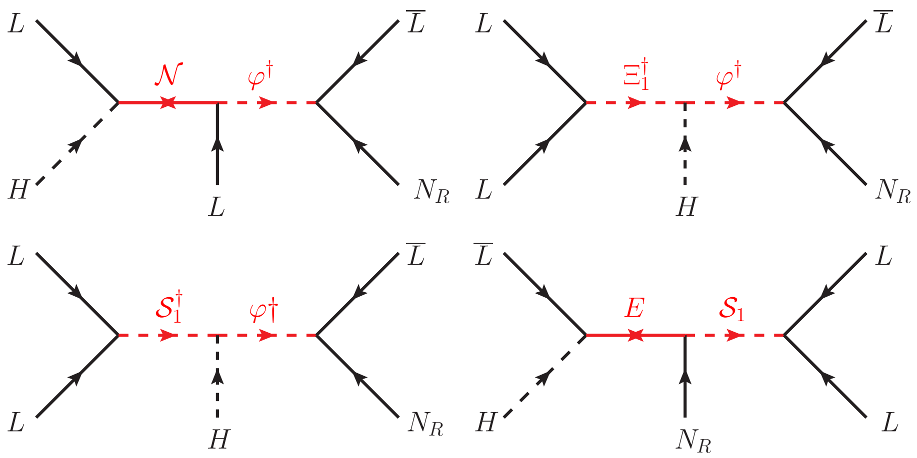

FIGURE 5.7: Four example decompositions for $\mathcal{O}_{LNLH}$. The two examples shown in the top row will give tree level contributions to the active neutrino masses via a type-I (left) or type-II seesaw (right). The decompositions in the bottom generate radiative neutrino masses at 1-loop (left) and 2-loops (right). The quantum numbers for the new fields are given in Tables 5.1, 5.2.

Let us discuss the tree level cases first. Consider the example decomposition shown in Fig. 5.7, top left. The Lagrangian contains the terms:

$$\mathcal{L} \propto y^{\varphi}_{NL} \left(\overline{N_R} L\right) \varphi + y^{\varphi}_{\mathcal{N}L} \left(\overline{\mathcal{N}} L\right) \varphi + y_{\mathcal{N}L} \left(\overline{\mathcal{N}} L\right) H + \frac{1}{2} M_{\mathcal{N}} \overline{\mathcal{N}^c} \mathcal{N} + \text{h.c.} \tag{5.6}$$

where $\mathcal{N}$ and φ are "heavy" copies of N_R and H.[10] The (dimensionful) Wilson coefficient generated from this diagram is matched via

$$c_{LNLH} = -\frac{1}{4} \frac{y^{\varphi}_{NL} y^{\varphi}_{\mathcal{N}L} y_{\mathcal{N}L}}{M_{\mathcal{N}} m^2_{\varphi}}. \tag{5.7}$$

On the other hand, $\mathcal{N}$ must be a Majorana field, otherwise the diagram can not be closed. Thus, $\mathcal{N}$ gives a contribution to the neutrino mass *á la* seesaw type-I:

$$m_\nu \propto y^2_{\mathcal{N}L} \frac{v^2}{M_{\mathcal{N}}}. \tag{5.8}$$

We can use this equation to put an upper limit on the coefficient c_{LNLH}:

$$c_{LNLH} \lesssim 10^{-6} \frac{y^{\varphi}_{NL} y^{\varphi}_{\mathcal{N}L}}{\Lambda^3} \left(\frac{\Lambda}{v}\right)^{1/2} \left(\frac{m_\nu}{0.1\,\text{eV}}\right), \tag{5.9}$$

where we have assumed $M_{\mathcal{N}} \simeq m_\varphi \simeq \Lambda$. This estimate shows that production of a

[10]Notice that we have omitted the explicit contraction of indices. To simplify the notation we omit them in the rest of this chapter.

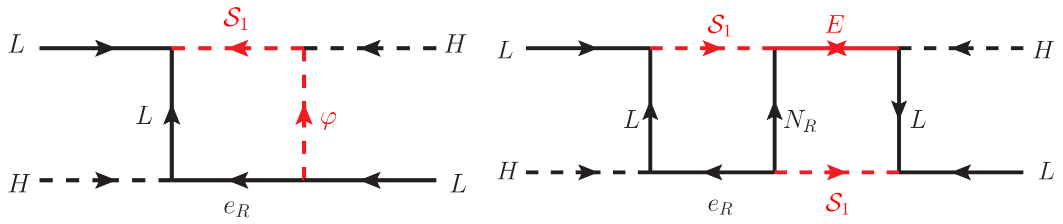

FIGURE 5.8: One-loop (left) and two-loop (right) neutrino mass diagrams, based on the decomposition of $\mathcal{O}_{LNLH}$ containing the BSM particles $(\mathcal{S}_1, \varphi)$ or $(E, \mathcal{S}_1)$.

N_R via this operator in a lepton collider is completely negligible for this model. We can also estimate the partial decay width of a N_R via $\mathcal{O}_{LNLH}$ given this constraint. We find the decay length is roughly

$$(c\tau) \sim \left(\frac{\Lambda}{\mathrm{TeV}}\right)^5 \left(\frac{m_{N_R}}{10\ \mathrm{GeV}}\right)^{-5} \left(\frac{0.1\,\mathrm{eV}}{m_\nu}\right)^2 10^8\,\mathrm{m}, \tag{5.10}$$

for $y^{\varphi}_{NL} = y^{\varphi}_{NL} = 1$. A decay length this large would render the N_R essentially stable for collider experiments, unless it is much heavier than indicated in Eq. (5.10). Note that similar arguments can be presented for all decompositions of $d = 7$ operators containing either $\mathcal{N}$ or Σ.

For decompositions containing Ξ_1, the situation is slightly more complicated. If we allow for LNV, the Lagrangian for a model with a Ξ_1 field contains the terms:

$$\mathcal{L} \propto y_L^{\Xi_1}\left(\overline{L^c}L\right)\Xi_1 + \kappa_{\Xi_1} HH\Xi_1^\dagger + \kappa_{\Xi_1\varphi}\Xi_1^\dagger H\varphi + \dots \tag{5.11}$$

The simultaneous presence of both terms will lead to a seesaw type-II contribution to the active neutrino mass matrix. We can use this to rewrite the Wilson coefficient for the decomposition shown in Fig. 5.7, top right as:

$$|c_{LNLH}| \lesssim y^{\varphi}_{NL}\frac{m_\nu}{v_{\Xi_1}}\frac{1}{\Lambda^3} \tag{5.12}$$

$$\lesssim 10^{-10} y^{\varphi}_{NL}\left(\frac{m_\nu}{0.1\,\mathrm{eV}}\right)\left(\frac{\mathrm{GeV}}{v_{\Xi_1}}\right)\frac{1}{\Lambda^3}, \tag{5.13}$$

where we have assumed $m_{\Xi_1} = m_\varphi = \kappa_{\Xi_1\varphi} = \Lambda$. The SM ρ-parameter puts an upper limit on the induced vacuum expectation value of the triplet, v_{Ξ_1}, of roughly $v_{\Xi_1} \lesssim 2$ GeV [168], which motivates the stringent constraint Eq. (5.13). Neutrino oscillation data, however, allow v_{Ξ_1} as small as $v_{\Xi_1} \sim 0.1$ eV. Obviously, no numerically relevant constraint on $|c_{LNLH}|$ can be derived in this case.

Let us turn now to decomposition #3 in Fig. 5.7, $(\mathcal{S}_1, \varphi)$. The same particle content appears also in decompositions of the operators $\mathcal{O}_{eNLH}$, $\mathcal{O}_{LNeH}$, $\mathcal{O}_{dQNeH}$ and $\mathcal{O}_{QuNeH}$. [11] In neutrino physics this combination of BSM particles is known as the Zee model [24]. Neutrino masses are generated at 1-loop level, see Fig. 5.8 to the left. The Lagrangian of the Zee model contains the terms:

$$\mathcal{L} \propto y_L^{\mathcal{S}_1}\left(\overline{L^c}L\right)\mathcal{S}_1 + y_{Ne}^{\mathcal{S}_1}\left(\overline{N_R^c}e_R\right)\mathcal{S}_1 + y_{eL}^{\varphi}\left(\overline{e_R}L\right)\varphi^\dagger + \kappa_{\mathcal{S}_1\varphi}\mathcal{S}_1^\dagger H\varphi + \text{h.c.} + \ldots \tag{5.14}$$

Disregarding flavor indices for simplicity, the neutrino mass in the Zee model can be estimated as:

$$m_\nu^{\text{Zee}} \simeq -\frac{1}{16\pi^2} y_L^{\mathcal{S}_1} m_\tau y_{eL}^{\varphi} \frac{\sqrt{2}v\kappa_{\mathcal{S}_1\varphi}}{m_{h_2^+}^2 - m_{h_1^+}^2} \log\left(\frac{m_{h_2^+}^2}{m_{h_1^+}^2}\right). \tag{5.15}$$

Here, $h_{1,2}$ are the two mass eigenstates formed by $\mathcal{S}_1$ and the charged component in φ. m_τ is the mass of the τ lepton and we have neglected terms proportional to $m_{\mu,e}$, which are not relevant for this discussion. Thus, neutrino masses will put a stringent constraint on the product $y_L^{\mathcal{S}_1} y_{eL}^{\varphi}(\kappa_{\mathcal{S}_1\varphi}/\Lambda)$, where $\Lambda \simeq m_{\mathcal{S}_1} \simeq m_\varphi$. Logically, this combination could be small because one, two or all three parameters are suppressed.

The matching of $\mathcal{O}_{LNLH}$, $\mathcal{O}_{eNLH}$ and $\mathcal{O}_{LNeH}$, on the other hand, is proportional to

$$\begin{aligned} c_{LNLH} &\propto y_L^{\mathcal{S}_1} y_{NL}^{\varphi} \frac{\kappa_{\mathcal{S}_1\varphi}}{\Lambda}, \\ c_{eNLH} &\propto y_{Ne}^{\mathcal{S}_1} y_{eL}^{\varphi} \frac{\kappa_{\mathcal{S}_1\varphi}}{\Lambda}, \\ c_{LNeH} &\propto y_{Ne}^{\mathcal{S}_1} y_{NL}^{\varphi} \frac{\kappa_{\mathcal{S}_1\varphi}}{\Lambda}. \end{aligned} \tag{5.16}$$

In case all three parameters entering the neutrino mass are small, i.e. $y_L^{\mathcal{S}_1} \sim y_{eL}^{\varphi} \sim (\kappa_{\mathcal{S}_1\varphi}/\Lambda) \sim \epsilon$, all of the coefficients in Eq. (5.16) will be suppressed. However, in the more optimistic case, where either $y_L^{\mathcal{S}_1}$ or y_{eL}^{φ} are suppressed by ϵ^3, while the other two parameters are order $\mathcal{O}(1)$, either c_{LNLH} or c_{eNLH} and c_{LNeH} can be large. However, given the constraint from neutrino masses, it is impossible that all three operators are observable at the same time.

Consider now decomposition #4 in Fig. 5.7, $(E, \mathcal{S}_1)$. This model allows to write the following terms in the Lagrangian:

$$\mathcal{L} \propto y_L^{\mathcal{S}_1}\left(\overline{L^c}L\right)\mathcal{S}_1 + y_{Ne}^{\mathcal{S}_1}\left(\overline{N_R^c}e_R\right)\mathcal{S}_1 + y_{LE}\left(\overline{L}E\right)H + y_{NE_L}^{\mathcal{S}_1}\left(\overline{N_R}E\right)\mathcal{S}_1 + m_E\overline{E}E + \ldots \tag{5.17}$$

Note that the vertex proportional to $y_{Ne}^{\mathcal{S}_1}$ does not appear in Fig. 5.7, but it is contained

[11] See Table 4.3 for the operator definitions and Tables 5.6, 5.7 for the corresponding decompositions.

in a decomposition for $\mathcal{O}_{LNeH}$ with the same particle content. Also, $y_{Ne}^{\mathcal{S}_1}$ is necessary for the 2-loop diagram in Fig. 5.8. In this diagram, from the N_R propagator $P_R(\not{q} + M_{N_R})P_L$, the momentum term survives. LNV stems from the simultaneous presence of $y_{Ne}^{\mathcal{S}_1}$ and $y_{NE_L}^{\mathcal{S}_1}$. Similar to the discussion for the Zee model, either $y_{Ne}^{\mathcal{S}_1}$ or $y_{NE_L}^{\mathcal{S}_1}$ (or both) must be small to fulfill the neutrino mass constraint. Thus, either $\mathcal{O}_{LNLH}$ or $\mathcal{O}_{LNeH}$ can have unsupressed Wilson coefficients, but not both at the same time.

We close this section summarizing: 1) Models for LNV in $d = 7$ N_RSMEFT operators will always also lead to active neutrino masses either at tree, 1- or 2-loop level. 2) For decompositions leading to seesaw type-I or type-III contributions to the neutrino mass, the Wilson coefficients will be severely suppressed, rendering the corresponding operators phenomenologically irrelevant for accelerator experiments. 3) For decompositions leading to radiative neutrino masses, the Wilson coefficients for some of the corresponding operators can be large, but the same UV decomposition contributes typically to more than one operator and neutrino mass constraints exclude the possibility that all corresponding operators are observable at the same time.

5.4 Summary

In this chapter, we discussed a systematic tree level decomposition of $d = 6$ and 7 N_RSMEFT operators, using a diagrammatic method. The resulting lists of BSM particles provide a complete dictionary of models, which can be used for studying N_R phenomenology. We have also briefly compared our lists of particles to the Granada dictionary for tree level UV completions for SMEFT at $d = 6$ [157]. Our lists of BSM particles are given in Tables 5.1 - 5.3. In Appendix A, we give all the Lagrangian terms involving N_R for the resulting models. There are additional terms involving the BSM fields necessary for the matching calculation of the UV models onto N_RSMEFT, and we provided them in supplementary material files accompanying our paper [156]. These Lagrangians were calculated with `Sym2Int` [142, 143]. The matching can be done automatically with the help of `Matchete` [145], and we added an example notebook for a number of models in the supplementary material.

We also discussed lepton number violation, that unavoidably appears if $d = 6$ and $d = 7$ operators are present in the theory at the same time. LNV is always linked to Majorana neutrino masses and LNV in N_RSMEFT is no exception, as we discussed in detail. We also discussed possible constraints on $d = 7$ operators from the observed neutrino masses. While some of the possible UV models for $d = 7$ operators must have tiny Wilson coefficients, due the neutrino mass constraint, there exist many models for which $d = 7$ N_RSMEFT operators could be observable in future experiments.

Part III

Phenomenology of Heavy Neutral Leptons at colliders

Chapter 6

Long-lived heavy neutral leptons from mesons in EFT

Heavy neutral leptons (HNLs) with masses in the GeV range can be produced in the decays of heavy mesons and, if long-lived, may yield striking displaced signatures at the LHC. While most phenomenological studies have focused on the *minimal* HNL scenario where HNLs couple to the SM only via active-sterile neutrino mixing, more general interactions can be described within N_RLEFT, the low-energy effective theory that extends the SM with right-handed neutrinos N_R.

In this context, various studies have considered four-fermion N_RLEFT operators with one N_R, a charged lepton, and a quark bilinear. Ref. [172] examined the sensitivity of far detectors at the LHC to those operators, while Refs. [173, 174] derived projected sensitivities for Belle II for the same set of operators. However, other classes of four-fermion N_RLEFT operators, such as those with two N_R fields, or with one N_R and one SM neutrino, have not yet been investigated in the context of meson decays.[1] The motivation for studying these operators is that they open up complementary discovery channels for HNLs in the mass range $\sim 0.1-5$ GeV, which is particularly well-suited to the capabilities of the far detectors, like MATHUSLA, ANUBIS or FASER2. This chapter, based on Ref. [175], explores the potential of these additional operators to produce long-lived HNLs in meson decays at the LHC and presents a sensitivity study of the proposed far detectors to such scenarios.

[1] Ref. [154] considers a similar set of operators and places bounds from CEνNS and invisible decays of light mesons.

The remainder of the chapter is structured as follows. In Section 6.1, we introduce the relevant $d = 6$ operators in the N_RLEFT and discuss their matching to $d = 6$ and $d = 7$ operators in the N_RSMEFT. Section 6.2 details HNL production from meson decays induced by the operators of interest. In Section 6.3, we present our simulation results and sensitivity projections for the far detectors. We conclude in Section 6.4.

6.1 EFT approach

6.1.1 N_RLEFT operators for meson decays

The appropriate framework to describe meson decays into HNLs with masses around or below the GeV scale is N_RLEFT. We introduced this framework in Section 4.3. For convenience, we provide here the general form of the N_RLEFT Lagrangian,

$$\mathcal{L}_{N_R\mathrm{LEFT}} = \mathcal{L}^{(4)} + \sum_{d\geq 5} \sum_i c_i^{(d)} \mathcal{O}_i^{(d)} \,, \tag{6.1}$$

where $\mathcal{L}^{(4)}$ is given by Eq. (4.5) and the dimensionful Wilson coefficients, $c_i^{(d)}$, of the higher-dimensional operators $\mathcal{O}_i^{(d)}$, scale as $1/\Lambda_{\mathrm{EW}}^{d-4}$, see discussion below Eq. (4.6).

The contact operators triggering meson decays into HNLs are four-fermion interactions at $d = 6$ involving a pair of quarks and a leptonic part, which in turn contains either (i) a pair of N_R, or (ii) N_R and ν_L, or else (iii) N_R and a charged lepton. The last possibility has been investigated in detail in Refs. [172, 173], in the context of long-lived HNLs that could be produced in meson decays at the high-luminosity LHC and Belle II, respectively. In this work, we focus on the operators with neutral leptons. In Tables 6.1 and 6.2, we summarize the pair-N_R and single-N_R operators of interest.

Though in our numerical analysis we will focus on the case of a single HNL generation ($n_N = 1$), in the tables we provide for completeness the numbers of independent real parameters associated with each operator for $n_N = 1$ and $n_N = 3$. We have checked these numbers using `Sym2Int` [142, 143]. In the group of pair-N_R operators, there are four lepton number conserving (LNC) structures and six lepton number violating (LNV) ones (of which two vanish identically for $n_N = 1$). Among the single-N_R operators, six structures conserve lepton number, whereas four violate it.

6.1.2 Matching to the N_RSMEFT

We assume that the N_RLEFT originates from the N_RSMEFT, and that there are no new particles between the meson decay energy scale and the electroweak scale, characterized by the Higgs VEV, v. At the latter scale, the two EFTs must be matched.

	Name	Structure	$n_N = 1$	$n_N = 3$
LNC	$\mathcal{O}_{dN}^{V,RR}$	$\left(\overline{d_R}\gamma_\mu d_R\right)\left(\overline{N_R}\gamma^\mu N_R\right)$	9	81
	$\mathcal{O}_{uN}^{V,RR}$	$\left(\overline{u_R}\gamma_\mu u_R\right)\left(\overline{N_R}\gamma^\mu N_R\right)$	4	36
	$\mathcal{O}_{dN}^{V,LR}$	$\left(\overline{d_L}\gamma_\mu d_L\right)\left(\overline{N_R}\gamma^\mu N_R\right)$	9	81
	$\mathcal{O}_{uN}^{V,LR}$	$\left(\overline{u_L}\gamma_\mu u_L\right)\left(\overline{N_R}\gamma^\mu N_R\right)$	4	36
LNV	$\mathcal{O}_{dN}^{S,RR}$	$\left(\overline{d_L}d_R\right)\left(\overline{N_R^c}N_R\right)$	18	108
	$\mathcal{O}_{dN}^{T,RR}$	$\left(\overline{d_L}\sigma_{\mu\nu}d_R\right)\left(\overline{N_R^c}\sigma^{\mu\nu}N_R\right)$	0	54
	$\mathcal{O}_{uN}^{S,RR}$	$\left(\overline{u_L}u_R\right)\left(\overline{N_R^c}N_R\right)$	8	48
	$\mathcal{O}_{uN}^{T,RR}$	$\left(\overline{u_L}\sigma_{\mu\nu}u_R\right)\left(\overline{N_R^c}\sigma^{\mu\nu}N_R\right)$	0	24
	$\mathcal{O}_{dN}^{S,LR}$	$\left(\overline{d_R}d_L\right)\left(\overline{N_R^c}N_R\right)$	18	108
	$\mathcal{O}_{uN}^{S,LR}$	$\left(\overline{u_R}u_L\right)\left(\overline{N_R^c}N_R\right)$	8	48

TABLE 6.1: N_RLEFT $d = 6$ operators involving two quarks and two HNLs. For each operator structure, we give the number of independent real parameters for $n_N = 1$ and $n_N = 3$ generations of N_R. We recall that in the N_RLEFT, $n_d = 3$ and $n_u = 2$. The LNV operator structures require (+h.c.).

At tree level, the matching of the $d = 6$ LNC operators has been worked out in [155] and that of the $d = 6$ LNV operators in [154].[2] Below we summarize the results of this matching relevant to the operators of interest. The N_RSMEFT operators contributing to the matching relations for the coefficients of the N_RLEFT operators from Tables 6.1 and 6.2 are given in Tables 6.3 and 6.4, respectively.

For the dimensionful Wilson coefficients of the N_RSMEFT operators, we use capital $C_i^{(d)}$. They scale as $\Lambda_{\rm NP}^{4-d}$, where $\Lambda_{\rm NP} \gg v$ is the scale of new physics. For simplicity, we assume only one generation of N_R, while considering a general structure of quark, charged lepton and left-handed neutrino flavor indices. We denote the quark flavor indices by $i\,,j$ and the lepton flavor index by α. Furthermore, we assume that in the N_RLEFT, quarks are in the mass basis, whereas the N_RSMEFT operators are written in the weak interaction basis.

The matching conditions for the coefficients of the LNC pair-N_R operators holding at the electroweak scale read

$$c_{dN,ij}^{V,RR} = C_{dN}^{ij} - \frac{g_Z^2}{m_Z^2} Z_{d_R}^{ij} Z_N \,, \qquad c_{uN,ij}^{V,RR} = C_{uN}^{ij} - \frac{g_Z^2}{m_Z^2} Z_{u_R}^{ij} Z_N \,, \tag{6.2}$$

[2]For the N_RLEFT operators with two quarks, a charged lepton and a neutrino, the tree level matching has been performed also in [176, 172]. For the first-generation charged fermions, such operators contribute, among other processes, to neutrinoless double beta decay [176, 177, 178, 179].

	Name	Structure	$n_N = 1$	$n_N = 3$
LNC	$\mathcal{O}_{d\nu N}^{S,RR}$	$\left(\overline{d_L} d_R\right)\left(\overline{\nu_L} N_R\right)$	54	162
	$\mathcal{O}_{d\nu N}^{T,RR}$	$\left(\overline{d_L} \sigma_{\mu\nu} d_R\right)\left(\overline{\nu_L} \sigma^{\mu\nu} N_R\right)$	54	162
	$\mathcal{O}_{u\nu N}^{S,RR}$	$\left(\overline{u_L} u_R\right)\left(\overline{\nu_L} N_R\right)$	24	72
	$\mathcal{O}_{u\nu N}^{T,RR}$	$\left(\overline{u_L} \sigma_{\mu\nu} u_R\right)\left(\overline{\nu_L} \sigma^{\mu\nu} N_R\right)$	24	72
	$\mathcal{O}_{d\nu N}^{S,LR}$	$\left(\overline{d_R} d_L\right)\left(\overline{\nu_L} N_R\right)$	54	162
	$\mathcal{O}_{u\nu N}^{S,LR}$	$\left(\overline{u_R} u_L\right)\left(\overline{\nu_L} N_R\right)$	24	72
LNV	$\mathcal{O}_{d\nu N}^{V,RR}$	$\left(\overline{d_R} \gamma_\mu d_R\right)\left(\overline{\nu_L^c} \gamma^\mu N_R\right)$	54	162
	$\mathcal{O}_{u\nu N}^{V,RR}$	$\left(\overline{u_R} \gamma_\mu u_R\right)\left(\overline{\nu_L^c} \gamma^\mu N_R\right)$	24	72
	$\mathcal{O}_{d\nu N}^{V,LR}$	$\left(\overline{d_L} \gamma_\mu d_L\right)\left(\overline{\nu_L^c} \gamma^\mu N_R\right)$	54	162
	$\mathcal{O}_{u\nu N}^{V,LR}$	$\left(\overline{u_L} \gamma_\mu u_L\right)\left(\overline{\nu_L^c} \gamma^\mu N_R\right)$	24	72

TABLE 6.2: N_RLEFT $d = 6$ operators involving two quarks, one active neutrino and one HNL. For each operator structure, we give the number of independent real parameters for $n_N = 1$ and $n_N = 3$ generations of N_R. We recall that in the N_RLEFT, $n_\nu = n_d = 3$ and $n_u = 2$. All operator structures require (+h.c.).

$$c_{dN,ij}^{V,LR} = V_{ki}^* V_{lj} C_{QN}^{kl} - \frac{g_Z^2}{m_Z^2} Z_{d_L}^{ij} Z_N \,, \qquad c_{uN,ij}^{V,LR} = C_{QN}^{ij} - \frac{g_Z^2}{m_Z^2} Z_{u_L}^{ij} Z_N \,. \tag{6.3}$$

Here, V is the CKM matrix defined through $d'_L = V d_L$ (assuming the up-type quarks are already in the diagonal basis), where d' and d are flavor and mass eigenstates, respectively. In addition,

$$g_Z \equiv \frac{e}{s_W c_W} \,, \qquad Z_\psi^{ij} \equiv \left(T_\psi^3 - Q_\psi s_W^2\right) \delta^{ij} \,, \qquad Z_N \equiv -\frac{v^2}{2} C_{HN} \,, \tag{6.4}$$

with ψ denoting a SM fermion, and T_ψ^3 and Q_ψ being its weak isospin and electric charge, respectively. Further, $s_W \equiv \sin\theta_W$ and $c_W \equiv \cos\theta_W$, where θ_W is the weak mixing angle, and m_Z is the mass of the Z boson. Note that in Z_ψ^{ij} we neglect the contributions of $d = 6$ N_RSMEFT operators (cf. Eq. (2.18) in Ref. [154]), since when multiplied by Z_N these would lead to $d = 8$ effects.

For the LNC single-N_R operators, we have

$$c_{d\nu N,ij\alpha}^{S,RR} = V_{ki}^* \left(C_{LNQd}^{\alpha kj} - \frac{1}{2} C_{LdQN}^{\alpha jk} \right) , \qquad c_{d\nu N,ij\alpha}^{T,RR} = -\frac{1}{8} V_{ki}^* C_{LdQN}^{\alpha jk} \,, \tag{6.5}$$

$$c_{u\nu N,ij\alpha}^{S,RR} = 0 \,, \qquad c_{u\nu N,ij\alpha}^{T,RR} = 0 \,, \tag{6.6}$$

$$c_{d\nu N,ij\alpha}^{S,LR} = 0 \,, \qquad c_{u\nu N,ij\alpha}^{S,LR} = C_{QuNL}^{ji\alpha *} \,. \tag{6.7}$$

	Name	Structure	$n_N = 1$	$n_N = 3$
$d=6$ (LNC)	$\mathcal{O}_{dN}$	$\left(\overline{d_R}\gamma_\mu d_R\right)\left(\overline{N_R}\gamma^\mu N_R\right)$	9	81
	$\mathcal{O}_{uN}$	$\left(\overline{u_R}\gamma_\mu u_R\right)\left(\overline{N_R}\gamma^\mu N_R\right)$	9	81
	$\mathcal{O}_{QN}$	$\left(\overline{Q}\gamma_\mu Q\right)\left(\overline{N_R}\gamma^\mu N_R\right)$	9	81
	$\mathcal{O}_{HN}$	$\left(H^\dagger i\overleftrightarrow{D}_\mu H\right)\left(\overline{N_R}\gamma^\mu N_R\right)$	1	9
$d=7$ (LNV)	$\mathcal{O}_{QNdH}$	$\left(\overline{Q}N_R\right)\left(\overline{N_R^c}d_R\right)H$	18	162
	$\mathcal{O}_{dQNH}$	$H^\dagger\left(\overline{d_R}Q\right)\left(\overline{N_R^c}N_R\right)$	18	108
	$\mathcal{O}_{QNuH}$	$\left(\overline{Q}N_R\right)\left(\overline{N_R^c}u_R\right)\widetilde{H}$	18	162
	$\mathcal{O}_{uQNH}$	$\widetilde{H}^\dagger\left(\overline{u_R}Q\right)\left(\overline{N_R^c}N_R\right)$	18	108

TABLE 6.3: N_RSMEFT $d = 6$ and $d = 7$ operators contributing to the tree level matching relations for the Wilson coefficients of the $d = 6$ N_RLEFT operators from Table 6.1. For each operator structure, we give the number of independent real parameters for $n_N = 1$ and $n_N = 3$ generations of N_R. The LNV operator structures require (+h.c.).

	Name	Structure	$n_N = 1$	$n_N = 3$
$d=6$ (LNC)	$\mathcal{O}_{LNQd}$	$\epsilon_{ab}\left(\overline{L^a}N_R\right)\left(\overline{Q^b}d_R\right)$	54	162
	$\mathcal{O}_{LdQN}$	$\epsilon_{ab}\left(\overline{L^a}d_R\right)\left(\overline{Q^b}N_R\right)$	54	162
	$\mathcal{O}_{QuNL}$	$\left(\overline{Q}u_R\right)\left(\overline{N_R}L\right)$	54	162
$d=7$ (LNV)	$\mathcal{O}_{dNLH}$	$\epsilon_{ab}\left(\overline{d_R}\gamma_\mu d_R\right)\left(\overline{N_R^c}\gamma^\mu L^a\right)H^b$	54	162
	$\mathcal{O}_{uNLH}$	$\epsilon_{ab}\left(\overline{u_R}\gamma_\mu u_R\right)\left(\overline{N_R^c}\gamma^\mu L^a\right)H^b$	54	162
	$\mathcal{O}_{QNLH1}$	$\epsilon_{ab}\left(\overline{Q}\gamma_\mu Q\right)\left(\overline{N_R^c}\gamma^\mu L^a\right)H^b$	54	162
	$\mathcal{O}_{QNLH2}$	$\epsilon_{ab}\left(\overline{Q}\gamma_\mu Q^a\right)\left(\overline{N_R^c}\gamma^\mu L^b\right)H$	54	162
	$\mathcal{O}_{NL1}$	$\epsilon_{ab}\left(\overline{N_R^c}\gamma_\mu L^a\right)\left(iD^\mu H^b\right)\left(H^\dagger H\right)$	6	18
	$\mathcal{O}_{NL2}$	$\epsilon_{ab}\left(\overline{N_R^c}\gamma_\mu L^a\right)H^b\left(H^\dagger i\overleftrightarrow{D^\mu}H\right)$	6	18

TABLE 6.4: N_RSMEFT $d = 6$ and $d = 7$ operators contributing to the tree level matching relations for the Wilson coefficients of the $d = 6$ N_RLEFT operators from Table 6.2. For each operator structure, we give the number of independent real parameters for $n_N = 1$ and $n_N = 3$ generations of N_R. All operator structures require (+h.c.).

We note that the Higgs exchange contributions (which a priori seem relevant) are parametrically of the same order as $d = 8$ terms, and thus, can be dropped when working at $d = 6$ [153].

The $d = 6$ LNV operators in the N_RLEFT are expected to get contributions from $d = 7$ LNV operators in the N_RSMEFT.[3] A subset of the $d = 7$ operators relevant for the matching we are interested in is collected in the bottom part of Tables 6.3 and 6.4.

For the LNV pair-N_R operators, the matching conditions read

$$c^{S,RR}_{dN,ij} = -\frac{v}{2\sqrt{2}} V^*_{ki} C^{kj}_{QNdH}\,, \qquad c^{S,RR}_{uN,ij} = -\frac{v}{2\sqrt{2}} C^{ij}_{QNuH}\,, \tag{6.8}$$

$$c^{S,LR}_{dN,ij} = \frac{v}{\sqrt{2}} V_{kj} C^{ik}_{dQNH}\,, \qquad c^{S,LR}_{uN,ij} = \frac{v}{\sqrt{2}} C^{ij}_{uQNH}\,. \tag{6.9}$$

Finally, for the LNV single-N_R operators, we have

$$c^{V,RR}_{d\nu N,ij\alpha} = -\frac{v}{\sqrt{2}} C^{ij\alpha}_{dNLH} - \frac{g_Z^2}{m_Z^2} Z^{ij}_{d_R} Z^{\alpha}_{\nu N}\,, \tag{6.10}$$

$$c^{V,RR}_{u\nu N,ij\alpha} = -\frac{v}{\sqrt{2}} C^{ij\alpha}_{uNLH} - \frac{g_Z^2}{m_Z^2} Z^{ij}_{u_R} Z^{\alpha}_{\nu N}\,, \tag{6.11}$$

$$c^{V,LR}_{d\nu N,ij\alpha} = -\frac{v}{\sqrt{2}} V^*_{ki} V_{lj} \left(C^{kl\alpha}_{QNLH1} - C^{kl\alpha}_{QNLH2} \right) - \frac{g_Z^2}{m_Z^2} Z^{ij}_{d_L} Z^{\alpha}_{\nu N}\,, \tag{6.12}$$

$$c^{V,LR}_{u\nu N,ij\alpha} = -\frac{v}{\sqrt{2}} C^{ij\alpha}_{QNLH1} - \frac{g_Z^2}{m_Z^2} Z^{ij}_{u_L} Z^{\alpha}_{\nu N}\,. \tag{6.13}$$

Here, the couplings $Z^{\alpha}_{\nu N}$ are defined as

$$Z^{\alpha}_{\nu N} \equiv \frac{v^3}{4\sqrt{2}} \left(C^{\alpha}_{NL1} + 2 C^{\alpha}_{NL2} \right). \tag{6.14}$$

6.1.3 Running of the N_RLEFT operators

Between the energy scale at which meson decays take place and the weak scale, the Wilson coefficients of the N_RLEFT operators evolve according to renormalization group equations (RGEs). These are analogous to the RGEs in the LEFT (without N_R) [180], and some partial results for the operators with N_R can be found in Refs. [155, 172, 154]. Below we provide the one-loop RGEs for the pair-N_R and single-N_R operators summarized in Tables 6.1 and 6.2. The operators given by the product of vector currents

[3] We recall that in the N_RSMEFT at $d = 6$, there is only one operator which violates lepton number, but conserves baryon number, namely, $\mathcal{O}_{NNNN} = (\overline{N^c_R} N_R)(\overline{N^c_R} N_R)$. However, it vanishes identically in the case of one generation of N_R.

are renormalized by QED corrections[4]

$$\dot{c}^{V,RR}_{qN,ij} = \dot{c}^{V,LR}_{qN,ij} = \frac{4}{3} e^2 Q_q N_c \delta_{ij} \left[Q_u \left(c^{V,RR}_{uN,kk} + c^{V,LR}_{uN,kk} \right) + Q_d \left(c^{V,RR}_{dN,kk} + c^{V,LR}_{dN,kk} \right) \right] , \tag{6.15}$$

$$\dot{c}^{V,RR}_{q\nu N,ij\alpha} = \dot{c}^{V,LR}_{q\nu N,ij\alpha} = \frac{4}{3} e^2 Q_q N_c \delta_{ij} \left[Q_u \left(c^{V,RR}_{u\nu N,kk\alpha} + c^{V,LR}_{u\nu N,kk\alpha} \right) + Q_d \left(c^{V,RR}_{d\nu N,kk\alpha} + c^{V,LR}_{d\nu N,kk\alpha} \right) \right] . \tag{6.16}$$

Here, $\dot{c} \equiv 16\pi^2 \mu \dfrac{\mathrm{d}c}{\mathrm{d}\mu}$, with μ being the renormalization scale; $q = d$ or u; e is the QED coupling constant, Q_q is the electric charge of the quark q; and $N_c = 3$ is the number of colors. The flavor index k runs over u and c for the up-type quarks, and over d, s, b for the down-type quarks. We see that only the coefficients with $i = j$ run, whereas those with $i \neq j$, which will be of interest to us in what follows, do not.

The operators of the scalar and tensor types are renormalized due to both QCD and QED corrections

$$\dot{c}^S_q = -6 \left(g^2 C_F + e^2 Q_q^2 \right) c^S_q \,, \qquad c^S_q = c^{S,RR}_{qN,ij} \,,\ c^{S,LR}_{qN,ij} \,,\ c^{S,RR}_{q\nu N,ij\alpha} \,,\ c^{S,LR}_{q\nu N,ij\alpha} \,, \tag{6.17}$$

$$\dot{c}^T_q = 2 \left(g^2 C_F + e^2 Q_q^2 \right) c^T_q \,, \qquad c^T_q = c^{T,RR}_{qN,ij} \,,\ c^{T,RR}_{q\nu N,ij\alpha} \,, \tag{6.18}$$

where g is the strong coupling constant, and $C_F = (N_c^2 - 1)/(2N_c) = 4/3$.

Solving these RGEs to the leading-logarithm approximation, we find

$$c^S_q(\mu) = \left[\frac{g(\mu)}{g(\mu_1)} \right]^{\frac{6C_F}{b_g}} \left[\frac{e(\mu)}{e(\mu_1)} \right]^{\frac{6Q_q^2}{b_e}} c^S_q(\mu_1) \,, \tag{6.19}$$

$$c^T_q(\mu) = \left[\frac{g(\mu)}{g(\mu_1)} \right]^{-\frac{2C_F}{b_g}} \left[\frac{e(\mu)}{e(\mu_1)} \right]^{-\frac{2Q_q^2}{b_e}} c^T_q(\mu_1) \,, \tag{6.20}$$

where $\mu_1 < \mu$ are two energy scales, and b_g and b_e are the coefficients of the one-loop QCD and QED beta functions, respectively[5]

$$b_g = \frac{11}{3} N_c - \frac{2}{3} \left(n_u + n_d \right) , \tag{6.21}$$

$$b_e = -\frac{4}{3} \left(Q_e^2 n_e + Q_d^2 N_c n_d + Q_u^2 N_c n_u \right) . \tag{6.22}$$

[4] In these equations, we ignore the contributions from the four-fermion leptonic operators $\mathcal{O}^{V,RR}_{eN}$ and $\mathcal{O}^{V,LR}_{eN}$ as well as from the double insertions of the $d = 5$ neutrino dipole operators.

[5] For the beta functions, we use $\dot{g} = -b_g g^3$ and $\dot{e} = -b_e e^3$.

Setting $\mu_1 = m_b$ and $\mu = v$, we find

$$c_u^S(v) = 0.68\, c_u^S(m_b)\,, \qquad c_d^S(v) = 0.69\, c_d^S(m_b)\,, \tag{6.23}$$
$$c_u^T(v) = 1.14\, c_u^T(m_b)\,, \qquad c_d^T(v) = 1.13\, c_d^T(m_b)\,. \tag{6.24}$$

Thus, when running from m_b to v, the scalar type operators get suppressed, whereas the tensor type operator get enhanced, cf. Ref. [154]. Finally, we note that the contribution to the running from QED corrections is practically negligible.

Concerning the running in the N_RSMEFT, i.e. between the EW scale and the scale of new physics, $\Lambda_{\rm NP}$, the one-loop RGEs for $d = 6$ operators with N_R have been derived in [181, 182, 183], while partial results for some $d = 7$ operators with N_R (relevant for neutrinoless double beta decay) have been obtained in [176].

6.1.4 Example UV completion for $d = 7$ N_RSMEFT

The operators including one or two N_R in the N_RSMEFT can be generated in the UV in a variety of ways, as discussed in Chapter 5. For example, leptoquark models can generate $d = 6$ N_RSMEFT operators, which have been discussed exhaustively in [161]. However, no complete classification of models for $d = 7$ operators in N_RSMEFT had been studied, up to our work in Ref. [156].

Here, we will briefly discuss one concrete, but very typical UV model as an example. This example model generates the operator $\mathcal{O}_{QNdH}$ (cf. Table 6.3). For the other $d = 7$ operators containing one or two N_R, other UV models can be constructed in an analogous manner.[6]

Our example model, (ω_1, Π_1), contains two scalar leptoquark states, with quantum numbers $\omega_1 \sim (\mathbf{3}, \mathbf{1}, -1/3)$ and $\Pi_1 \sim (\mathbf{3}, \mathbf{2}, 1/6)$, under $(SU(3)_C, SU(2)_L, U(1)_Y)$. Apart from the mass and kinetic terms for the leptoquark states, the model allows to write down the following interactions, in addition to the SM Lagrangian,

$$-\mathcal{L} \supset y_{QN}^{\Pi_1} \left(\overline{Q} N_R\right) \Pi_1 + y_{Nd}^{\omega_1} \left(\overline{N_R^c} d_R\right) \omega_1^\dagger + \mu \left(H \Pi_1^\dagger \omega_1\right) + \text{h.c.} + \cdots\,, \tag{6.25}$$

where, for simplicity, we have suppressed generation indices. Note that this Lagrangian violates lepton number, but lepton number is recovered in the limit $\mu \to 0$

[6] We refer to Tables 5.6 and 5.7 in Chapter 5 for the complete list of tree level decompositions of the $d = 7$ operators.

[184]. Integrating out both leptoquarks will produce $\mathcal{O}_{QNdH}$ with

$$C_{QNdH} = \frac{\mu y_{QN}^{\Pi_1} y_{Nd}^{\omega_1}}{m_{\omega_1}^2 m_{\Pi_1}^2} \,. \tag{6.26}$$

In the limit $\mu = m_{\omega_1} = m_{\Pi_1} = \Lambda_{\rm NP}$, this gives the correct $C_{QNdH} \propto \Lambda_{\rm NP}^{-3}$ dependence for a $d = 7$ operator, as expected. Clearly, this model will also generate $d = 6$ operators with N_R. For example, the term proportional to $y_{QN}^{\Pi_1}$ ($y_{Nd}^{\omega_1}$) times its hermitian conjugate will generate $\mathcal{O}_{QN}$ ($\mathcal{O}_{dN}$). However, these are only examples, as actually more $d = 6$ operators can be generated in this model; note the dots in Eq. (6.25).

6.2 HNL production in meson decays

We are interested in HNLs produced in meson decays. In the N_RLEFT, such decays are triggered by both active-sterile neutrino mixing and higher-dimensional operators. The HNL production via mixing, i.e. in the minimal scenario, has been studied in detail in the literature, see e.g. Refs. [122, 185, 186] for recent reappraisals. The HNL production via effective interactions has been considered in [172] for the four-fermion operators with two quarks, one charged lepton and N_R. In this section, we focus on the meson decay modes triggered by the operators with two quarks and two neutral leptons (either a pair of N_R, or N_R and ν_L) discussed in Section 6.1.

Given their large production rates at the LHC, we focus on pseudoscalar mesons containing either a c or b quark and a light quark, i.e. D- and B-mesons. Vector mesons with the same quark content have much smaller lifetimes, and thus, their contribution to the HNL production is subdominant [172]. Mesons containing s quarks, i.e. kaons, require a dedicated study and we adressed them in a separated work [187].

In Fig. 6.1, we depict two- and three-body pseudoscalar meson decays triggered by the effective operators of interest. The same N_RLEFT operator induces a leptonic two-body decay as well as contributes to a number of semi-leptonic three-body decays. In the diagram corresponding to the three-body decay, q can be any quark but top, since the latter does not form bound states and is not present in the spectrum of the N_RLEFT. For the transition $q_j \to q_i$ with $i \neq j$, both quarks have to be of either the up- or down-type, since the operators considered involve quark bilinears with zero electric charge. In addition, $m_{q_j} > m_{q_i}$ for the decay to be kinematically allowed.[7]

[7] This condition is necessary, but not sufficient, since a meson mass is not a simple sum of the masses of its constituent quarks.

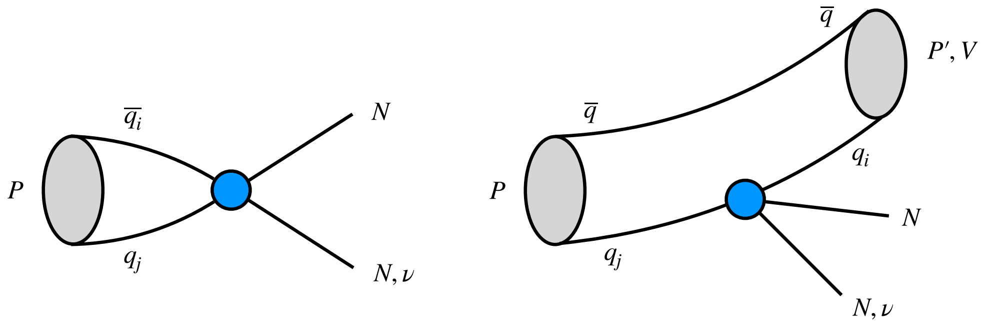

FIGURE 6.1: Two- and three-body pseudoscalar meson decays triggered by the effective operators with a pair of HNLs, or one HNL and one SM neutrino. The blue blob denotes the insertion of an effective operator. In the right diagram, the quark q can be u, d, s, c or b, whereas the quarks q_i and q_j are both of either the up- or down-type, with $m_{q_j} > m_{q_i}$. $P^{(\prime)}$ and V denote pseudoscalar and vector mesons, respectively.

These considerations lead to the following four possibilities: $c \to u$ (for the up-quark sector), and $b \to d$, $b \to s$ and $s \to d$ (for the down-quark sector).

In Table 6.5, we list the mesons involved in the allowed two-body ($P \to NN, \nu N$) and three-body ($P \to P'(V) + NN, \nu N$) decays for each of the four possibilities, where $P^{(\prime)}$ (V) denotes a pseudoscalar (vector) meson. The leptonic part in the final state (which we ommit in the table) contains either NN or νN, depending on the effective operator under consideration. Each row under $P \to P'(V)$ corresponds to a different choice of the spectator quark ($q = u, d, s, c, b$). In addition, only those processes marked in bold will be considered in our study.

In what follows, we will not take into account the decays of η_c, η_b and B_c^+. The η_c meson has a lifetime of $\mathcal{O}(10^{-23})$ s [168], which is much smaller than that of other pseudoscalar mesons and comparable with the lifetimes of vector mesons. The same argument applies for η_b. Concerning B_c^+, its production rate at the LHC is much smaller than that of D- and B-mesons, see e.g. Ref. [188]. We will not consider either the decay modes involving $s \to d$ transitions. This is because for the listed D_s^+ and $\overline{B_s^0}$ decays, the available mass window is very small, and for the light mesons' decays (kaons and η'), the numerical predictions from `Pythia8` [189, 190], which we will use for numerical simulation in this work, do not agree well with the LHCf experiment [191].

We have computed the corresponding partial decay widths assuming both N and ν are (i) Dirac and (ii) Majorana particles. In Appendix B, we provide the formulae for the two-body decay widths and the three-body decay amplitudes in both cases. To compute the three-body decay widths, we have used the procedure described in Ref. [172], which is also summarized in Appendix B for completeness.

$q_j \to q_i$	P	$P \to P'(V)$	$q_j \to q_i$	P	$P \to P'(V)$
$\boldsymbol{c \to u}$	$\boldsymbol{D^0}$	$\boldsymbol{D^0 \to \pi^0, \eta, \eta'(\rho, \omega)}$ $\boldsymbol{D^+ \to \pi^+(\rho^+)}$ $\boldsymbol{D_s^+ \to K^+(K^{*+})}$ $\eta_c \to \overline{D^0}(\overline{D^{*0}})$ $B_c^+ \to B^+(B^{*+})$	$\boldsymbol{b \to s}$	$\boldsymbol{B_s^0}$	$\boldsymbol{B^+ \to K^+(K^{*+})}$ $\boldsymbol{B^0 \to K^0(K^{*0})}$ $\boldsymbol{B_s^0 \to \eta, \eta'(\phi)}$ $B_c^+ \to D_s^+(D_s^{*+})$ $\eta_b \to \overline{B_s^0}(\overline{B_s^{*0}})$
$\boldsymbol{b \to d}$	$\boldsymbol{B^0}$	$\boldsymbol{B^+ \to \pi^+(\rho^+)}$ $\boldsymbol{B^0 \to \pi^0, \eta, \eta'(\rho, \omega)}$ $\boldsymbol{B_s^0 \to \overline{K^0}(\overline{K^{*0}})}$ $B_c^+ \to D^+(D^{*+})$ $\eta_b \to \overline{B^0}(\overline{B^{*0}})$	$s \to d$	K^0	$K^+ \to \pi^+$ $K^0 \to \pi^0$ $\eta' \to \overline{K^0}(\overline{K^{*0}})$ $D_s^+ \to D^+$ $\overline{B_s^0} \to \overline{B^0}(\overline{B^{*0}})$

TABLE 6.5: Mesons involved in the two-body ($P \to NN, \nu N$) and three-body ($P \to P'(V) + NN, \nu N$) decays depicted in Fig. 6.1 for different choices of the quark flavors. Four main flavor transitions exist: $c \to u$, $b \to d$, $b \to s$ and $s \to d$. For each one, we distinguish different three-body decays depending on the spectator quark $q = u, d, s, c, b$, corresponding to the five rows in each category. For further details, see text.

If the products of HNL decays are not detected, the modes we consider here contribute to the $P \to$ inv. or $P \to P'/V\nu\overline{\nu}$ decays. The existing upper limits on the branching ratios of such decays are listed in Table 6.6. In what follows, we will take these constraints into account.

In the three panels of Fig. 6.2, we show the branching ratios of D- and B-meson decays induced by the LNC pair-N_R operators $\mathcal{O}_{uN,12}^{V,RR}$ (top), $\mathcal{O}_{dN,31}^{V,RR}$ (middle) and $\mathcal{O}_{dN,32}^{V,RR}$ (bottom), assuming N is Majorana. We turn on one operator at a time, setting the corresponding Wilson coefficient to $10^{-3}v^{-2}$. This choice allows us to avoid the bounds from (semi-)invisible meson decays summarized in Table 6.6. We see that the two-body decay dominates over the three-body ones for $m_N \gtrsim 325$ MeV in the case of $\mathcal{O}_{uN,12}^{V,RR}$, for $m_N \gtrsim 1.2$ GeV in the case of $\mathcal{O}_{dN,31}^{V,RR}$, and for $m_N \gtrsim 1.05$ GeV in the case of $\mathcal{O}_{dN,32}^{V,RR}$. For small m_N, the two-body decay is suppressed, since the corresponding decay width is proportional to m_N^2, see Eq. (B.13) in Appendix B. Turning on the LR operators $\mathcal{O}_{uN,12}^{V,LR}$, $\mathcal{O}_{dN,31}^{V,LR}$, and $\mathcal{O}_{dN,32}^{V,LR}$ (one at a time) would lead to the same results as can be seen from Eqs. (B.13), (B.24) and (B.25).

In Fig. 6.3, we display the branching ratios of the same meson decays, but this time triggered by the LNV pair-N_R operators $\mathcal{O}_{uN,12}^{S,RR}$ (top), $\mathcal{O}_{dN,31}^{S,RR}$ (middle), and $\mathcal{O}_{dN,32}^{S,RR}$ (bottom). Again, we turn on one operator at a time and set the corresponding Wilson

Decay	Limit on $\mathcal{B}$	Decay	Limit on $\mathcal{B}$	Decay	Limit on $\mathcal{B}$
$D^0 \to$ inv.	$\mathbf{9.4 \times 10^{-5}}$	$B^0 \to$ inv.	$\mathbf{2.4 \times 10^{-5}}$	$B_s^0 \to \phi\nu\overline{\nu}$	5.4×10^{-3}
		$B^0 \to \pi^0\nu\overline{\nu}$	$\mathbf{9.0 \times 10^{-6}}$	$B^0 \to K^0\nu\overline{\nu}$	2.6×10^{-5}
		$B^0 \to \rho^0\nu\overline{\nu}$	4.0×10^{-5}	$B^0 \to K^{*0}\nu\overline{\nu}$	1.8×10^{-5}
		$B^+ \to \pi^+\nu\overline{\nu}$	1.4×10^{-5}	$B^+ \to K^+\nu\overline{\nu}$	$\mathbf{1.6 \times 10^{-5}}$
		$B^+ \to \rho^+\nu\overline{\nu}$	3.0×10^{-5}	$B^+ \to K^{*+}\nu\overline{\nu}$	4.0×10^{-5}

TABLE 6.6: Upper limits on the branching ratios ($\mathcal{B}$) of (semi-)invisible D- and B-meson decays extracted from Ref. [168]. The limits highlighted in bold provide the most stringent constraints on the corresponding Wilson coefficients, see Section 6.3.

coefficient to $10^{-3}v^{-2}$.[8] Contrary to the LNC operators, now the leptonic two-body decays dominate for all kinematically available values of m_N, since there is no helicity suppression from m_N, cf. Eq. (B.13). Switching on the LR operators $\mathcal{O}^{S,LR}_{uN,12}$, $\mathcal{O}^{S,LR}_{dN,31}$, and $\mathcal{O}^{S,LR}_{dN,32}$ (one at a time) would lead to the same results as can be inferred from Eqs. (B.13), (B.24), and (B.25). The tensor operators $\mathcal{O}^{T,RR}_{dN}$ and $\mathcal{O}^{T,RR}_{uN}$ vanish identically for one generation of N_R. For this reason, we do not consider them in what follows.

Concerning single-N_R operators, we have also studied their contribution to two- and three-body D- and B- meson decays, showing some results in Appendix B.2. In particular, we present in Fig. B.1 the branching ratios of B-meson decays induced by the LNC operators $\mathcal{O}^{S,RR}_{d\nu N,31\alpha}$ and $\mathcal{O}^{T,RR}_{d\nu N,31\alpha}$ and the LNV operator $\mathcal{O}^{V,RR}_{d\nu N,31\alpha}$. We observe that our results are analogous to the ones obtained in Ref. [172], cf. Fig. 2 therein, for single-N_R operators including a charged lepton. Therefore, we expect the constraints derived from the far detectors to be essentially the same for the neutral-current single-N_R operators, and we hence do not include the latter in our numerical simulation.

Before closing the section, we mention that with only one N_R generation, pair-N_R operators cannot make the HNL decay by themselves, in contrast to single-N_R operators. In Appendix B.3, we have computed the partial decay widths of HNLs into a light meson and an active neutrino triggered by the neutral single-N_R operators. Since we only simulate HNLs produced by pair-N_R operators and only turn on one N_RLEFT operator at a time, we consider that the HNL decay is exclusively due to active-sterile neutrino mixing. The partial decay widths of HNL via mixing are computed according to the formulae given in Refs. [121, 122, 172].

[8] In the case of non-hermitian operators, as e.g. $\mathcal{O}^{S,RR}_{qN}$, $q = u$ or d, "one operator at a time" means $c^{S,RR}_{qN,ij} \neq 0$, whereas $c^{S,RR}_{qN,ji} = 0$. We note also that $c^{S,RR}_{dN,31} = 10^{-3}v^{-2}$ violates slightly the limit on $\mathcal{B}(B^0 \to \text{inv.})$ from Table 6.6. However, we opt for this value of the Wilson coefficient to be uniform with the other plots.

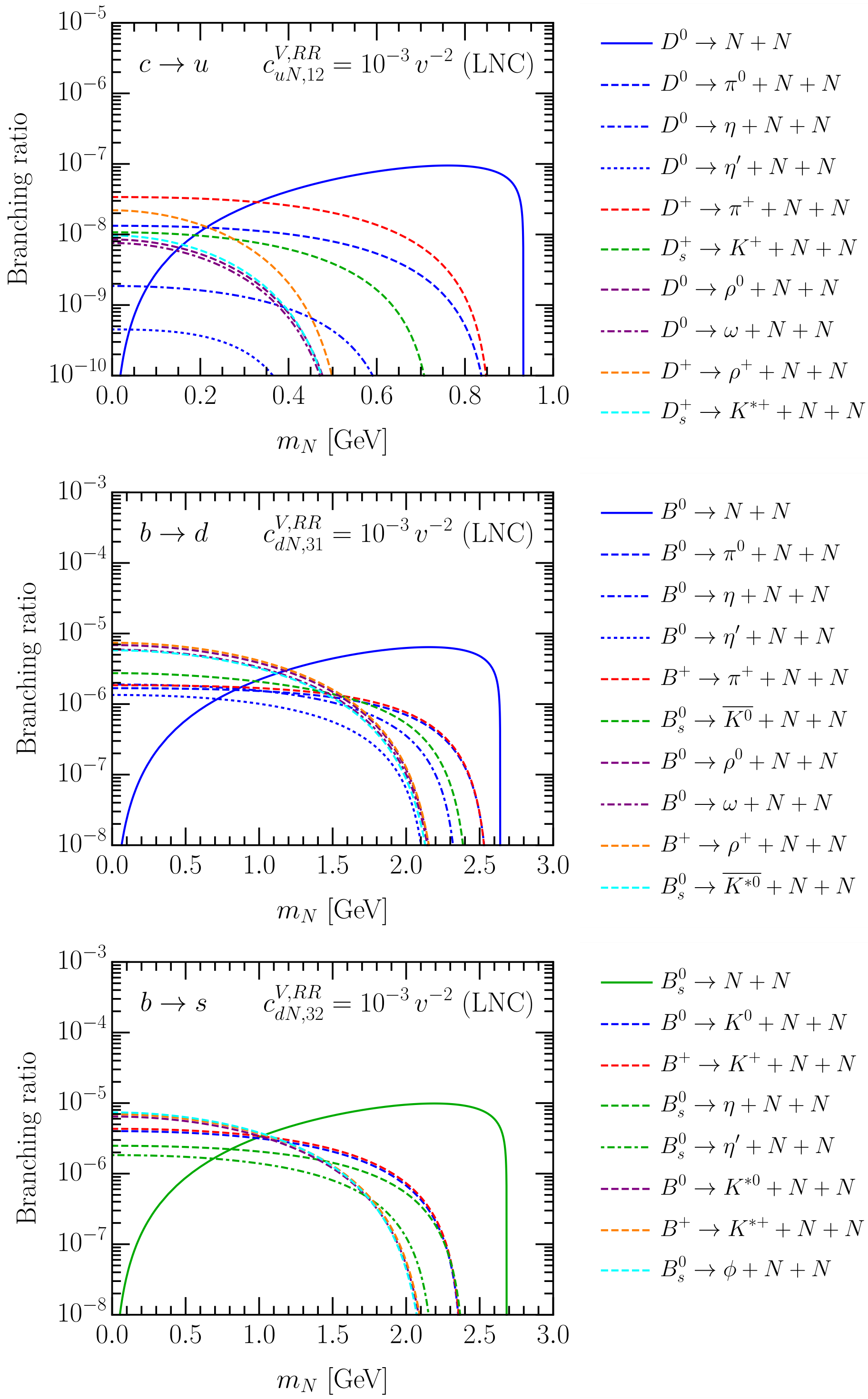

FIGURE 6.2: Branching ratios of D- and B-meson decays triggered by the LNC pair-N_R operators $\mathcal{O}^{V,RR}_{uN,12}$ (top), $\mathcal{O}^{V,RR}_{dN,31}$ (middle) and $\mathcal{O}^{V,RR}_{dN,32}$ (bottom). The corresponding Wilson coefficient has been set to $10^{-3} v^{-2}$.

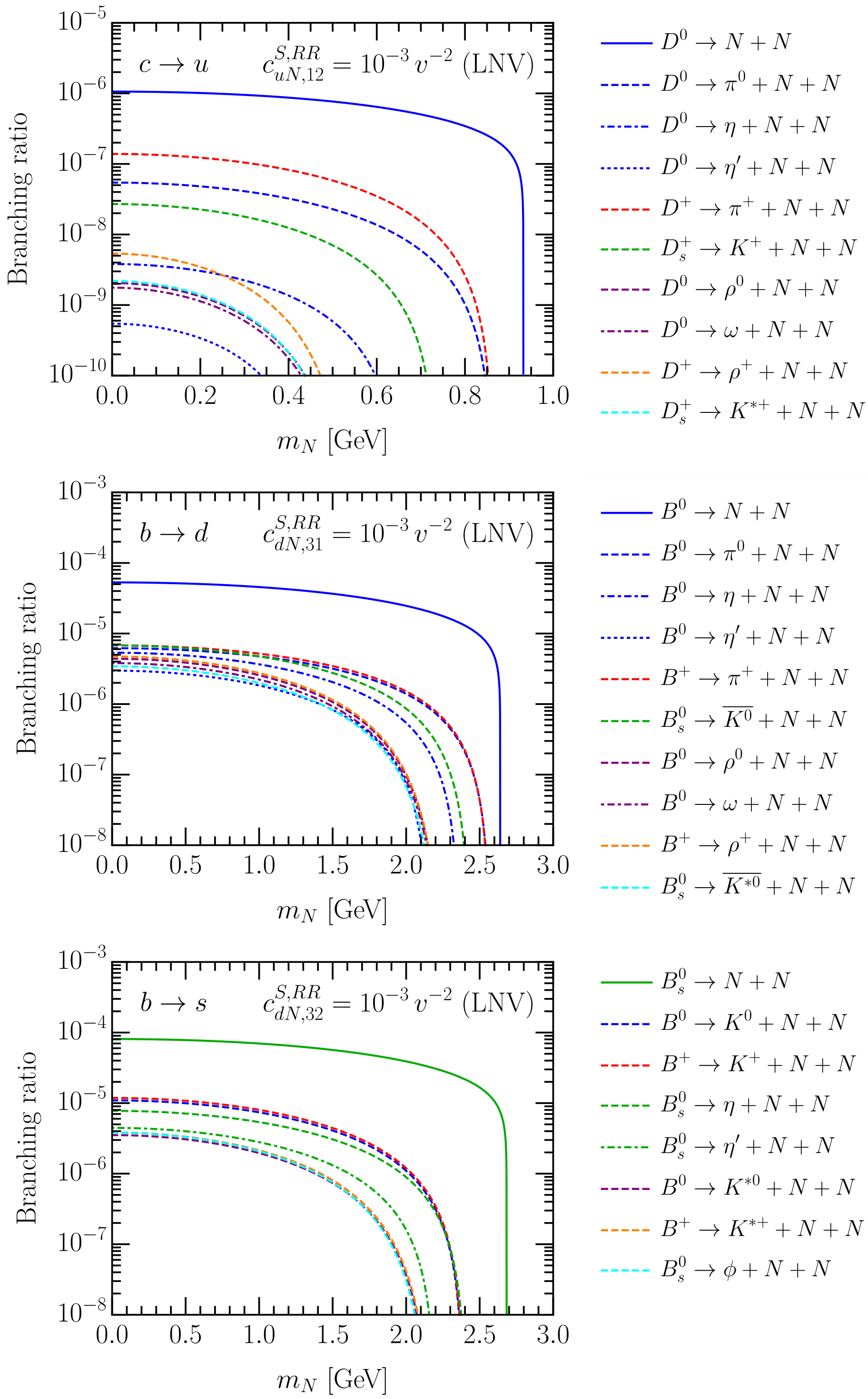

FIGURE 6.3: Branching ratios of D- and B-meson decays triggered by the LNV pair-N_R operators $\mathcal{O}_{uN,12}^{S,RR}$ (top), $\mathcal{O}_{dN,31}^{S,RR}$ (middle) and $\mathcal{O}_{dN,32}^{S,RR}$ (bottom). The corresponding Wilson coefficient has been set to $10^{-3}v^{-2}$.

6.3 Sensitivity prospects for the far detectors

6.3.1 Details of simulation

In this work, we focus on the far detector experiments proposed (or even approved) at the LHC. In particular, we consider ANUBIS [105], AL3X [192],[9] CODEX-b [108], FACET [111], FASER and FASER2 [109, 110], MAPP1 and MAPP2 [106, 107], and MATHUSLA [193, 102].[10] We refer to Section 3.3 in Chapter 3 for more details about the experiments. We recall, that, since the far detectors are supposed to be operated at different interaction points (IPs) and time scales of the LHC, the projected integrated luminosities also vary, ranging from as low as 30 fb^{-1} for MAPP1, up to the full HL-LHC target, 3 ab^{-1} for ANUBIS, FACET, FASER2, and MATHUSLA. Moreover, typically these far detectors are located with a distance of $\mathcal{O}(1) - \mathcal{O}(100)$ m to their corresponding IP, allowing for sufficient amount of rock, lead, or other shielding material to effectively remove the potential SM background events stemming from the IP. As a result, vanishing background is usually assumed for phenomenological studies on these experiments.

Here, we study HNLs pair-produced at the LHC with the center-of-mass energy $\sqrt{s} = 14$ TeV from D- and B-mesons rare decays mediated by a N_RLEFT operator. These HNLs then travel a certain distance before decaying via their mixing with the SM active neutrino. If the boosted decay length of the HNLs falls into a suitable range, they have a high probability of decaying inside some of the far detectors. Since the HNLs mostly decay to channels that are not fully invisible (three active neutrinos), the decay vertex can be reconstructed by these experiments.

While we analytically compute the production and decay rates of the HNLs, we rely on a Monte Carlo simulation tool, `Pythia8.3` [190, 189], to estimate the decay probabilities of the HNLs inside each of the far detectors. Depending on the flavor indices of the EFT operator we choose to turn on, `Pythia8` can generate either the $pp \to c\bar{c}$ or $pp \to b\bar{b}$ process inclusively for D- or B-meson production at the LHC, respectively. These mesons then decay to different channels including at least two HNLs, with relative decay branching ratios implemented according to the analytical computation detailed in Section 6.2. This allows for maximal usage of all the simulated data while respecting the relative importance of each decay channel.

[9] AL3X is no longer considered for construction. Nevertheless we will show its sensitivity prospects for comparison.

[10] This work is prior to the appearance of the new geometry designs for MATHUSLA and ANUBIS, hence we use here the geometries of the original proposals.

D^0	$D^{\pm}$	$D_s^{\pm}$	B^0	$B^{\pm}$	B_s^0
4.12×10^{16}	2.16×10^{16}	7.02×10^{15}	1.58×10^{15}	1.58×10^{15}	2.73×10^{14}

TABLE 6.7: Inclusive production numbers of D- and B-mesons for an integrated luminosity of 3 ab^{-1}. The original numbers from Ref. [172] have been multiplied by correction factors to account for the increase in the meson producction cross section from $\sqrt{s} = 13$ TeV to 14 TeV [196].

Since `Pythia8` provides the kinematics of each simulated HNL, we can compute its decay probability in each detector according to the geometry and position with respect to the IP. We then take the average of the decay probabilities of all the simulated HNLs, to obtain the expected acceptance rate at each detector, $\langle P[N \text{ decay}] \rangle$. This allows us to compute the projected number of signal events, N_S, with the following equation

$$N_S = \sum_i 2 \cdot N_{M_i} \cdot \mathcal{B}(M_i \to NN + \text{anything}) \cdot \langle P[N \text{ decay}] \rangle \cdot \mathcal{B}(N \to \text{vis.}), \quad (6.27)$$

where the factor 2 accounts for the fact that each meson decays into a pair of HNLs, N_{M_i} is the number of the mother mesons, and $\mathcal{B}(N \to \text{vis.})$ denotes the decay branching ratio of the HNLs into visible final states. For our study, we consider only the decay channel into three active neutrinos to be invisible.

In Table 6.7, we show the inclusive production rates of the relevant heavy mesons from Ref. [172], which were obtained therein combining both LHCb measurements and extrapolation with the simulation tools `FONLL` [194, 195] and `Pythia8`. Note that in Table 6.7 we have in addition multiplied the production rates of these heavy mesons given in [172] by a factor of 1.08 (1.06) for the B- (D-) mesons in order to take into account the fact that we consider $\sqrt{s} = 14$ TeV instead of 13 TeV [196].

In principle, the decay probability of each HNL can be computed with the simple formula (assuming the flight path of the HNL traverses the detector)

$$P[N \text{ decay}] = \mathrm{e}^{-L_1/\beta\gamma c\tau} - \mathrm{e}^{-L_2/\beta\gamma c\tau}, \quad (6.28)$$

where β, γ, and τ are the speed, Lorentz boost factor, and the proper lifetime of the HNL, c is the speed of light, and L_1 and L_2 label respectively the distance from the IP (where we assume the heavy mesons decay into the HNLs instantly) to the incoming and outgoing sides of the detector. This formula holds perfectly for a far detector with a spherical-shell shape facing towards the IP. However, since the far detector experiments mostly have a more complicated geometrical shape and relative orientation with respect to the IP, more sophisticated formulae are required for more accurate estimate of the decay probability. Here, we strictly follow [172] for computing the decay probabilities in each far detector.

We also mention that since `Pythia8` is not well validated for heavy meson production in the very forward direction, we use `FONLL` to correct the differential production cross section of mesons for various ranges of small transverse momentum and large pseudorapidity, for three experiments: FACET, FASER, and FASER2.

6.3.2 Results of numerical analysis

We now present our numerical results, focusing on Majorana HNLs and the LNC and LNV pair-N_R operators in the N_RLEFT that mediate meson decays as discussed in Section 6.2. Specifically, we consider the LNC operators $\mathcal{O}^{V,RR}_{uN,12}$, $\mathcal{O}^{V,RR}_{dN,31}$ and $\mathcal{O}^{V,RR}_{dN,32}$ and the LNV ones $\mathcal{O}^{S,RR}_{uN,12}$, $\mathcal{O}^{S,RR}_{dN,31}$ and $\mathcal{O}^{S,RR}_{dN,32}$.[11] The former operator in each set triggers D-meson decays (*charm* scenario), while the latter two operators in each set mediate B-meson decays (*bottom* scenarios), see Table 6.5. In addition to the Wilson coefficients of the operators, $c_{\mathcal{O}}$, the relevant parameters are the HNL mass, m_N, and the active-sterile mixing, V_{lN}, which together determine the decay length and hence whether the HNL is long-lived. We consider HNLs mixing predominantly with e or μ (τ-mixing is not considered due to lower expected sensitivities).

Figs. 6.4 and 6.5 show the sensitivity contours of the far detectors in the $|V_{lN}|^2$ vs. m_N plane for the LNC and LNV scenarios, respectively. These isocurves are for three signal events, corresponding to 95% confidence level (C.L.) limits, given zero background events. Each plot assumes one operator is switched on at a time, with $c_{\mathcal{O}} = 10^{-3}v^{-2}$. This corresponds to a NP scale $\Lambda_{\rm NP} \sim 7.8$ TeV for $c_{\mathcal{O}} \sim 1/\Lambda^2_{\rm NP}$, about 700 times smaller than G_F. For this choice, bounds from D^0 and B^0 invisible decays as well as from $P \to P'/V\nu\bar{\nu}$ are avoided (see Section 6.2).

In Fig. 6.4, the B-meson (bottom) scenarios, in the top-right and bottom-left plots, show better reach in $|V_{lN}|^2$ compared to the D-meson (charm) case, in the top-left plot, despite the higher production rates of D-mesons at the LHC (about one order of magnitude larger than for B-mesons, cf. Table 6.7). This is mainly due to the significantly larger B-meson branching ratios into HNLs (cf. Fig. 6.2), assuming the same value of the Wilson coefficients. The mass reach is also higher for HNLs coming from B-mesons because they are heavier than D-mesons.

Among the far detectors, MATHUSLA provides the best reach, probing $|V_{lN}|^2$ as low as 10^{-12} (10^{-15}) in charm (bottom) scenarios. It is followed by ANUBIS and AL3X. FASER shows the weakest sensitivity due to its smaller volume. Notably, MAPP1 with only 30 fb^{-1} can outperform FASER2, thanks to its larger volume and proximity to the interaction point. CODEX-b, MAPP2, and FACET exhibit comparable performance.

[11] The corresponding LR operators would yield the same results if switched on individually.

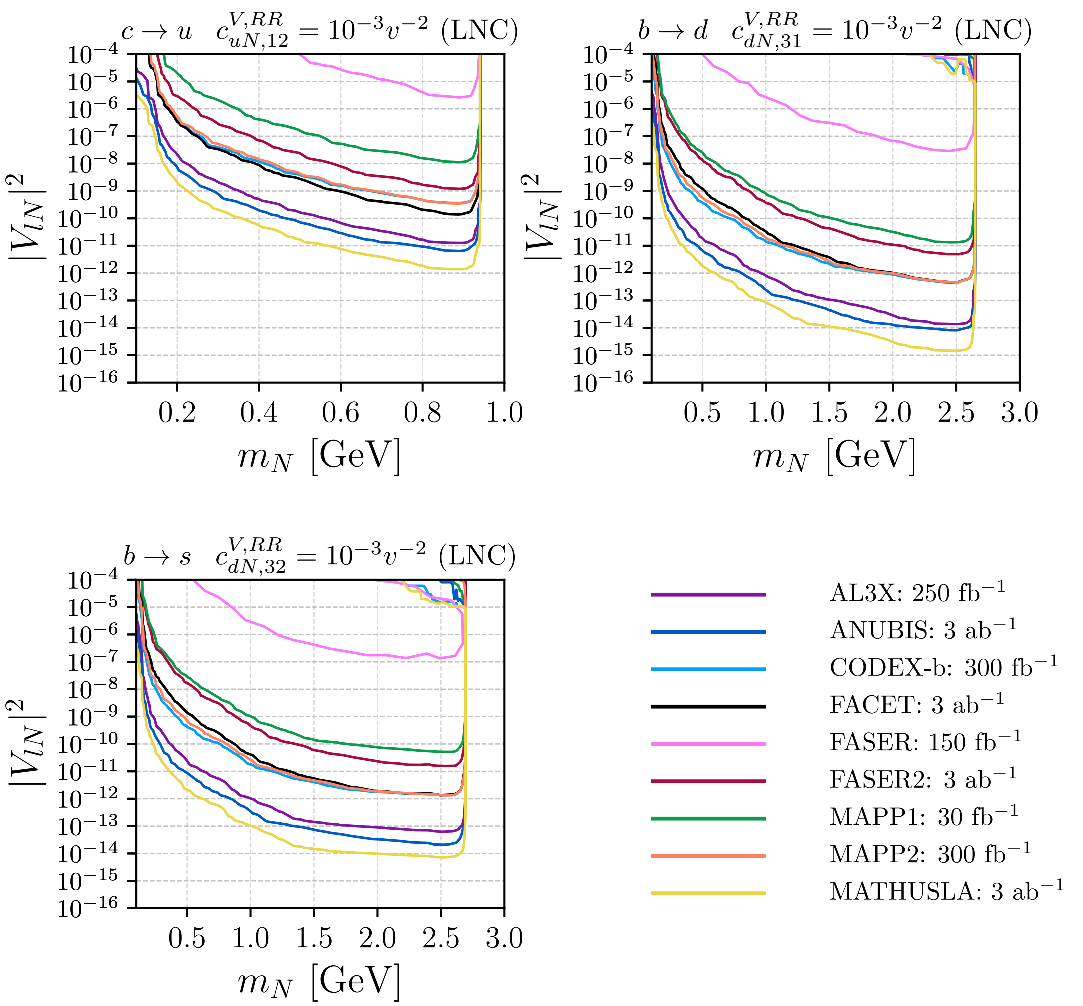

FIGURE 6.4: Exclusion limits in the plane $|V_{lN}|^2$ vs. m_N, for the three LNC pair-N_R operators we consider, with the corresponding Wilson coefficients fixed to $10^{-3}v^{-2}$.

The LNV results in Fig. 6.5 are qualitatively similar, with slightly stronger limits in $|V_{lN}|^2$, owing to the larger meson branching ratios into HNL pairs in the LNV case (see Figs. 6.2, 6.3), again assuming the same value of the corresponding Wilson coefficients.

For comparison, current experimental bounds for *minimal* HNLs (where production and decay proceed via mixing only) reach $|V_{lN}|^2 \sim 10^{-9} - 10^{-5}$, depending on m_N, see Fig. 3.5 in Chapter 3. These are not directly comparable to our results, where production is enhanced by effective operators. A consistent reinterpretation would require detailed analysis of each experiment and is beyond the scope of this work; hence we do not overlay those bounds in Figs. 6.4 and 6.5.

Figs. 6.6 and 6.7 present sensitivity curves in the $c_{\mathcal{O}}$ vs. m_N plane for two fixed values

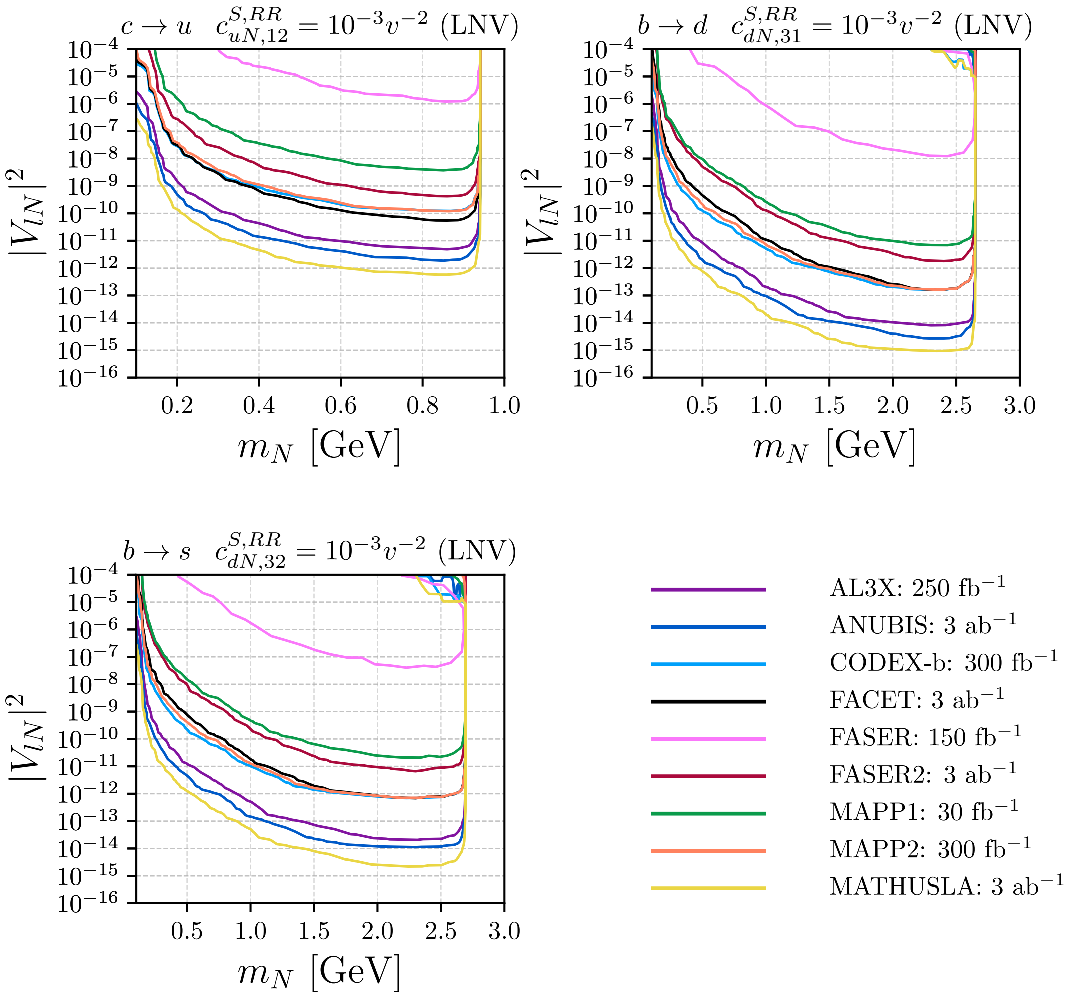

FIGURE 6.5: The same plots as Fig. 6.4, but for the three LNV pair-N_R operators.

of mixing: $|V_{lN}|^2 = 10^{-7}$ and 10^{-10}. To obtain these plots, for each case, we determine the minimum $c_\mathcal{O}$ (as a function of m_N) giving three signal events.[12] We find the same hierarchy in the experiment sensitivities as in the $|V_{lN}|^2$ vs. m_N plots, but the reach in $c_\mathcal{O}$ depends strongly on the mixing. This is because, for fixed m_N, modifying $|V_{lN}|^2$ changes the proper HNL lifetime and hence the detector acceptance to these HNLs. For instance, the acceptance difference between $|V_{lN}|^2 = 10^{-10}$ and 10^{-7} is about three orders of magnitude, translating into a factor $\sqrt{1000} \approx 32$ difference in $c_\mathcal{O}$, since the HNL production rate (and thus the number of signal events) scales as $c_\mathcal{O}^2$.

[12]This simple rescaling using Eq. (6.27) can be done because the HNL production and decay processes are decoupled: $c_\mathcal{O}$ controls HNL production and V_{lN} controls the decay.

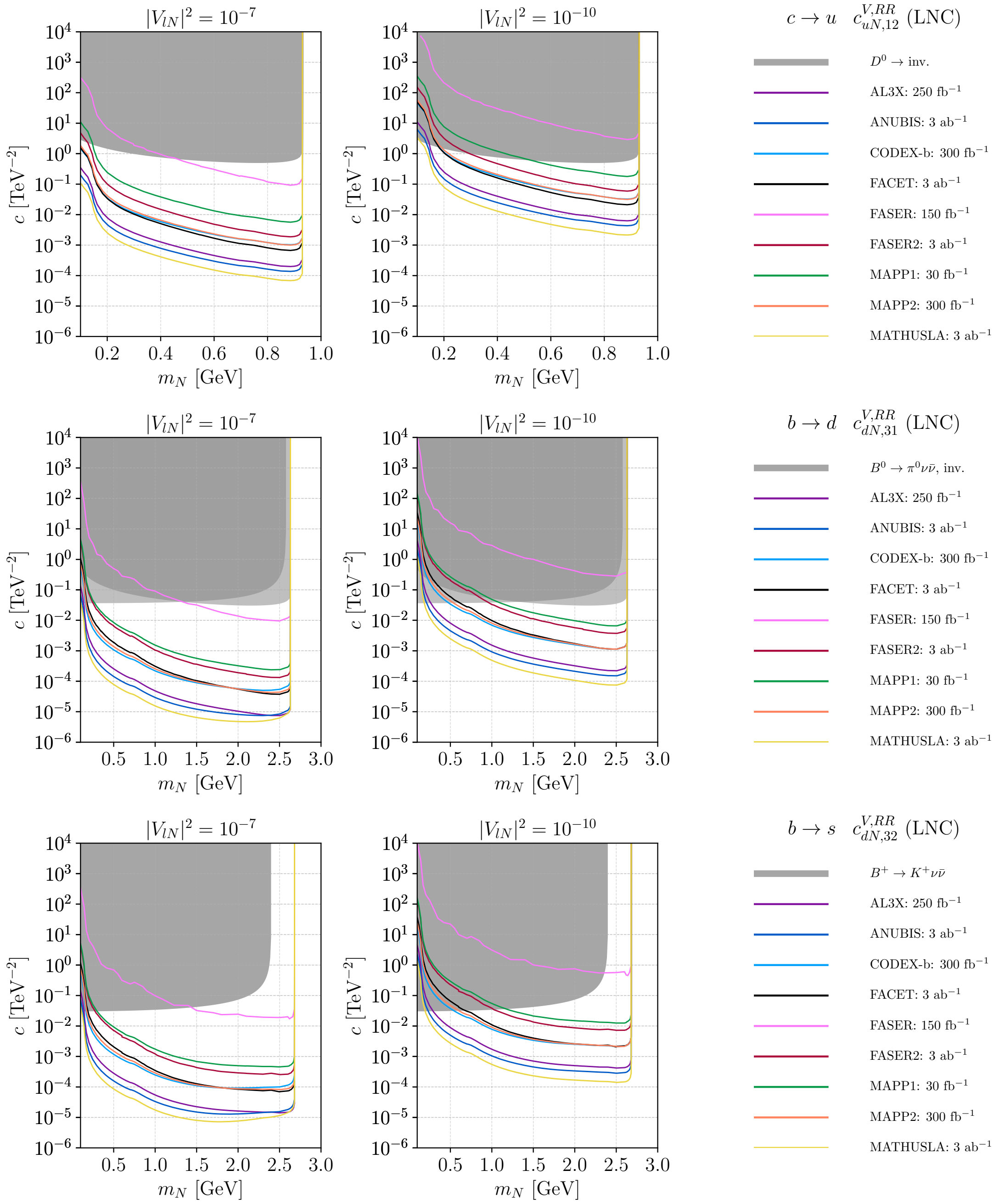

FIGURE 6.6: Exclusion limits in the plane $c_{\mathcal{O}}$ vs. m_N, for the three LNC pair-N_R operators we consider, with $|V_{lN}|^2$ fixed at 10^{-7} or 10^{-10}. The top panels correspond to the *charm* scenario (D-meson decays), whereas the middle and bottom panels correspond to the *bottom* scenarios (B-meson decays).

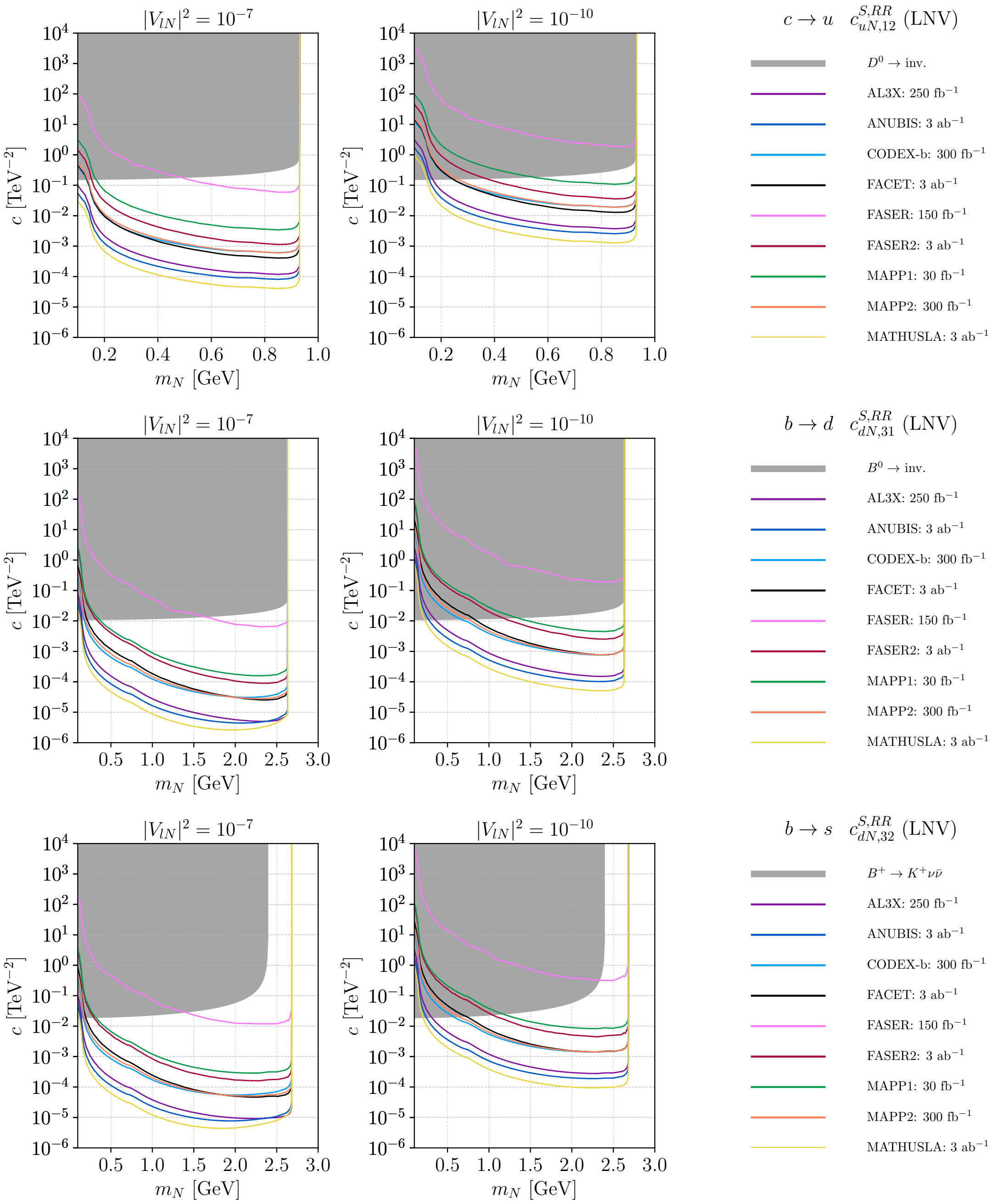

FIGURE 6.7: The same plots as Fig. 6.6, but for the three LNV pair-N_R operators. Again, the top panels correspond to the *charm* scenario (D-meson decays), whereas the middle and bottom panels correspond to the *bottom* scenarios (B-meson decays).

In the *charm* case and for $|V_{lN}|^2 = 10^{-7}$ (top-left panel), the best experiments (MATHUSLA and ANUBIS) reach $c_{\mathcal{O}} \sim 10^{-4}$ TeV^{-2}, while weaker ones (FASER) probe down to $\sim 10^{-3}$ TeV^{-2}. In the *bottom* case (middle and bottom panels), limits improve by roughly an order of magnitude. For the LNC operators, $c_{\mathcal{O}} \sim 10^{-4}$ (10^{-5}) TeV^{-2} corresponds to $\Lambda_{\rm NP} \sim 100$ (316) TeV.

Finally, as in the $|V_{lN}|^2$ plots, the LNV operators yield slightly stronger reaches than the LNC ones. Interpreting those reaches in terms of the new physics scale is, however, more subtle: below the electroweak scale the $d = 6$ LNV operators are matched to $d = 7$ operators in the N_RSMEFT that contain a Higgs field. Using the relation $c_{\mathcal{O}} \simeq v/(2\sqrt{2}\Lambda_{\rm NP}^3)$, and neglecting QCD running, the benchmarks $c_{\mathcal{O}} \sim 10^{-4}(10^{-5})$ TeV^{-2} translate to $\Lambda_{\rm NP} \sim 10(21)$ TeV, roughly an order of magnitude lower than the equivalent LNC scales.

The grey bands in Figs. 6.6, 6.7 show the most stringent existing limits from invisible and semi-invisible D- and B-meson decays (Table 6.6).[13] In the charm scenario the dominant bound comes from $D_0 \to$ inv., whereas in the $b \to d$ case it is a combination of $B_0 \to \pi^0\nu\bar{\nu}$ at low m_N and $B_0 \to$ inv. at larger masses. For $b \to s$, the leading constraint is $B^+ \to K^+\nu\bar{\nu}$. In all plots, these existing bounds lie well above the projected far detector sensitivities showcased here, leaving ample discovery space for the operators under study.

6.4 Summary

In this chapter, we have studied the phenomenology of $d = 6$ four-fermion operators in the N_RLEFT involving a pair of right-handed neutrinos N_R. We have considered both lepton number conserving (LNC) and lepton number violating (LNV) operators, which can induce rare meson decays into a pair of heavy neutral leptons (HNLs). In particular, we considered three representative quark flavor combinations leading to $c \to u$, $b \to d$, and $b \to s$ transitions, and examined the meson decay modes mediated by (i) the LNC operators $\mathcal{O}^{V,RR}_{uN,12}$, $\mathcal{O}^{V,RR}_{dN,31}$, and $\mathcal{O}^{V,RR}_{dN,32}$, and (ii) the LNV operators $\mathcal{O}^{S,RR}_{uN,12}$, $\mathcal{O}^{S,RR}_{dN,31}$, and $\mathcal{O}^{S,RR}_{dN,32}$. These lead to either two-body or three-body decays of D- and B-mesons into a pair of HNLs, depending on the available phase space.

Since these operators produce a pair of HNLs but do not mediate their decays, we assume the HNLs decay via mixing with active neutrinos. For GeV-scale masses and small mixings, the HNLs become naturally long-lived, making LLP searches at the

[13] All these bounds have been derived by equating $\mathcal{B}(P \to NN)$ [$\mathcal{B}(P \to P'NN)$] obtained using Eq. (B.13) [Eq. (B.24)] to the corresponding upper limit on $\mathcal{B}(P \to \text{inv.})$ [$\mathcal{B}(P \to P'\nu\overline{\nu})$] from Table 6.6.

LHC especially relevant. We consider the sensitivity of several proposed or ongoing far detector experiments, namely AL3X, ANUBIS, CODEX-b, FACET, FASER and FASER2, MAPP1 and MAPP2, and MATHUSLA, which are designed to operate at distances of $\mathcal{O}(10-100)$ m from the interaction points and offer background-free environments. Using Monte Carlo simulations with `Pythia8`, we estimated the detector acceptances and signal rates for HNLs pair-produced in meson decays and decaying via mixing.

Our results are presented in two types of planes: $|V_{lN}|^2$ vs. m_N in Figs. 6.4 and 6.5, and $c_{\mathcal{O}}$ vs. m_N in Figs. 6.6 and 6.7. In the $|V_{lN}|^2$ vs. m_N plots, we find these experiments can probe $|V_{lN}|^2$ as low as 10^{-15}–10^{-6} for GeV-scale HNLs. Then, for two fixed benchmark values of $|V_{lN}|^2 = 10^{-7}$ and $|V_{lN}|^2 = 10^{-10}$, we obtain the sensitivity reach in the Wilson coefficients $c_{\mathcal{O}}$ as functions of the HNL mass. We further convert $c_{\mathcal{O}}$ to the new-physics (NP) scale Λ_{NP}. We find for $|V_{lN}|^2 = 10^{-7}$, the considered experiments can probe $\Lambda \lesssim 10-300$ TeV, depending on the operator and flavor structure. For $|V_{lN}|^2 = 10^{-10}$, the reach in Λ_{NP} is reduced by slightly less than one order of magnitude, as a result of the larger decay length and hence smaller acceptance.

Among all the studied far detectors, MATHUSLA and ANUBIS offer the best sensitivities, while FASER and FASER2 tend to provide the weakest reach. In particular, MAPP1 achieves similar performance to FASER2 with only a fraction of the integrated luminosity, owing to its closer location and larger geometric acceptance. Finally, we find that the LNV operators generally yield stronger sensitivity than the LNC ones, as the associated meson decay rates are typically an order of magnitude larger for the same Wilson coefficient, see Figs. 6.2 and 6.3.

In summary, these results demonstrate the capabilities of far detectors at the LHC to explore new physics scenarios involving HNLs through rare meson decays, offering a novel and complementary probe to other collider and intensity frontier searches.

Chapter 7

Heavy neutrino magnetic moments at the LHC

Electromagnetic properties of neutrinos, such as magnetic dipole moments, constitute a promising avenue for probing new physics connected to the neutrino sector. The inclusion of right-handed (RH) or sterile neutrinos allows for the possibility of transition magnetic moments, either between active and sterile neutrinos or between two sterile states. The former, active-to-sterile transitions, have been extensively explored in the literature [197, 57, 198, 199, 123], particularly due to their implications for oscillation experiments and cosmology.

In contrast, sterile-to-sterile transition magnetic moments remain relatively unconstrained, particularly for sterile neutrinos with masses above the heavy meson mass range. These transitions have gathered attention in the context of LLP searches at the far detectors proposed for the LHC, e.g. MATHUSLA, ANUBIS, CODEX-b or FASER, as well as in next-generation experiments like DUNE and SHiP [200, 201, 202]. However, for heavier sterile neutrinos beyond the kinematic reach of meson decays, LLP searches at the LHC main detectors offer a unique opportunity to probe these magnetic moments. This possibility has only recently begun to be explored [203, 204, 205].

This chapter, based on Ref. [206], contributes to this direction by investigating the phenomenology of heavy sterile neutrino transition magnetic moments at the LHC and how they can be probed with novel LLP searches featuring non-pointing photons, a particularly distinctive signature. We study both active-to-sterile and sterile-to-sterile dipole transitions, which can be described using $d = 5$ operators in the N_RLEFT framework. In addition, we discuss a possible UV completion — a generalization of the model proposed in Ref. [207] — that generates these effective operators at one-loop level, and we explore its associated low-energy phenomenology, including constraints from charged lepton flavor violation (cLFV).

The structure of the chapter is as follows. Section 7.1 introduces the relevant effective dipole operators, while Section 7.2 presents a simple UV model generating those operators at low energies. We explicitly perform the one-loop matching between the UV model and the EFT. Then, in Section 7.3, we review current phenomenological constraints on the model from collider data and cLFV searches. Section 7.4 discusses the expected collider signatures, with an emphasis on non-pointing photon signals, and outlines our implementation and simulation strategy for determining the sensitivity of LLP searches to this scenario. Our numerical results, in both EFT and UV-model parameter space, are presented in Section 7.5. We conclude in Section 7.6.

7.1 Sterile neutrino magnetic moments: EFT approach

In the presence of RH or sterile neutrinos N_R with masses below the electroweak (EW) scale, transition magnetic moments are described by the effective Lagrangian

$$\mathcal{L}_{N_R\mathrm{LEFT}} \supset d'^{ij}_{NN\gamma}\, \mathcal{O}^{ij}_{NN\gamma} + d'^{\alpha i}_{\nu N\gamma}\, \mathcal{O}^{\alpha i}_{\nu N\gamma} + \text{h.c.}\,, \tag{7.1}$$

with the $d = 5$ operators[1]

$$\mathcal{O}^{ij}_{NN\gamma} = (\bar{N}^c_{Ri}\sigma_{\mu\nu}N_{Rj})F^{\mu\nu}\,, \quad \mathcal{O}^{\alpha i}_{\nu N\gamma} = (\bar{\nu}_{L\alpha}\sigma_{\mu\nu}N_{Ri})F^{\mu\nu}\,, \tag{7.2}$$

where $F_{\mu\nu}$ is the photon field strength. Here, we use $\alpha \in \{1, 2, 3\}$ to denote the generation of SM lepton and $i, j \in \{1, 2, \ldots\}$ for the sterile neutrino generation. The operators $\mathcal{O}^{ij}_{NN\gamma}$ and $\mathcal{O}^{\alpha i}_{\nu N\gamma}$ correspond to sterile-to-sterile and active-to-sterile neutrino transition magnetic moments, respectively. The former is antisymmetric in the indices i, j and vanishes for a single sterile state. We note that these effective interactions in N_RLEFT are only applicable well below the EW symmetry breaking, as discussed in Chapter 4. We use a prime superscript to distinguish the N_RLEFT Wilson coefficients from the basis of operators obtained after rotating N_RSMEFT operators at the EW symmetry breaking scale, but not integrating out degrees of freedom such as W and Z, which will be defined shortly.

[1] In the literature, there is sometimes a factor of $1/2$ in the definition of $\mathcal{O}_{NN\gamma}$ so that the normalization is analogous to the Majorana and Dirac mass terms. We do not include it here so we can easily compare our results to Ref. [207].

Here, we assume the N_RLEFT operators in Eq. (7.2) arise from operators above the EW scale in the N_RSMEFT, in particular, the operators (up to $d = 6$)

$$\mathcal{L}_{N_R\text{SMEFT}} \supset C^{(5)ij}_{NNB}\,\mathcal{O}^{(5)ij}_{NNB} + C^{(6)\alpha i}_{NB}\,\mathcal{O}^{(6)\alpha i}_{NB} + C^{(6)\alpha i}_{NW}\,\mathcal{O}^{(6)\alpha i}_{NW} + \text{h.c.}\,, \tag{7.3}$$

where we have introduced dimensionfull Wilson coefficients and[2]

$$\mathcal{O}^{(5)ij}_{NNB} = (\bar{N}^c_{Ri}\sigma_{\mu\nu}N_{Rj})B^{\mu\nu}\,, \tag{7.4}$$
$$\mathcal{O}^{(6)\alpha i}_{NB} = (\bar{L}_\alpha\sigma_{\mu\nu}N_{Ri})\tilde{H}B^{\mu\nu}\,, \quad \mathcal{O}^{(6)\alpha i}_{NW} = (\bar{L}_\alpha\sigma_{\mu\nu}N_{Ri})\tau^I\tilde{H}W^{I\mu\nu}\,. \tag{7.5}$$

The operator $\mathcal{O}^{ij}_{NN\gamma}$ in Eq. (7.2) arises from the N_RSMEFT operator at $d = 5$, $\mathcal{O}^{(5)ij}_{NNB}$, while the operator $\mathcal{O}^{\alpha i}_{\nu N\gamma}$ arises from those at $d = 6$, after expanding around the Higgs VEV and transforming to the weak-rotated basis of gauge fields.

At the next lowest dimension in the (N_R)SMEFT are the $d = 7$ operators [208]

$$\mathcal{O}^{(7)\alpha\beta}_{LH^2B} = (\bar{L}_\alpha\tilde{H})\sigma_{\mu\nu}(\tilde{H}^TL^c_\beta)B^{\mu\nu}\,, \quad \mathcal{O}^{(7)\alpha\beta}_{LH^2W} = (\bar{L}_\alpha\tilde{H})\sigma_{\mu\nu}(\tilde{H}^T\tau^IL^c_\beta)W^{I\mu\nu}\,, \tag{7.6}$$
$$\mathcal{O}^{(7)ij}_{NH^2B} = (\bar{N}^c_{Ri}\sigma_{\mu\nu}N_{Rj})(H^\dagger H)B^{\mu\nu}\,, \quad \mathcal{O}^{(7)ij}_{NH^2W} = (\bar{N}^c_{Ri}\sigma_{\mu\nu}N_{Rj})(H^\dagger\tau^IH)W^{I\mu\nu}\,, \tag{7.7}$$

which generate active-to-active neutrino magnetic moments $\mathcal{O}^{\alpha\beta}_{\nu\nu\gamma} = (\bar{\nu}^c_{L\alpha}\sigma_{\mu\nu}\nu_{L\beta})F^{\mu\nu}$ and further modify $\mathcal{O}^{ij}_{NN\gamma}$. However, we neglect the effect of these $d = 7$ operators.

In the context of high-energy collider processes, it is convenient to define a basis of rotated N_RSMEFT operators at the EW symmetry breaking scale. In this basis, there are two additional $d = 5$ operators that involve the Z boson field strength,

$$\mathcal{O}^{ij}_{NNZ} = (\bar{N}^c_{Ri}\sigma_{\mu\nu}N_{Rj})Z^{\mu\nu}\,, \quad \mathcal{O}^{\alpha i}_{\nu NZ} = (\bar{\nu}_{L\alpha}\sigma_{\mu\nu}N_{Ri})Z^{\mu\nu}\,. \tag{7.8}$$

These operators are not present in the usual N_RLEFT because Z is integrated out [148, 154, 149]; however, they are convenient to use near the Z pole, where they describe the production and subsequent decay of the sterile neutrinos via a dipole-like coupling to the Z boson. We will denote the weak-rotated interactions near the Z pole as

$$\mathcal{L}^{Z\text{-pole}}_{N_R\text{LEFT}} \supset d^{ij}_{NN\gamma}\,\mathcal{O}^{ij}_{NN\gamma} + d^{\alpha i}_{\nu N\gamma}\,\mathcal{O}^{\alpha i}_{\nu N\gamma} + d^{ij}_{NNZ}\,\mathcal{O}^{ij}_{NNZ} + d^{\alpha i}_{\nu NZ}\,\mathcal{O}^{\alpha i}_{\nu NZ} + \text{h.c.} \tag{7.9}$$

[2]We slightly change the notation with respect to Chapter 4: $\mathcal{O}^{(5)}_{NNB} \Leftrightarrow \mathcal{O}_{NNB}$, $\mathcal{O}^{(6)}_{NB} \Leftrightarrow \mathcal{O}_{NBH}$ and $\mathcal{O}^{(6)}_{NW} \Leftrightarrow \mathcal{O}_{NWH}$ (this chapter $\Leftrightarrow$ Chapter 4).

Now, considering the N_RSMEFT operators up to $d = 6$, the dipole moments in Eq. (7.9) are related to the N_RSMEFT Wilson coefficients in the unbroken phase as

$$d^{ij}_{NN\gamma} = c_w C^{(5)ij}_{NNB}\,, \quad d^{ij}_{NNZ} = -s_w C^{(5)ij}_{NNB}\,, \tag{7.10}$$

$$d^{\alpha i}_{\nu N\gamma} = \frac{v}{\sqrt{2}}\left(c_w C^{(6)\alpha i}_{NB} + \frac{s_w}{2} C^{(6)\alpha i}_{NW}\right), \quad d^{\alpha i}_{\nu NZ} = \frac{v}{\sqrt{2}}\left(-s_w C^{(6)\alpha i}_{NB} + \frac{c_w}{2} C^{(6)\alpha i}_{NW}\right), \tag{7.11}$$

where $s_w = \sin\theta_w$ and $c_w = \cos\theta_w$, with θ_w the weak mixing angle, and v is the Higgs vacuum expectation value. From Eq. (7.10), we observe the ratio $d^{ij}_{NNZ}/d^{ij}_{NN\gamma} = -t_w$ between the sterile-to-sterile couplings, with $t_w = s_w/c_w$. In general, a UV-complete model will also predict some relation between the Wilson coefficients $C^{(6)\alpha i}_{NB}$ and $C^{(6)\alpha i}_{NW}$; if we take $C^{(6)\alpha i}_{NW}/C^{(6)\alpha i}_{NB} = a(g/g') = a/t_w$, where a is an arbitrary parameter and g and g' are the $SU(2)_L$ and $U(1)_Y$ couplings, respectively, we obtain the following ratio between the active-to-sterile couplings

$$\frac{d^{\alpha i}_{\nu NZ}}{d^{\alpha i}_{\nu N\gamma}} = \frac{a - 2t_w^2}{(2+a)t_w}\,. \tag{7.12}$$

There are therefore two flat directions in the parameter space of couplings; $d^{\alpha i}_{\nu N\gamma} = 0$ for $a = -2$ and $d^{\alpha i}_{\nu NZ} = 0$ for $a = 2t_w^2 \approx 0.6$.

In addition to the operators in Eq. (7.8), there is also the $d = 5$ charged current dipole operator with the W boson field strength,

$$\mathcal{L}^{Z\text{-pole}}_{N_R\text{LEFT}} \supset d^{\alpha i}_{eNW}\left(\bar{e}_{L\alpha}\sigma_{\mu\nu}N_{Ri}\right)W^{\mu\nu} + \text{h.c.}\,. \tag{7.13}$$

The associated dipole moment is related to the N_RSMEFT Wilson coefficient $C^{(6)}_{NW}$ in the unbroken phase as

$$d^{\alpha i}_{eNW} = \frac{v}{2}C^{(6)\alpha i}_{NW} \quad \Rightarrow \quad \frac{d^{\alpha i}_{eNW}}{d^{\alpha i}_{\nu N\gamma}} = \frac{\sqrt{2}a}{(2+a)s_w}\,. \tag{7.14}$$

Clearly, we have $d^{\alpha i}_{eNW} = 0$ for $a = 0$. This operator is important for the production of a heavy N with a charged lepton or in the decay of N to a charged lepton plus jets.

We note that, from a phenomenological point of view, the free parameters of the model can be taken to be $\{m_N, C^{(5)ij}_{NNB}, C^{(6)\alpha i}_{NB}, C^{(6)\alpha i}_{NW}\}$ or $\{m_N, d^{ij}_{NN\gamma}, d^{\alpha i}_{\nu N\gamma}, a\}$, with general flavor structure. In any UV realization of these couplings, however, the flavor structure will be fixed. We take both approaches in this paper. First, we consider model-independent constraints on the couplings from LLP searches at the LHC. We then express $d^{ij}_{NN\gamma}$ and $d^{\alpha i}_{\nu N\gamma}$ in terms of the parameters of a specific UV scenario, which fixes both the flavor structure and the parameter a. We discuss this UV model next.

Field(s)	Irrep	Couplings	Z_2 allowed	Op. at tree level	Op. at one-loop
N_R	$(\mathbf{1}, \mathbf{1}, 0)$	Y_ν	✓	–	–
E	$(\mathbf{1}, \mathbf{1}, -1)$	Y_E	×	$\mathcal{O}_{HL}^{(1)}, \mathcal{O}_{HL}^{(3)}$	$\mathcal{O}_{eB}, \mathcal{O}_{eW}, \ldots$
ϕ	$(\mathbf{1}, \mathbf{1}, -1)$	$f, \lambda_{\phi H}$	×	$\mathcal{O}_{LL}$	$\mathcal{O}_{eB}, \mathcal{O}_{eW}, \ldots$
N_R, ϕ	–	f'	×	$\mathcal{O}_{LNLe}, \mathcal{O}_{eN}$	$\mathcal{O}_{NB}^{(6)}, \mathcal{O}_{NW}^{(6)}, \ldots$
N_R, E	–	–	–	–	$\mathcal{O}_{NB}^{(6)}, \mathcal{O}_{NW}^{(6)}, \ldots$
N_R, E, ϕ	–	h, h'	✓	${}^*\mathcal{O}_{LNeH}, {}^*\mathcal{O}_{LNLH}$	$\mathcal{O}_{NNB}^{(5)}, \ldots$

TABLE 7.1: Fields in the UV model generating sterile neutrino magnetic moments. We indicate the relevant renormalizable couplings that can be written when one, two or all of the fields are present. In the fourth column, check marks indicate the allowed couplings when E and ϕ are odd under Z_2. We also show the lowest dimension (N_R)SMEFT operators generated at tree and one-loop level after integrating out E and ϕ, giving interesting observable effects at low energies. The two operators marked with a star are $d = 7$ N_RSMEFT operators, which we do not consider further.

7.2 A UV model for sterile neutrino magnetic moments

In this work, we consider a simple UV extension of the SM with RH gauge singlet fermions N_R. To generate magnetic moments for these states, we add the same minimal ingredients as Refs. [207, 155]; a single vector-like lepton E and a scalar ϕ.[3] Both are singlets under $SU(3)_c$ and $SU(2)_L$ and have the hypercharges $Y(E) = Y(\phi) = -1$. However, we do not impose an additional Z_2 symmetry under which the new fields transform as $E \to -E$ and $\phi \to -\phi$ [207]. Without this extra discrete symmetry, the following renormalizable terms can be written, which are not present in the SM,

$$\begin{aligned}\mathcal{L} \supset\ & \bar{E}\left(i\not{D} - m_E\right)E + (D_\mu\phi)^*(D^\mu\phi) - m_\phi^2|\phi|^2 - \lambda_{\phi\phi}|\phi|^4 - \lambda_{\phi H}|\phi|^2(H^\dagger H) \\ & - \Big[\bar{N}_R h E_L \phi^* + \bar{N}_R^c h' E_R \phi^* \\ & \quad + \bar{L} Y_E H E_R + \bar{E}_L m_{eE} e_R + \bar{L} f \tilde{L} \phi + \bar{N}_R^c f' e_R \phi^* + \text{h.c.}\Big]\,, \end{aligned} \tag{7.15}$$

where $\tilde{L} = i\sigma_2 L^c$. The RH neutrinos N_R can also have the Yukawa-type and Majorana mass terms $-\bar{L} Y_\nu \tilde{H} N_R - \frac{1}{2}\bar{N}_R^c M_R N_R + \text{h.c.}$, which will be discussed later. Note that, because of the removal of the Z_2 symmetry, we obtain four additional terms in the last line of Eq. (7.15) with respect to [207].

We summarize the field content of the model in Table 7.1, showing the renormalizable couplings that are present when one, two or all of the fields are considered. With check marks (crosses), we indicate which couplings are allowed (forbidden) when the Z_2

[3]Comparing to our notation in Chapter 5, we identify $\phi \Leftrightarrow \mathcal{S}_1^*$ [156].

symmetry, under which E and ϕ are odd, is enforced. We also show the (N_R)SMEFT operators which are generated after integrating out E and ϕ. Among these are the operators $\mathcal{O}^{(5)}_{NNB}$, $\mathcal{O}^{(6)}_{NB}$ and $\mathcal{O}^{(6)}_{NW}$, which induce sterile-to-sterile and active-to-sterile neutrino magnetic moments, and also operators which are relevant for other low-energy probes, such as cLFV processes. These are the $d = 6$ SMEFT operators

$$\mathcal{O}^{(1)}_{HL} = (H^\dagger i\overleftrightarrow{D}_\mu H)(\bar{L}\gamma^\mu L)\,, \quad \mathcal{O}_{eB} = \left(\bar{L}\sigma^{\mu\nu}e_R\right)HB_{\mu\nu}\,, \tag{7.16}$$

$$\mathcal{O}^{(3)}_{HL} = (H^\dagger i\overleftrightarrow{D}^I_\mu H)(\bar{L}\tau^I\gamma^\mu L)\,, \quad \mathcal{O}_{eW} = \left(\overline{L}\sigma^{\mu\nu}e_R\right)\tau^I HW^I_{\mu\nu}\,, \tag{7.17}$$

$$\mathcal{O}_{LL} = (\bar{L}\gamma_\mu L)(\bar{L}\gamma^\mu L)\,, \quad \mathcal{O}_{eH} = (H^\dagger H)\bar{L}He_R\,. \tag{7.18}$$

Additionally, two $d = 7$ N_RSMEFT operators are generated at tree level after integrating out E and ϕ. Since we restrict ourselves to operators up to $d = 6$, we do not consider them further.

After EW symmetry breaking, mixing is induced between the SM charged leptons and the vector-like lepton E. In the broken phase, the Lagrangian contains the following extended 4×4 mass matrix

$$\mathcal{L} \supset -\begin{pmatrix}\bar{e}_L & \bar{E}_L\end{pmatrix}\mathcal{M}_E\begin{pmatrix}e_R\\ E_R\end{pmatrix} + \text{h.c.}\,; \quad \mathcal{M}_E = \begin{pmatrix}\frac{vY_e}{\sqrt{2}} & \frac{vY_E}{\sqrt{2}}\\ m_{eE} & m_E\end{pmatrix}\,, \tag{7.19}$$

where the upper-left entry arises from the SM lepton Yukawa term $-\bar{L}Y_eHe_R + \text{h.c.}$. Without loss of generality, the weak eigenbasis RH fields e_R and E_R, which have identical gauge interactions, can be chosen such that all of the entries of m_{eE}, which is a 3×1 matrix, are zero [209]. This is equivalent to rotating away nonzero m_{eE} via redefinitions of Y_e, Y_E and m_E. Now, the mass matrix $\mathcal{M}_E$ can be diagonalized with the following rotation of fields,

$$\begin{pmatrix}e_{L\alpha}\\ E_L\end{pmatrix} = \begin{pmatrix}V^L_{\alpha\beta} & V^L_{\alpha E}\\ V^L_{E\beta} & V^L_{EE}\end{pmatrix}P_L\begin{pmatrix}e'_\beta\\ E'\end{pmatrix}\,, \quad \begin{pmatrix}e_{R\alpha}\\ E_R\end{pmatrix} = \begin{pmatrix}V^R_{\alpha\beta} & V^R_{\alpha E}\\ V^R_{E\beta} & V^R_{EE}\end{pmatrix}P_R\begin{pmatrix}e'_\beta\\ E'\end{pmatrix}\,, \tag{7.20}$$

such that $V^{L\dagger}\mathcal{M}_E V^R = \mathcal{M}^{\text{diag}}_E = \text{diag}(m_e, m_\mu, m_\tau, m_{E'})$. Here, e'_β and E' represent the physical mass eigenstate fields, with the former $e'_\beta \in \{e, \mu, \tau\}$ and the latter being a single heavy charged lepton. With abuse of notation, we relabel $e'_\alpha \to e_\alpha$ and $E' \to E$ in the following. In the limit $Y_e \sim Y_E \ll \sqrt{2}m_E/v$, it becomes possible to block-diagonalize $\mathcal{M}_E$ with the approximate seesaw-like mixing

$$V^L_{\alpha E} = -V^{L*}_{E\alpha} \approx \frac{vY^\alpha_E}{\sqrt{2}m_E}\,, \quad V^R_{\alpha E} = -V^{R*}_{E\alpha} \approx \frac{v^2[Y_e]^*_{\alpha\gamma}Y^\gamma_E}{2m^2_E}\,, \tag{7.21}$$

where we see that the mixing between the RH fields is further suppressed by v/m_E with respect to the mixing between LH fields. Given that the LH mixing is less suppressed, we can also consider the following non-unitarity in the $V^L_{\alpha i}$ entry,

$$V^L_{\alpha\beta} \approx \delta_{\alpha\beta} - \frac{v^2 Y_E^\alpha Y_E^{\beta *}}{4m_E^2}\,. \tag{7.22}$$

Similarly, non-unitarity is seen in the V^L_{EE} entry, but is irrelevant phenomenologically.

Expanding the covariant derivatives in the SM Lagrangian and Eq. (7.15), and transforming to the weak-rotated gauge fields, the gauge interactions of ν_L, $e_{L/R}$, $E_{L/R}$ and ϕ in the broken phase are found to be

$$\begin{aligned}\mathcal{L} \supset &-eQ\Big[\bar{e}\gamma_\mu e + \bar{E}\gamma_\mu E + i\phi^* \overset{\leftrightarrow}{\partial}_\mu \phi\Big]A^\mu - \left[\frac{g}{\sqrt{2}}\bar{e}_L\gamma_\mu\nu_L W^\mu + \text{h.c.}\right] \\ &- \frac{g}{c_w}\left[g_L^\nu \bar{\nu}_L\gamma_\mu\nu_L + g_L^e \bar{e}_L\gamma_\mu e_L + g_R^e\left(\bar{E}_L\gamma_\mu E_L + \begin{pmatrix}\bar{e}_R & \bar{E}_R\end{pmatrix}\gamma_\mu\begin{pmatrix}e_R \\ E_R\end{pmatrix} + i\phi^*\overset{\leftrightarrow}{\partial}_\mu\phi\right)\right]Z^\mu\,,\end{aligned} \tag{7.23}$$

where, as usual, the electric charge is $Q = \tau^3 + Y$ and the LH and RH Z couplings are $g_L^f = \tau^3 - Qs_w^2$ and $g_R^f = -Qs_w^2$, respectively. Additionally, the charged lepton and vector-like lepton fields must be rotated to the mass basis according to Eq. (7.20); then Eq. (7.23) results in the photon and Z couplings to e_R and E_R being diagonal in the mass basis, as insertions of the LH and RH mixing cancel due to unitarity. However, the LH mixing V^L remains in the charged current term and the neutral current terms involving e_L and E_L. In the seesaw limit, the Lagrangian becomes

$$\begin{aligned}\mathcal{L} \supset &-\left[\frac{g}{\sqrt{2}}\bar{e}_\alpha\left(\delta_{\alpha\beta} - \frac{v^2 Y_E^\alpha Y_E^{\beta *}}{4m_E^2}\right)\gamma_\mu P_L \nu_\beta W^\mu + \text{h.c.}\right] \\ &- \frac{g}{c_w}\bar{e}_\alpha\left(g_L^e\delta_{\alpha\beta} + \frac{v^2 Y_E^\alpha Y_E^{\beta *}}{4m_E^2}\right)\gamma_\mu P_L e_\beta Z^\mu\,.\end{aligned} \tag{7.24}$$

The former induces lepton flavor universality (LFU) violating charged current processes. The latter describes off-diagonal Z couplings or flavor changing neutral currents (FCNCs), which are subject to a plethora of stringent bounds from EW precision observables and cLFV. We note that Eq. (7.24) is equivalent to integrating out E at low energies, which gives nonzero tree level matching conditions for the coefficients of the SMEFT operators $\mathcal{O}_{HL}^{(1)}$ and $\mathcal{O}_{HL}^{(3)}$,

$$C_{HL}^{(1)\alpha\beta} = C_{HL}^{(3)\alpha\beta} = -\frac{Y_E^\alpha Y_E^{\beta *}}{4m_E^2}\,, \tag{7.25}$$

which has been used previously in the literature [210, 157, 211]. Constraints on the Yukawa coupling Y_E from these probes are detailed in Section 7.3.

Next, the Lagrangian in Eq. (7.15) results in the Higgs interactions

$$\mathcal{L} \supset -\frac{1}{\sqrt{2}}\,\bar{e}_L \begin{pmatrix} Y_e & Y_E \end{pmatrix} \begin{pmatrix} e_R \\ E_R \end{pmatrix} h + \text{h.c.}\,. \tag{7.26}$$

This term can also be rotated to the mass basis, where the RH mixing V^R is no longer cancelled due to unitarity. The resulting couplings of the Higgs to charged leptons are

$$\mathcal{L} \supset -\frac{1}{\sqrt{2}}\bar{e}_\alpha \left(\delta_{\alpha\gamma} - \frac{3v^2 Y_E^\alpha Y_E^{\gamma *}}{4m_E^2}\right)[Y_e]_{\gamma\beta} P_R e_\beta h + \text{h.c.}\,, \tag{7.27}$$

which modify SM Higgs decays and induce cLFV Higgs decays via the off-diagonal couplings. The second term corresponds to the tree level matching of the UV theory onto the SMEFT operator $\mathcal{O}_{eH}$, with the Wilson coefficient

$$C_{eH}^{\alpha\beta} = \frac{Y_E^\alpha Y_E^{\gamma *}[Y_e]_{\gamma\beta}}{2m_E^2}\,. \tag{7.28}$$

Moving now to the scalar sector of the UV theory, the term $-\bar{L} f \tilde{L}\phi$ in Eq. (7.15) can be written explicitly as $-f_{\alpha\beta}\bar{\nu}_{L\alpha} e^c_{L\beta}\phi$, where f is antisymmetric in flavor space, i.e. $f_{\alpha\beta} = -f_{\beta\alpha}$. This interaction also induces LFU violating and cLFV processes at tree level and one-loop. If the scalar ϕ is heavy and integrated out at low energies, the previous term generates the SMEFT operator $\mathcal{O}_{LL}$ at tree level, with the Wilson coefficient [212, 213, 214],

$$C_{LL}^{\alpha\beta\gamma\delta} = \frac{f_{\alpha\gamma} f^*_{\delta\beta}}{m_\phi^2}\,. \tag{7.29}$$

Including also the term $\bar{N}_R^c f' e_R \phi^*$ from Eq. (7.15), integrating out ϕ generates the N_RSMEFT operators $\mathcal{O}_{LNLe} = (\bar{L}N_R)\epsilon(\bar{L}e_R)$ and $\mathcal{O}_{eN} = (\bar{e}_R\gamma_\mu e_R)(\bar{N}_R\gamma^\mu N_R)$ at tree level, with [156]

$$C_{LNLe}^{\alpha i\beta\gamma} = \frac{2f_{\alpha\beta} f'_{i\gamma}}{m_\phi^2}\,, \quad C_{eN}^{\alpha\beta ij} = \frac{f'^*_{i\alpha} f'_{j\beta}}{2m_\phi^2}\,. \tag{7.30}$$

This exhausts the tree level phenomenology of the UV model at low energies, which would have been absent if the Z_2 symmetry had been imposed. At the one-loop level, many more operators are induced in the (N_R)SMEFT, with partial matching results, predominantly in the SMEFT, available in the literature [155, 215, 144, 145]. The focus of the remainder of this section is the one-loop matching of the operators $\mathcal{O}^{(5)}_{NNB}$, $\mathcal{O}^{(6)}_{NB}$

and $\mathcal{O}_{NW}^{(6)}$, which can induce LLP signatures at the LHC. But first, we review the generation of neutrino masses when adding two sterile neutrinos to the particle content.

Neutrino masses

For sterile-to-sterile neutrino magnetic moments to be present, at least two RH neutrinos N_R are required in the model. As mentioned below Eq. (7.15), it is possible to write the renormalizable terms $-\bar{L}Y_\nu\tilde{H}N_R - \frac{1}{2}\bar{N}_R^c M_R N_R + \text{h.c.}$ in the Lagrangian. Below the EW scale, these terms lead to mixing between the active neutrinos ν_L and the sterile states, as discussed in previous chapters. The Lagrangian contains

$$\mathcal{L} \supset -\frac{1}{2}\begin{pmatrix}\bar{\nu}_L & \bar{N}_R^c\end{pmatrix}\mathcal{M}_\nu\begin{pmatrix}\nu_L^c \\ N_R\end{pmatrix} + \text{h.c.}\,; \quad \mathcal{M}_\nu = \begin{pmatrix}0 & \frac{vY_\nu}{\sqrt{2}} \\ \frac{vY_\nu^T}{\sqrt{2}} & M_R\end{pmatrix}\,, \tag{7.31}$$

where the extended neutrino mass matrix $\mathcal{M}_\nu$ is symmetric. Without loss of generality, M_R can be made to be diagonal via a rotation among the RH neutrinos, such that $M_R = \text{diag}(m_{N_1}, m_{N_2}, \ldots)$ and the resulting massive states are Majorana fermions, with $N_i = N_i^c$. However, we will keep M_R general in the following. The mass matrix can be diagonalized with the following unitary rotation [18]

$$\begin{pmatrix}\nu_{L\alpha}^c \\ N_{Rj}\end{pmatrix} = \begin{pmatrix}U_{\alpha i}^* & V_{\alpha N_i}^* \\ \tilde{V}_{ji} & \tilde{U}_{jN_i}\end{pmatrix} P_R \begin{pmatrix}\nu_i' \\ N_i'\end{pmatrix}\,, \tag{7.32}$$

such that $V^T\mathcal{M}_\nu V = \mathcal{M}_\nu^{\text{diag}} = \text{diag}(m_1, m_2, m_3, m_{N_1'}, \ldots)$. Here, $\nu_i' = \nu_i'^c$ and $N_i' = N_i'^c$ are the physical Majorana mass eigenstate fields in the broken phase, with the former corresponding to the observed light neutrinos and the latter to heavy sterile neutrinos. Similar to the charged leptons, we will relabel $\nu_i' \to \nu_i$ and $N_i' \to N_i$. In the limit $Y_\nu \ll \sqrt{2}M_R/v$, $\mathcal{M}_\nu$ can be diagonalized with

$$V_{\alpha N_i} \approx \frac{v}{\sqrt{2}}\big(Y_\nu M_R^{-1}\big)_{\alpha j}\tilde{U}_{jN_i}^*\,, \quad \tilde{V}_{ji} \approx -\frac{v}{\sqrt{2}}\big(M_R^{-1}Y_\nu^T\big)_{j\alpha}U_{\alpha i}^*\,, \tag{7.33}$$

to obtain the sub-blocks

$$[M_\nu]_{\alpha\beta} = U_{\alpha i}U_{\beta i}m_i \approx -\frac{v^2}{2}\big(Y_\nu M_R^{-1}Y_\nu^T\big)_{\alpha\beta}\,, \quad [M_N]_{ij} = \tilde{U}_{iN_i}^*\tilde{U}_{jN_i}^* m_{N_i} \approx [M_R]_{ij}\,, \tag{7.34}$$

where U and $\tilde{U}$ diagonalize M_ν and M_N, respectively. Note that $\tilde{U}_{jN_i} = \delta_{ij}$ if we had taken M_R to be diagonal. Combining Eqs. (7.33) and (7.34), it is possible to find the well-known relation for the active-sterile neutrino mixing [216]

$$V_{\alpha N_i} = iU_{\alpha j}\mathcal{R}_{ji}\sqrt{\frac{m_j}{m_{N_i}}}\,, \tag{7.35}$$

where $\mathcal{R}$ is an arbitrary orthogonal matrix, i.e. $\mathcal{R}_{ji}\mathcal{R}_{ki} = \delta_{jk}$.

In this work, we consider heavy sterile states N_i within the kinematic reach of the LHC, i.e., m_{N_i} from 1 GeV up to 1 TeV. For this range of masses, there are two possible ways to produce the observed light neutrino masses via the tree level relations in Eq. (7.34). The first scenario is that the heavy states N_i are dominantly Majorana (or, in other words, the masses m_{N_i} are well separated). Then, the light neutrino masses are given by $[M_\nu]_{\alpha\beta} = -\frac{v^2}{2}[Y_\nu]_{\alpha i}[Y_\nu]_{\beta i}/m_{N_i}$, which is the standard Type-I seesaw relation. For $m_N \sim 100$ GeV, neutrino masses $m_\nu \sim 0.1$ eV then require Yukawa couplings of size $[Y_\nu]_{\alpha i} \sim 10^{-6}$. The active-sterile mixing is governed by Eq. (7.35) with $|\mathcal{R}_{ji}| \leq 1$, or $V_{\ell N} \sim \sqrt{m_\nu/m_N}$. However, for heavy sterile states in the mass range relevant for the LHC, this active-sterile mixing $V_{\ell N}$ is too suppressed to give observable effects unless some additional new physics is present.

The second scenario is when pairs of heavy sterile states N_i form pseudo-Dirac states with small mass splittings. In this limit, cancellations in the matrix product $Y_\nu M_R^{-1} Y_\nu^T$ ensure small light neutrino masses instead of suppressed Yukawa couplings. Now that Y_ν can in principle be large, so can the active-sterile mixing in Eq. (7.33); equivalently, this corresponds to the limit $|\mathcal{R}_{ji}| \gg 1$ in Eq. (7.35). This interesting scenario is minimally obtained, for instance, in the inverse or linear seesaw mechanisms. To demonstrate this, we consider the simplified scenario where two heavy sterile states, $N_{R1} \equiv N_R$ and $N_{R2} \equiv S_L^c$, only interact with one generation of active neutrino. The relevant mass terms can be written as

$$\mathcal{L} \supset -m_{\nu N}\bar{\nu}_L N_R - m_{\nu S}\bar{\nu}_L S_L^c - \frac{1}{2}\left(\mu_N \bar{N}_R^c N_R + \mu_S \bar{S}_L S_L^c\right) - M_{NS}\bar{S}_L N_R + \text{h.c.}\,, \tag{7.36}$$

where $(m_{\nu N}, m_{\nu S}) \equiv (vY_\nu/\sqrt{2}, vY_S/\sqrt{2})$. As such, the extended neutrino mass matrix (assuming one generation of active neutrino) in the basis $(\nu_L^c, N_R, S_L^c)^T$ takes the form

$$\mathcal{M}_\nu = \begin{pmatrix} 0 & m_{\nu N} & m_{\nu S} \\ m_{\nu N} & \mu_N & M_{NS} \\ m_{\nu S} & M_{NS} & \mu_S \end{pmatrix}\,, \tag{7.37}$$

where $m_{\nu S}, \mu_N, \mu_S$ are expected to be small in the 't Hooft sense [82], as total lepton number symmetry is restored in the limit $m_{\nu S}, \mu_N, \mu_S \to 0$. We note that the inverse and linear seesaw can be obtained in the limits $m_{\nu S} = \mu_N = 0$ and $\mu_N = \mu_S = 0$, respectively. The symmetric mass matrix $\mathcal{M}_\nu$ can then be diagonalized as before; the inclusion of N_R and S_L^c leads to two Majorana eigenstates N_1 and N_2 with a small mass splitting compared to the Dirac mass M_{NS}. The unitary rotation matrix V can be solved perturbatively by using the Hermitian combination $\mathcal{M}_\nu^\dagger \mathcal{M}_\nu$ (or $\mathcal{M}_\nu \mathcal{M}_\nu^\dagger$),

$$V^\dagger \mathcal{M}_\nu^\dagger \mathcal{M}_\nu V = \left(V^T \mathcal{M}_\nu V\right)^\dagger \left(V^T \mathcal{M}_\nu V\right) = \text{diag}(m_\nu^2, m_{N_1}^2, m_{N_2}^2)\,, \tag{7.38}$$

where the V diagonalizing $\mathcal{M}_\nu \mathcal{M}_\nu^\dagger$ is the same as that in Eq. (7.38). One straightforward case is obtained in the limit where $m_{\nu S} = 0$ and assuming $\mu_N, \mu_S \ll m_{\nu N} \ll M_{NS}$. In this limit, the mass eigenvalues can be solved perturbatively to obtain

$$m_\nu \simeq \frac{|m_{\nu N}|^2 |\mu_S|}{|m_{\nu N}|^2 + |M_{NS}|^2}\,, \tag{7.39}$$

$$m_{N_1}^2 \simeq |m_{\nu N}|^2 + |M_{NS}|^2 - \frac{\left|\mu_S^* M_{NS}^2 + \mu_N \left(|m_{\nu N}|^2 + |M_{NS}|^2\right)\right|}{\sqrt{|m_{\nu N}|^2 + |M_{NS}|^2}}\,, \tag{7.40}$$

$$m_{N_2}^2 \simeq |m_{\nu N}|^2 + |M_{NS}|^2 + \frac{\left|\mu_S^* M_{NS}^2 + \mu_N \left(|m_{\nu N}|^2 + |M_{NS}|^2\right)\right|}{\sqrt{|m_{\nu N}|^2 + |M_{NS}|^2}}\,. \tag{7.41}$$

Another interesting case occurs when $\mu_N \sim \mu_S$ and $m_{\nu N} \sim m_{\nu S}$. The mass matrix can be exactly solved in this scenario, and assuming the parameters to be real, it leads to the masses

$$m_\nu^2 = 2m_{\nu N}^2 + \frac{1}{2}(M_{NS} + \mu_S)^2 \left[1 - \sqrt{1 + \frac{8m_{\nu N}^2}{(M_{NS} + \mu_S)^2}}\,\right]\,, \tag{7.42}$$

$$m_{N_1}^2 = 2m_{\nu N}^2 + \frac{1}{2}(M_{NS} + \mu_S)^2 \left[1 + \sqrt{1 + \frac{8m_{\nu N}^2}{(M_{NS} + \mu_S)^2}}\,\right]\,, \tag{7.43}$$

$$m_{N_2}^2 = (M_{NS} - \mu_S)^2\,. \tag{7.44}$$

This case corresponds to the scenario where N_2 is decoupled, which can be protected in the presence of an explicit symmetry, and only N_1 mixes with the active state. We note that any new interactions involving N_1 and N_2, e.g., a transition magnetic dipole moment, is in general not diagonal in this basis and may lead to corrections to the mass matrix $\mathcal{M}_\nu$. However, to restrict ourselves to these two limiting cases, we will assume any such correction to be small.

In the presence of the fields E and ϕ and their interactions in Eq. (7.15), it is possible to draw the one-loop diagrams in Fig. 7.1 which renormalize the Yukawa coupling Y_ν

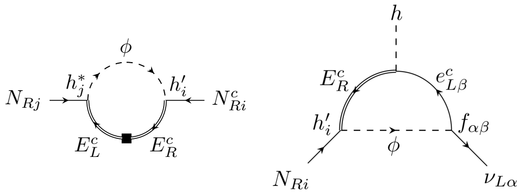

FIGURE 7.1: Diagrams at one-loop in the UV model which renormalize the RH neutrino mass matrix M_R (left) and Yukawa coupling Y_ν (right). For the Yukawa coupling, there are two other one-loop diagrams; one similar to that above with the replacements $E_R^c \to e_{R\rho}^c$, $h_i' \to f_{i\rho}'$ and $Y_E^{\beta *} \to [Y_e]_{\beta\rho}^*$ and another with an internal Higgs line and an insertion of $[Y_\nu]_{\alpha i}$.

and the RH neutrino mass M_R. The threshold corrections from these diagrams are

$$[Y_\nu]_{\alpha i} = [Y_\nu^{(0)}]_{\alpha i} - \frac{1}{8\pi^2}\Bigg[f_{\alpha\beta}Y_E^{\beta *}h_i'\left(1 + \frac{r\log r}{1-r} + \log\frac{\mu^2}{m_E^2}\right) + f_{\alpha\beta}[Y_e]_{\beta\rho}^* f_{i\rho}'\left(1 + \log\frac{\mu^2}{m_\phi^2}\right)$$
$$- \frac{1}{2}Y_E^\alpha Y_E^{\beta *}[Y_\nu^{(0)}]_{\beta i}\left(1 - \frac{\mu_H^{(0)2}}{m_E^2}\right)\left(1 + \log\frac{\mu^2}{m_E^2}\right)\Bigg], \tag{7.45}$$

$$[M_R]_{ij} = [M_R^{(0)}]_{ij} - \frac{(h_i' h_j^* + h_i^* h_j')m_E}{16\pi^2}\left(1 + \frac{r\log r}{1-r} + \log\frac{\mu^2}{m_E^2}\right), \tag{7.46}$$

where $r = m_\phi^2/m_E^2$ and μ_H is the usual parameter in the Higgs potential. While it is always possible to absorb the finite corrections to Y_ν and M_R in their renormalized values, these expressions are nevertheless useful to verify if fine-tuning between the tree level and one-loop contributions is required to obtain the desired heavy masses m_{N_i} and transition magnetic moments, calculated in the following sections.

Sterile-to-sterile neutrino magnetic moments

In our model, the $d = 5$ N_RSMEFT dipole operator $\mathcal{O}_{NNB}^{(5)}$ is generated at one-loop, as shown by the diagrams in Fig. 7.2, which then induces sterile-to-sterile transition magnetic moments $\mathcal{O}_{NN\gamma}$ and $\mathcal{O}_{NNZ}$ in the broken phase. We perform the matching of the UV model to the effective operator coefficient $C_{NNB}^{(5)}$ using the diagrammatic approach, which involves computing the one-light-particle-irreducible (1LPI) amplitudes in the effective and UV theories and requiring that they coincide at the matching scale.

The amplitude $\langle N_i N_j B\rangle$ in the N_RSMEFT via the operator $\mathcal{O}_{NNB}^{(5)ij}$ is

$$i\mathcal{M}_{ij}^{\text{EFT}} = 4\bar{u}(p_{N_i})\sigma_{\mu\nu}p_B^\nu\Big[C_{NNB}^{(5)ij}P_R - C_{NNB}^{(5)ij*}P_L\Big]u(p_{N_j})\epsilon^{\mu *}(p_B), \tag{7.47}$$

where $p_B = p_{N_j} - p_{N_i}$. Here, the indices i, j are fixed so there is an additional factor of 2

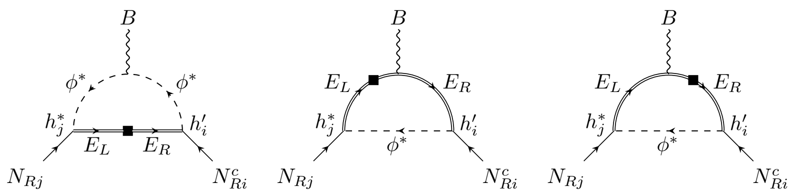

FIGURE 7.2: Diagrams at one-loop in the UV model which generate the $d = 5$ dipole operator $\mathcal{O}^{(5)}_{NNB}$. The black square indicates an insertion of the vector-like lepton mass m_E. At low energies, these induce electromagnetic sterile-to-sterile dipole moments $\mathcal{O}_{NN\gamma}$. Near the Z pole, sterile-to-sterile dipole couplings to Z, $\mathcal{O}_{NNZ}$, are also induced.

in the amplitude to account for the contribution from the antisymmetric term $-C^{(5)ji}_{NNB}$, which arises because of the Majorana nature of the sterile neutrinos. The amplitude $\langle N_i N_j B\rangle$ in the UV model is instead given by

$$\begin{aligned} i\mathcal{M}^{\rm UV}_{ij} = g' Y \bar{u}(p_{N_i}) \Big[&(h_i' P_R + h_i P_L)\Gamma_\mu (h_j^* P_R + h_j'^* P_L) \\ &- (h_i^* P_R + h_i'^* P_L)\Gamma_\mu (h_j' P_R + h_j P_L)\Big] u(p_{N_j})\epsilon^{\mu *}(p_B)\,, \end{aligned} \tag{7.48}$$

where $Y(E) = Y(\phi) = -1$ and Γ_μ denotes the loop integral

$$\begin{aligned} \Gamma_\mu = \mu^{2\epsilon}\int \frac{d^d k}{(2\pi)^d}\Bigg[&\frac{(\not{p}_{N_i} - \not{k} + m_E)\gamma_\mu(\not{p}_{N_j} - \not{k} + m_E)}{\left[k^2 - m_\phi^2\right]\left[(p_{N_i} - k)^2 - m_E^2\right]\left[(p_{N_j} - k)^2 - m_E^2\right]} \\ &- \frac{(\not{k} + m_E)(p_{N_i} + p_{N_j} - 2k)_\mu}{\left[k^2 - m_E^2\right]\left[(p_{N_i} - k)^2 - m_\phi^2\right]\left[(p_{N_j} - k)^2 - m_\phi^2\right]}\Bigg]\,, \end{aligned} \tag{7.49}$$

where k is the loop momentum. The first and second terms inside the square brackets of Eq. (7.49) originate from the coupling of B_μ to E and ϕ, respectively. Expanding the loop integral in powers of the external momenta and, assuming $m_{N_i} \ll m_E, m_\phi$, we obtain the amplitude

$$i\mathcal{M}^{\rm UV}_{ij} = \frac{g'}{16\pi^2 m_E} f(r)\bar{u}(p_{N_i})\sigma_{\mu\nu}p_B^\nu\Big[(h_i' h_j^* - h_i^* h_j')P_R - (h_i'^* h_j - h_i h_j'^*)P_L\Big]u(p_{N_j})\epsilon^{\mu *}(p_B)\,, \tag{7.50}$$

where we define the loop function

$$f(r) = \frac{1}{1-r} + \frac{r\log r}{(1-r)^2}\,, \tag{7.51}$$

again with $r = m_\phi^2/m_E^2$. For $m_E = m_\phi$, the limit of this function is $f(r)\big|_{r\to 1} = \frac{1}{2}$.

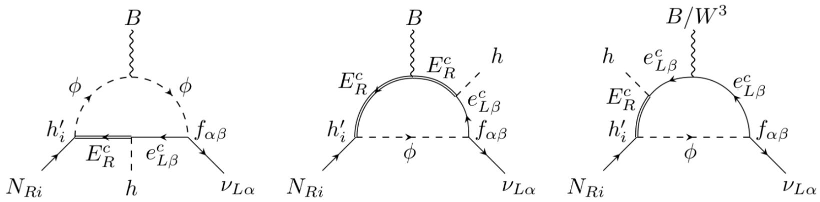

FIGURE 7.3: Diagrams at one-loop in the UV model which generate the $d = 6$ dipole operators $\mathcal{O}_{NB}^{(6)}$ and $\mathcal{O}_{NW}^{(6)}$. At low energies, these induce the electromagnetic active-to-sterile dipole moment $\mathcal{O}_{\nu N\gamma}$. Additionally, at energies near the EW scale, the dipole moments $\mathcal{O}_{eNW}$ and $\mathcal{O}_{\nu NZ}$ are generated. Note that there are additional diagrams with $E_R^c \to e_{R\rho}^c$, $h'_i \to f'_{i\rho}$ and $Y_E^{\beta *} \to [Y_e]_{\beta\rho}^*$ and others with an internal Higgs line and an insertion of $[Y_\nu]_{\alpha i}$, which also contribute to Eq. (7.55).

The amplitudes in Eqs. (7.47) and (7.50) can now be equated to find

$$C_{NNB}^{(5)ij} = \frac{g'(h'_i h_j^* - h_i^* h'_j)}{64\pi^2 m_E} f(r)\,, \tag{7.52}$$

which is in agreement with the result of [207]. We see that the flavor structure is determined entirely by the combination $h'_i h_j^* - h_i^* h'_j$, with the diagonal elements vanishing, as expected. In the broken phase of the SM, but at energies where the Z boson is not yet integrated out, $C_{NNB}^{(5)}$ results in the γ and Z couplings ($d_{NN\gamma}$ and d_{NNZ}) according to Eq. (7.10). For $m_E = m_\phi$, Eqs. (7.52) and (7.10) give dipole couplings of size,

$$d_{NN\gamma}^{ij} = c_w C_{NNB}^{(5)ij} \approx 2.4 \times 10^{-6}\ \text{GeV}^{-1} \left(\frac{h'_i h_j^* - h_i^* h'_j}{10}\right)\left(\frac{1\ \text{TeV}}{m_E}\right). \tag{7.53}$$

Thus, even with values of the couplings at the perturbative limit, $h, h' \lesssim \sqrt{4\pi}$, values of the dipole coupling can only be obtained up to $d_{NN\gamma}^{ij} \sim 10^{-4}\ \text{GeV}^{-1}$ with m_E and m_ϕ just above the current lower limits from collider searches, $m_E, m_\phi \gtrsim 200$ GeV (see Section 7.3 for further details).

Examining Eq. (7.46), we observe that the one-loop correction to $[M_R]_{ij}$ depends on the same couplings entering $C_{NNB}^{(5)ij}$ in Eq. (7.52), but with an orthogonal combination of the couplings. Therefore, it is possible to obtain large sterile-to-sterile neutrino magnetic moments for sterile states in the GeV-TeV range without generating large contributions to $[M_R]_{ij}$.

Active-to-sterile neutrino magnetic moments

The $d = 6$ operators $\mathcal{O}_{NB}^{(6)}$ and $\mathcal{O}_{NW}^{(6)}$, which induce active-to-sterile neutrino transition magnetic moments $\mathcal{O}_{\nu N\gamma}$ and $\mathcal{O}_{\nu NZ}$, as well as the charged current dipole $\mathcal{O}_{eNW}$, are also generated in the UV model at one-loop, as depicted in Fig. 7.3. These diagrams do not require mixing between the active and sterile neutrinos and thus avoid mixing suppression. However, they do rely on the Yuwawa coupling Y_E of the lepton doublet L with vector-like lepton E_R and Higgs doublet H. In the following, we use the same procedure as the previous section to find the matching between $C_{NB}^{(6)}$ and $C_{NW}^{(6)}$ and the parameters of the UV model.

In the N_RSMEFT, the amplitude $\langle \nu_\alpha N_i B h \rangle$ is given by

$$i\mathcal{M}_{\alpha i}^{\text{EFT}} = \sqrt{2} C_{NB}^{(6)\alpha i} \bar{u}(p_{\nu_\alpha}) \sigma_{\mu\nu} p_B^\nu P_R u(p_{N_i}) \epsilon^{\mu *}(p_B) \,, \tag{7.54}$$

where $p_B = p_{N_i} - p_{\nu_\alpha}$. In the UV model, the amplitude $\langle \nu_\alpha N_i B h \rangle$ is determined in part by the three one-loop diagrams shown in Fig. 7.3. It is also possible to draw one-loop diagrams analogous to those in Fig. 7.3, but with $E_R^c \to e_{R\rho}^c$, $h_i' \to f_{i\rho}'$ and $Y_E^{\beta *} \to [Y_e]_{\beta\rho}^*$, and another with an internal Higgs line proportional to $Y_E^\alpha Y_E^{\beta *} [Y_\nu]_{\beta i}$. Including all of these contributions, the UV amplitude $\langle \nu_\alpha N_i B h \rangle$ can be calculated and compared with the EFT amplitude, as enacted in the previous section. This gives the matching condition,

$$C_{NB}^{(6)\alpha i} = \frac{g'}{64\pi^2 m_E^2} \left[3 f_{\alpha\beta} Y_E^{\beta *} h_i' f(r) - \frac{f_{\alpha\beta} [Y_e]_{\beta\rho}^* f_{i\rho}'}{r} \left(\frac{5}{2} + 3 \log \frac{\mu^2}{m_\phi^2} \right) + Y_E^\alpha Y_E^{\beta *} [Y_\nu]_{\beta i} \right] , \tag{7.55}$$

where the flavor indices β and ρ are summed over and the loop function $f(r)$ is the same as in Eq. (7.51), with $r = m_\phi^2 / m_E^2$.

As seen in the diagram to the right of Fig. 7.3, the intermediate charged lepton can also couple to W_μ^3, which generates the operator $\mathcal{O}_{NW}^{(6)}$. The amplitude for $\langle \nu_\alpha N_i W^3 h \rangle$ from this operator is

$$i\mathcal{M}_{\alpha i}^{\text{EFT}} = \frac{C_{NW}^{(6)\alpha i}}{\sqrt{2}} \bar{u}(p_{\nu_\alpha}) \sigma_{\mu\nu} p_W^\nu P_R u(p_{N_i}) \epsilon^{\mu *}(p_W) \,, \tag{7.56}$$

for $p_W = p_{N_i} - p_{\nu_\alpha}$. The UV amplitude $\langle \nu_\alpha N_i W^3 h \rangle$ can be calculated from the diagrams entering $\langle \nu_\alpha N_i B h \rangle$ where it is possible to replace $B \to W^3$. The resulting matching condition is

$$C_{NW}^{(6)\alpha i} = \frac{g}{32\pi^2 m_E^2} \left[f_{\alpha\beta} Y_E^{\beta *} h_i' f(r) - \frac{f_{\alpha\beta} [Y_e]_{\beta\rho}^* f_{i\rho}'}{r} \left(\frac{3}{2} + \log \frac{\mu^2}{m_\phi^2} \right) + Y_E^\alpha Y_E^{\beta *} [Y_\nu]_{\beta i} \right] . \tag{7.57}$$

From Eqs. (7.55) and (7.57) we see that, in principle, there are multiple contributions to these operators. To simplify this dependence on the UV model parameters, we note that we are only interested in the scenario where the coefficient $C_{NNB}^{(5)ij}$ is sizable, requiring large h'. Then, if we assume that the first terms in Eqs. (7.55) and (7.57) dominate over the others, we obtain the particularly simple relation between the coefficients

$$C_{NW}^{(6)\alpha i} = \frac{2}{3t_w} C_{NB}^{(6)\alpha i} \approx 1.22\, C_{NB}^{(6)\alpha i}\,. \tag{7.58}$$

Thus, as discussed in Section 7.1, the UV model sets the parameter $a = 2/3$. Now, using Eqs. (7.10) and Eq. (7.57), we find the corresponding active-to-sterile dipole couplings in the broken phase to be

$$d_{\nu N\gamma}^{\alpha i} = \frac{4vc_w}{3\sqrt{2}} C_{NB}^{(6)\alpha i} \approx 1.7 \times 10^{-9}\ \mathrm{GeV}^{-1} \left(\frac{f_{\alpha\beta} Y_E^{\beta *} h_i'}{10^{-2}}\right) \left(\frac{1\ \mathrm{TeV}}{m_E}\right)^2 . \tag{7.59}$$

Using Eq. (7.12) and $a = 2/3$, we also find the ratio

$$\frac{d_{\nu NZ}^{\alpha i}}{d_{\nu N\gamma}^{\alpha i}} = \frac{(1 - 3t_w^2)}{(4t_w)} \approx 4.5 \times 10^{-2}\,. \tag{7.60}$$

The active-to-sterile dipole coupling with Z is therefore relatively suppressed with respect to $d_{\nu N\gamma}^{\alpha i}$ in this scenario. Finally, we note that the flavor structure of the couplings $d_{\nu N\gamma}^{\alpha i}$ and $d_{\nu NZ}^{\alpha i}$ exhibits an interesting dependence on the parameters of the UV model. In the case of flavor universal couplings, at least one of the entries of $d_{\nu N\gamma}^{\alpha i}$ and $d_{\nu NZ}^{\alpha i}$ for $\alpha \in \{e, \mu, \tau\}$ must vanish, with the other two being equal and opposite in sign; for the choice $Y_E^e = Y_E^\mu = Y_E^\tau$ and $f_{e\mu} = f_{e\tau} = f_{\mu\tau}$, we obtain $d_{\nu N\gamma}^{\mu i} = d_{\nu NZ}^{\mu i} = 0$, for example. In the scenario where only the μ-τ couplings are nonzero, for example $Y_E^\mu = Y_E^\tau$ and $f_{\mu\tau}$, we would instead have $d_{\nu N\gamma}^{ei} = d_{\nu NZ}^{ei} = 0$, $d_{\nu N\gamma}^{\mu i} = -d_{\nu N\gamma}^{\tau i}$ and $d_{\nu NZ}^{\mu i} = -d_{\nu NZ}^{\tau i}$. Finally, if only couplings involving τ are present (e.g., Y_E^τ, $f_{e\tau} = f_{\mu\tau}$), we would obtain $d_{\nu N\gamma}^{\tau i} = d_{\nu NZ}^{\tau i} = 0$, $d_{\nu N\gamma}^{ei} = d_{\nu N\gamma}^{\mu i}$ and $d_{\nu NZ}^{ei} = d_{\nu NZ}^{\mu i}$. These particular limits can be readily translated to other flavor combinations.

Active-to-active neutrino magnetic moments

Here, we finally comment that active-to-active neutrino magnetic moments are naturally suppressed in the UV model. With the fields and couplings available in Eq. (7.15) and assuming $m_{N_i} \ll m_E, m_\phi$, the lowest-order 1LPI amplitudes that contribute to the $d = 7$ SMEFT operators $C_{LHB}^{(7)\alpha\beta}$ and $C_{LHW}^{(7)\alpha\beta}$ are at two loops, as shown in Fig. 7.4.

However, in the broken phase, and at energies where the RH neutrinos may also be

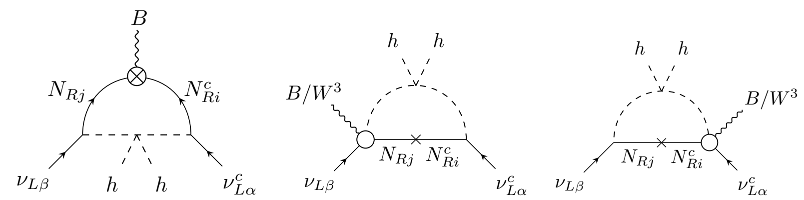

FIGURE 7.4: Diagrams at two loops in the UV model which contribute negligibly to the $d = 7$ dipole operators $\mathcal{O}^{(7)}_{LH^2B}$ and $\mathcal{O}^{(7)}_{LH^2W}$. The crossed circle in the left diagram refers to the sterile-to-sterile one-loop diagrams in Fig. 7.2, while the circle in the other two diagrams correspond to the active-to-sterile diagrams in Fig. 7.3.

integrated out, active-to-active neutrino magnetic moments are induced via the active-sterile mixing $V_{\ell N}$, i.e.,

$$\begin{aligned} d^{\alpha\beta}_{\nu\nu\gamma} &= V^*_{\alpha N_i} V^*_{\beta N_j} d^{ij}_{NN\gamma} + \left[V^*_{\alpha N_i} d^{\beta i}_{\nu N\gamma} - V^*_{\beta N_i} d^{\alpha i}_{\nu N\gamma} \right] \\ &\approx 10^{-16}\,\text{GeV}^{-1} \left[\left(\frac{V^*_{\alpha N_i} V^*_{\beta N_j}}{10^{-10}} \right) \left(\frac{d^{ij}_{NN\gamma}}{10^{-6}\,\text{GeV}^{-1}} \right) + \left(\frac{V^*_{\alpha N_i}}{10^{-5}} \right) \left(\frac{d^{\beta i}_{\nu N\gamma}}{10^{-11}\,\text{GeV}^{-1}} \right) \right], \end{aligned} \tag{7.61}$$

where in the second line we have assumed that $\alpha \neq \beta$ and $d^{\alpha i}_{\nu N\gamma} = 0$. For active-sterile mixing of the size predicted by the Type-I seesaw mechanism, $V_{\ell N} \sim \sqrt{m_\nu / m_N} \sim 10^{-6}$, this contribution is highly suppressed both by the mixing and the one-loop suppressed $d^{ij}_{NN\gamma}$ and $d^{\alpha i}_{\nu N\gamma}$. Thus, even with the larger mixing $V_{\ell N}$ in the inverse seesaw scenario, we can still expect the active-to-active neutrino magnetic moments to safely satisfy the bounds from TEXONO [217], GEMMA [218], LSND [219] and Borexino [220], $d^{\alpha\beta}_{\nu\nu\gamma} \lesssim 2 \times 10^{-8}\,\text{GeV}^{-1}$.

7.3 Phenomenological constraints on the UV model

In this section, we review the constraints on the UV-complete extension of the SM outlined in Section 7.2. We begin by examining the direct production of E and ϕ in collider experiments. We then consider rare low-energy processes which are not present or highly-suppressed in the SM, but could be enhanced by non-diagonal flavor couplings after integrating out E and ϕ.

Constraints from direct collider searches

A recasting of direct searches for selectrons and smuons at the LHC provides useful constraints on the singly-charged scalar ϕ in our UV scenario. The dominant limit comes from the Drell-Yan pair production process $pp \to \gamma/Z \to \phi^+\phi^-$ followed by the decay $\phi^\pm \to \ell^\pm\nu$. In [221, 222, 223, 213], the most recent ATLAS search [224] for oppositely-charged electron and muon pairs with 139 fb^{-1} of collected data was recast for the singly-charged scalar scenario. The ATLAS search places a lower bound on the slepton masses of approximately 450 GeV for a 100% branching ratio of the slepton in the specific channel. The major difference between this analysis and the pair production of $\phi^+\phi^-$ is the cross section in the two scenarios. In [213], a simple scaling factor was used to map the production cross section for $pp \to \phi^+\phi^-$ obtained with `MadGraph5` at leading order onto the production cross section given by ATLAS for the RH slepton pair. Allowing for further uncertainties, a conservative lower limit of $m_\phi \gtrsim 200$ GeV was found. In addition, monophoton searches for dark matter at LEP [225, 226] can also be recast to obtain the limit $m_\phi/|f_{e\mu}| \gtrsim 350$ GeV [213].

In general, $SU(2)_L$ singlet vector-like leptons E are subject to much weaker bounds compared to their $SU(2)_L$ doublet counterparts, due to their relatively smaller production cross sections. Initially, searches at LEP [227] were able to exclude the masses $m_E < 101.2$ GeV. More recently, the ATLAS collaboration has performed a search for heavy charged leptons decaying to a Z boson and an electron or muon, excluding the mass range 129–176 GeV (114–168 GeV) for mixing with only electrons (muons), except for the interval 144–163 GeV (153–160 GeV) [228]. In [229], the prospects of probing singlet vector-like leptons with multi-lepton searches at the LHC were explored, with some reach for exclusion at the HL-LHC. In our specific model, the pair-produced vector-like leptons can also decay to a sterile neutrino and the singly-charged scalar, $E^\pm \to N_i\phi^\pm$. The subsequent decay $\phi^\pm \to \ell^\pm\nu$ therefore leads to the signature of two oppositely charged leptons plus missing energy. This is a signature similar to that from $\phi^+\phi^-$ pair production and is expected to yield a similar constraint, $m_E \gtrsim 200$ GeV.

Finally, EW precision data from LEP, complemented by the measurement of the Higgs mass, have been used to perform a global fit for the SM plus heavy new physics effects, parameterized by $d = 6$ SMEFT operators [210, 230, 212]. From this fit, flavor-dependent upper bounds can be placed on the mixing between the charged leptons and E, which alternatively can be written as the lower limits $m_E/|Y_E^e| > 8.3$ TeV, $m_E/|Y_E^\mu| > 5.8$ TeV and $m_E/|Y_E^\tau| > 5.3$ TeV (95% C.L.). The singly-charged scalar is similarly constrained as $m_\phi/|f_{e\mu}| > 12.5$ TeV (95% C.L.).

Constraints from charged lepton flavor violation

As mentioned in Section 7.2, charged lepton flavor violating (cLFV), lepton flavor universality (LFU) violating observables and precision tests of observables such as $(g-2)_\mu$ can be used to constrain the parameter space of the UV model [231, 232, 233, 213, 211,

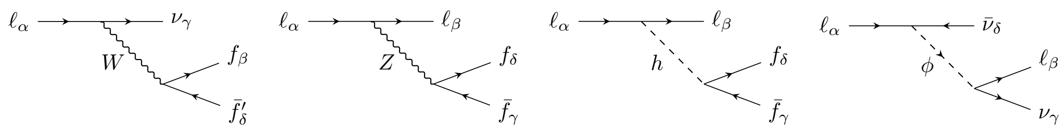

FIGURE 7.5: Diagrams at tree level in the UV extension which result in violations of LFU and non-vanishing rates for the cLFV processes $\ell_\alpha \to \ell_\beta \ell\bar{\ell}$ and $\tau \to \ell_\beta X$, where X is a light meson.

234, 214, 235, 236]. In the presence of the Yukawa couplings Y_E, mixing is induced between the SM charged leptons and the vector-like lepton E, modifying the SM charged current, neutral current and Higgs interactions at low energies, as seen in Eqs. (7.24) and (7.27).[4]

Equivalently, from the EFT perspective, the operators $\mathcal{O}_{HL}^{(1)}$, $\mathcal{O}_{HL}^{(3)}$ and $\mathcal{O}_{eH}$ are induced at tree level after integrating out E. Likewise, the operator $\mathcal{O}_{LL}$ is generated after integrating out ϕ. SM processes such as $\ell_\alpha \to \ell_\beta \nu\bar{\nu}$, $\pi \to \ell_\alpha \nu$, $\tau \to \pi\nu$ and $B \to D^{(*)}\ell_\alpha \nu$ are modified in the presence of these operators, while cLFV processes such as $\ell_\alpha \to \ell_\beta \gamma$, $\ell_\alpha \to \ell_\beta \ell\bar{\ell}$, $\mu - e$ conversion in nuclei, $Z \to \ell_\alpha^+ \ell_\beta^-$ and $h \to \ell_\alpha^+ \ell_\beta^-$ are induced. The $\ell_\alpha \to \ell_\beta \gamma$ process additionally receives contributions directly from the dipole operators $\mathcal{O}_{eB}$ and $\mathcal{O}_{eW}$, both of which are generated after integrating out E and ϕ at one-loop. In the following, we assume that E and ϕ are integrated out at a scale well above the low energies of the considered processes. Thus, one should consider the running of the operators from the high scale down to the EW scale, match to $SU(3)_c \times U(1)_Y$ invariant operators, and then run down to the low scale. However, we neglect the sub-leading effects of running as we only aim to obtain bounds on the model for comparison with those from LLP searches in Section 7.4.

For the bounds from LFU violation, we consider here as an example only the purely leptonic LFU ratios, which measure deviations from the SM predictions for $\ell_\alpha \to \ell_\beta \nu\bar{\nu}$. In the UV model, we obtain the ratio [211, 238]

$$\frac{\Gamma(\ell_\alpha \to \ell_\beta \nu\bar{\nu})}{\Gamma(\ell_\alpha \to \ell_\beta \nu\bar{\nu})\big|_{\text{SM}}} = 1 + v^2 \left[\frac{|Y_E^\alpha|^2 + |Y_E^\beta|^2}{2m_E^2} + \frac{2|f_{\alpha\beta}|^2}{m_\phi^2} \right], \tag{7.62}$$

where we only take into account the interference between the SM and the NP contributions. The first and second terms in the square brackets of Eq. (7.62) arise from the exchange of W and ϕ, respectively, as seen in the left- and right-most diagrams of Fig. 7.5. The Z and h exchange diagrams do not contribute at this level, because there are no FCNCs at tree level in the SM. This ratio can be used to determine the ratio of

[4]The Yukawa coupling Y_ν, which induces the active-sterile mixing $V_{\ell N}$, also modifies the charged and neutral current interactions and therefore contributes to cLFV processes [237]. For simplicity, we assume that $Y_\nu \ll 1$ for the purposes of deriving bounds on the UV model.

couplings $|g_\alpha/g_\beta|$, obtained as

$$\left|\frac{g_\alpha}{g_\beta}\right| \approx 1 + v^2 \left[\frac{|Y_E^\alpha|^2 - |Y_E^\beta|^2}{4m_E^2} + \frac{|f_{\alpha\rho}|^2 - |f_{\beta\rho}|^2}{m_\phi^2}\right] . \tag{7.63}$$

From Eq. (7.63), it is clear that LFU violation vanishes for flavor universal couplings, e.g., the choice $Y_E^e = Y_E^\mu = Y_E^\tau$ and $f_{e\mu} = f_{e\tau} = f_{\mu\tau}$. Current experimental values of these coupling ratios are $|g_\tau/g_\mu| = 1.0009(14)$, $|g_\tau/g_e| = 1.0027(14)$, $|g_\mu/g_e| = 1.0019(14)$ [239, 240]. From the first of these results, taking only Y_E^τ to be nonzero gives $m_E/|Y_E^\tau| > 4.1$ TeV.

The tree level Z and Higgs exchange diagrams in Fig. 7.5 induce the cLFV processes $\ell_\alpha \to \ell_\beta \ell \bar{\ell}$, which are subject to stringent constraints from SINDRUM [71] and Belle [73]. The branching ratio for this general process, neglecting final-state lepton masses, is [241, 242]

$$\mathcal{B}(\ell_\alpha \to \ell_\beta \ell_\gamma \bar{\ell}_\delta) \approx \frac{m_\alpha^5}{768\pi^3 \Gamma_\alpha (1+\delta_{\beta\gamma})} \frac{|Y_E^{\alpha *} Y_E^\beta|^2}{m_E^4} \left[(1+\delta_{\beta\gamma})(g_L^e)^2 + (g_R^e)^2\right] . \tag{7.64}$$

We assume that the dominant contribution to Eq. (7.64) comes from the Z exchange diagrams, or correspondingly the operators $\mathcal{O}_{HL}^{(1)}$ and $\mathcal{O}_{HL}^{(3)}$. The contribution of the Higgs exchange diagram, or the operator $\mathcal{O}_{eH}$, can be safely neglected as it is further suppressed by the lepton masses, as seen in Eqs. (7.26) and (7.27). In Eq. (7.64), we also neglect the contributions from E and ϕ at one-loop via penguin and box diagrams, or equivalently via the operators $\mathcal{O}_{eB}$, $\mathcal{O}_{eW}$ and $\mathcal{O}_{LL}$ [213]. The one-loop contribution of ϕ will only be relevant if the Yukawa couplings inducing $\ell_\alpha \to \ell_\beta \ell \bar{\ell}$ at tree level satisfy $Y_E^\alpha, Y_E^\beta \ll f_{\alpha\beta}$. If we assume that the tree level contribution dominates, the branching ratio in Eq. (7.64) and the corresponding experimental upper limits can be used to place lower bounds on the combination $m_E/|Y_E^{\alpha *} Y_E^\beta|^{1/2}$ for $\alpha \neq \beta$. The SINDRUM experiment provides the upper limit $\mathcal{B}(\mu^+ \to e^+ e^+ e^-) < 1 \times 10^{-12}$ (90% C.L.), giving $m_E/|Y_E^{\mu *} Y_E^e|^{1/2} > 120$ TeV. Likewise, the upper limits $\mathcal{B}(\tau^- \to e^- e^- e^+) < 2.7 \times 10^{-8}$ and $\mathcal{B}(\tau^- \to \mu^- \mu^- \mu^+) < 2.1 \times 10^{-8}$ from Belle translate to $m_E/|Y_E^{\tau *} Y_E^e|^{1/2} > 5.9$ TeV and $m_E/|Y_E^{\tau *} Y_E^\mu|^{1/2} > 6.3$ TeV, respectively. The equivalent constraints from $\mathcal{B}(\tau^- \to e^- \mu^- \mu^+)$ and $\mathcal{B}(\tau^- \to \mu^- e^- e^+)$ are comparable. We note that the cLFV processes $\ell_\alpha \to \ell_\beta q \bar{q}$, i.e., hadronic τ decays $\tau \to \ell_\beta X$, where X is a light pseudoscalar, scalar or vector meson, are also generated. Constraints on such decay modes from Belle and BaBar are comparible to those on $\tau \to \ell_\beta \ell \bar{\ell}$ [243].

In the presence of the flavor-changing Z couplings at tree level, the exotic process of muon conversion to electrons in nuclei can also occur. The rate for this process, divided by the total capture rate Γ_{capt}, is [244, 245]

$$\mathrm{CR}(\mu \to e) = \frac{m_\mu^5}{\Gamma_{\text{capt}}} \frac{\left|Y_E^{\mu *} Y_E^e\right|^2}{m_E^4} \left|(g_L^u + g_R^u)(2V^{(p)} + V^{(n)}) + (g_L^d + g_R^d)(V^{(p)} + 2V^{(n)})\right|^2, \tag{7.65}$$

where $V^{(p)}$ and $V^{(n)}$ are nucleus-dependent overlap integrals over the proton and neutron densities and the muon and electron wavefunctions [244]. In Eq. (7.65), we again assume that the dominant contribution arises at tree level via the operators $\mathcal{O}_{HL}^{(1)}$ and $\mathcal{O}_{HL}^{(3)}$, neglecting the contributions of E and ϕ at one-loop via penguin diagrams. The SINDRUM experiment has placed an upper bound on the $\mu - e$ conversion rate on ${}^{197}_{79}$Au of $\mathrm{CR}(\mu \to e) < 7 \times 10^{-13}$ (90% C.L.) [246], which results in the constraint $m_E/|Y_E^{\mu *} Y_E^e|^{1/2} > 290$ TeV.

Next, the radiative cLFV process $\ell_\alpha \to \ell_\beta \gamma$ is generated at one-loop, as depicted in Fig. 7.6. The corresponding branching ratio is given by [242, 247, 248]

$$\mathcal{B}(\ell_\alpha \to \ell_\beta \gamma) \approx \frac{m_\alpha^5}{512\pi^3 \Gamma_\alpha} \frac{\alpha}{2\pi} \left[\left| \frac{Y_E^{\alpha *} Y_E^\beta}{4m_E^2} \left(1 + \frac{8}{3} g_L^e\right) + \frac{f_{\rho\alpha}^* f_{\rho\beta}}{3m_\phi^2} \right|^2 + \left| \frac{f'_{i\alpha} f'^*_{i\beta}}{12 m_\phi^2} \right|^2 \right], \tag{7.66}$$

where the indices ρ and i are summed over. The term in Eq. (7.66) proportional to $Y_E^{\alpha *} Y_E^\beta$ originates from the operators $\mathcal{O}_{HL}^{(1)}$, $\mathcal{O}_{HL}^{(3)}$, $\mathcal{O}_{eB}$ and $\mathcal{O}_{eW}$, generated after integrating out E, while the terms proportional to $f_{\rho\alpha}^* f_{\rho\beta}$ and $f'_{i\alpha} f'^*_{i\beta}$ arise from the contributions of ϕ to $\mathcal{O}_{eB}$ and $\mathcal{O}_{eW}$. Contributions of the operator $\mathcal{O}_{eH}$ via two-loop Barr-Zee type diagrams are neglected, as C_{eH} is suppressed by the lepton masses. If we assume only nonzero Y_E^α values, the current upper limit from the MEG experiment [66], $\mathcal{B}(\mu \to e\gamma) < 4.2 \times 10^{-13}$ (90% C.L.), corresponds to the constraint $m_E/|Y_E^{\mu *} Y_E^e|^{1/2} > 75$ TeV. For τ decays, the BaBar experiment gives the upper limits $\mathcal{B}(\tau \to e\gamma) < 3.3 \times 10^{-8}$ and $\mathcal{B}(\tau \to \mu\gamma) < 4.4 \times 10^{-8}$ (90% C.L.) [68], enforcing $m_E/|Y_E^{\tau *} Y_E^e|^{1/2} > 2.9$ TeV and $m_E/|Y_E^{\tau *} Y_E^\mu|^{1/2} > 2.7$ TeV, respectively.

Finally, limits can be placed from the cLFV decays $Z \to \ell_\alpha^+ \ell_\beta^-$ and $h \to \ell_\alpha^+ \ell_\beta^-$. With nonzero values of Y_E^α, the branching ratios of these are [249, 250, 231, 236]

$$\mathcal{B}(Z \to \ell_\alpha^+ \ell_\beta^-) = \frac{m_Z}{6\pi \Gamma_Z} \frac{m_Z^2}{v^2} \left[\left(\left(g_L^e\right)^2 + \left(g_R^e\right)^2 + g_L^e \frac{v^2 |Y_E^\alpha|^2}{2m_E^2} \right) \delta_{\alpha\beta} + \frac{v^4 |Y_E^{\alpha *} Y_E^\beta|^2}{16 m_E^4} \right], \tag{7.67}$$

$$\mathcal{B}(h \to \ell_\alpha^+ \ell_\beta^-) = \frac{m_h}{8\pi \Gamma_h} \frac{m_\alpha^2}{v^2} \left[\left(1 - \frac{3v^2 |Y_E^\alpha|^2}{2m_E^2}\right) \delta_{\alpha\beta} + \frac{9v^4 |Y_E^{\alpha *} Y_E^\beta|^2}{16 m_E^4} \right]. \tag{7.68}$$

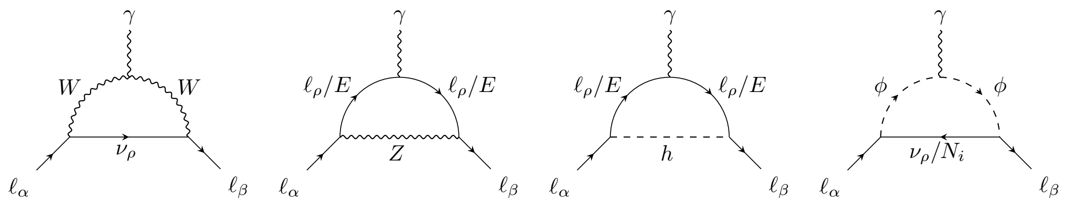

FIGURE 7.6: Diagrams at one-loop in the UV model which induce the cLFV process $\ell_\alpha \to \ell_\beta\gamma$ and contribute to the anomalous magnetic moment of charged leptons, a_ℓ. From left to right, the first three diagrams are the result of the modified W, Z and Higgs interactions in Eqs. (7.23) and (7.26), respectively, while the fourth diagram is induced by the $-\bar{L}f\tilde{L}\phi$ and $-\bar{N}_R^c f'\ell_R\phi^*$ interactions. The first and last diagrams are further modified in the presence of the active-sterile mixing $V_{\ell N}$.

We note that $\mathcal{B}(Z \to \ell_\alpha^\pm\ell_\beta^\mp)$ and $\mathcal{B}(h \to \ell_\alpha^\pm\ell_\beta^\mp)$ are found by adding the branching ratios with $\alpha \leftrightarrow \beta$ to those above. Upper bounds on these decays have been placed by OPAL [251], ATLAS [252, 253] and CMS [254]. Taking the most stringent, $\mathcal{B}(Z \to e^\pm\mu^\mp) < 4.2 \times 10^{-7}$ at 90% C.L. [252], gives $m_E/|Y_E^{\mu*}Y_E^e|^{1/2} > 4.1$ TeV.

To conclude this section, we observe that $\ell_\alpha \to \ell_\beta\ell\bar{\ell}$ and $\mu - e$ conversion in nuclei provide the most stringent constraints on the UV model, with the latter probing values of m_E up to 290 TeV for $\mathcal{O}(1)$ Yukawa couplings Y_E. The coupling Y_E^α enters the active-to-sterile dipole couplings, as seen in Eq. (7.55) and (7.57), and therefore these constraints must be taken into account when considering nonzero $d_{\nu N\gamma}^{\alpha i}$. However, we note that these constraints can be easily evaded if the couplings of E and ϕ are not flavor universal. For example, one can consider only nonzero couplings in the μ-τ (e-τ) sector; for $Y_E^e = 0$ ($Y_E^\mu = 0$), the strong bounds from $\mu \to 3e$ and $\mu - e$ conversion are no longer applicable. The only bounds that then apply are the much weaker limits from LFU violation, $\tau \to \mu\gamma$ ($\tau \to e\gamma$), and $\tau \to 3\mu$ ($\tau \to 3e$). One can also consider the case where only one Yukawa coupling is nonzero, e.g. Y_E^τ. Then the strongest bounds come from the one-loop contributions of ϕ to $\mu \to e\gamma$, $\mu \to 3e$ and $\mu - e$ conversion.

7.4 Long-lived particle searches at the LHC using non-pointing photons

In this section, we discuss the potential of searches for non-pointing photons at the LHC to constrain sterile neutrino magnetic moments. To keep our analysis general, we adopt the EFT approach introduced in Section 7.1 and consider the operators $\mathcal{O}_{NNB}^{(5)}$, $\mathcal{O}_{NB}^{(6)}$ and $\mathcal{O}_{NW}^{(6)}$.

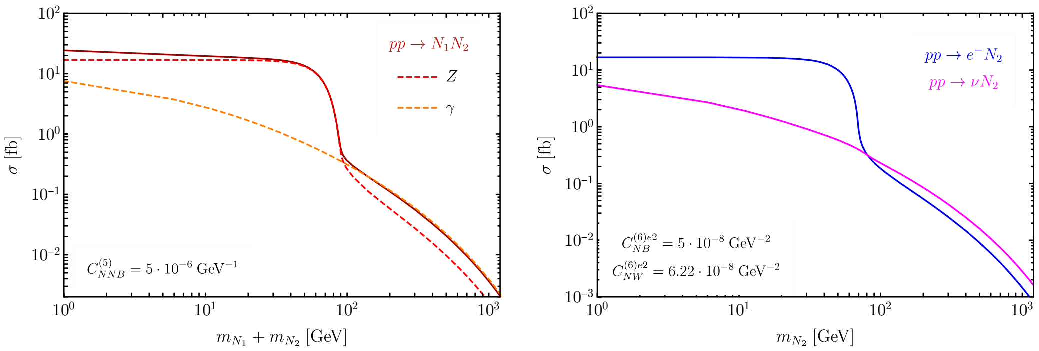

FIGURE 7.7: Example cross sections at the LHC ($\sqrt{s} = 14$ TeV). The left plot shows the contribution of $C^{(5)}_{NNB}$ to $\sigma(pp \to N_1 N_2)$ as a function of $m_{N_1} + m_{N_2}$. Dashed lines represent the partial contributions from the Z and γ channels. The right plot displays the production cross section of the processes mediated by $C^{(6)}_{NB}$ and $C^{(6)}_{NW}$. The cross section for the charged current process given by the chosen values of these couplings is the same as the cross section for the production of N_2 via the mixing $|V_{eN_2}|^2 \simeq 3 \times 10^{-6}$.

7.4.1 Sterile neutrino production and decay mechanisms

In what follows, we first discuss the sterile neutrino production and decay processes triggered by the EFT Wilson coefficients $C^{(5)ij}_{NNB}$ and $C^{(6)\alpha i}_{NX}$, where $X = B, W$. Influenced by the UV model discussed in Section 7.2, here, we assume the relation $C^{(6)\alpha i}_{NW} = 2/(3t_w) C^{(6)\alpha i}_{NB}$ (see Eq. (7.58)). We also comment on the contributions from the active-sterile neutrino mixing, characterized by $V_{\ell N}$.

Hereafter we simplify notation by omitting flavor indices. First, we take $C^{(5)12}_{NNB} \equiv C^{(5)}_{NNB}$ and since $\mathcal{O}^{(5)}_{NNB}$ is an antisymmetric operator, we are implicitly assuming $C^{(5)21}_{NNB} = -C^{(5)12}_{NNB}$. Second, we also omit the lepton flavor α in $C^{(6)\alpha i}_{NX}$, ($C^{(6)\alpha i}_{NX} \equiv C^{(6)}_{N_i X}$), as processes which involve active neutrinos do not reveal which neutrino flavor is participating. These simplifications will also apply to the coefficients in the broken phase.

The coupling $C^{(5)}_{NNB}$ contributes to pair-production of the sterile neutrinos via $pp \to \gamma/Z \to N_1 N_2$, while $C^{(6)}_{N_i X}$ leads to the production of a single N_i through $pp \to \gamma/Z \to N_i \nu$ and $pp \to W^\pm \to N_i \ell^\pm$. Fig. 7.7 shows some example cross sections for fixed values of $C^{(5)}_{NNB}$ (left) and $C^{(6)}_{N_i X}$ (right). For $m_{N_1} + m_{N_2} < m_Z$, pair production through $C^{(5)}_{NNB}$ is dominated by the Z exchange diagram, whereas for larger masses photon exchange dominates. Single sterile neutrino production through $C^{(6)}_{N_i X}$, on the other hand, is dominated by the charged current. The neutral channel is subdominant compared to the charged one in this case because of the suppression between $d_{\nu N_i \gamma}$ and $d_{\nu N_i Z}$ discussed below Eq. (7.59). Note that sterile neutrino production at the LHC through mixing (nonzero $V_{\ell N_i}$) proceeds through charged current events with the same dependence on the mass m_{N_i} as for $C^{(6)}_{N_iX}$. We therefore do not show production via mixing separately in Fig. 7.7 (right).

For sterile neutrino decays, the interaction $C^{(5)}_{NNB}$ induces the two-body decay $N_2 \to N_1\gamma$ and, if N_2 is heavy enough, $N_2 \to N_1 Z$. Note that the lightest N_1 can not decay through $C^{(5)}_{NNB}$. The relevant partial decay widths of N_2, in terms of the broken phase parameters ($d_{NN\gamma}$, d_{NNZ}), defined in Eq. (7.10), are given by

$$\Gamma(N_2 \to N_1\gamma) = \frac{2|d_{NN\gamma}|^2}{\pi} m^3_{N_2}\left(1 - \frac{m^2_{N_1}}{m^2_{N_2}}\right)^3 = \frac{2|d_{NN\gamma}|^2}{\pi} m^3_{N_2}\,(2-\delta)^3\,\delta^3\,, \tag{7.69}$$

$$\Gamma(N_2 \to N_1 Z) = \frac{|d_{NNZ}|^2}{\pi}\, m^3_{N_2}\, f_Z\left(\frac{m_{N_1}}{m_{N_2}}, \frac{m_Z}{m_{N_2}}\right)\, \lambda^{1/2}\left(1, \frac{m^2_{N_1}}{m^2_{N_2}}, \frac{m^2_Z}{m^2_{N_2}}\right), \tag{7.70}$$

with $\delta \equiv 1 - \frac{m_{N_1}}{m_{N_2}}$ denoting the mass splitting between the two sterile states and

$$f_Z(x,y) = \left((1-x)^2 - y^2\right)\left(2(1+x)^2 + y^2\right)\,, \tag{7.71}$$

$$\lambda(x,y,z) = (x-y-z)^2 - 4yz\,. \tag{7.72}$$

We recall that we use the notation $d^{12}_{NN\gamma} \equiv d_{NN\gamma}$ in this section, and because of the antisymmetric nature of the coupling, there is an additional factor of 4 in the decay width of $N_2 \to N_1\gamma$ compared to that of $N_i \to \nu\gamma$ (see Eqs. (7.69) and (7.73)).

The couplings $C^{(6)}_{N_iB}$ and $C^{(6)}_{N_iW}$ generate the decays $N_i \to \nu\gamma$, $N_i \to \nu Z$ and $N_i \to \ell^\pm W^\mp$. While the $\nu\gamma$ final state is always kinematically allowed, final states with Z and W are possible only if m_{N_i} is larger than the gauge boson masses.[5] The relevant partial decay widths, written in terms of the broken phase parameters ($d_{\nu N\gamma}, d_{\nu NZ}, d_{eNW}$), defined in Eqs. (7.11) and (7.14), are given by

$$\Gamma(N_i \to \nu\gamma) \;=\; \frac{|d_{\nu N_i\gamma}|^2}{2\pi} m^3_{N_i}, \tag{7.73}$$

$$\Gamma(N_i \to \nu Z) \;=\; \frac{|d_{\nu N_i Z}|^2}{8\pi} m_{N_i}(2m^2_{N_i} + m^2_Z)\lambda\left(1, 0, \frac{m^2_Z}{m^2_{N_i}}\right), \tag{7.74}$$

$$\Gamma(N_i \to \ell^- W^+) \;=\; \frac{|d_{eN_iW}|^2}{16\pi} m_{N_i}(2m^2_{N_i} + m^2_W)\lambda\left(1, 0, \frac{m^2_W}{m^2_{N_i}}\right), \tag{7.75}$$

where, for simplicity, we have neglected the charged lepton masses. In the computation of the total width of a Majorana N_i, the latter two partial decay widths are multiplied by 2 to account for the Majorana nature of N and the charged conjugated

[5]For m_{N_i} below the weak gauge boson masses, three-body decays through off-shell Z/W occur, but we have checked that these are always subdominant in comparison to the γ channel. Therefore, we safely neglect their contributions in our numerical study.

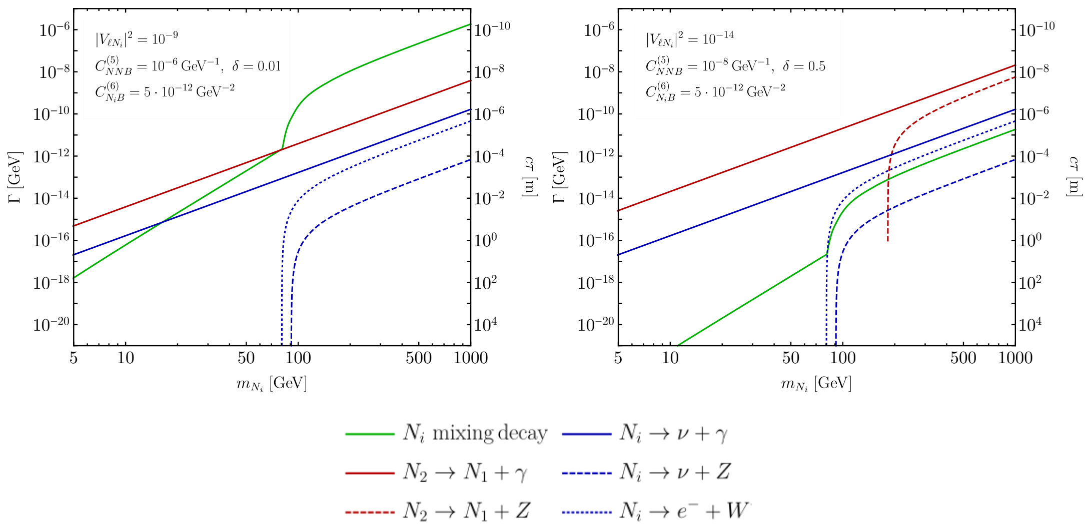

FIGURE 7.8: Partial decay widths of the decay modes induced by neutrino mixing, $C^{(5)}_{NNB}$ and $C^{(6)}_{N_iB}$ ($C^{(6)}_{N_iW} = 2/(3t_w)C^{(6)}_{N_iB}$). We have chosen different benchmark values of the coefficients in each plot, see the corresponding legend.

channel ℓ^+W^-. Sterile neutrinos will also decay via mixing. These decays have been thoroughly studied in the literature. For our numerical analysis, we use the decay width formulas of [121, 122].

In Fig. 7.8 we show the previous partial decay widths as a function of the sterile neutrino masses for various coefficient values. Here, $C^{(6)}_{N_iB}$ and $C^{(6)}_{N_iW}$ are fixed as $C^{(6)}_{N_iB} = 5 \times 10^{-12}$ GeV^{-2} and $C^{(6)}_{N_iW} = 2/(3t_w)C^{(6)}_{N_iB} \approx 6.22 \times 10^{-12}$ GeV^{-2}. These control the decay channels to $\nu\gamma$, νZ, e^-W^+. For comparison, we also show the neutrino mixing partial decay width for two different values of $|V_{\ell N_i}|^2$. In the left (right) plot, we fix $|V_{\ell N_i}|^2 = 10^{-9}$ (10^{-14}), motivated by an inverse seesaw (or naive Type-I seesaw) estimation. Additionally, we show the partial decay width of $N_2 \to N_1\gamma$ and $N_2 \to N_1 Z$ controlled by $C^{(5)}_{NNB}$ and δ. In the left plot, these parameters have been fixed to $C^{(5)}_{NNB} = 10^{-6}$ GeV^{-1} and $\delta = 0.01$, and in the right plot, to $C^{(5)}_{NNB} = 10^{-8}$ GeV^{-1} and $\delta = 0.5$. These values are chosen to illustrate the regimes in which sterile neutrinos ranging from a few GeV to a few hundred GeV could have decay lengths $\mathcal{O}(10^{-2} - 1)$ m, which are interesting for LLP searches. Notice that only the right plot shows a curve for $N_2 \to N_1 Z$, as a large mass splitting is needed for this channel.

From Figs. 7.7 and 7.8 we can compare the relative sizes of $C^{(5)}_{NNB}$, $C^{(6)}_{N_iX}$ and $V_{\ell N_i}$, determining the dominant sterile neutrino production and decay mechanisms. There are nine distinct possibilities, which we define as shown in Fig. 7.9. The scenarios in the same row have the same dominant production mechanism, whereas the scenarios

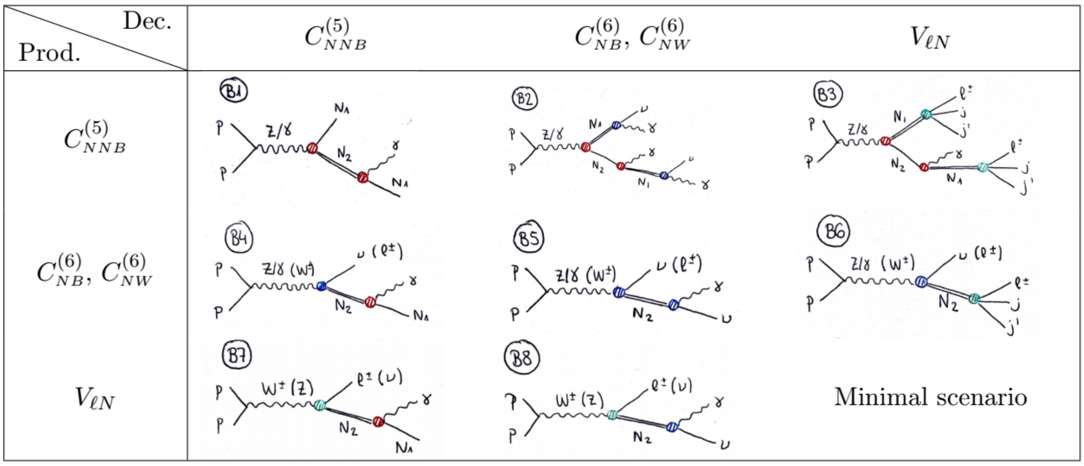

FIGURE 7.9: Nine different process classes: This classification distinguishes scenarios, depending on which couplings dominate N production and decay. The sterile-to-sterile (active-to-sterile) magnetic moment is controlled by $C^{(5)}_{NNB}$ ($C^{(6)}_{NB}$, $C^{(6)}_{NW}$). The active-sterile neutrino mixing is parameterized by $V_{\ell N}$.

in the same column share the same dominant decay mode for the sterile neutrino. In practice, not all combinations will lead to non-pointing photons and we present the features of all these scenarios below.

Scenarios **B1**-**B3** assume that production is controlled by $C^{(5)}_{NNB}$, thus N_2 and N_1 are pair produced. Then:

- **B1**: N_2 will decay to $N_1\gamma$, whereas N_1 escapes undetected. The decay length of N_2 is controlled by $C^{(5)}_{NNB}$ and the mass difference $\delta = 1 - m_{N_1}/m_{N_2}$. N_2 is long-lived if $\delta \ll 1$. Too small δ, however, leads to photons too soft to be tagged. The signal consists of one non-pointing photon plus missing energy.
- **B2**: N_1 will decay to $\nu\gamma$ and for small enough $C^{(6)}_{N_1X}$ this decay is long-lived. N_2 will decay to $N_1\gamma$ either promptly or, if $\delta \ll 1$, with a finite decay length. The signature of this scenario contains up to three photons, either two or three of which are non-pointing. There is also missing energy in the event, from ν and the potential undetected photons.
- **B3**: The mixing parameter $V_{\ell N_1}$ controls the decay of N_1. Again, N_2 will decay to $N_1\gamma$ promptly (or delayed if $\delta \ll 1$). The potential final state signal is a prompt (or non-pointing) photon plus one or two displaced vertices (DV) with charged tracks from the N_1 decays. Unless two displaced vertices and the photon are all found, the event again contains missing energy.

In scenarios **B4**-**B6**, production is controlled by $C^{(6)}_{N_iX}$:

- **B4**: Comparing the production cross sections in Fig. 7.7 to the decay widths in Eqs. (7.69) and (7.73) it becomes quickly clear that this scenario can not be realized, since $C^{(5)}_{NNB}$ large enough to dominate the decay width over $C^{(6)}_{N_iX}$ would also dominate the cross section.
- **B5**: In this scenario $C^{(6)}_{N_iX}$ is assumed to be also dominant in the decay of N_i. Comparing the width (7.73) to the production cross section in Fig. 7.7 (right), it is clear that the decays $N_i \to \nu\gamma$ are too fast to lead to non-pointing photons since there is no kinematic suppression ($\delta \simeq 1$) if $C^{(6)}_{N_iX}$ is large enough to give a sizable cross section. The signal in this case is a prompt lepton accompanied by a prompt photon.
- **B6**: $V_{\ell N_i}$ is assumed to dominate the decay. Given the discussion above for (B5), it is clear that decays will be prompt in this case. There are no photons in the final state, thus no difference in signal to the minimal mixing case.

Finally, for **B7**-**B9** we assume production is dominated by mixing, $V_{\ell N_i}$.

- **B7**: The conditions defining this scenario can be fulfilled only in a narrow range of parameters. The cross section from the dipole and the one from mixing are roughly of the same order for some particular ratio of $C^{(5)}_{NNB}$ to $V_{\ell N_i}$. For this ratio, the width from $C^{(5)}_{NNB}$ will be smaller than the one from mixing for $m_{N_2} >$ 15 GeV, for $\delta = 0.01$. For a smaller ratio (and thus a more dominant production via mixing), the partial width through the dipole can dominate only for smaller values of m_{N_2}. In this narrow parameter range some events with a non-pointing photon would be generated, however, always together with a certain number of displaced vertex events.
- **B8**: The decay caused by $C^{(6)}_{N_iX}$ can easily dominate over the decay via mixing for $m_{N_i} < m_Z$, without $C^{(6)}_{N_iX}$ dominating the cross section. Since a minimum size of $V_{\ell N_i}$ is needed to give a sizable cross section, however, decay lengths will be shorter than in the pure mixing scenario. The signal is a prompt lepton plus a photon (prompt or non-pointing, depending on $C^{(6)}_{N_iX}$).
- **B9**: This scenario is phenomenologically the same as the minimal mixing scenario. It has been discussed extensively in the literature.

Given the discussion above, the most interesting scenarios are **B1**-**B3**. We therefore choose these three scenarios for our numerical simulation, which we detail next.

Scenario	Model parameters		Simulated decay
	Scan	Fixed	
B1	$m_{N_2}, C^{(5)}_{NNB}$	δ	$N_2 \to N_1\gamma$
B2	$m_{N_1}, C^{(6)}_{N_1X}$	$m_{N_2}, C^{(5)}_{NNB}$	$N_2 \to N_1\gamma$ $N_1 \to \nu\gamma$
B3	$m_{N_1}, \lvert V_{eN_1}\rvert^2$	$m_{N_2}, C^{(5)}_{NNB}$	$N_2 \to N_1\gamma$ $N_1 \to ejj$

TABLE 7.2: Parameters entering the numerical simulation in each benchmark. The scan parameters define the two-dimensional space to be surveyed, while the other model parameters remain fixed. The last column indicates the decay channel studied in the simulation.

7.4.2 Simulation Details

In order to determine the sensitivity reach of ATLAS for probing sterile neutrino magnetic moments, we performed a numerical study of the representative chosen benchmarks, using Monte Carlo simulations. We first implemented our model described by Eq. (7.3) (only up to $d = 6$) plus the interactions induced by active-sterile neutrino mixing in `FeynRules` [255, 256]. The generated UFO files [257] were embedded in `MadGraph5` [258], where we generated the collision process $pp \to N_1N_2$ at $\sqrt{s} = 14\,\text{TeV}$, induced by $C^{(5)}_{NNB}$ in the selected benchmarks. We generated 10^5 events at each point of the grid covering the parameter plane $(m_{\text{LLP}}, c_{\text{decay}})$, where the LLP is the sterile neutrino providing the displaced signature at the detector and c_{decay} denotes the interaction dominating the LLP decay width. These two parameters define the two-dimensional space we scan over in our simulation for each benchmark scenario, as shown in the second column of Table 7.2. In the third column, we display the remaining parameters of the model, which are fixed to some numerical value. In scenario B1, we keep the mass splitting δ fixed such that m_{N_1} varies in the scan along with m_{N_2}. Whereas in scenarios B2 and B3 we fix m_{N_2} and $C^{(5)}_{NNB}$, since they do not affect the long-lived nature of N_1.

The sterile neutrino decays are treated separately in `MadSpin` [259]. To ensure numerical stability for small decay widths, the N_i was forced to decay into the final state of interest (shown in the last column of Tab. 7.2) in all simulated events. The decay LHE event files, given as an output by `MadSpin`, were then processed by `Pythia8` [189] to estimate the ATLAS efficiency in detecting the characteristic LLP signature of each benchmark: non-pointing photons in B1 and B2, and displaced vertices in B3. Specific details of each search strategy are outlined below.

Non-pointing photons are emitted in the decay of the long-lived sterile neutrinos.

These decays occur at a secondary vertex, displaced from the collision point or primary vertex (PV), causing the photon direction to point away from the PV. The ATLAS (and CMS) Electromagnetic Calorimeter (ECAL) can detect energetic photons and reconstruct their trajectories precisely. The photon displacement is quantified using the impact parameter (IP), defined as the minimum distance of the photon trajectory to the PV. The IP can be decomposed into its transverse and longitudinal components, d_{XY} and d_Z, which can be obtained with

$$d_{XY} = x_{LLP}\frac{p_Y}{p_T} - y_{LLP}\frac{p_X}{p_T}, \tag{7.76}$$

$$d_Z = \frac{z_{LLP} - (\vec{r}\cdot\vec{p})p_Z/|\vec{p}|^2}{1 - p_Z^2/|\vec{p}|^2}, \tag{7.77}$$

where $\vec{r} = \{x_{LLP}, y_{LLP}, z_{LLP}\}$ is the LLP decay position and $\vec{p} = \{p_X, p_Y, p_Z\}$ is the photon momentum.

In our simulation, we have access to the true decay positions of the sterile neutrinos as well as to the kinematic properties of the outgoing particles. Therefore, we can use the previous equations to compute d_{XY} or d_Z for each photon emitted in the decay of N_i. In practice, measuring d_Z requires knowing the exact location of the PV along the beamline (z-axis). However, this can be challenging in the high-luminosity conditions at the LHC, where multiple collisions occur per bunch crossing, leading to the production of several PVs. Moreover, in our specific case (scenarios B1-B3), sterile neutrinos are produced at the collision point without any accompanying charged particle. This limitation extends, in general, to scenarios where only neutral particles are produced at the origin and they decay far from the PV. Therefore, we can only use the variable d_{XY}, which can be measured with respect to the beamline.

It is worth mentioning that recent works have been performed in this direction. ATLAS, for instance, presented results from a search using non-pointing and delayed photons in [260], and in Refs. [205, 261], the authors have recast it for constraining Higgs decays into sterile neutrinos in the context of dimension-5 operators. However, the search relies on d_Z and the time delay t_γ, which also requires knowing the PV location. We cannot apply this search to our selected benchmarks and accordingly propose an alternative search strategy. Our approach is inspired by an old CMS search [262], which looked for non-pointing photons using instead a trigger on d_{XY}.

In Table 7.3, we summarize the cuts for the non-pointing photon search that we apply in scenarios B1 and B2. The event selection starts by triggering photons satisfying $|p_T^\gamma| > 10$ GeV and $|\eta^\gamma| < 2.47$. Subsequently, we demand the LLP to decay before it reaches the outer layer of the ECAL. This requirement imposes the following cuts on the transverse plane and longitudinal axis: $r_{\rm DV} < 1450$ mm and $|z_{\rm DV}| < 3450$ mm, respectively. Finally, the energetic photons passing the initial selection criteria and originating from one of the DVs are required to have $|d^{\gamma}_{XY}| > 6$ mm. This last cut is expected to reduce SM background significantly [262]. In Figure 3 of this paper, the CMS data indicates that backgrounds decrease exponentially with the transverse impact parameter, with less than one background event remaining after a cut of $6 - 7$ mm. However, since the CMS search used only 2.2 fb^{-1} of statistics, a larger cut will be necessary for the high-luminosity LHC. This adjustment will affect our sensitivity results (see next section), in particular, the upper parts of the sensitivity curves (in the plane coupling vs. mass), as the upper limit is determined by the LLP being too short-lived to leave a measurably displaced photon. Strengthening the cut on $|d^{\gamma}_{XY}|$ to larger minimum values would reduce the sensitivity curves from the top. Predicting the exact value of this cut is challenging due to the predominantly instrumental nature of the background, thus we will restrict ourselves to the original 6 mm cut.

On the other hand, in scenario B3, the LLP candidate decays via the active-sterile neutrino mixing. The dominant decay modes contain charged particles that leave tracks stemming from a displaced vertex (DV). ATLAS and CMS have looked for long-lived sterile neutrinos (in the minimal scenario) using a DV search strategy and have placed bounds on the neutrino mixing parameter [124, 263]. Here, we follow Ref. [264] and use their DV search strategy, which targets a heavy N decaying into ejj. We summarize the main selection cuts of this search in the lower part of Table 7.3. The event selection starts by identifying electrons with $|p^e_T| > 120$ GeV, $|\eta^e| < 2.47$. Then, we select events with a DV lying inside the ATLAS inner tracker detector, which imposes a cut in the transverse and longitudinal positions: 4 mm $< r_{\rm DV} < 300$ mm, $|z_{\rm DV}| < 300$ mm. To reconstruct the DV, at least four displaced charged particle tracks are needed. We require them to have a transverse impact parameter of $|d_0| > 2$ mm.[6] Additionally, one of the displaced tracks must correspond to the energetic electrons passing the initial trigger. A final cut on the invariant mass of the DV ($m_{\rm DV} > 5$ GeV) is applied to remove SM background from B-mesons. Further details can be found in Section III of Ref. [264].

The total number of signal events for the three selected benchmarks is obtained with:

$$N^{\rm B1}_{\rm sig.} = \sigma \cdot \mathcal{L} \cdot \mathcal{B}\left(N_2 \to N_1 \gamma\right) \cdot \epsilon^{\rm B1}_{\rm sel}, \tag{7.78}$$

[6] The approximate transverse impact parameter in this case is defined as $d_0 = r \cdot \Delta\phi$, where r is the transverse distance of the track from the interaction point, and $\Delta\phi$ is the azimuthal angle between the track and the direciton of N_1.

Scenario	Signature	Selection cuts
B1	Non-pointing γ	$\lvert p_T^\gamma \rvert > 10$ GeV , $\lvert \eta^\gamma \rvert < 2.47$ $r_{\mathrm{DV}} < 1450$ mm , $\lvert z_{\mathrm{DV}} \rvert < 3450$ mm $\lvert d_{XY}^\gamma \rvert > 6$ mm
B2	Non-pointing γ ($\times 2$) (+ prompt γ)	
B3	Displaced Vertex ($\times 2$) (+ prompt γ)	$\lvert p_T^e \rvert > 120$ GeV, $\lvert \eta^e \rvert < 2.47$ 4 mm $< r_{\mathrm{DV}} < 300$ mm, $\lvert z_{\mathrm{DV}} \rvert < 300$ mm 4 tracks with $\lvert d_0 \rvert > 2$ mm $m_{\mathrm{DV}} > 5$ GeV

TABLE 7.3: Summary of selection cuts for a non-pointing photon search (B1 and B2) and a displaced vertex search (B3) at the ATLAS detector.

$$N_{\text{sig.}}^{\text{B2}} = \sigma \cdot \mathcal{L} \cdot \mathcal{B}\,(N_2 \to N_1 \gamma) \cdot 2 \cdot \mathcal{B}\,(N_1 \to \nu\gamma) \cdot \epsilon_{\text{sel}}^{\text{B2}}, \tag{7.79}$$

$$N_{\text{sig.}}^{\text{B3}} = \sigma \cdot \mathcal{L} \cdot \mathcal{B}\,(N_2 \to N_1 \gamma) \cdot 2 \cdot \mathcal{B}\,(N_1 \to ejj) \cdot \epsilon_{\text{sel}}^{\text{B3}}, \tag{7.80}$$

where σ in all three formulas is the cross section of the process $pp \to N_1 N_2$ that depends on the sterile neutrino masses and the interaction $C_{NNB}^{(5)}$, and $\mathcal{L}$ corresponds to the total integrated luminosity during the high-luminosity phase, 3 ab^{-1}. The branching ratios $\mathcal{B}$ into the corresponding final states are also a function of the masses and the coupling responsible for the decay in each scenario (see second column in Table 7.2). The factor ϵ_{sel} denotes the efficiency of event selection in ATLAS after applying the cuts in Table 7.3. Notice that there is an additional factor of two in the formula for B2 and B3 since we only require one displaced photon/vertex and there are two N_1 in each event.

We derive the 95% confidence level (C.L.) sensitivity prospects of ATLAS, under the assumption of zero background, by requiring 3 signal events.[7] Exclusion limits can be placed in the corresponding parameter space if no signal events are found at the end of the experiment. However, in case of a discovery, a larger number of events would be necessary to identify the scenario. For instance, looking for a second photon in the non-pointing photon search could distinguish a potential signal event from B1 and B2. In scenario B3, on top of the displaced vertex search, an additional trigger on a prompt photon associated with the event containing the DV would distinguish this scenario from other models, such as the minimal scenario.

[7] As discussed previously, the zero background assumption might be too optimistic for the cut of $\lvert d_{XY}^\gamma \rvert > 6$ mm at the high-luminosity LHC. For this reason, we will also show lines for 10 or 30 events in the sensitivity plots, corresponding to roughly 25 and 225 background events for 95% C.L. sensitivities.

7.5 Results and discussion

Following the methodology described in the previous section, we estimate the experimental sensitivity of ATLAS for probing sterile neutrinos interacting via dipole interactions. We work at the level of N_RSMEFT operators in the unbroken phase and then make the conversion to the broken phase parameters using Eqs. (7.10) and (7.11). Besides, we consider the active-sterile neutrino mixing as an independent parameter and, for simplicity, focus on the mixing of the light sterile neutrino with the electron sector only, i.e. $V_{\ell N_1} = V_{eN_1}$. The scenarios under study are B1-B3 in Fig. 7.9. In these scenarios, sterile neutrinos are pair-produced in proton-proton collisions through the operator $\mathcal{O}^{(5)}_{NNB}$. The difference lies in the interaction dominating the long-lived sterile neutrino decays: $C^{(5)}_{NNB}$, $C^{(6)}_{N_1X}$ ($X = B, W$) or V_{eN_1}.

Fig. 7.10 shows the sensitivity reach of the non-pointing photon search applied to scenario B1 $\left(pp \to N_1 N_2 \to N_1(N_1\gamma)^{\rm LLP}\right)$, in which N_2 is the LLP decaying within the detector. Contours corresponding to 3 (30) signal events are shown as solid (dashed) lines in the $d_{NN\gamma}$ vs m_{N_2} plane, for four mass splittings between the sterile neutrinos: $\delta = 0.1$, $\delta = 0.05$, $\delta = 0.01$ and $\delta = 0.005$. The sensitivity in mass goes beyond $m_{N_2} \simeq 3$ GeV, $m_{N_2} \simeq 5$ GeV, $m_{N_2} \simeq 14$ GeV and $m_{N_2} \simeq 16$ GeV, respectively. Dipole couplings as small as $d_{NN\gamma} \simeq 3 \times 10^{-7}$ (8×10^{-7}) GeV^{-1} can be probed if $\delta = 0.1$ (0.01), improving the current limits from LEP [197] (shown as the grey area) by more than one order of magnitude in the corresponding mass ranges. For $\delta = 0.005$, the sensitivity reaches $d_{NN\gamma} \simeq 2 \times 10^{-6}$ GeV^{-1}. The shape of the curve can be understood in the following way. The lower part of the curve is the long-lived limit, for a given mass and δ, a smaller coupling results in N_2 being too long-lived, escaping the detector without decaying. The upper part represents the opposite situation. A larger coupling value would make the N_2 decay too promptly and the emitted photon would point back to the primary vertex, losing the LLP signature. Moreover, since the production cross section is proportional to $|d_{NN\gamma}|^2$, we quickly lose events as the dipole coefficient becomes smaller. However, we determined that the results are highly sensitive to the p_T^γ cut in this scenario. The smaller the mass splitting, the less energetic the final photons are and for $\delta \lesssim 0.005$ they become too soft to be detected in the ECAL.

We display the results for scenario B2 ($pp \to N_1 N_2(\to N_1\gamma) \to (\nu\gamma + \nu\gamma)^{\rm LLP}\gamma$) in Fig. 7.11 in the $d_{\nu N_1\gamma}$ vs. m_{N_1} plane. In this case, production and decay of the LLP candidate, N_1, are decoupled since they depend on different interactions. We fix $C^{(5)}_{NNB} = 10^{-5}$ GeV^{-1}, corresponding to $d_{NN\gamma} \simeq 8.8 \times 10^{-6}$ GeV^{-1}, to ensure it dominates sterile neutrino production. Two mass values of N_2 are considered: $m_{N_2} = 700$ GeV and $m_{N_2} = 80$ GeV. We recall that the scan parameters are m_{N_1} and $C^{(6)}_{N_1B}$, which

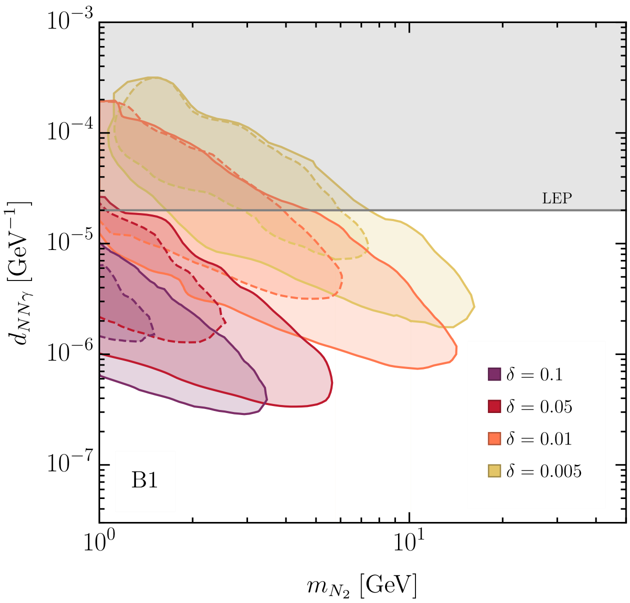

FIGURE 7.10: Sensitivity prospects of the non-pointing photon search at ATLAS ($\sqrt{s} = 14$ TeV, 3 ab^{-1}) for scenario B1 $\left(pp \to N_1 N_2 \to N_1 (N_1\gamma)^{\text{LLP}}\right)$. The 3 (30) signal event contours are shown as solid (dashed) lines in the plane $d_{NN\gamma}$ vs. m_{N_2} for four values of the mass splitting $\delta = 1 - m_{N_1}/m_{N_2}$. The grey area shows the current constraint from LEP [197].

then we convert onto $d_{\nu N_1 \gamma}$ using Eq. (7.11).[8] The solid (dashed) lines again correspond to 3 (30) signal events. Equivalently, the dashed lines correspond to 3 events for $C^{(5)}_{NNB} \approx 3 \times 10^{-6}$ GeV^{-1}. The shape of the curves is similar to that of Fig. 7.10, but the probed parameter space is much larger, precisely because the production and decay mechanisms of N_1 are decoupled. The sensitivity reach in mass is limited by the kinematic threshold $m_{N_1} \lesssim m_{N_2}$, resulting in these vertical lines at $m_{N_1} = 700$ GeV and $m_{N_1} = 80$ GeV. As concerns active-to-sterile magnetic moments, values as small as $d_{\nu N_1 \gamma} \simeq 5 \times 10^{-13}$ (2×10^{-12}) GeV^{-1} can be probed for $m_{N_2} = 700$ (80) GeV. In contrast to the previous scenario, the non-pointing photons are considerably more energetic since they arise in the decay $N_1 \to \nu\gamma$. Consequently, almost all simulated photons pass the corresponding cuts of the non-pointing photon search, giving a large event selection efficiency. Even with a stronger p_T^γ cut, the area enclosed by the sensitivity curves comprises unexplored parameter space. Indeed, current exclusion bounds are much weaker and do not appear in the plot.

For scenario B3 ($pp \to N_1 N_2(\to N_1\gamma) \to (ejj + ejj)^{\text{LLP}}\gamma$), the results of the displaced vertex search are shown in Fig. 7.12. We display the 3 (solid) and 10 (dashed) signal event contours in the $|V_{eN_1}|^2$ vs. m_{N_1} plane. Analogously to B2, production and

[8] The contribution of $d_{\nu N_1 Z}$ and $d_{e N_1 W}$ to the total decay width of N_1 are also taken into account, since we are considering the EFT operators in the unbroken phase.

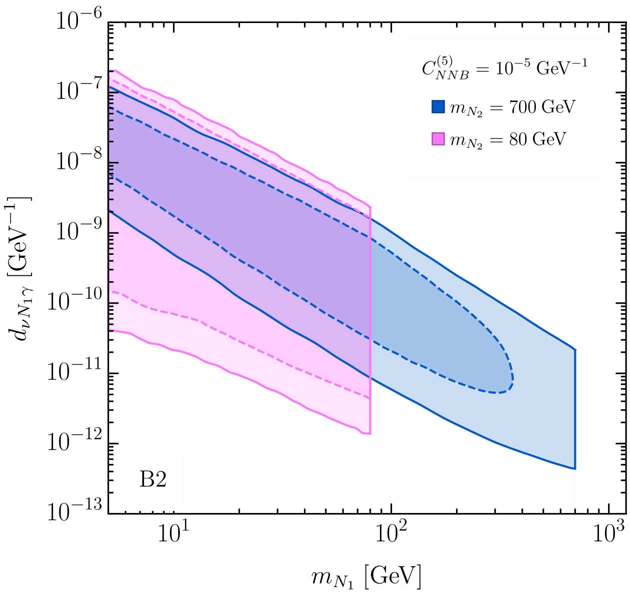

FIGURE 7.11: Sensitivity prospects of the non-pointing photon search at ATLAS ($\sqrt{s} = 14$ TeV, 3 ab^{-1}) for scenario B2: $pp \to N_1 N_2(\to N_1\gamma) \to (\nu\gamma + \nu\gamma)^{\rm LLP}\gamma$. Solid (dashed) lines corresponding to 3 (30) signal events are shown in the $d_{\nu N\gamma}$ vs. m_{N_1} plane for fixed values of m_{N_2} and $C^{(5)}_{NNB}$. The vertical lines in the upper mass reach come from the kinematic threshold ($m_{N_1} < m_{N_2}$). Current exclusion bounds are weaker and are not shown.

decay of N_1 are decoupled. We fix the production coupling ($C^{(5)}_{NNB} = 10^{-5}$ GeV^{-1}) and choose two values for m_{N_2}. For $m_{N_2} = 600$ GeV, the sensitivity extends across 10 orders of magnitude in $|V_{eN_1}|^2$, reaching down to 10^{-17}, and saturates the kinematic threshold of $m_{N_1} \simeq 600$ GeV. The slope of the curve changes around $m_{N_1} \approx m_W$ because the N_1 can decay to on-shell weak bosons via the two-body decays $N_1 \to W^\pm e^\mp$ and $N_1 \to Z\nu$. This increase in the decay width is compensated by smaller values of the mixing parameter. For the chosen parameter values, 30 events are not reached and 10 events are reached only within two isolated regions of the parameter space.

Conversely, for $m_{N_2} = 80$ GeV, 30 signal events can be obtained although we do not show the corresponding curve in the plot. The probed region, in this case, is one order of magnitude larger in $|V_{eN_1}|^2$ than for $m_{N_2} = 600$ GeV, reaching values as small as $|V_{eN_1}| \simeq 10^{-13}$ at $m_{N_1} \simeq 80$ GeV. Present exclusion bounds on the mixing parameter $|V_{eN}|^2$ are weaker in this sterile neutrino mass range and hence are not shown. However, we display the sensitivity prospects of displaced vertex searches by ATLAS and CMS [265, 266, 267], represented with the grey and black lines. Their results are derived in the context of the minimal scenario (only neutrino mixing) and, to be precise, these searches cannot be directly recast into our parameter space as they require prompt leptons at the origin. Nevertheless, we show them for illustrative purposes,

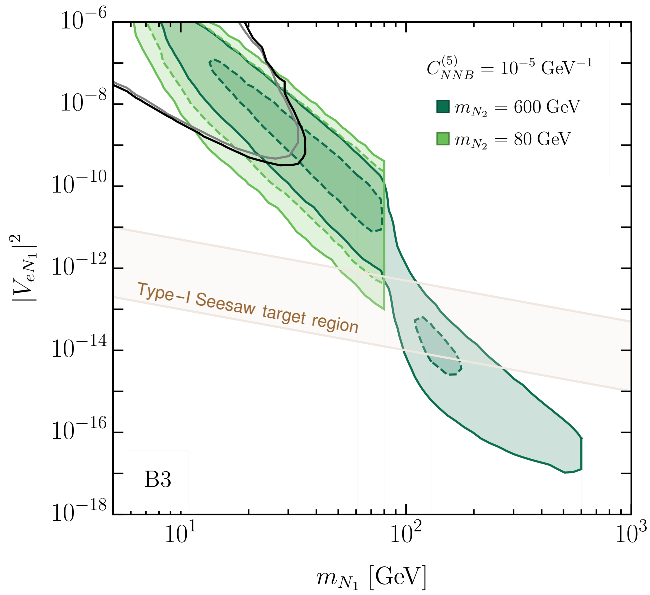

FIGURE 7.12: Sensitivity prospects of the displaced vertex search at ATLAS ($\sqrt{s} = 14$ TeV, 3 ab^{-1}) for scenario B3: $pp \to N_1 N_2 (\to N_1 \gamma) \to (ejj + ejj)^{\rm LLP}\gamma$. Solid (dashed) lines corresponding to 3 (10) events are shown in the $|V_{eN}|^2$ vs. m_{N_1} plane for fixed values of m_{N_2} and $C^{(5)}_{NNB}$. The kinematic threshold ($m_{N_1} < m_{N_2}$) cuts the upper reach in mass with the vertical lines. The black and grey solid lines represent the CMS and ATLAS sensitivity prospects of a DV + prompt lepton search [265, 266, 267].

revealing that much smaller squared mixing values can be explored in the presence of sizable sterile neutrino dipole moments, even accessing the type-I seesaw band.[9]

Finally, we can map the values of the dipole couplings to which experiments are sensitive onto the parameters of the UV-complete model, namely the masses of the singly-charged scalar and vector-like lepton (m_ϕ, m_E) and the Yukawa-type couplings in Eq. (7.15) (f, f', Y_E, h, h'). The sterile-to-sterile and active-to-sterile dipoles are related to these parameters via

$$d^{ij}_{NN\gamma} = \frac{e}{128\pi^2 m_E}\left(h'_i h^*_j - h^*_i h'_j\right), \tag{7.81}$$

$$d^{\alpha i}_{\nu N\gamma} = \frac{ev}{32\sqrt{2}\pi^2 m_E^2} f_{\alpha\beta} Y_E^{\beta *} h'_i \,, \tag{7.82}$$

where we have assumed $m_E = m_\phi$, hence replacing $f(r)\big|_{r\to 1} = \frac{1}{2}$. Since there are products of two or even three couplings entering these equations, we find it convenient to plot the generated magnetic moments as functions of the specific coupling combinations and the vector-like lepton mass.

[9]The type-I seesaw target region in the plot is obtained using the naive type-I seesaw relation and active neutrino masses of 0.05 and 0.001 eV.

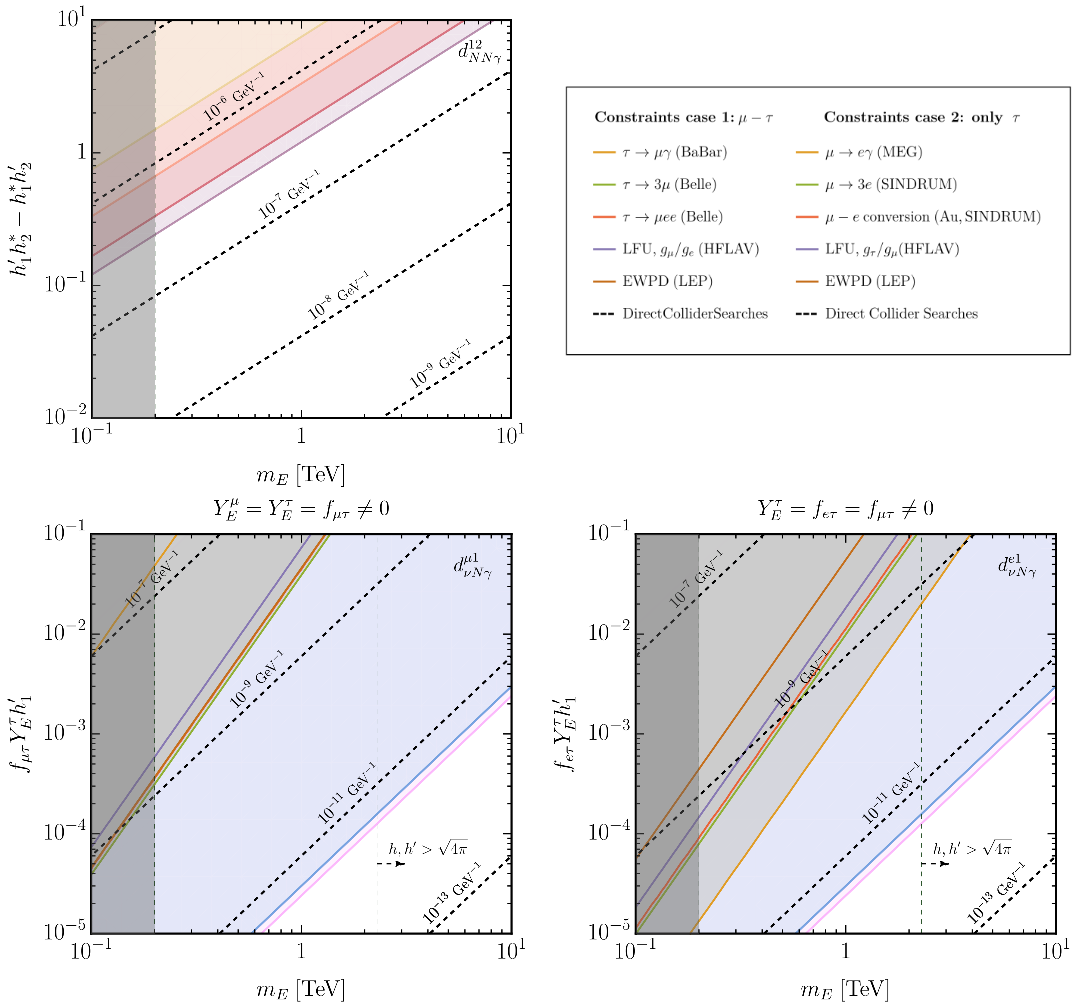

FIGURE 7.13: **Top left panel**: Sterile-to-sterile neutrino magnetic moment as a function of the relevant parameters of the UV model. The colored areas correspond to the probed regions in Fig. 7.10: $\delta = 0.005$ in yellow, $\delta = 0.01$ in orange, $\delta = 0.05$ in red, $\delta = 0.1$ in purple. The grey shaded area is excluded by direct collider searches. **Bottom panels**: Active-to-sterile neutrino magnetic moment as a function of the relevant parameters of the UV model. The pink ($m_{N_2} = 80$ GeV) and blue ($m_{N_2} = 700$ GeV) areas cover the probed dipole values in Fig. 7.11 for $C_{NNB}^{(5)} = 3 \times 10^{-6}$ GeV^{-1}. The parameter space excluded by collider searches and cLFV processes is shown in grey for two flavor scenarios. The legend with the different constraints is displayed in the top right panel.

In the top panel of Fig. 7.13, we show fixed values of $d_{NN\gamma}$ ($d_{NN\gamma}^{12}$) ranging from 10^{-5} to 10^{-9} GeV^{-1} in the plane $(h_1'h_2^* - h_1^*h_2')$ vs. m_E. Additionally, the colored areas correspond to the probed regions in Fig. 7.10, marginalizing the dependence on m_{N_2}. Direct collider searches exclude the low mass region of m_E (see discussion in Section 7.3).

The bottom panels of Fig. 7.13 show active-to-sterile magnetic moments ranging from

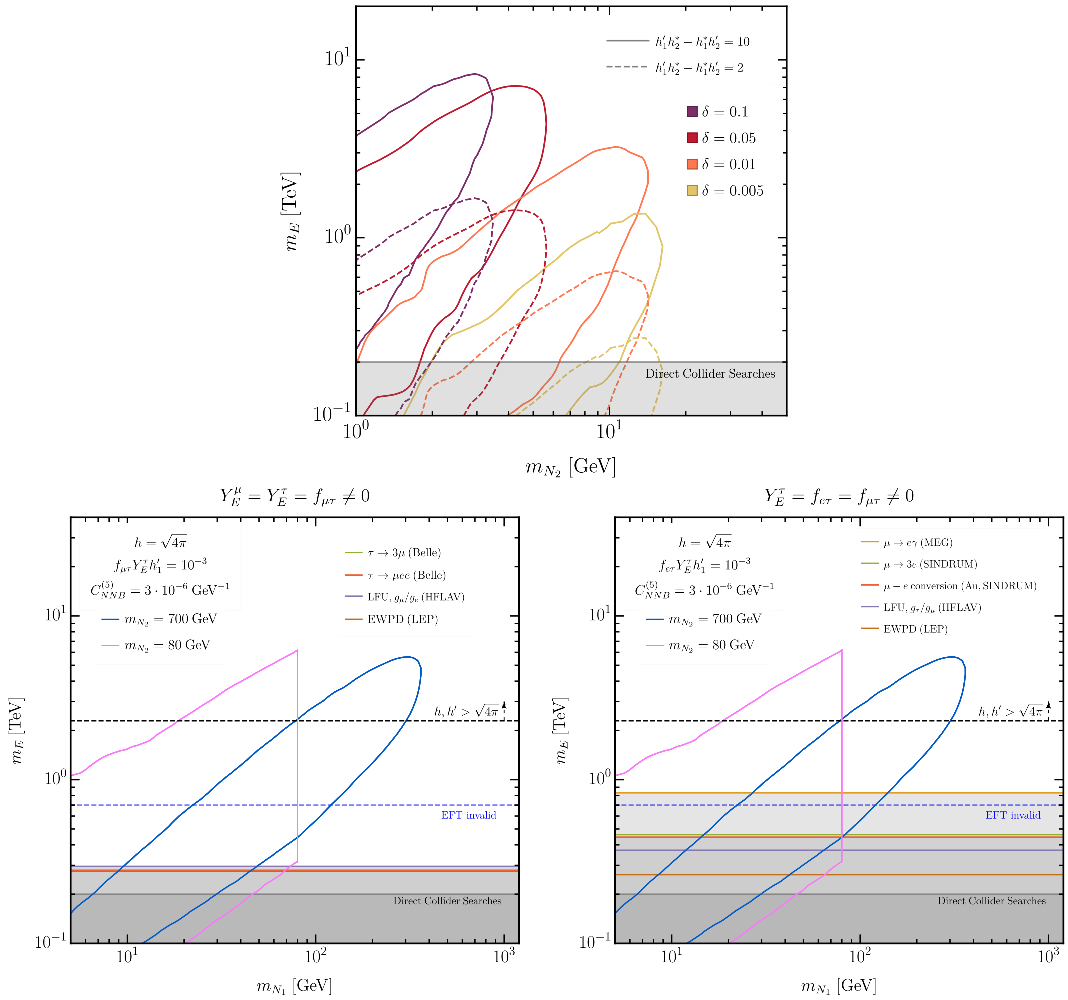

FIGURE 7.14: **Top panel**: Sensitivity projections from Fig. 7.10 in the plane m_E vs. m_{N_2} for fixed coupling values. Direct collider searches exclude the lower grey band. **Bottom panels**: Sensitivity projections from Fig. 7.11 for $C_{NNB}^{(5)} = 3 \times 10^{-6}$ GeV^{-1} in the plane m_E vs. m_{N_1}. The left (right) plot assumes μ–τ (only τ) couplings of the vector-like lepton. Above the grey dashed line we enter the non-perturbative regime of $h, h' > \sqrt{4\pi}$, given the value of $C_{NNB}^{(5)}$. The lower grey regions are excluded by different cLFV processes and EWPD, which depend on the flavor scenario.

10^{-7} to 10^{-13} GeV^{-1} in the plane $(f_{\alpha\beta} Y_E^\beta h'_1)$ vs. m_E for two flavor configurations. The left plot assumes μ-τ couplings for the vector-like lepton ($Y_E^\mu = Y_E^\tau \gg Y_E^e \approx 0$ and $f_{\mu\tau} \neq 0$), while the right plot assumes couplings only to τ ($Y_E^\tau \gg Y_E^{e,\mu} \approx 0$ and $f_{e\tau} = f_{\mu\tau} \neq 0$). In both plots, the pink and blue areas cover the probed regions illustrated in Fig. 7.11 within the 30 event contours assuming $C_{NNB}^{(5)} = 10^{-5}$ GeV^{-1} (equivalent to 3 event contours assuming $C_{NNB}^{(5)} = 3 \times 10^{-6}$ GeV^{-1}), again marginalizing the dependence on m_{N_1}. In addition to the collider constraints, we show bounds from cLFV processes (see discussion in Section 7.3) for the two flavor scenarios considered. Furthermore, as we have fixed $C^{(5)}_{NNB}$, there is an upper limit on m_E above which the couplings of the sterile-to-sterile magnetic moment enter the non-perturbative regime. Masses above the grey dashed line lead to $h, h' > \sqrt{4\pi}$.

Finally, in Fig. 7.14, we display in three different panels the sensitivity projections from Figs. 7.10 and 7.11. These are shown in the planes m_E vs. m_{N_2} for B1 (top panel) and m_E vs. m_{N_1} for B2 (bottom panels). We overlay current constraints from direct collider searches and cLFV processes as before. In the bottom panels, we also show the non-perturbative regime $h, h' > \sqrt{4\pi}$. Additionally, the region corresponding to $m_E < m_{N_2} = 700$ GeV compromises the EFT validity. As can be seen from the top plot of Fig. 7.14, for scenario B1 (where the decay of sterile neutrinos is dominated by the sterile-to-sterile transition magnetic moment) LLP searches can be sensitive to vector-like lepton masses as high as several TeV (depending on the assumed value for the couplings) for sterile neutrino masses less than 10 GeV. However, the cLFV processes do not place additional constraints on this scenario because the couplings entering the cLFV rates are independent of the sterile-to-sterile transition magnetic moment.

In contrast, for scenario B2 (where the decay of sterile neutrinos is dominated by the active-to-sterile transition magnetic moment), the complementarity between LLP searches at the LHC and the constraints from cLFV becomes evident, as can be seen from the bottom two plots of Figs. 7.13 and 7.14. In this scenario, for a lepton flavor universal coupling of the vector-like lepton ($Y_E^e = Y_E^\mu = Y_E^\tau$), the stringent constraints from the current measurements of cLFV processes involving the first two generations of the charged leptons (combined with the perturbativity of Yukawa couplings) exclude the whole model parameter space. On the other hand, for the lepton flavor non-universal case, we have viable parameter space to be explored by LLP searches with non-pointing photons. If the vector-like lepton couples mainly to μ and τ with similar strength (with negligible coupling to the first-generation charged lepton, $Y_E^\mu = Y_E^\tau \approx f_{\mu\tau} \gg Y_E^e \approx 0$) then the viable parameter space of the model in vector-like lepton mass spans between $(0.30 - 2.3)$ TeV, with the lower limit coming from the current constraint from the $\tau \to \mu\gamma$ and the current measurement of LFU from tau decays. The upper limit corresponds to the perturbativity of the Yukawa couplings. If the vector-like lepton couples only to τ (with negligible coupling to the first two generations of charged lepton, $Y_E^\tau \approx f_{e\tau} = f_{\mu\tau} \gg Y_E^{e,\mu} \approx 0$) then the viable parameter space of the model in vector-like lepton mass spans between $(0.8 - 2.3)$ TeV, with the lower limit coming from the current constraints from the cLFV process $\mu \to e\gamma$ and the upper limit from the perturbativity of the Yukawa couplings.

7.6 Summary

In this chapter, we explored LLP searches at the LHC involving non-pointing photons as a novel probe of sterile neutrino transition magnetic moments. We focused on scenarios with two Majorana sterile states with masses in the range of a few GeV up to several hundred GeV, which interact via sizable sterile-to-sterile and active-to-sterile transition magnetic moments, in addition to the usual active-sterile neutrino mixing.

We first identified the relevant operators in the N_RSMEFT and its low-energy counterpart N_RLEFT that can induce neutrino magnetic moments, namely $\mathcal{O}^{(5)}_{NNB}$, $\mathcal{O}^{(6)}_{NB}$ and $\mathcal{O}^{(6)}_{NW}$. As a concrete realization, we then introduced a simplified UV-complete model in which sterile neutrino transition dipole moments are generated radiatively at one-loop. The model, which leads to rich phenomenology, can be constrained by direct collider searches and charged lepton flavor violating processes.

For our phenomenological analysis of sterile neutrino magnetic moments at the LHC, we used the EFT approach, taking into account as well the active-sterile neutrino mixing. We identified nine possible scenarios based on the dominant production and decay modes of the sterile neutrinos, and explored the three physically realizable cases in detail. In these, sterile neutrino production is dominated by the sterile-to-sterile magnetic moment, while decays proceed either through magnetic moments or via active-sterile mixing. Importantly, since there are no associated charged tracks from the primary vertex for the scenarios of interest, we have put forward a search strategy employing the transverse impact parameter of non-pointing photons, which does not rely on the location of the primary vertex.

For these scenarios, we presented sensitivity results from numerical simulations of LLP searches at the high-luminosity LHC. We found that non-pointing photon searches could probe regions of parameter space well beyond current LEP bounds. In particular, sterile-to-sterile magnetic moments down to $\mathcal{O}\left(10^{-7}\right)$ GeV^{-1} could be probed for sub-10 GeV sterile neutrino masses, while active-to-sterile neutrino magnetic moments could be probed to much lower values for sterile neutrino masses $\mathcal{O}(100)$ GeV.

Finally, we applied the EFT results to our simplified model and examined the interplay with cLFV constraints. For sterile-to-sterile transitions, LLP searches are sensitive to vector-like lepton masses of several TeV, while cLFV bounds can be avoided for suitable choices of flavor couplings. In contrast, active-to-sterile transitions are tightly constrained by cLFV searches, especially under flavor-universal assumptions. The complementarity between LHC LLP signatures and low-energy probes thus offers a powerful way to test the flavor structure of such BSM scenarios.

Chapter 8

Long-lived HNLs from four-fermion single-N_R operators

This chapter, based on Ref. [267], studies the phenomenology of HNLs with masses above the GeV scale, which can be directly produced in proton-proton collisions at the LHC. Continuing with the EFT approach of previous chapters, we focus on a subset of dimension-six operators in the N_RSMEFT, specifically, four-fermion operators involving at least one right-handed neutrino. These operators can be classified into two categories: (i) operators with two N_R fields and (ii) operators with a single N_R. The phenomenology of long-lived HNLs arising from pair-N_R operators has been analyzed in Ref. [264]. Here, we turn our attention to the second class.

The motivation for studying single-N_R operators is twofold. First, single-N_R operators typically dominate the HNL decay width in regions of parameter space where they are also responsible for production. In contrast, pair-N_R operators cannot, by themselves, mediate the decay of the lightest HNL, relying on some additional interaction for the decay to occur. Thus, the parameter space that can be explored for these two types of operators is very different. Second, the HNL production through single-N_R operators has an associated prompt lepton, either a neutrino or a charged lepton, while pair operators generally do not yield prompt leptons.[1] This has important consequences for the search strategy and makes a separate analysis necessary. Here, we estimate the ATLAS sensitivity to long-lived HNLs produced via single-N_R operators, using the displaced vertex search strategy proposed in Ref. [266].

[1] An exception arises when the HNL decay length is sufficiently short that the decay products are misidentified as prompt leptons produced directly in the *pp* collisions at the interaction point.

Name	Structure (+ h.c.)	$n_N = 1$	$n_N = 3$
$\mathcal{O}_{duNe}$	$(\overline{d_R}\gamma^\mu u_R)\,(\overline{N_R}\gamma_\mu e_R)$	54	162
$\mathcal{O}_{LNQd}$	$(\overline{L}N_R)\,\epsilon\,(\overline{Q}d_R)$	54	162
$\mathcal{O}_{LdQN}$	$(\overline{L}d_R)\,\epsilon\,(\overline{Q}N_R)$	54	162
$\mathcal{O}_{QuNL}$	$(\overline{Q}u_R)\,(\overline{N_R}L)$	54	162
$\mathcal{O}_{LNLe}$	$(\overline{L}N_R)\,\epsilon\,(\overline{L}e_R)$	54	162

TABLE 8.1: LNC four-fermion single-N_R operators. For each operator structure, we provide the number of independent real parameters for $n_N = 1$ and $n_N = 3$ generations of N_R.

The chapter is organized as follows. Section 8.1 presents the relevant N_RSMEFT operators and briefly discusses how these interactions could arise from ultraviolet completions such as leptoquarks or two Higgs doublet models. Section 8.2 outlines the simulation setup used to model HNL production and decay within the ATLAS detector. In Section 8.3, we present our numerical results and sensitivity estimates for the various single-N_R operators. We conclude with a summary in Section 8.4.

8.1 Theoretical framework: single-N_R operators in N_RSMEFT

8.1.1 HNL production and decay

Within the framework of N_RSMEFT, we focus on the lepton number conserving (LNC) four-fermion interactions containing one N_R and three SM fermions. These interactions appear at $d = 6$ and are described by the effective Lagrangian

$$\mathcal{L} = \mathcal{L}^{(4)} + \frac{1}{\Lambda^2}\sum_i c_{\mathcal{O}_i}\mathcal{O}_i^{(6)}\,, \tag{8.1}$$

where the new physics (NP) scale Λ suppresses their effects. The renormalizable terms in $\mathcal{L}^{(4)}$ include the SM interactions, a mass term for N_R, which can be either Dirac or Majorana (see the discussion below Eq. (4.2) in Chapter 4),[2] and the Yukawa coupling between N_R and the SM doublet. This Yukawa term, after EWSB, induces active-sterile neutrino mixing, typically characterized by $V_{\ell N}$, with $\ell = e, \mu, \tau$.

The complete list of four-fermion operators involving a single N_R is given in Table 8.1. For each operator structure, we indicate the number of independent parameters once flavor indices are taken into account. All operators except for $\mathcal{O}_{LNLe}$ include quark fields and thus can mediate HNL production at hadron colliders. In particular, operators involving first- and second-generation quarks can give rise to sizable production

[2] We will comment on the differences between the Dirac and Majorana cases throughout this chapter.

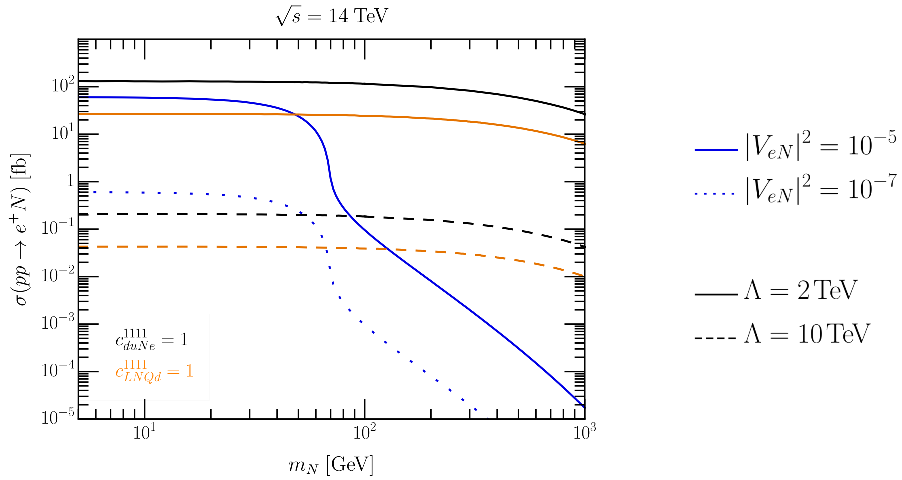

FIGURE 8.1: Cross section of the process $pp \to e^+N$ at the LHC at $\sqrt{s} = 14$ TeV as a function of the HNL mass. We show the contributions from the single-N_R operators $\mathcal{O}_{duNe}$ (black) and $\mathcal{O}_{LNQd}$ (orange) for two values of Λ, as well as the contribution from active-sterile neutrino mixing for $|V_{eN}|^2 = 10^{-5}$ (solid blue) and $|V_{eN}|^2 = 10^{-7}$ (dotted blue).

cross sections at the LHC, especially when compared to the *minimal* scenario, where HNL production is solely due to active-sterile neutrino mixing. These operators contribute, for instance, to the process $pp \to \ell N$, with $\ell = e, \mu, \tau$.

As an illustration, in Fig. 8.1, we show the production cross section for $pp \to e^+N$ at the LHC ($\sqrt{s} = 14$ TeV), mediated by the operators $\mathcal{O}_{duNe}$ and $\mathcal{O}_{LNQd}$. We switch on the flavor combinations c^{1111}_{duNe} and c^{1111}_{LNQd}, where these indices refer to the first-generation quarks, electrons, and the lightest HNL. We consider two benchmark values for the NP scale, $\Lambda = 2, 10$ TeV, and compare the resulting cross sections with those arising from active-sterile neutrino mixing alone, for $|V_{eN}|^2 = 10^{-5}$ and 10^{-7}. Depending on the value of Λ and $|V_{eN}|^2$, either the EFT operator or the mixing can dominate the production rate. However, in different seesaw realizations (e.g. type-I seesaw), the mixing is expected to be smaller than the selected values, making the EFT contribution dominant as long as the NP scale is not too large.

In addition to contributing to HNL production, these single-N_R operators also mediate HNL decays into one lepton and two quarks. The total decay width depends on the operator structure. Neglecting the masses of the lepton and light quarks, the partial decay width for the channel $N \to \ell q q'$ is given by[3]

$$\Gamma(N \to \ell q q') = \frac{c_{\mathcal{O}}^2 m_N^5}{f_{\mathcal{O}} 512\pi^3 \Lambda^4}\,, \tag{8.2}$$

[3]We denote the HNL as N, which can be either Dirac or Majorana, while N_R in the operators refers only to the right-handed component of this field. If the HNL is Majorana, $N = N_R + N_R^c$.

Heavy scalar	Irrep.	Operator	Matching relation
Leptoquark ω_1	$(\mathbf{3}, \mathbf{1}, -1/3)$	$\mathcal{O}_{duNe}$	$\frac{c_{duNe}}{\Lambda^2} = \frac{y^{\omega_1}_{dN} y^{\omega_1}_{ue}}{2m^2_{\omega_1}}$
Leptoquark Π_1	$(\mathbf{3}, \mathbf{2}, 1/6)$	$\mathcal{O}_{LdQN}$	$\frac{c_{LdQN}}{\Lambda^2} = \frac{y^{\Pi_1}_{dL} y^{\Pi_1}_{QN}}{m^2_{\Pi_1}}$
Inert doublet φ	$(\mathbf{1}, \mathbf{2}, 1/2)$	$\mathcal{O}_{LNQd}$	$\frac{c_{LNQd}}{\Lambda^2} = \frac{y^{\varphi}_{LN} y^{\varphi}_{Qd}}{m^2_{\varphi}}$
		$\mathcal{O}_{QuNL}$	$\frac{c_{QuNL}}{\Lambda^2} = \frac{y^{\varphi}_{Qu} y^{\varphi}_{LN}}{m^2_{\varphi}}$

TABLE 8.2: Heavy scalars with their gauge quantum numbers and the four-fermion single-N_R operators they can generate. The last column reports the tree level matching relations between the Wilson coefficients and the couplings of the UV model.

with m_N being the HNL mass, $c_{\mathcal{O}}$ the Wilson coefficient, and $f_{\mathcal{O}}$ a numerical factor specific to the operator: $f_{\mathcal{O}} = 1$ for $\mathcal{O}_{duNe}$; $f_{\mathcal{O}} = 4$ for $\mathcal{O}_{LNQd}$, $\mathcal{O}_{LdQN}$, and $\mathcal{O}_{QuNL}$.

To obtain the total decay width, one must also include the final state with neutrinos ($\nu q q'$), which arises for all operators except $\mathcal{O}_{duNe}$. These channels have the same partial decay widths as the charged lepton modes, thus the total width is two times Eq. (8.2). This result applies for Dirac neutrinos. For Majorana HNLs, the inclusion of the charge-conjugated processes introduces an additional factor of 2. Therefore, for Majorana neutrinos, the full width is four times larger (twice from the neutral mode, twice from charge conjugation), except in the case of $\mathcal{O}_{duNe}$, where the factor is only 2.

8.1.2 Example UV completions

The single-N_R operators of interest can be generated in ultraviolet (UV) complete models containing heavy scalars or vectors. Here, we give a few examples involving scalar leptoquarks and an inert $SU(2)_L$ doublet scalar. For a complete classification of the models generating these operators we refer to Table 5.4 in Chapter 5.[4]

The operator $\mathcal{O}_{duNe}$ can arise from a model with a scalar leptoquark, ω_1, having the gauge quantum numbers of the down quark, cf. Table 8.2. The interaction Lagrangian of ω_1 is given by

$$-\mathcal{L}_{\omega_1} = y^{\omega_1}_{dN} \overline{d_R} N^c_R \omega_1 + y^{\omega_1}_{ue} \overline{u_R} e^c_R \omega_1 + y^{\omega_1}_{QL} \overline{Q} \epsilon L^c \omega_1 + \text{h.c.} \tag{8.3}$$

[4]In this section, we follow the same notation as in Chapter 5 and Appendix A.

Upon integrating out ω_1, the operator $\mathcal{O}_{duNe}$ is generated with the tree level matching condition for the Wilson coefficient c_{duNe} given in the last column of Table 8.2, where, for simplicity, we have assumed the renormalizable couplings to be real and suppressed flavor indices. Analogously, a scalar leptoquark, Π_1, with the quantum numbers of the $SU(2)_L$ quark doublet can lead to $\mathcal{O}_{LdQN}$. The Yukawa interactions of Π_1 read

$$-\mathcal{L}_{\Pi_1} = y^{\Pi_1}_{QN}\overline{Q}N_R\Pi_1 + y^{\Pi_1}_{dL}\overline{d_R}L^T\epsilon\Pi_1 + \text{h.c.} \tag{8.4}$$

We note that the first terms in Eqs. (8.3) and (8.4) also generate the pair-N_R operators $\mathcal{O}_{qN} = (\overline{q}\gamma^\mu q)(\overline{N_R}\gamma_\mu N_R)$, where $q = d_R$ and $q = Q$, respectively, cf. Ref. [264].

The operators $\mathcal{O}_{LNQd}$ and $\mathcal{O}_{QuNL}$, in turn, can originate from a two Higgs doublet model, after the second, heavy doublet, φ, has been integrated out. The interactions of interest in the UV model have the following form

$$-\mathcal{L}_\varphi = y^\varphi_{Qd}\overline{Q}\varphi d_R + y^\varphi_{Qu}\overline{Q}\tilde{\varphi}u_R + y^\varphi_{LN}\overline{N_R}L\varphi + \text{h.c.}, \tag{8.5}$$

where $\tilde{\varphi} = \epsilon\varphi^*$. From Table 8.2, it is clear that the Wilson coefficients of the operators depend on different combinations of independent couplings in the UV model. Therefore, in this example, the generated operators are uncorrelated.

We have implemented these renormalizable models in `FeynRules` [255, 256] for both Dirac and Majorana HNLs. Using the generated UFO [257] model files and `MadGraph5` [268, 258], we have checked that both cases lead to the same single-N_R production cross section.[5] The fact that the HNL nature does not affect the production triggered by the four-fermion single-N_R operators allows us to implement these operators directly in `FeynRules` for Dirac HNLs and use the resulting UFO model file in `MadGraph5`.[6]

8.2 Simulation details

According to the HNL production and decay channels studied in Section 8.1, our signal topology contains a prompt lepton and a displaced vertex (DV) stemming from the HNL decay to leptons and quarks. Our stage to reconstruct such a signature is the ATLAS detector, specifically its inner tracker, as it has the capability to reconstruct vertices displaced from the interaction point (IP) by few millimeters to tens of centimeters. Our analysis strategy builds up on that presented in Ref. [266] and is inspired from ATLAS multi-track displaced searches [269, 270].

[5] We note that the cross section for N_R pair production triggered by the four-fermion operators with two N_R is different for Dirac and Majorana HNLs, especially for values of $m_N \gtrsim 100$ GeV at LHC energies (we refer the interested reader to Sec. 3.1 of Ref. [264]).

[6] `MadGraph5` can not handle Majorana fermions in operators with more than two fermions.

We consider the collision process $pp \to \ell N$ with $\ell = e, \mu, \tau$, at $\sqrt{s} = 14$ TeV at the high-luminosity LHC with an integrated luminosity of 3 ab^{-1}. We generate LHE events with displaced information at the parton level with `MadGraph5`, which are read by `Pythia8` [189] for showering and hadronization. Our detector simulation is based on a custom made code within `Pythia8`, where we first reconstruct isolated prompt electrons, muons, and taus (with help from `FastJet` [271]), taking into account detector acceptance, resolution, and smearing on their transverse momenta (for details, see Ref. [266]).

After selecting events with a prompt lepton, the displaced vertex reconstruction starts by selecting tracks[7] with $p_T > 1$ GeV and a large impact parameter, d_0, defined as $d_0 = r_{\text{trk}} \times \Delta\phi$. Here, $\Delta\phi$ corresponds to the azimuthal angle between the track and the direction of the long-lived HNL, and r_{trk} corresponds to the transverse distance of the track from the origin. We require $|d_0| > 2$ mm.

As we have access in the simulation to truth-level Monte Carlo information, we also identify the truth HNL decay positions in the transverse and longitudinal planes, namely, r_{DV} and z_{DV}, respectively. An additional step (with respect to Ref. [266]) of the vertex reconstruction implemented in this work is the requirement that $r_{\text{trk}} - r_{\text{DV}} < 4$ mm. It is not always the case that the "starting" point of the displaced track matches the displaced vertex position. This is more evident in the case where we have a tau produced from the HNL displaced decay, as taus also have an additional displacement.[8] With this requirement, we emulate what an experimental displaced-vertex reconstruction would do when fitting nearby displaced tracks to a common origin [269]. This will lead to an additional reduction in efficiency when reconstructing displaced vertices containing taus.

After selecting optimal displaced tracks, we demand displaced vertices within the ATLAS inner tracker acceptance, namely, 4 mm $< r_{\text{DV}} <$ 300 mm and $|z_{\text{DV}}| <$ 300 mm. Further cuts are applied on the number of high-quality tracks coming from the DV, N_{trk}, and its invariant mass, m_{DV}, assuming all tracks have the pion mass. Specifically, we require $N_{\text{trk}} > 3$ and $m_{\text{DV}} \geq 5$ GeV. As detailed in Refs. [269, 270, 272], these last two cuts ensure that we are in a region where signal is expected to be found free of backgrounds (including B-mesons). Further detector response to DVs is quantified by applying the 13 TeV ATLAS parameterized efficiencies [270] as a function of m_{DV} and N_{trk}, where we assume these will remain the same at 14 TeV.

[7]A track in our simulation is a final state charged particle. These come from the HNL decays, which can be either an electron, a muon, or a charged particle coming from the hadronization of quarks or from tau decays.

[8]The proper decay distance of tau leptons is $c\tau = 87.1\ \mu$m. This will lead, for example, to decay distances of $\gamma c\tau \sim$ 5mm at 100 GeV.

The total number of signal events at ATLAS is then calculated with

$$N_S^{\text{ATLAS}} = \sigma \cdot \mathcal{L} \cdot \mathcal{B}(N \to \ell jj + \nu jj) \cdot \epsilon \,, \tag{8.6}$$

where the cross section σ is a function of m_N and depends on the Wilson coefficients of the operators. The branching ratio $\mathcal{B}(N \to \ell jj + \nu jj)$ is the sum of both channels with charged and neutral leptons in the final state. The ϵ factor encodes the detector acceptance and the efficiency for reconstructing one displaced vertex in an event (following the selection cuts specified above). This efficiency depends on both the HNL mass and proper lifetime.

Under the zero background assumption, we derive 95% C.L. exclusion limits by requiring three signal events, which we present and discuss next.

8.3 Numerical Results

In this section, we present the experimental sensitivity of our displaced search at the ATLAS detector to a long-lived HNL interacting with the SM via four-fermion single-N_R operators in the N_RSMEFT. Here, we take the coefficients of the operators $c_\mathcal{O}/\Lambda^2$ and the mass of the HNL, m_N, as independent parameters. In this scenario, both the production and the decay of the HNL can be dominated by the same operator $\mathcal{O}$, unlike the case of effective operators with two HNLs [264], where the pair-N_R operators dominantly induce the HNL production, but the decay of the HNL still proceeds only via mixing with the active neutrinos. In our analysis we have assumed that the contributions to the production and decay of the HNL from its mixing with active neutrinos $V_{\ell N}$ are subdominant and negligible compared to the effective operator contributions. For mixing angles smaller than $|V_{\ell N}|^2 \lesssim 10^{-9}$, this assumption is always fulfilled.

The production of the HNLs considered in our analysis, $pp \to \ell N$, is always accompanied by a prompt charged lepton (an electron, muon, or tau, depending on the flavor structure of the effective operator considered). The presence of this charged lepton is important in our analysis as it is used to trigger the signal. The decay of the HNLs will occur via the same operator leading to two jets and one neutral or charged lepton, $N \to \ell(\nu)jj$. The production cross sections of the HNLs will depend on the type of quarks that the respective operator includes. In our analysis, we have only considered effective operators with quarks of the first two generations.

In Fig. 8.2, we show the experimental sensitivity of the ATLAS detector to a long-lived HNL in the Λ vs. m_N plane. In our analysis, we have considered the contributions of one operator at a time, setting the value of the corresponding operator coefficient

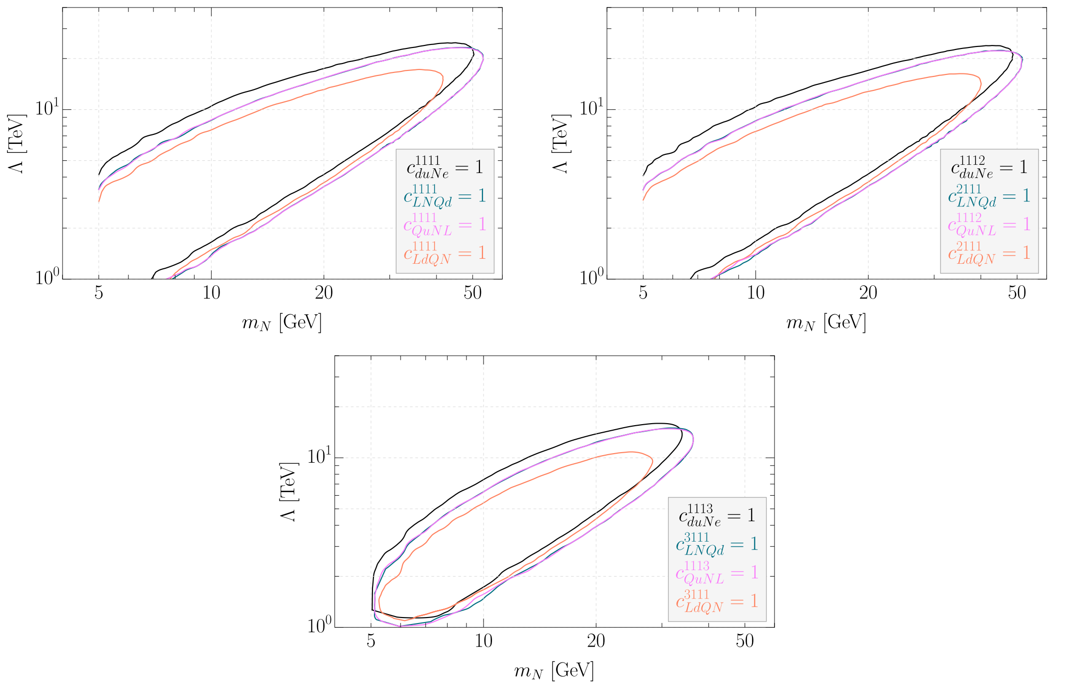

FIGURE 8.2: Exclusion limits on the NP scale Λ as a function of m_N in the EFT scenario with operators including the first-generation quarks only, for an integrated luminosity of 3 ab^{-1}. The top panels consider operators with charged leptons of the first and second generation: electrons (left) and muons (right). The bottom panel considers operators with tau leptons.

$c_{\mathcal{O}} = 1$, and the rest of the operator coefficients to zero. In Fig. 8.2, we have considered only operators with quarks of the first generation. We recall that the numbers in the superscript of e.g. c^{1112}_{duNe} refer to the first-generation quarks (d and u), the lightest N_R and the second-generation charged lepton (the muon). As can be seen in this figure, for an integrated luminosity of 3 ab^{-1}, ATLAS can reach values of the new physics scale up to (and above) $\Lambda \sim 20$ TeV for masses $m_N \gtrsim 50$ GeV in the case of operators with an electron or muon. In the case of operators with a tau lepton, ATLAS can reach $\Lambda \gtrsim 10$ TeV at masses m_N of $\mathcal{O}(10)$ GeV. It is worth mentioning that our limits start at $m_N \gtrsim 5$ GeV. The reason is the kinematic cut at $m_{\rm DV} \geq 5$ GeV imposed in the selection criteria. This cut is necessary to remove the SM background coming from B-mesons. We also note that the projected exclusion limits are rather similar for the four types of single-N_R operators, in particular for $\mathcal{O}_{LNQd}$ and $\mathcal{O}_{QuNL}$.

Fig. 8.3 contains our limits in the plane Λ vs. m_N for the effective operators with quarks of the second generation only. As expected, the sensitivity regions for operators with second-generation quarks are smaller than those corresponding to operators with first-generation quarks (Fig. 8.2). This is due to the predominant content of quarks u and d in the proton versus the quarks c and s. We find that limits shown in

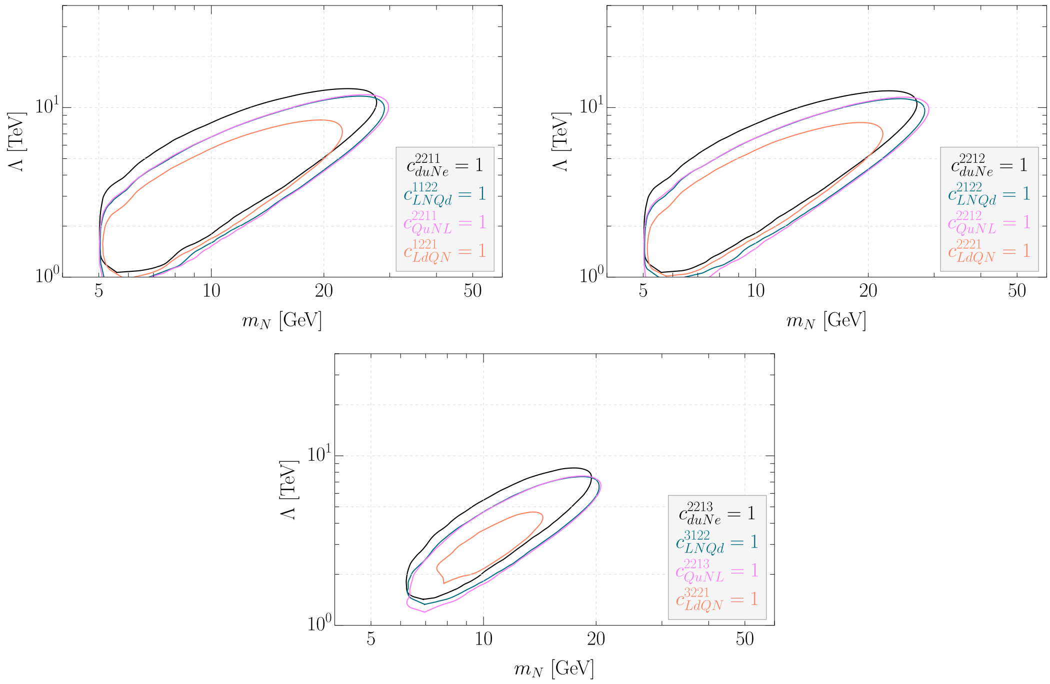

FIGURE 8.3: The same as Fig. 8.2, but for operators with second-generation quarks only.

Fig. 8.3 can reach $\Lambda \sim 13$ TeV for $m_N \sim 23$ GeV in the cases of electrons and muons, and up to $\Lambda \sim 9$ TeV for $m_N \sim 18$ GeV in the case of taus. All numbers assume an integrated luminosity of 3 ab^{-1}. Other possible combinations of quark flavors for the N_RSMEFT include (u, s) and (c, d). The sensitivity reaches for these operators lie between the two cases shown in Figs. 8.2 and 8.3 (for (u, d) and (c, s)). We therefore do not show results for these cases explicitly. Operators with third-generation quarks have not been considered in this work, since they require special treatment. We discuss them in Chapter 9.

We also note that Figs. 8.2 and 8.3 have been calculated for Dirac HNLs. As mentioned above, production cross sections for single-N_R operators are the same for Dirac and Majorana HNLs, while the half-lives for Majorana HNLs are smaller by a factor of two. The sensitivity regions for Majorana HNLs therefore differ slightly from the regions shown in the figures. We do not repeat the plots for the Majorana case and instead opt for a short explanation of the differences. First, the maximal value of the HNL mass, to which this kind of search is sensitive is determined by the smallest decay length that is accessible in the experiment. Since the decay width scales as m_N^5, for a Majorana HNL the largest mass accessible is a factor $(1/2)^{1/5} \simeq 0.87$ smaller than in the Dirac case. Second, the maximal value of Λ reached in our sensitivity curves is essentially determined by the total cross section (times luminosity). Since cross sections are the same for Dirac and Majorana HNLs, this maximal value of Λ does not change for Majorana HNLs. Finally, in the regime where the decay lengths are large (i.e. for large values of Λ at values of m_N smaller than the one where the maximal value of Λ is reached), the event number depends linearly on the half-life, while both the cross section and the decay width scale as Λ^{-4}. For Majorana HNLs, in this part of the parameter space, slightly larger values of Λ are accessible than for the Dirac case, i.e. an increase by roughly a factor $2^{1/8} \simeq 1.09$.

Let us briefly comment on existing limits. First of all, our choice of switching "on" always only one Wilson coefficient at a time guarantees that there is no new source of lepton (or quark) flavor violation. It is well known that UV completions, such as the leptoquark models we discussed, are strongly constrained by searches for lepton flavor violating processes. These will put lower bounds on $m_{LQ} \simeq \Lambda$ that are much stronger than anything achievable in direct searches [273, 2]. Thus, *in all accelerator searches* it is customary to assume that new resonances, such as leptoquarks, couple only to one SM fermion generation at a time. Direct searches for leptoquarks from pair and single leptoquark production have been performed by both, CMS [274, 275, 276] and ATLAS [277, 278]. The best limits approach now $m_{LQ} \simeq 2$ TeV. Thus, the long-lived particle search discussed here will probe so-far uncharted parts of parameter space. Let us also mention that, since $d = 6$ operators have Wilson coefficients of the form $c_{\mathcal{O}}/\Lambda^2$, limits on Λ will scale proportional to $\sqrt{c_{\mathcal{O}}}$. Thus for $c_{\mathcal{O}} \lesssim 10^{-2}$ our search will no longer probe values of Λ not already excluded by direct LHC searches.

We will close this discussion with one additional comment. Our simulated analysis focused on the ATLAS detector and its reconstruction capabilities to displaced vertices inside the inner tracker, starting from 4 mm in multi-track searches [269, 270]. Relaxing this requirement to decay distances below 4 mm (both in d_0, r_{DV} and z_{DV}) will allow to extend the reach in parameter space towards larger HNL masses. Of course, with the loosening of these cuts we may depart from the zero background case assumption, and a detailed study on the multi-track search backgrounds would be needed, which goes beyond the scope of the present work. Nevertheless, past displaced lepton searches — whose tracks are fitted to a common vertex — at CMS [279] could probe transverse decay lengths starting from $\approx 200\ \mu$m.[9] In addition, a recent 13 TeV CMS search [280] demonstrates that lepton tracks with $|d_0| > 0.1$ mm are displaced enough to be considered for analysis.

Finally, the recent CMS note on an HNL search with an explicit displaced vertex requirement does not even demand a constraint on the DV minimal distance [281]. This

[9]The explicit analysis requirement in Ref. [279] demands tracks to have a transverse impact parameter significance with respect to the primary vertex of $|d_0|/\sigma_d > 12$, where σ_d is the uncertainty on $|d_0|$.

provides feasibility to experimentally go below the 4 mm threshold. We stress that an improvement of the DV search towards smaller decay lengths by such a larger factor (up to 40 for 0.1 mm) would allow to test HNL masses larger by a factor 2 with respect to the values in our figures, i.e. extend the searches from $m_N \simeq 50$ GeV to roughly 100 GeV. We hope that this large potential gain motivates the experimental collaborations to study the lowering of the transverse cuts in displaced vertex searches to the sub-millimeter range.

8.4 Summary

In this chapter, we have focused on lepton number conserving (LNC) four-fermion single-N_R operators associated with a charged lepton and two quarks, which can induce both production and decay of the HNLs simultaneously. For HNLs of $\mathcal{O}(10)$ GeV mass, such operators with a NP scale above ~ 1 TeV can easily make the HNLs become long-lived, leading to displaced vertices at the LHC. We have therefore proposed a displaced vertex search strategy based on a prompt lepton trigger and selection of high-quality displaced tracks. By performing Monte Carlo simulations with `MadGraph5` and `Pythia8`, we have estimated the sensitivity reaches for ATLAS in the high-luminosity LHC era with 3 ab^{-1} integrated luminosity, to four single-N_R EFT operators: $\mathcal{O}_{duNe}$, $\mathcal{O}_{LNQd}$, $\mathcal{O}_{LdQN}$, and $\mathcal{O}_{QuNL}$.

Multiple combinations of quark and lepton flavors can be studied. Here, we have considered mainly two combinations: (u, d) and (c, s). The first (second)-generation-quark only flavor combination is then projected to have the best (worst) sensitivities, because of their portion in the proton content. For both quark combinations, we also studied all possible lepton generations, i.e. electron, muon and tau. In addition, for simplicity, we did not take into account the effect of the active-sterile neutrino mixing, which is supposed to be negligible if the type-I seesaw relation is assumed. For the (u, d) and (c, s) combinations, we find in general for the considered single-N_R operators, ATLAS can probe Λ up to 20 TeV and above for $m_N \gtrsim 20$ GeV, if we switch on one operator at a time.

In summary, we conclude that a displaced vertex search at ATLAS for HNLs can probe new physics scales up to about 20 TeV and, in some cases above, for HNL mass between about 5 GeV and 50 GeV, depending on the quark and lepton flavors associated with the single-N_R operator under consideration.

Chapter 9

Heavy neutral leptons and top quarks in EFT

HNLs interacting with top quarks via effective operators represent a novel and relatively unexplored direction for probing BSM physics. This possibility is especially compelling given the large top quark production rate at the LHC. One of the few studies in this direction is Ref. [282], which considers non-standard top decays into collider-stable (nearly massless) HNLs. However, in the case of stable HNLs, the resulting final states of the top quark decays closely resemble those of the SM, leading to large backgrounds and weak projected bounds. Specifically, that study finds only a mild limit on the new physics (NP) scale, $\Lambda \gtrsim 0.33$ TeV for an integrated luminosity of $\mathcal{L} = 3$ ab^{-1}. More recently, Ref. [283] discussed production and decay rates of long-lived SM singlets, including HNLs, via four-fermion top quark operators. However, no detector simulations were performed therein.

In this chapter, based on Ref. [284], we try to cover this gap and explore the LHC sensitivity to long-lived HNLs produced either in association with a top quark or from top decays, in the N_RSMEFT framework. Depending on the operator type, the HNL can be produced and decay via the same effective interaction or, alternatively, decay only through active-sterile neutrino mixing. We focus on scenarios where the HNL decays with a measurable displacement, either in the main LHC detectors or in proposed far detectors such as MATHUSLA and ANUBIS, which allows to significantly suppress SM backgrounds. This results in a substantial improvement in sensitivity to NP scales.[1]

[1] While our focus is on direct LHC sensitivities, it would also be worthwhile to investigate indirect bounds on these top-N_R operators, similarly to recent studies for top operators in the SMEFT [285].

The chapter is organized as follows. In Section 9.1, we define the dimension-6 operators under study and discuss the associated production and decay channels of the HNL. Section 9.2 describes the numerical simulations used for ATLAS and the far detectors. In Section 9.3, we present and discuss the projected sensitivities. We conclude in Section 9.4.

9.1 Effective operators and benchmark scenarios

We consider a scenario where heavy new states at a scale $\Lambda \gg v$ mediate interactions between N_R and the top quark. At low energies, these interactions are captured by higher-dimensional operators involving N_R and t, as discussed, e.g., in Ref. [282]. We restrict ourselves to $d = 6$ operators. In addition, at $d = 4$, we include the standard Yukawa coupling between N_R, the SM lepton doublet, and the Higgs, leading (after electroweak symmetry breaking) to active-sterile neutrino mixing $V_{\ell N}$, treated here as a free parameter. Note that, without specifying the nature of the HNL, it is not possible to relate $V_{\ell N}$ (or, equivalently, the Yukawa coupling) to the active neutrino masses. The HNL may be of Dirac or Majorana type. Our main results will be shown for a Dirac HNL, with brief comments on the Majorana case near the end of Section 9.3.

We focus on lepton and baryon number conserving four-fermion operators involving N_R, the top quark, and first-generation leptons and quarks. For simplicity, second-generation quark indices are not considered; including them would not significantly affect the production cross sections, as previously noted in Chapter 8. The relevant operators fall into two categories: those involving a pair of N_R fields, and those involving a single N_R. These are listed in Table 9.1. Therefore, this work extends the analysis of the operator sets studied in Refs. [264] and [267] (see Chapter 8) to include operators involving third-generation quarks, which were not considered previously.

Note that, among the single-N_R operators, $\mathcal{O}^{i3}_{LdQN}$ and $\mathcal{O}^{3i}_{LNQd}$ share the same field content but differ in Lorentz structure. They are related via

$$\begin{aligned}
\mathcal{O}^{i3}_{LdQN} &= \left(\overline{L}d_{iR}\right)\epsilon\left(\overline{Q_3}^T N_R\right) = \left(\overline{\nu_L}d_{iR}\right)\left(\overline{b_L}N_R\right) - \left(\overline{e_L}d_{iR}\right)\left(\overline{t_L}N_R\right) \\
&= -\frac{1}{2}\mathcal{O}^{3i}_{LNQd} - \frac{1}{8}\left[\left(\overline{\nu_L}\sigma^{\mu\nu}N_R\right)\left(\overline{b_L}\sigma_{\mu\nu}d_{iR}\right) - \left(\overline{e_L}\sigma^{\mu\nu}N_R\right)\left(\overline{t_L}\sigma_{\mu\nu}d_{iR}\right)\right] .
\end{aligned}$$

In the remainder of this section, we discuss the novel HNL production modes involving a top quark for each operator structure in Table 9.1, as well as the new decay channels triggered by the single-N_R operators. Finally, we define four representative benchmark scenarios featuring long-lived HNLs for our numerical analysis.

	Name	Structure (+ h.c. when needed)
Pair-N_R	$\mathcal{O}^{13}_{uN}$	$\boldsymbol{(\overline{u_R}\gamma^\mu t_R)\,(\overline{N_R}\gamma_\mu N_R)}$
	$\mathcal{O}^{33}_{uN}$	$(\overline{t_R}\gamma^\mu t_R)\,(\overline{N_R}\gamma_\mu N_R)$
	$\mathcal{O}^{13}_{QN}$	$(\overline{Q_1}\gamma^\mu Q_3)\,(\overline{N_R}\gamma_\mu N_R) = \boldsymbol{(\overline{u_L}\gamma^\mu t_L)\,(\overline{N_R}\gamma_\mu N_R)} + (\overline{d_L}\gamma^\mu b_L)\,(\overline{N_R}\gamma_\mu N_R)$
	$\mathcal{O}^{33}_{QN}$	$(\overline{Q_3}\gamma^\mu Q_3)\,(\overline{N_R}\gamma_\mu N_R) = (\overline{t_L}\gamma^\mu t_L)\,(\overline{N_R}\gamma_\mu N_R) + (\overline{b_L}\gamma^\mu b_L)\,(\overline{N_R}\gamma_\mu N_R)$
Single-N_R	$\mathcal{O}^{13}_{duNe}$	$\boldsymbol{(\overline{d_R}\gamma^\mu t_R)\,(\overline{N_R}\gamma_\mu e_R)}$
	$\mathcal{O}^{33}_{duNe}$	$\boldsymbol{(\overline{b_R}\gamma^\mu t_R)\,(\overline{N_R}\gamma_\mu e_R)}$
	$\mathcal{O}^{31}_{LNQd}$	$(\overline{L}N_R)\,\epsilon\left(\overline{Q_3}^T d_R\right) = (\overline{\nu_L}N_R)\,(\overline{b_L}d_R) - \boldsymbol{(\overline{e_L}N_R)\,(\overline{t_L}d_R)}$
	$\mathcal{O}^{33}_{LNQd}$	$(\overline{L}N_R)\,\epsilon\left(\overline{Q_3}^T b_R\right) = (\overline{\nu_L}N_R)\,(\overline{b_L}b_R) - \boldsymbol{(\overline{e_L}N_R)\,(\overline{t_L}b_R)}$
	$\mathcal{O}^{13}_{LdQN}$	$(\overline{L}d_R)\,\epsilon\left(\overline{Q_3}^T N_R\right) = (\overline{\nu_L}d_R)\,(\overline{b_L}N_R) - \boldsymbol{(\overline{e_L}d_R)\,(\overline{t_L}N_R)}$
	$\mathcal{O}^{33}_{LdQN}$	$(\overline{L}b_R)\,\epsilon\left(\overline{Q_3}^T N_R\right) = (\overline{\nu_L}b_R)\,(\overline{b_L}N_R) - \boldsymbol{(\overline{e_L}b_R)\,(\overline{t_L}N_R)}$
	$\mathcal{O}^{13}_{QuNL}$	$(\overline{Q_1}t_R)\,(\overline{N_R}L) = \boldsymbol{(\overline{u_L}t_R)\,(\overline{N_R}\nu_L)} + \boldsymbol{(\overline{d_L}t_R)\,(\overline{N_R}e_L)}$
	$\mathcal{O}^{31}_{QuNL}$	$(\overline{Q_3}u_R)\,(\overline{N_R}L) = \boldsymbol{(\overline{t_L}u_R)\,(\overline{N_R}\nu_L)} + (\overline{b_L}u_R)\,(\overline{N_R}e_L)$
	$\mathcal{O}^{33}_{QuNL}$	$(\overline{Q_3}t_R)\,(\overline{N_R}L) = (\overline{t_L}t_R)\,(\overline{N_R}\nu_L) + \boldsymbol{(\overline{b_L}t_R)\,(\overline{N_R}e_L)}$

TABLE 9.1: Four-fermion pair-N_R and single-N_R operators with the top quark. The indices label the quark generations. We focus on the first and third quark generations. The terms in boldface are relevant for the HNL production and/or decay associated with one top quark.

9.1.1 HNL production

Pair-N_R operators. The interactions $\mathcal{O}^{13}_{uN}$ and $\mathcal{O}^{13}_{QN}$ induce the flavor violating rare top decay $t \to uN\bar{N}$. The corresponding decay width is given by [282] [2]

$$\Gamma(t \to uN\bar{N}) = \frac{m_t^5 g(x)}{1536\pi^3\Lambda^4}\left[\left(c^{13}_{uN}\right)^2 + \left(c^{13}_{QN}\right)^2\right], \tag{9.1}$$

where

$$\begin{aligned} g(x) &= \left(1 - 14x - 2x^2 - 12x^3\right)\sqrt{1-4x} \\ &\quad - 12x^2\left(1 - x^2\right)\left[\ln\frac{1-\sqrt{1-4x}}{1+\sqrt{1-4x}} - \ln\frac{1+\sqrt{1-4x}-2x}{2x}\right], \end{aligned} \tag{9.2}$$

and $x = m_N^2/m_t^2$. At the same time, these operators mediate the direct production of an $N\bar{N}$-pair in association with a top quark (as well as with a bottom quark for $\mathcal{O}^{13}_{QN}$) in pp collisions at the LHC, through the diagrams shown in Fig. 9.1.

[2] In Ref. [282], m_N is assumed to be negligibly small. In what follows, we keep track of it, since we are interested in a broad range of HNL masses.

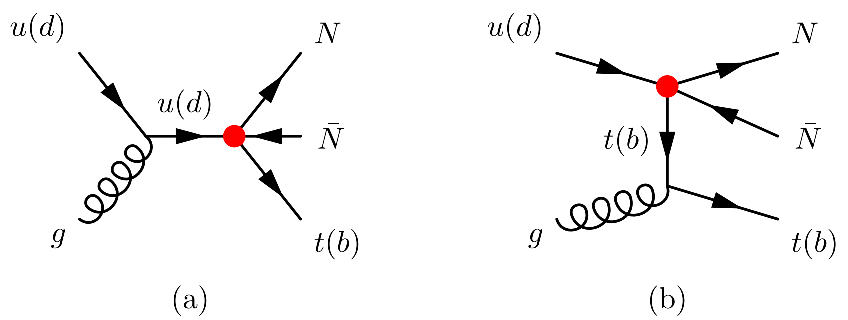

FIGURE 9.1: Production of an $N\bar{N}$-pair in association with a t quark (t or b quark) through $\mathcal{O}_{uN}^{13}$ ($\mathcal{O}_{QN}^{13}$) denoted by the red blob. The diagrams with the particles in parentheses are present for $\mathcal{O}_{QN}^{13}$, but not for $\mathcal{O}_{uN}^{13}$.

At the LHC, top quarks are dominantly produced in pairs through the strong interaction. The inclusive cross section of $t\bar{t}$ production at the LHC with $\sqrt{s} = 13$ TeV is $\sigma_{t\bar{t}} = 830 \pm 38$ pb [286]. The single-top production through the weak interaction has a smaller cross section: $\sigma_{tq+\bar{t}q} = 221 \pm 13$ pb at $\sqrt{s} = 13$ TeV [287]. In what follows, when considering the SM production of the top quark, we will focus on the top quark pair production.

To give an example of the relative importance of the two HNL production mechanisms introduced above, we simulate with `MadGraph5` [268, 258] (i) $pp \to t\bar{t}$ with a subsequent rare top decay $t \to uN\bar{N}$, (ii) $pp \to tN\bar{N}$, and (iii) $pp \to \bar{t}N\bar{N}$ induced by the operator $\mathcal{O}_{uN}^{13}$. The resulting cross sections obtained for $\Lambda = 1$ TeV and $\sqrt{s} = 14$ TeV are shown in the upper-left panel of Fig. 9.2. The individual production modes are identified by labels in the plots. We observe that $\sigma(pp \to tN\bar{N})$ and $\sigma(pp \to \bar{t}N\bar{N})$ dominate over $\sigma(pp \to t\bar{t})[\mathcal{B}(t \to uN\bar{N}) + \mathcal{B}(\bar{t} \to \bar{u}N\bar{N})]$ in the whole HNL mass range of interest, where $\mathcal{B}$ denotes decay branching ratio.[3] The main difference between the shape of the cross sections for these two production modes is the behavior at larger m_N values. The contribution from top decays is highly suppressed when m_N approaches $m_t/2$, whereas in direct pp collisions the cross section remains relatively flat up to a few hundreds of GeV. The difference in the cross sections for $pp \to tN\bar{N}$ and $pp \to \bar{t}N\bar{N}$ is due to the larger parton distribution function (PDF) of the u quark compared to that of $\bar{u}$ inside the proton. We note that the production cross sections for the states $tN\bar{N}/\bar{t}N\bar{N}$ from the operator $\mathcal{O}_{QN}^{13}$ are identical to the ones shown for $\mathcal{O}_{uN}^{13}$. We therefore do not show plots for this case.

[3]We generate events at leading order and multiply only the $t\bar{t}$ production cross section by a flat factor of $k \sim 1.7$ corresponding to the cross section determined at NNLO+NNLL by the `Top++2.0` program [288]. We do not introduce correction factors for the HNL production rate in direct pp collisions.

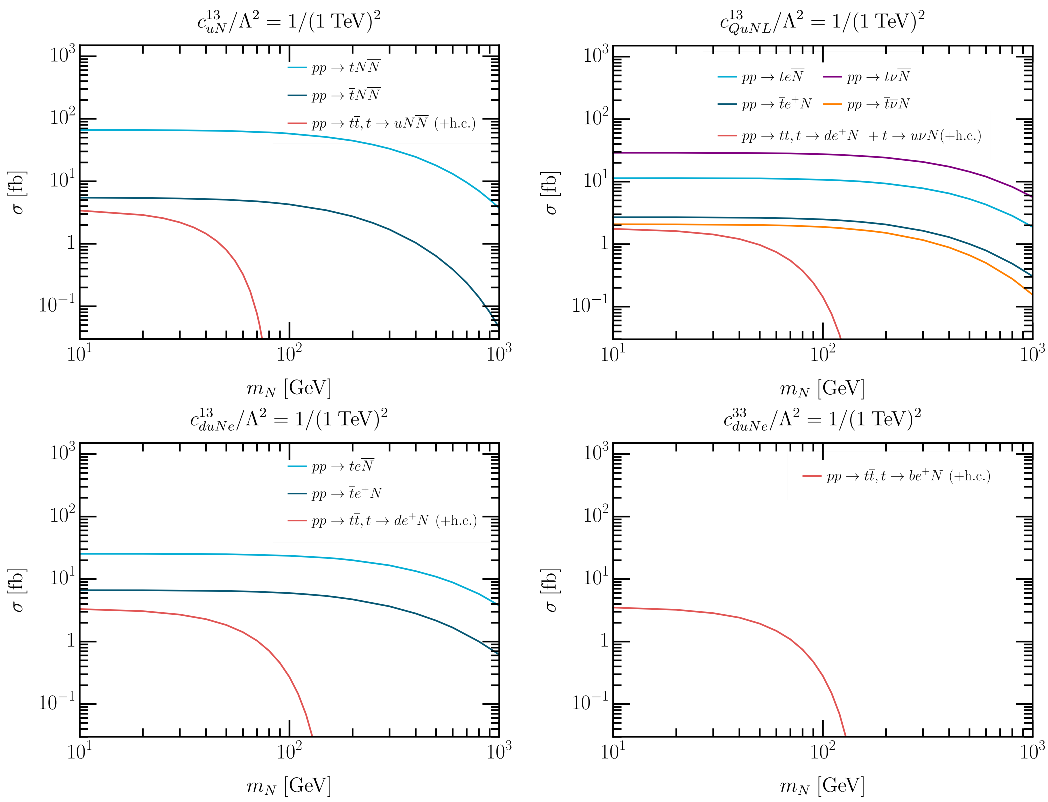

FIGURE 9.2: HNL production cross sections induced by the operators $\mathcal{O}_{uN}^{13}$ (top left), $\mathcal{O}_{QuNL}^{13}$ (top right), $\mathcal{O}_{duNe}^{13}$ (bottom left), $\mathcal{O}_{duNe}^{33}$ (bottom right), for $c_{\mathcal{O}}^{ij} = 1$ and $\Lambda = 1$ TeV at the LHC with $\sqrt{s} = 14$ TeV.

The operators $\mathcal{O}_{uN}^{33}$ and $\mathcal{O}_{QN}^{33}$ neither trigger a top decay, nor do they contribute to the direct HNL production in pp collisions. Therefore, we will not consider them in what follows.

Single-N_R operators. The operators with off-diagonal quark-flavor indices, *viz.* 13 and 31, trigger the flavor-violating decays $t \to de^+N$ and $t \to u\bar{\nu}N/u\nu\bar{N}$with the following widths [282]

$$\Gamma(t \to de^+N) = \frac{m_t^5 f(x)}{6144\pi^3\Lambda^4}\Big[4\left(c_{duNe}^{13}\right)^2 + \left(c_{QuNL}^{13}\right)^2 \\ + \left(c_{LNQd}^{31}\right)^2 + \left(c_{LdQN}^{13}\right)^2 - c_{LNQd}^{31}c_{LdQN}^{13}\Big], \tag{9.3}$$

$$\Gamma(t \to u\bar{\nu}N) = \frac{m_t^5 f(x)}{6144\pi^3\Lambda^4}\left(c_{QuNL}^{13}\right)^2 \quad \text{and} \quad \Gamma(t \to u\nu\bar{N}) = \frac{m_t^5 f(x)}{6144\pi^3\Lambda^4}\left(c_{QuNL}^{31}\right)^2, \tag{9.4}$$

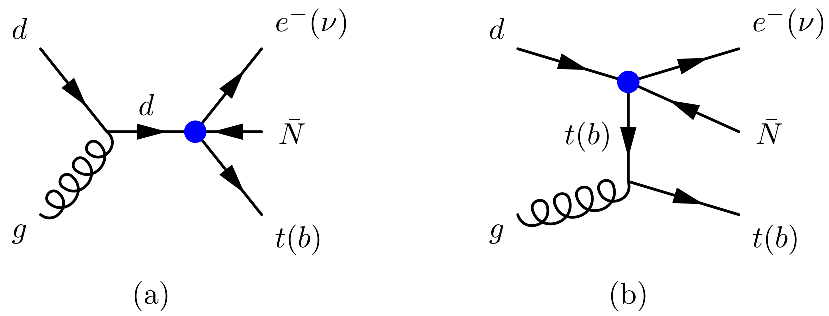

FIGURE 9.3: HNL production in association with e^- and t (e^- and t or ν and b) through $\mathcal{O}^{13}_{duNe}$ ($\mathcal{O}^{31}_{LNQd}$) denoted by the blue blob. The diagrams with the particles in parentheses are present for $\mathcal{O}^{31}_{LNQd}$, but not for $\mathcal{O}^{13}_{duNe}$.

where $f(x) = 1 - 8x + 8x^3 - x^4 - 12x^2 \ln x$, and $x = m_N^2/m_t^2$. The same operators also contribute to the single-top production in association with either a charged lepton and an HNL, or an SM neutrino and an HNL, directly in pp collisions.

The operators with $Q_3 = (t_L, b_L)^T$, i.e. $\mathcal{O}^{31}_{LNQd}$, $\mathcal{O}^{13}_{LdQN}$, and $\mathcal{O}^{31}_{QuNL}$, in addition give a contribution to the single-bottom production in association with either $\nu\bar{N}$ or e^+N. As an example, we show in Fig. 9.3 the diagrams for the processes triggered by $\mathcal{O}^{13}_{duNe}$ and $\mathcal{O}^{31}_{LNQd}$.

In the lower-left panel of Fig. 9.2, we display the cross sections for (i) $pp \to t\bar{t}$ followed by the decay $t \to de^+N$, (ii) $pp \to te^-\bar{N}$, and (iii) $pp \to \bar{t}e^+N$, triggered by $\mathcal{O}^{13}_{duNe}$, setting $\Lambda = 1$ TeV. As in the case of the pair-N_R operator $\mathcal{O}^{13}_{uN}$, the direct HNL production in pp collisions dominates over the production through the new top quark decay. Compared to $\mathcal{O}^{13}_{uN}$, the cross section for $pp \to te^-\bar{N}$ is smaller than that for $pp \to tN\bar{N}$, which is due to a smaller PDF of the d quark with respect to the one of the u quark.

In the upper-right panel of Fig. 9.2, we show the cross sections for the processes induced by $\mathcal{O}^{13}_{QuNL}$. Since this operator involves $SU(2)_L$ doublets Q_1 and L, we have both $te\bar{N}$ and $t\nu\bar{N}$ final states (as well as their charge conjugates). As in the previous cases, the direct HNL production in pp collisions dominates over the production through new top quark decays.

The operators with the 33 quark-flavor indices lead to the flavor conserving decay $t \to be^+N$ for which the width can be computed by Eq. (9.3) with all quark-flavor indices set to 33.[4] The contribution of these flavor-diagonal operators to the single-top and single-bottom production (in association with an electron or neutrino and an

[4]Note that constraints on these operators derived from the measured top quark width are very weak, namely, $\Lambda \gtrsim 0.14$ TeV [289], which is actually below the scale of EFT validity. Thus, all our study points fulfill this limit automatically.

Operator		**HNL production modes**		**HNL decay channels**	
Name	Flavor	Top decay	pp collision	5-body	3-body
$\mathcal{O}_{uN}$	13	$t \to uN\bar{N}$	$pp \to tN\bar{N}$	$\times$	$\times$
$\mathcal{O}_{QN}$	13	$t \to uN\bar{N}$	$pp \to tN\bar{N}/bN\bar{N}$	$\times$	$\times$
$\mathcal{O}_{QuNL}$	13	$t \to u\bar{\nu}N/de^+N$	$pp \to t\nu\bar{N}/te^-\bar{N}$	$N \to \nu\, t^*\bar{u}/e^- t^*\bar{d}$	$\times$
	31	$t \to u\nu\bar{N}$	$pp \to t\bar{\nu}N/be^+N$	$N \to \nu\, u\,\bar{t}^*$	$N \to e^- u\bar{b}$
	33	$t \to be^+N$	$\times$	$N \to e^- t^*\bar{b}/\nu t^*\bar{t}^*$	$\times$
$\mathcal{O}_{duNe}$	13	$t \to de^+N$	$pp \to te^-\bar{N}$	$N \to e^- t^*\bar{d}$	$\times$
	33	$t \to be^+N$	$\times$	$N \to e^- t^*\bar{b}$	$\times$
$\mathcal{O}_{LNQd}$	31	$t \to de^+N$	$pp \to te^-\bar{N}/b\nu\bar{N}$	$N \to e^- t^*\bar{d}$	$N \to \nu b\bar{d}$
	33	$t \to be^+N$	$\times$	$N \to e^- t^*\bar{b}$	$N \to \nu b\bar{b}$

TABLE 9.2: HNL production modes and tree level decay channels induced by the four-fermion operators with N_R and third-generation quarks. Pair-N_R operators contribute only to HNL production, while single-N_R operators also induce 5-body and in some cases 3-body HNL decays. The virtual top quark t^* decays as $t^* \to bW^* \to b(q'\bar{q}$ or $\ell^+\nu)$. The operators $\mathcal{O}^{13}_{LdQN}$ and $\mathcal{O}^{33}_{LdQN}$ lead to the same processes as $\mathcal{O}^{31}_{LNQd}$ and $\mathcal{O}^{33}_{LNQd}$, respectively, hence we omit them in the table.

HNL) is negligible because of the smallness of the b quark PDF. As an example, we show in the lower-right panel of Fig. 9.2 the only HNL production process that is induced by $\mathcal{O}^{33}_{duNe}$.

In Table 9.2, we summarize all the HNL production modes described above, and the allowed decay channels for each effective operator of interest. We discuss the latter in the next subsection.

9.1.2 HNL decays

Pair-N_R operators. The pair-N_R interactions cannot make the HNL decay. Hence, in these scenarios, the N decay can proceed only via active-sterile neutrino mixing. In this case, we use the formulae for the HNL decay width provided in Ref. [122].

Single-N_R operators. These operators lead to HNL decays even in the absence of active-sterile neutrino mixing. We discuss the corresponding decay modes below.

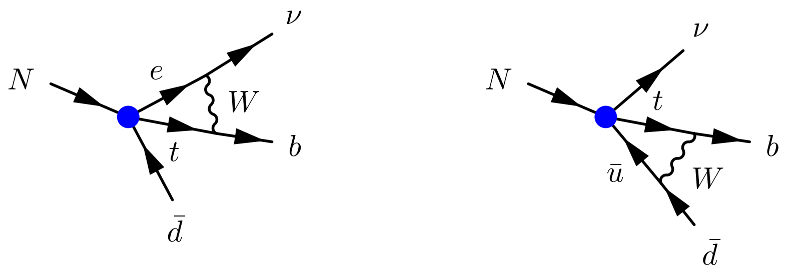

(a) (b)

FIGURE 9.4: One-loop diagrams (in the unitary gauge) for the 3-body decay $N \to \nu b \bar{d}$ induced by the operator $\mathcal{O}^{13}_{QuNL}$.

- All single-N_R operators induce 5-body decays of N through an off-shell top quark, t^*, and an off-shell W-boson, W^*. For example, the decay chain triggered by $\mathcal{O}^{33}_{duNe}$ is $N \to e^- t^* \bar{b} \to e^- b W^* \bar{b} \to e^- b\bar{b}\,(q'\bar{q}$ or $\ell^+\nu_\ell)$.[5] Analogous decay chains for the other single-N_R operators are given in Table 9.2.

- Operators containing two terms, one of which does not involve the top quark, trigger 3-body decays.[6] There are five flavor structures in this category: $\mathcal{O}^{31}_{LNQd}$, $\mathcal{O}^{33}_{LNQd}$, $\mathcal{O}^{13}_{LdQN}$, $\mathcal{O}^{33}_{LdQN}$, and $\mathcal{O}^{31}_{QuNL}$, cf. Table 9.1. For example, in the case of $\mathcal{O}^{33}_{LNQd}$, we have $N \to \nu b \bar{b}$. The corresponding 3-body decays for the other operator structures are shown in Table 9.2.

- At the one-loop level, the operators leading to 5-body tree level decays will also trigger 3-body decays. The corresponding decay rates can be sizable for the operators with a particular chiral structure. For example, the operators $\mathcal{O}^{13}_{QuNL}$ and $\mathcal{O}^{33}_{QuNL}$ contain light left-handed fields together with a right-handed top quark t_R, which can be easily turned to a left-handed top quark t_L by the large top Yukawa coupling and coupled to the W-boson [283]. The corresponding one-loop diagrams are shown in Fig. 9.4 for the case of $\mathcal{O}^{13}_{QuNL}$.

The relative contributions of these decay modes to the total HNL decay width will depend on the model parameters, i.e. the HNL mass, m_N, and the interaction couplings, $c_{\mathcal{O}}/\Lambda^2$ and $V_{\ell N}$. To give an example, in what follows we consider three operator structures, $\mathcal{O}^{33}_{duNe}$, $\mathcal{O}^{33}_{LNQd}$, and $\mathcal{O}^{13}_{QuNL}$, and compare their contributions to the N decay width with that in the minimal scenario, characterized by active-sterile neutrino mixing only.

[5] If m_N is large enough, this decay becomes either 4- or 3-body, with respectively an on-shell W or an on-shell t in the final state.

[6] We assume that m_N is sufficiently large for b quark(s) to go on shell.

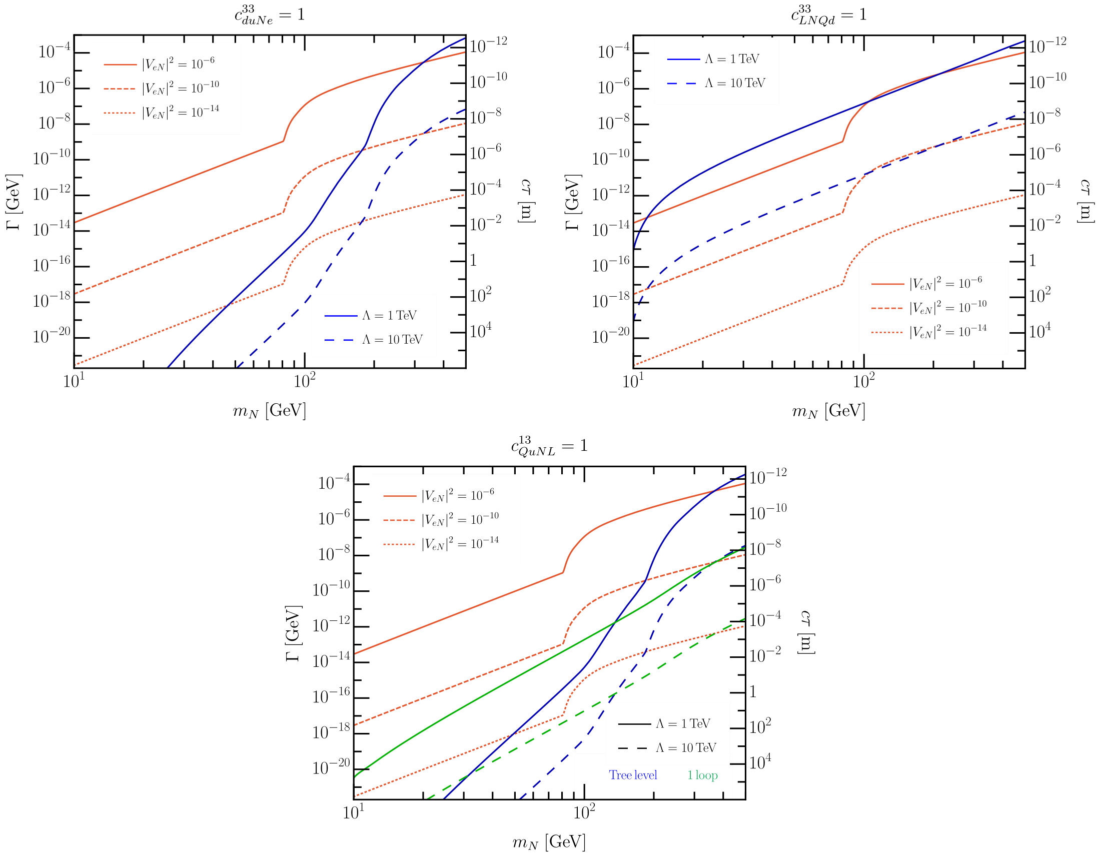

FIGURE 9.5: Mixing and operator contributions to the HNL decay width as a function of its mass. The operator contributions (blue and green lines) come from $\mathcal{O}^{33}_{duNe}$ (top left), $\mathcal{O}^{33}_{LNQd}$ (top right), and $\mathcal{O}^{13}_{QuNL}$ (bottom), and we have set two values of Λ. Contributions from three values of $|V_{eN}|^2$ are shown for comparison in orange.

In the upper-left panel of Fig. 9.5, we display the HNL partial decay widths induced by $\mathcal{O}^{33}_{duNe}$, namely, $\Gamma(N \to e^- b\bar{b}q'\bar{q}) + \Gamma(N \to e^- b\bar{b}\ell^+\nu_\ell)$, where $q'\bar{q} = \{u\bar{d}, u\bar{s}, c\bar{s}, c\bar{d}\}$ and $\ell^+\nu_\ell = \{e^+\nu_e, \mu^+\nu_\mu, \tau^+\nu_\tau\}$.[7] We have set $c^{33}_{duNe}/\Lambda^2 = 1/(1\text{ TeV})^2$. For comparison, we show the mixing contribution to the decay width for three different values of the squared mixing parameter $|V_{eN}|^2$. Notice the y-axis spans around 20 orders of magnitude along the mass range under consideration. There are two sudden increases in the operator contribution, which occur at $m_N \simeq m_W + 2m_b$ and $m_N \simeq m_t + m_b$, as the decays to on-shell W-bosons and top quarks, respectively, become possible. A similar behavior can be observed in the mixing curves at $m_N \simeq m_W$, when the decay channel to on-shell W opens.

[7] The decays to $q'\bar{q} = \{u\bar{b}, c\bar{b}\}$ are strongly suppressed by the corresponding small CKM elements. By summing over all possible final states we are taking into account the contributions from off-shell and on-shell top quark and W-boson.

In the upper-right panel of Fig. 9.5, we show the HNL partial decay width of the 3-body decay $N \to \nu b\bar{b}$ triggered by the operator $\mathcal{O}^{33}_{LNQd}$ (it dominates over the 5-body decays, which we do not show). We have set $c^{33}_{LNQd}/\Lambda^2 = 1/(1\text{ TeV})^2$. The operator contribution wins over the mixing one if Λ is not too large, as $\Gamma_{\mathcal{O}} \propto \Lambda^{-4}$ and $\Gamma_{\text{mix}} \propto |V_{eN}|^2$, and it easily leads to prompt decays. Therefore, we do not further consider this operator structure, neither the other structures featuring HNL 3-body decays at tree level.

In the bottom panel of Fig. 9.5, by the green lines we show the decay width of the 3-body decay $N \to \nu b\bar{d}$ induced by $\mathcal{O}^{13}_{QuNL}$ through the one-loop diagrams depicted in Fig. 9.4. We have computed this decay width using the pipeline `FeynArts` [290] + `FormCalc` [291] + `LoopTools` [291]. We find perfect agreement with the corresponding result shown in Fig. 6 of Ref. [283]. The blue lines correspond to the sum of the 5-body tree level decay widths for $N \to e^- t^* \bar{d} \to e^- W^* b\bar{d} \to e^- b\bar{d}(q'\bar{q}$ or $\ell^+\nu_\ell)$ and $N \to \nu_e t^* \bar{u} \to \nu_e W^* b\bar{u} \to \nu_e b\bar{u}(q'\bar{q}$ or $\ell^+\nu_\ell)$, induced by $\mathcal{O}^{13}_{QuNL}$ at tree level and computed with `MadGraph5`. As can be seen, for $c^{13}_{QuNL}/\Lambda^2 = 1/(1\text{ TeV})^2$, the loop-induced 3-body decay dominates over the tree level 5-body decays for HNL masses up to approximately $m_N \approx 130$ GeV.

In the case of $\mathcal{O}^{33}_{QuNL}$, we have a similar 3-body decay $N \to \nu b\bar{b}$. However, now, in addition to the diagrams with the W-boson in the loop, we also have diagrams with exchange of the Z-boson and the Higgs boson. We have checked that for $\Lambda = 1$ TeV and $m_N \gtrsim 15$ GeV, this operator leads to prompt decays with $c\tau \lesssim 0.01$ mm. Thus, we will not consider it in what follows among our benchmark scenarios featuring a long-lived HNL.

9.1.3 Benchmark scenarios

In Section 9.3, we will study numerically a few representative scenarios, each characterized by an effective operator with given quark-flavor indices. We will switch on one operator structure at a time and investigate its phenomenological implications at the LHC main detector ATLAS, as well as at the current and future far detector facilities, including MoEDAL-MAPP2, MATHUSLA, ANUBIS and CODEX-b.

We describe the characteristic features of each selected scenario below, and we refer the reader to Table 9.2 for a summary of the HNL production and decay modes.

1. $\mathcal{O}^{13}_{uN}$: Being a pair-N_R operator, it only contributes to pair production of HNLs. The dominant channel is $pp \to tN\bar{N}$, cf. the upper-left panel of Fig. 9.2. HNL decay, on the other hand, is completely controlled by the mixing parameter. We note in passing that a scenario with $\mathcal{O}^{13}_{QN}$ would be qualitatively very similar.

2. $\mathcal{O}_{QuNL}^{13}$: This operator contributes to both HNL production and decay. As discussed above and shown in the bottom panel of Fig. 9.5, the 3-body decay induced at one-loop dominates over 5-body decays induced at tree level. In our numerical simulation, we will take into account both the 3-body decay via the operator and tree level decays via mixing.

3. $\mathcal{O}_{duNe}^{13}$: This operator structure also contributes to both production and decay. HNLs are dominantly produced directly in pp collisions, as can be inferred from the upper-right panel of Fig. 9.2. The operator contribution to the decay is naturally suppressed (compared to mixing) for $m_N < m_W$, since the only allowed channel is a 5-body decay.[8] This is no longer true for $m_N > m_W(m_t)$, when 4-body (3-body) decays are possible. Therefore, the operator contribution should be taken into account along with the mixing contribution.

4. $\mathcal{O}_{duNe}^{33}$: The operator contributes to HNL production and decay. However, production now occurs only through top quark decays, leading to smaller cross-sections than in the previous scenarios; see Fig. 9.2. As for the decay, analogously to scenarios 2 and 3, the operator contribution competes with the mixing one and has to be taken into account, see the upper-left panel of Fig. 9.5 and the related discussion.

9.2 Simulation details

In this work, we consider the ATLAS experiment[9] and the proposed far detectors dedicated to LLP searches at the LHC. Here, we introduce the search strategies of these experiments, and outline the simulation procedure employed for determining their sensitivity reach to long-lived HNLs coupled to top quarks.

9.2.1 ATLAS

For the ATLAS experiment, we focus on a signature characterized by a displaced vertex (DV) arising from the HNL decay, accompanied by jets originating from either top quark decays or the HNL decay itself. The latest DV search with jets at ATLAS [292] is not optimal for our signal, mainly because of its too strong thresholds on the transverse momenta of jets and multi-jet cuts. Therefore, we propose a new search strategy with optimal jet cuts and the optional requirement of a b-jet. Our strategy is inspired

[8]This is true only at tree level. One can consider 3-body decays via W-loop. Their contribution to the total decay width is negligible though for this particular operator structure.

[9]We do not simulate explicitly for the CMS experiment, for which we expect similar results.

by the recast [293] for the ATLAS "DV+jets" search [292] and by a past 8-TeV search for DVs at ATLAS [269].

We implement the operators of interest in a UFO file with `Feynrules` [255, 256]. With this model file, we then simulate HNL production in pp collisions at $\sqrt{s} = 14$ TeV using `MadGraph5` [268, 258] with the NNPDF3.1 PDF set [294]. For each benchmark scenario, we focus on the dominant production channel of the HNL: either direct pp collision in association with a top or bottom quark, or top quark decay if the former is absent (see Table 9.2). We generate 10^5 events at multiple parameter points in a grid covering the plane $|V_{eN}|^2$ vs. m_N, while keeping $c^{ij}_{\mathcal{O}}/\Lambda^2$ constant for each benchmark. HNL decays are then handled in `MadSpin` [259], where signal decays to final states with jets are enforced for numerical stability. In particular, we simulate the decay into ejj and νjj via mixing, and for benchmarks 2 – 4, we additionally simulate the HNL decays induced by the single-N_R operators, which all contain at least two jets.

The generated events are processed in `Pythia8` [189] for showering, hadronization, and event selections. We implement a toy-detector module in `Pythia8` for reconstructing truth-level jets, following the definition from the HEPData accompanying note from Ref. [292]. Truth jets are reconstructed using `FastJet` [271], with the anti-k_t algorithm and $R = 0.4$, excluding neutrinos and muons. This jet definition includes particles from the HNL decays. The detector response for measurement of jet p_T is also modeled taking into account detector acceptance, resolution, and smearing on their transverse momenta, following the same criteria and threshold as in Ref. [295].

Event selection proceeds in two stages: (1) event-level selections; and (2) DV-level selections.

Event-level selections: we impose preliminary selections based on the number of jets in the event meeting specific p_T-criteria — events must have 4, 5, or 6 jets with $p_T > 90, 65$, or 55 GeV, respectively, following Ref. [269]. This choice of multi-jet cuts enhances the sensitivity to our signal, as opposed to considering the jet selections imposed in the recast done in Ref. [293]. The search [292] that was recast in that paper was intended for directly pair-produced LLPs (decaying to several jets). For our benchmarks, sensitivity is largely lost at the event-level when using these 13-TeV-search jet cuts [292], and therefore we propose to retain the jet-p_T thresholds as low as the ATLAS 8-TeV search [269].[10]

[10] This proposal can be further justified by the potential and prospective leverage that some specialized data taking techniques (i.e. such as data parking [296]) can have on BSM physics on data collected with low triggering thresholds. Such techniques were used by LHC experiments in searches for HNLs; see e.g. Ref. [297].

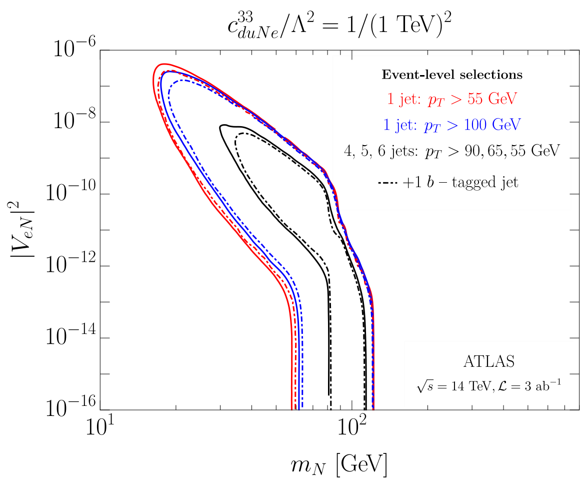

FIGURE 9.6: ATLAS sensitivity for one example operator, $\mathcal{O}^{33}_{duNe}$, in the plane $|V_{eN}|^2$ vs. m_N for the proposed complete search strategy with different jet-selection cuts at the event-level (see text for more details).

In Fig. 9.6, we show the impact on the sensitivity limits to one of our benchmarks when requiring different jet-p_T thresholds. When aiming at discovery prospects, one may further consider identifying b quark jets associated to our event signatures (see Table 9.2). We treat a jet as a b-jet based on the flavor of the truth quark that initiated the jet. From all truth jets in the event with $p_T > 20$ GeV and $|\eta| < 2.5$, we tag a jet as a b-jet if a Monte-Carlo truth b quark with $p_T > 5$ GeV is found within a cone of size $\Delta R = 0.3$ around the jet direction. We additionally force a flat b-jet identification efficiency of 77% [298].

DV-level selections: we implement DV reconstruction according to the recast [293] of the ATLAS "DV+jets" search [292], where at least one vertex in the event must satisfy the following conditions:

1. The transverse distance from the vertex to the interaction point (IP) must be within 4 mm $< R_{xy} <$ 300 mm and the longitudinal position of the vertex must satisfy $|z| <$ 300 mm.
2. At least one track should have an absolute transverse impact parameter $|d_0| >$ 2 mm.
3. The DV must contain at least 5 tracks all satisfying the two requirements below:
   (a) They should have a boosted transverse decay length larger than 520 mm.
   (b) Their p_T and charge q should satisfy $p_T/|q| > 1$ GeV.

4. The invariant mass of the DV, reconstructed from the tracks passing the requirements above for which the masses are all assumed to be that of a charged pion, should be larger than 10 GeV.

The ATLAS collaboration [292] provided parameterized efficiencies at both event level and vertex level, to account for further, more intricate event selections that are difficult to simulate, for recasting purpose. The event-level (vertex-level) efficiencies[11] are functions of the transverse position of the DV and the sum of the truth-jet p_T (the transverse position of the DV, the number of charged particles associated to the truth decay vertex, as well as the vertex invariant mass). We apply the parameterized efficiencies at vertex-level only, in our proposed search. Thus, the events that pass the jet-selection criteria and contain at least one reconstructed vertex meeting the above requirements contribute to the final signal-efficiency cutflow.

The expected number of signal events at ATLAS is then calculated with

$$\begin{aligned} N_S^{\text{ATLAS}} &= \sigma \cdot \mathcal{L} \cdot \left\{ \mathcal{B}_{\text{mix}} \cdot \varepsilon^{\text{mix}} + \mathcal{B}_{\text{op}} \cdot \varepsilon^{\text{op}} \right\} , \\ \mathcal{B}_{\text{mix}} &= \mathcal{B}(N \to ejj) + \mathcal{B}(N \to \nu jj), \\ \mathcal{B}_{\text{op}} &= \mathcal{B}(N \to \text{5-body tree}) + \mathcal{B}(N \to \text{3-body loop}) , \end{aligned} \tag{9.5}$$

where σ is the production cross section of the HNL N, $\mathcal{L} = 3$ ab^{-1} is the integrated luminosity, and $\mathcal{B}_{\text{mix/op}}$ represents the sum of the branching fractions of the HNL decay modes of interest induced by the mixing or the operator. We remark that the latter term is not present in benchmark 1. Here, "j" denotes a jet including the up, down, charm, strange, or bottom quark. The final cutflow efficiencies, $\varepsilon^{\text{mix/op}}$, are the ones obtained from implementing both event- and vertex-level selections in each case (including the acceptances and parameterized efficiencies) to the final states induced via mixing/operator in our custom code implemented within `Pythia8`.

We note that the vertex-level selection criteria are designed to suppress all SM backgrounds,[12] allowing us to derive the 95% C.L. exclusion limits by requiring at least 3 signal events. We additionally provide exclusion limits for 10 and 30 signal events for certain scenarios, which would correspond to the exclusion limits at the same level if approximately 25 and 225 background events were present, respectively.

[11] The ATLAS search [292] employs two signal regions, the high-p_T-jet one and the trackless-jet one. The two SRs share the same vertex-level efficiencies.

[12] The ATLAS "DV+jets" search reported in Ref. [292] applies stricter cuts on jet-p_T thresholds. However, in that search, background suppression is driven primarily by DV requirements rather than by requirements on the jets in the event, justifying our assumption that the DV selections alone are sufficient to eliminate the background events.

9.2.2 Far detectors

We recall that the far detector experiments can be classified into two categories according to their relative direction with respect to their corresponding IPs, namely, transverse detectors (MATHUSLA, ANUBIS, MoEDAL-MAPP1(2) and CODEX-b) and forward detectors (FASER(2) and FACET). In the present work, the considered HNLs, with masses above the GeV, are assumed to stem from either top quark decays or direct production in pp collisions. In this case, the polar angle distribution of the production cross section is symmetric (not boosted in the forward direction). We have numerically checked that the forward experiments have no sensitivities to these scenarios and, therefore, we will not discuss further these experiments.

For computing the sensitivity of the far detectors, we follow a different procedure than that used for ATLAS, as we do not simulate the HNL decay in this case. We start by generating 10^5 events for various HNL masses using `MadGraph5` and pass the resulting Les Houches Event Files (LHEF) [299] directly to `Pythia8`. We then calculate the probability for the HNL to decay within each far detector, and derive the average decay probability over all the simulated HNLs,

$$\langle P\left[N \text{ decay in f.v.}\right]\rangle = \frac{1}{k}\sum_{i=1}^{k} P\left[N^i \text{ decay in f.v.}\right], \tag{9.6}$$

where $k = 10^5$ or 2×10^5 (depending on whether in each signal event one or two HNLs are produced) is the total number of the simulated HNLs for each HNL mass and "f.v." stands for fiducial volume. The probability in each case is determined by the HNL's boosted decay length and momentum angle besides the geometry and position of the far detectors. The expected number of signal events is then given by

$$N_S^{\text{FD}} = \sigma \cdot \mathcal{L} \cdot \langle P\left[N \text{ decay in f.v.}\right]\rangle \cdot \mathcal{B}(N \to \text{vis.}) \cdot \varepsilon\,, \tag{9.7}$$

where the integrated luminosity $\mathcal{L}$ depends on the far detector experiment (3 ab^{-1} for MATHUSLA and ANUBIS and 300 fb^{-1} for MAPP2 and CODEX-b) and $\mathcal{B}(N \to \text{vis.})$ denotes the decay branching ratio of the HNL into visible final states (that can be induced either via mixing or the operator), for which we have only excluded the fully invisible tri-neutrino final states. We assume a detection efficiency of $\varepsilon = 100\%$ for simplicity.

As vanishing background is expected at the far detectors, we derive the 95% C.L. exclusion limits by requiring at least 3 signal events. However, MATHUSLA and ANUBIS are now considering new geometries different from the original designs [300, 301], affecting the total acceptances. In addition, ANUBIS with its relatively close distance from the IP might suffer from a nonzero level of background events. Therefore, we will also provide sensitivity limits for larger numbers of signal events using the original designs, to facilitate deriving sensitivities corresponding to other values of the acceptances or background levels.

9.3 Numerical Results

In this section, we present the numerical results obtained using the simulation procedure outlined above. We analyze the sensitivities of ATLAS and the far detectors, focusing on the four benchmark scenarios defined in Section 9.1.3, characterized by different effective operators containing a top quark and at least one HNL. In each case, a single effective operator structure is switched on, together with the standard active-sterile neutrino mixing. The mixing parameter $|V_{\ell N}|^2$, the HNL mass m_N, and the operator coefficients $c_{\mathcal{O}}^{ij}/\Lambda^2$ are treated as independent parameters. For simplicity, we consider a single kinematically relevant HNL that mixes exclusively with electron neutrinos, i.e. $V_{\ell N} = V_{eN}$.[13]

We note that for the plots of the results shown in this section, we do not assume that the bottom quarks in the event have been tagged. Thus, our regions are, strictly speaking, not discovery regions but exclusion prospects. We choose to do so, to obtain a fair comparison of the far detectors and ATLAS, because only ATLAS can identify the top quark(s) in the event. However, as shown in Fig. 9.6, discovery regions (including b-tagging) are similar to, albeit slightly smaller than, exclusion prospects in the ATLAS simulation.

The benchmark scenarios are divided into two categories: pair-N_R operators (scenario 1) and single-N_R operators (scenarios 2–4). For pair-N_R operators, HNL production is dominated by the operator, while the HNL decays occur solely via mixing, resulting in decoupled production and decay processes. In this case, the mixing parameter V_{eN} drives leptonic and semileptonic HNL decays through off-shell or on-shell W- and Z-bosons, depending on the HNL mass. Conversely, for single-N_R operators, the operator contributes to both production and decay, with the latter potentially dominating over the mixing in some parts of the parameter space. In either case, the final states containing charged particles are detectable by the far detectors, while the final states with jets contribute to the searched signal in ATLAS.

[13] We note that, based on our study for first-generation quark operators [267], we expect that results for muons will be very similar.

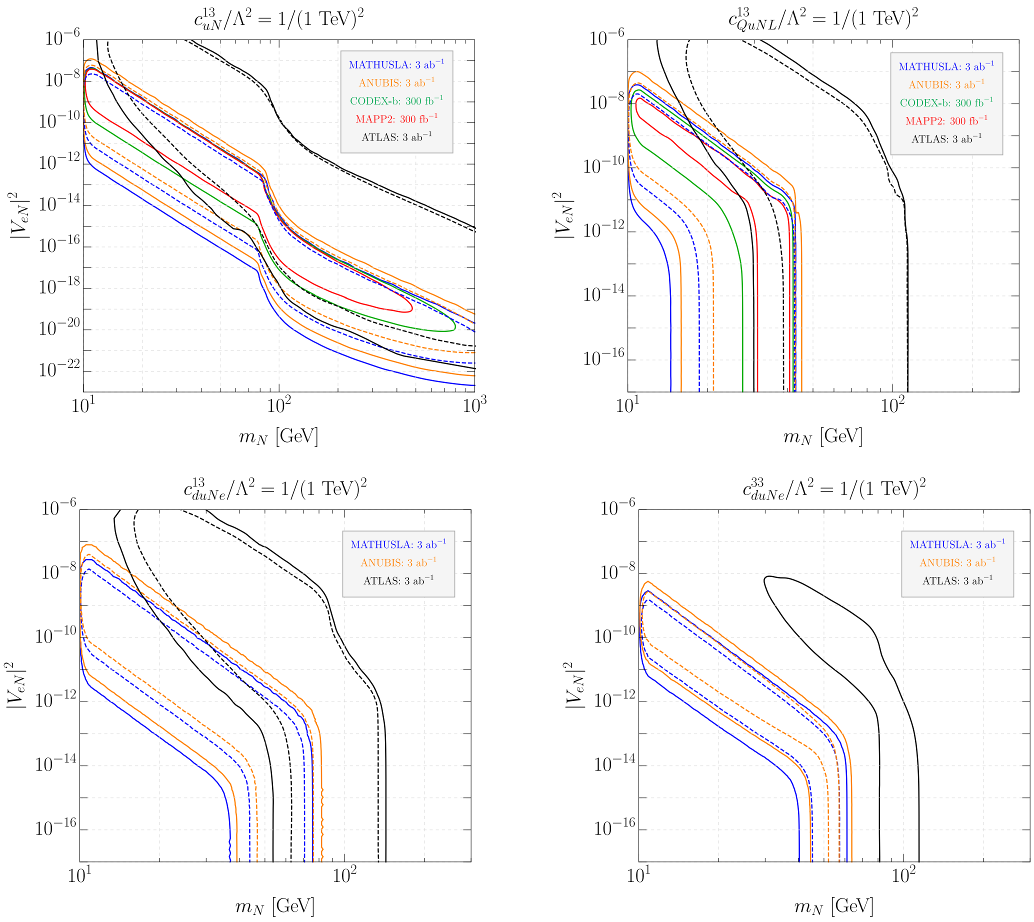

FIGURE 9.7: Sensitivities of ATLAS and the far detectors in the plane $|V_{eN}|^2$ vs. m_N to scenarios 1 (top left), 2 (top right), 3 (bottom left), and 4 (bottom right). Solid lines correspond to 3 signal events. Dashed lines are for 30 events in all the plots, except for the lower-right panel, where they correspond to 10 events.

In Fig. 9.7, we display the sensitivity contours of ATLAS and the far detectors in the $|V_{eN}|^2$ vs. m_N plane. The upper-left panel corresponds to scenario 1, where the pair-N_R operator structure $\mathcal{O}^{13}_{uN}$ is switched on, assuming $c^{13}_{uN} = 1$ and $\Lambda = 1$ TeV. Solid lines correspond to 3 signal events, while dashed lines, which are present for MATHUSLA, ANUBIS, and ATLAS, are for 30 signal events.[14] Since the production process is controlled by the operator coefficient and decoupled from decay, these experiments can probe very small values of active-sterile neutrino mixing and large HNL masses. Among the far detectors, MATHUSLA and ANUBIS exhibit the strongest sensitivities, reaching HNL masses in excess of 1 TeV. However, the EFT validity requires m_N to be

[14]Note that the smaller version of MATHUSLA, recently discussed in Ref. [300] is roughly a factor 10 smaller in volume than the original MATHUSLA design [302], used in our simulation. The 30-event lines thus correspond roughly to the 3-event curves of the smaller design.

significantly below the new physics scale, and we limit the plot range accordingly for our choice of $\Lambda = 1$ TeV. CODEX-b and MAPP2 cover smaller regions of the parameter space, but still can reach values of $|V_{eN}|^2$ as low as 10^{-20} and 10^{-19}, respectively, and masses up to 800 GeV (CODEX-b) and 500 GeV (MAPP2). Compared to the far detectors, ATLAS can probe larger values of mixing for the same HNL mass range, because of its better sensitivity to LLPs with shorter lifetimes.

The sensitivities to single-N_R operator scenarios are shown in the other panels of Fig. 9.7. In the upper-right panel, we switch on the operator $\mathcal{O}^{13}_{QuNL}$ (scenario 2), and in the lower-left and lower-right panels, we consider the operators $\mathcal{O}^{13}_{duNe}$ (scenario 3) and $\mathcal{O}^{33}_{duNe}$ (scenario 4), respectively. For these plots, we assume the respective operator coefficient $c^{ij}_{\mathcal{O}} = 1$ and $\Lambda = 1$ TeV. The solid and dashed lines follow the same conventions as in scenario 1, except for the lower-right panel, where dashed lines correspond to 10 signal events only (30 events are not reached as a result of the smaller HNL production cross section in scenario 4, see Fig. 9.2).

In all the three single-N_R operator scenarios, the sensitivity curves exhibit a funnel-like feature in a certain mass region, i.e. a region where the sensitivity curves become independent of the mixing parameter. More specifically, in this mass region, the chosen value of the operator coefficient alone leads to more than 3 (30) signal events inside the solid (dashed) contour. In general, this funnel-like behavior appears when the operator starts to dominate the HNL decay, generating sufficient number of signal events even when the mixing parameter is negligible. Note, however, this does not imply sensitivity to infinitely small values of mixing: if the operator did not contribute to the HNL decay, the sensitivity regions in the $|V_{eN}|^2$ vs. m_N plane would be bounded from below. The upper mass reach in these scenarios is limited by the size of the detectors. For larger masses, the HNLs decay too promptly to leave an imprint in the far detectors or produce a displaced vertex in ATLAS.

There are qualitative differences among these scenarios. In scenario 2 with the $\mathcal{O}_{QuNL}$ operator (upper-right panel), the sensitivity in mass is limited to $m_N \lesssim 40$ GeV for the far detectors because of the larger decay width with this operator in this mass range. In contrast, for scenarios 3 and 4 (bottom panels), the far detectors can probe larger masses, with sensitivities up to $m_N \lesssim 80$ GeV. On the other hand, ATLAS is sensitive to $m_N \lesssim 120$ GeV in all three scenarios. Moreover, only the experiments with an expected integrated luminosity of $\mathcal{L} = 3$ ab^{-1} (MATHUSLA, ANUBIS, and ATLAS) exhibit sensitivity to scenarios 3 and 4. This is because the operator $\mathcal{O}_{duNe}$ generates smaller production cross sections compared to $\mathcal{O}_{uN}$ and $\mathcal{O}_{QuNL}$, requiring higher luminosities for detection.

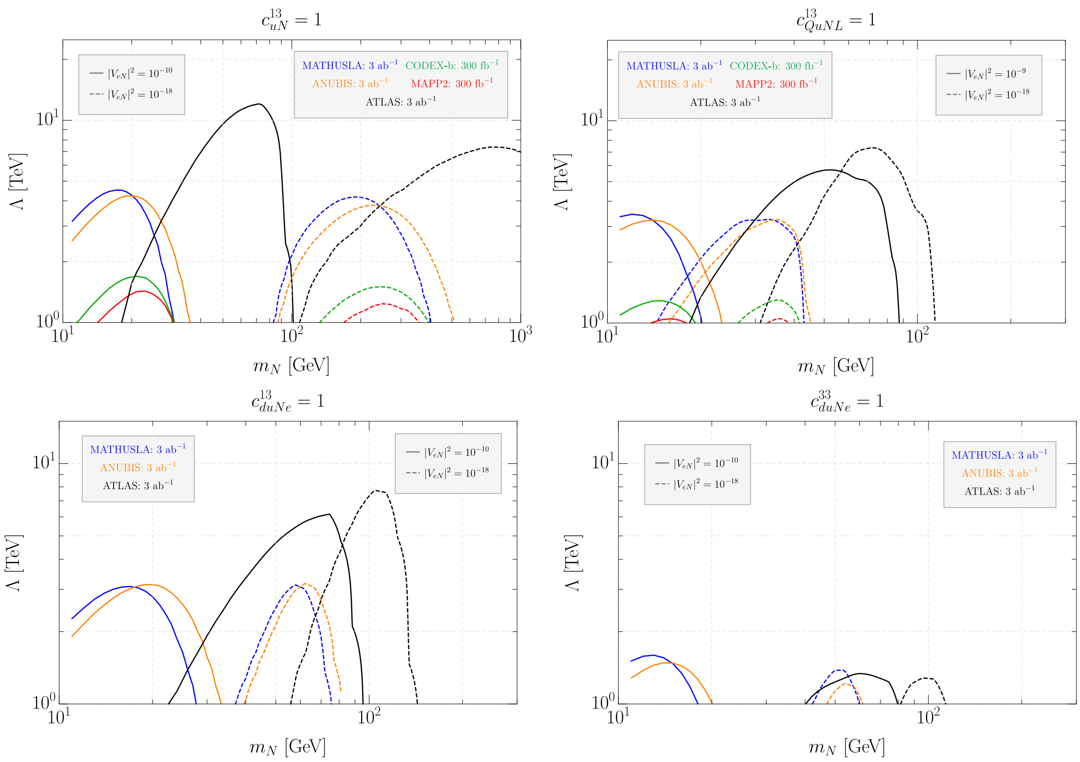

FIGURE 9.8: Sensitivities of ATLAS and the far detectors in the plane Λ vs. m_N to scenarios 1 (top left), 2 (top right), 3 (bottom left), and 4 (bottom right). Solid (dashed) lines correspond to $|V_{eN}|^2 = 10^{-10}$ (10^{-18}), except for scenario 2, where solid lines are for $|V_{eN}|^2 = 10^{-9}$.

We also explore the sensitivity limits in the Λ vs. m_N plane for fixed values of the active-sterile neutrino mixing. They are displayed in the four panels of Fig. 9.8, corresponding to the operators $\mathcal{O}^{13}_{uN}$ (top left), $\mathcal{O}^{13}_{QuNL}$ (top right), $\mathcal{O}^{13}_{duNe}$ (bottom left), and $\mathcal{O}^{33}_{duNe}$ (bottom right). We show the reach to Λ for two mixing values: $|V_{eN}|^2 = 10^{-10}$ (solid lines)[15] and $|V_{eN}|^2 = 10^{-18}$ (dashed lines). The chosen values of the mixing parameter allow us to neglect either the operator or the mixing contribution to the HNL decay, such that we have a simple scaling of the number of signal events with Λ. In all four scenarios considered, we observe that (i) the probed HNL masses depend strongly on the assumed value of $|V_{eN}|^2$, and (ii) for the same value of $|V_{eN}|^2$, ATLAS and the far detectors cover complementary mass ranges.

The accessible parameter space varies significantly between scenarios. Scenario 1 exhibits the highest sensitivities in both m_N and Λ. In particular, for $|V_{eN}|^2 = 10^{-10}$, ATLAS can probe the new physics scale Λ in excess of 10 TeV for 40 GeV $\lesssim m_N \lesssim$ 80 GeV. MATHUSLA (ANUBIS) reaches $\Lambda \approx 4.5$ (4) TeV for m_N slightly smaller than 20 GeV,

[15]For scenario 2, we have fixed instead $|V_{eN}|^2 = 10^{-9}$ to guarantee that the operator contribution to the HNL decay is negligible compared to the mixing one; see the bottom panel in Fig. 9.5.

whereas CODEX-b (MAPP2) can exclude $\Lambda \lesssim 1.5$ (1.2) TeV for m_N slightly larger than 20 GeV. Assuming $|V_{eN}|^2 = 10^{-18}$, a similar reach in Λ occurs for $m_N \gtrsim 100$ GeV. In scenario 2, ATLAS can reach $\Lambda \approx 7$ TeV (more than 8 TeV) for m_N around 50 (70) GeV if $|V_{eN}|^2 = 10^{-9}$ (10^{-18}). MATHUSLA and ANUBIS can be sensitive to scales as large as 3 TeV, whereas the sensitivities of CODEX-b and MAPP2 extend to only slightly above $\Lambda = 1$ TeV. Scenario 3 exhibits similar sensitivities, with ATLAS being capable of probing Λ values up to 7–8 TeV, and MATHUSLA and ANUBIS being sensitive to new physics scales of up to 3 TeV. However, the far detectors in this scenario can probe larger masses than those in scenario 2, for the same values of $|V_{eN}|^2$. In contrast, for scenario 4, the sensitivities are generally much weaker. Its limited reach is a result of the small production cross sections, which result in insufficient numbers of HNLs even for moderate values of Λ. In fact, CODEX-b and MAPP2 are not sensitive at all to scenarios 3 and 4 for the same reason, while ATLAS can only probe $\Lambda \lesssim 1.5$ TeV in a relatively small m_N range in the latter scenario.

All plots in this section were calculated with the assumption that the HNL is a Dirac particle. Let us close this section with a brief discussion on how our results would change, if we consider Majorana HNLs instead. There are two effects. First of all, in case of pair-N_R operators, as demonstrated in [264], cross sections for Majorana and Dirac HNLs are the same, except for large values of m_N, say $m_N \sim \text{(few)}$(100 GeV). At the largest masses, for Majorana HNLs cross sections are suppressed relative to the Dirac case. Thus, the mass reach is reduced for $\mathcal{O}_{uN}$ relative to the values shown in Fig. 9.7. Note that Fig. 9.7 cuts m_N at 1 TeV. The nature of the HNL also affects its decay width. Majorana HNLs have a twice larger decay width, compared to Dirac HNLs at the same value of $|V_{eN}|^2$. Thus, roughly one has to divide $|V_{eN}|^2$ by a factor of 2 to obtain the corresponding plots for Majorana HNLs. Note that the different plots in Fig. 9.7 show ranges of $|V_{eN}|^2$ which vary between (11–17) orders of magnitude. Thus, we consider a change of a factor of 2 not essential. Strictly speaking this is correct only in the limit where mixing dominates the decay. For single-N_R operators, at the largest values of m_N the decays are dominated by the operator contribution. A change of this width by a factor of two for the Majorana cases will lead then to a reduction of the largest m_N, to which our search is sensitive, by roughly 15%.

9.4 Summary

In this chapter, we have explored a class of four-fermion operators in the N_RSMEFT that couple HNLs to top quarks, as motivated by possible top-philic new physics at the TeV scale. These operators, listed in Table 9.1, give rise to novel production and decay mechanisms for HNLs at the high-luminosity LHC. We focused on scenarios in which the HNL is sufficiently long-lived to yield displaced vertex (DV) signatures in either main detectors like ATLAS or in proposed far detectors such as MATHUSLA and ANUBIS.

The analysis distinguishes between two types of operators: pair-N_R operators, which mediate HNL production but not decay (the latter proceeds via active-sterile mixing V_{eN}), and single-N_R operators, which can contribute to both production and decay. Depending on the operator and its quark-flavor structure, HNLs can be produced directly in proton collisions or via rare top decays, as illustrated in Table 9.2 and Figs. 9.1 and 9.3. For single-N_R operators, HNL decays can be dominated either by mixing or by the effective interaction itself, depending on the mass and coupling scales.

We selected four benchmark operators representative of the different structures: $\mathcal{O}_{uN}^{13}$ (pair-N_R) and $\mathcal{O}_{QuNL}^{13}$, $\mathcal{O}_{duNe}^{13}$, $\mathcal{O}_{duNe}^{33}$ (single-N_R). We computed production cross sections and decay rates for these scenarios. Using dedicated Monte Carlo simulations, we have evaluated the experimental sensitivity to these interactions. For the ATLAS main detector, we proposed a "DV+jets" search strategy, inspired by previous LLP searches; for the far detectors, we estimated the number of signal events based on geometric acceptance and decay probabilities.

Our results show that the experiments could probe extremely small values of $|V_{eN}|^2$, down to 10^{-20} in the case of $\mathcal{O}_{uN}^{13}$ and HNL masses above 100 GeV, assuming $c_{\mathcal{O}}^{ij}/\Lambda^2 = 1/\text{TeV}^2$. Far detectors like MATHUSLA and ANUBIS provide the best sensitivity for low m_N, while ATLAS becomes more sensitive at higher masses. The reach in the new physics scale Λ also varies significantly: for fixed $|V_{eN}|^2 = 10^{-10}$, values up to several TeV can be probed, with the best reach again obtained in the pair-N_R case. In single-N_R scenarios, the interplay between the effective operators and neutrino mixing leads to distinctive features in the sensitivity plots, such as funnel-shaped regions where the decay is dominated by the effective operator rather than mixing.

Overall, this study highlights the potential of DV searches at ATLAS and the proposed far detectors to probe so far unconstrained HNL-related top-philic new physics that may be hiding at a few TeV.

CONCLUDING REMARKS

Conclusions

The existence of nonzero neutrino masses tells us that physics beyond the SM must exist, but it does not reveal where this new physics might be hiding. A compelling possibility is that the particles responsible for neutrino mass generation lie at high, but potentially accessible, energy scales. Guided by this idea, tremendous efforts have been made to probe the energy frontier, with the LHC leading this exploration. However, after nearly 15 years of operation, no direct signs of such new physics have been observed.

In light of this absence, alternative hypotheses about the nature of new physics have gained attention. One scenario is that new particles are too heavy to be produced directly, and can only be probed indirectly through their low-energy effects. Alternatively, new particles might lie within the reach of current experiments but remain undetected due to their super-weak interactions with SM particles. In this thesis, we have explored both of these avenues. The first is naturally addressed using effective field theories (EFTs), while the second is intimately linked to the phenomenology of long-lived particles (LLPs). These two aspects are brought together in our study of new physics prompted by the neutrino mass problem.

Motivated by various neutrino mass models, we focused on sterile neutrinos, also referred to as heavy neutral leptons (HNLs). To explore the rich ways in which HNLs could manifest at colliders, we adopted a model-agnostic framework that goes beyond the minimal mixing scenario, namely the EFT of the SM extended with sterile neutrinos, N_RSMEFT, and its low-energy counterpart N_RLEFT.

On the theoretical side, we investigated possible ultraviolet (UV) completions of the effective operators appearing in N_RSMEFT. In particular, we provided a systematic classification of tree level decompositions for dimension-6 and dimension-7 operators involving sterile neutrinos [156]. This UV-EFT dictionary acts as a bridge between phenomenology and model building: if new particles were to be discovered at future experiments, these results would help identify which effective operators could be generated and guide the search for related processes, shedding light on the underlying physics. Of course, this is only a first step. Our analysis is restricted to operators up to dimension 7 that can be generated at tree level. Therefore, extending the matching to loop level decompositions and to higher dimensional operators would be a natural continuation of this work.

On the phenomenological side, this thesis presents a novel and systematic application of EFT frameworks to the study of HNLs at colliders. Within N_RSMEFT and N_RLEFT, we explored new interactions between the HNLs and SM particles, focusing on electromagnetic dipole interactions and four-fermion operators involving quarks. We considered subsets of effective operators up to dimension 6 describing these interactions and identified previously unexplored production and decay modes of HNLs, many of which give rise to striking LLP signatures.

One avenue we explored was the possibility of HNLs having sizable transition magnetic moments [206]. Such interactions can lead to production of two distinct HNLs, and if nearly degenerate, the heavier one becomes long-lived and decays into a photon and missing energy, producing non-pointing photon signatures in the detectors. Alternatively, dipole interactions between HNLs and SM neutrinos can also generate displaced photon signals that may be observable in the electromagnetic calorimeters of the main LHC detectors.

A second class of scenarios relevant for LHC phenomenology involves four-fermion interactions with quarks. For HNLs lighter than a GeV, these operators can mediate meson decays into HNLs [175], while for heavier masses, they lead to enhanced production rates in proton-proton collisions compared to the minimal mixing case [267]. We also studied the possibility that HNLs couple preferentially to top quarks at low energies due to some top-philic UV completions [284]. In such scenarios, HNLs can be produced via rare top decays or in association with top quarks in pp collisions, again leading to enhanced production rates. These scenarios typically feature long-lived HNLs, which yield displaced vertex signatures with jets or other visible tracks in the detectors.

In light of the expanding LLP search program, we derived sensitivity prospects for ATLAS and several proposed far detectors at the LHC (e.g. MATHUSLA, ANUBIS, CODEX-b, MOEDAL-MAPP, FASER and FACET) showing how they can probe long-lived HNLs across the different EFT scenarios. These analyses underscore the importance of pushing forward both LLP searches and the development of far detectors, as they can be uniquely sensitive to certain regions of parameter space inaccessible to traditional searches.

Taken together, our study demonstrates how different operator structures lead to distinct experimental signatures for HNLs with masses ranging from a few MeV up to the TeV scale. While our exploration of the N_RSMEFT framework has already revealed rich phenomenology, several directions remain open. In particular, further investigation of dimension-6 and dimension-7 operators is needed. Of special interest are lepton number violating operators at dimension 7, which can induce same-sign dilepton final states potentially observable at the LHC. These avenues provide natural extensions to the work presented here.

Beyond its specific technical results, this thesis establishes a versatile framework that can support future explorations of sterile neutrinos and other weakly coupled new physics. By organizing possible interactions through effective operators and linking them to experimental observables, it provides a bridge between bottom-up searches and top-down model building. This approach enables both theorists and experimentalists to identify promising signals, interpret potential anomalies, and design future searches in a more targeted and flexible way. In doing so, it contributes to the development of a broader paradigm where EFTs and LLP searches together form a powerful strategy for uncovering new physics.

In summary, this thesis illustrates the value of combining theoretical and experimental perspectives: EFTs as a model-independent language for new physics, and LLP searches as a uniquely sensitive probe of hidden sectors. While the experimental search for HNLs is still in its early stages, the next generation of dedicated LLP detectors, together with the high-luminosity phase of the LHC and future colliders, offer unprecedented opportunities. The work presented here lays the foundation for further studies aiming to chart the landscape of HNL signatures and their ultraviolet origins. In this way, neutrino physics continues to guide our search for answers to some of the most fundamental questions in particle physics.

Resumen de la Tesis

Introducción y objetivos

Uno de los descubrimientos más importantes en la física de partículas del siglo XXI ha sido la confirmación de que los neutrinos tienen masa. Este hecho, demostrado experimentalmente mediante la observación de oscilaciones de sabor entre distintos tipos de neutrinos, contradice las predicciones del Modelo Estándar (*Standard Model*, SM), en el cual los neutrinos son estrictamente no masivos. La existencia de masas de neutrinos constituye, por tanto, una evidencia inequívoca de nueva física más allá del SM, ofreciendo una ventana única hacia sus posibles extensiones.

El estudio del origen de las masas de los neutrinos ha motivado una gran variedad de modelos teóricos, que incorporan nuevas partículas, interacciones o simetrías con el objetivo de explicar este fenómeno. Entre ellos, los modelos *seesaw*, y en particular el *seesaw* tipo I y sus variantes, proponen la existencia de nuevos fermiones neutros, conocidos como neutrinos estériles o leptones neutros pesados (*heavy neutral leptons*, HNLs), que interactúan muy débilmente con las partículas del SM. En el caso del *seesaw* tipo I, por ejemplo, estas nuevas partículas pueden generar masas de neutrinos mediante un mecanismo de supresión natural, al introducir una escala de masa mucho mayor que la escala electrodébil. Sin embargo, otras variantes del mecanismo permiten ubicar la nueva física cerca de la escala electrodébil, haciendo que las partículas asociadas puedan ser accesibles a los experimentos actuales.

En este contexto, si los HNLs existen con masas por debajo de la escala electrodébil, podrían ser producidos en colisionadores como el LHC o en otros experimentos a bajas energías. No obstante, los modelos que introducen HNLs predicen que sus interacciones están fuertemente suprimidas, lo que dificulta su potencial detectabilidad. Esto se debe, en parte, a las pequeñas tasas de producción asociadas y al hecho de que los detectores fueron concebidos inicialmente para detectar partículas masivas desintegrándose en las proximidades de los puntos de colisión. En cambio este tipo de partículas superdébilmente acopladas suelen recorrer distancias macroscópicas antes de desintegrarse, dejando señales en regiones alejadas del vértice primario de colisión. Este tipo de comportamiento es característico de las llamadas partículas de vida media larga (*long-lived particles*, LLPs).

Las LLPs pueden producir señales experimentales exóticas, como vértices desplazados, fotones que no apuntan al vértice primario, o trazas provenientes de partículas cargadas pesadas y lentas. Estas señales son muy difíciles de imitar por parte de las partículas que conocemos del SM y, por tanto, presentan un número de eventos de fondo extremadamente reducido, lo que ha motivado un creciente interés experimental en su búsqueda. Actualmente, tanto los detectores principales del LHC (ATLAS, CMS y LHCb) como propuestas específicas de detectores lejanos como MATHUSLA, FASER, ANUBIS, CODEX-b y MOEDAL-MAPP están explorando activamente este tipo de fenómenos.

Desde el punto de vista teórico, la diversidad de posibles extensiones del SM que dan lugar a nuevas partículas con interacciones superdébiles hace difícil abordar el estudio de la posible fenomenología asociada a la escala de los experimentos. Cada modelo ultravioleta (UV) a altas energía predice diferentes observables que dependen de los parámetros concretos del modelo y estudiar cada uno de estos modelos de manera individual es prácticamente imposible. En este contexto, el enfoque mediante teorías efectivas (*effective field theories*, EFTs) se ha convertido en una herramienta potente y versátil para abordar esta tarea de una forma sistemática. Las EFTs permiten parametrizar los efectos de la nueva física de forma general a bajas energías, sin necesidad de especificar los detalles del modelo completo a alta energías, siempre que exista una separación considerable entre ambas escalas. En particular, la teoría efectiva más ampliamente utilizada es la EFT del Modelo Estándar (*Standard Model* EFT, SMEFT), que introduce operadores de dimensión superior a cuatro ($d > 4$) construidos únicamente con los campos del SM, y cuyos efectos están suprimidos por potencias de una escala de nueva física Λ. El Lagrangiano del modelo puede escribirse como

$$\mathcal{L}_{\text{EFT}} = \mathcal{L}^{(4)} + \sum_{d\geq 5} \frac{1}{\Lambda^{d-4}} \sum_i c_i^{(d)} \mathcal{O}_i^{(d)} \,,$$

donde los coeficientes $c_i^{(d)}$ que acompañan a los operadores esconden los parámetros del modelo a altas energías.

Sin embargo, si se introducen explícitamente neutrinos estériles como nuevos grados de libertad activos por debajo de la escala Λ, el marco efectivo debe extenderse. En esta tesis, se utiliza una versión extendida del SMEFT que incluye neutrinos estériles dextrógiros (con quiralidad derecha), conocida como N_RSMEFT. Esta teoría efectiva permite estudiar de forma sistemática las interacciones de neutrinos estériles con el SM, tanto desde un punto de vista teórico, por ejemplo, clasificando los posibles operadores efectivos y sus orígenes en modelos UV, como desde un punto de vista fenomenológico, analizando sus implicaciones en observables experimentales.

El objetivo general de esta tesis doctoral es explorar el papel de las partículas superdébilmente acopladas, en particular los HNLs, en la física de neutrinos y en la fenomenología de colisionadores, mediante el uso del formalismo de teorías efectivas. Para ello, se abordan dos aspectos principales:

1. **Marco teórico efectivo con neutrinos estériles**: Se presenta y discute la extensión del SMEFT con neutrinos estériles (N_RSMEFT), y su versión a bajas energías (N_RLEFT), la cual permite describir procesos como desintegraciones de mesones. Se identifican los operadores relevantes hasta dimensión 6 en N_RLEFT y hasta dimensión 7 en N_RSMEFT. Asimismo, se analiza el posible origen de estos últimos en modelos ultravioletas (UV). Se emplea una metodología sistemática para clasificar las posibles descomposiciones de estos operadores a partir de nuevas partículas mediadoras a altas energías.

2. **Fenomenología de HNLs como partículas de vida media larga**: Se estudia la posibilidad de que los HNLs generen señales observables en el LHC u otros experimentos, actuando como partículas de vida media larga (LLPs). Se analiza el impacto de subconjuntos específicos de operadores de N_RSMEFT sobre la producción y desintegración de HNLs, considerando distintos rangos de masa para los HNLs. Se identifican en cada caso las señales experimentales más características, destacando los vértices desplazados, o fotones que no apuntan al origen de la colisión.

La tesis está organizada en tres partes. La primera parte introduce la física de neutrinos como un portal hacia nueva física, repasando brevemente los modelos de masas de neutrinos más característicos que introducen neutrinos estériles y los desafíos para detectar partículas débilmente acopladas. En la segunda parte se presenta el marco teórico de EFTs con neutrinos estériles, detallando tanto el formalismo de N_RSMEFT como su relación con modelos ultravioletas mediante una clasificación completa de posibles descomposiciones a nivel árbol de los operadores de dimensión 6 y 7. En la tercera parte se estudia la fenomenología asociada a distintas clases de operadores efectivos, analizando cómo los HNLs pueden generar señales en experimentos actuales o propuestos, y qué regiones del espacio de parámetros pueden ser exploradas en el futuro cercano por éstos.

En resumen, los objetivos principales de esta tesis se pueden sintetizar en los siguientes puntos:

- Estudiar y aplicar una teoría efectiva que incluya explícitamente neutrinos estériles para describir de forma general sus posibles interacciones con el SM.
- Clasificar los posibles orígenes ultravioletas de los operadores efectivos relevantes, utilizando herramientas automatizadas y un método diagramático.
- Analizar la fenomenología de los HNLs como partículas de vida media larga en el LHC y otros experimentos, identificando las señales más características y estimando el alcance y sensibilidad de dichos experimentos para detectar estas partículas.
- Contribuir al programa de búsqueda de nueva física desde un enfoque independiente del modelo UV existente a altas energías, combinando herramientas de EFT, fenomenología de LLPs y motivaciones desde la física de neutrinos.

METODOLOGÍA Y RESULTADOS

Esta tesis propone un enfoque sistemático para el estudio de partículas superdébilmente acopladas, en particular leptones neutros pesados (HNLs), mediante teorías de campos efectivas (EFTs). El objetivo principal de esta metodología es establecer un puente entre descripciones a baja energía y posibles teorías subyacentes de nueva física a altas energías, explorando tanto su estructura teórica como sus manifestaciones experimentales en colisionadores.

La tesis se articula en tres ejes principales:

1. La revisión del formalismo N_RSMEFT, una EFT que extiende el SMEFT para incluir explícitamente neutrinos estériles como nuevos grados de libertad.
2. La descomposición sistemática a nivel árbol de operadores efectivos en posibles completaciones ultravioletas (UV).
3. La exploración fenomenológica de HNLs como partículas de vida media larga (LLPs) en el LHC y futuros detectores especializados en LLPs.

Cada uno de estos ejes emplea metodologías diferenciadas que combinan técnicas analíticas y herramientas computacionales, simulaciones numéricas y análisis de sensibilidad de distintos experimentos. A continuación se detallan los métodos y resultados correspondientes a cada uno de los tres bloques.

1. N_RSMEFT: FORMALISMO Y CATÁLOGO DE OPERADORES

El punto de partida teórico de esta tesis es el marco conocido como N_RSMEFT (*Standard Model Effective Field Theory with Right-Handed Neutrinos*), una extensión del SMEFT en la que se introduce al menos un campo fermiónico singlete N_R, interpretado como un neutrino estéril. Este enfoque permite parametrizar de manera general los efectos de modelos de nueva física (que involucran a HNLs) a la escala electrodébil, sin necesidad de especificar una teoría UV concreta.

Si bien el N_RSMEFT ha sido propuesto y desarrollado previamente en la literatura, en esta tesis se presenta una revisión sistemática del contenido de operadores hasta dimensión 7, con el objetivo de establecer un marco de referencia común para los análisis posteriores de completaciones UV y aplicaciones fenomenológicas. Esta revisión incluye la organización y discusión de los operadores más relevantes desde el punto de vista teórico y experimental.

La base de operadores considerada está compuesta por términos invariantes bajo el grupo de simetría gauge del Modelo Estándar, $SU(3)_C \times SU(2)_L \times U(1)_Y$, construidos a partir de campos del SM y al menos una copia de N_R. Estos operadores, sin embargo, pueden conservar o violar el número leptónico y/o el número bariónico.

La presentación se organiza según la dimensión de los operadores, y según su contenido de campos — derivadas, fermiones, campos escalares (Higgs) y vectores de gauge. Se presta especial atención a aquellas estructuras potencialmente relevantes para procesos observables en colisionadores o en experimentos de baja energía.

Entre los ejemplos más destacados que se discuten en la tesis se encuentran:

- Operadores con cuatro fermiones que contienen quarks y singletes N_R. Este tipo de operadores permite producir HNLs en procesos hadrónicos, como las colisiones protón-protón que tienen lugar en el LHC. Se incluyen en esta categoría operadores con dos singletes N_R, como por ejemplo, $\mathcal{O}_{QN} = (\overline{Q}\gamma_\mu Q)(\overline{N_R}\gamma^\mu N_R)$, y con un singlete, como $\mathcal{O}_{duNe} = (\overline{d_R}\gamma_\mu u_R)(\overline{N_R}\gamma^\mu e_R)$.
- Operadores que involucran los vectores de gauge del grupo $SU(2)_L \times U(1)_Y$, capaces de generar momentos magnéticos de los neutrinos a bajas energía. Esta categoría incluye el operador a $d = 5$ $\mathcal{O}_{NNB} = (\overline{N_R^c}\sigma_{\mu\nu}N_R)B^{\mu\nu}$ y los operadores a $d = 6$ $\mathcal{O}_{NHB} = (\overline{L}\sigma_{\mu\nu}N_R)\tilde{H}B^{\mu\nu}$ y $\mathcal{O}_{NHW} = (\overline{L}\sigma_{\mu\nu}N_R)\tau^I\tilde{H}W^{I\mu\nu}$.

En la discusión también se identifican los operadores que violan el número bariónico, altamente restringidos por las cotas experimentales sobre la vida media del protón, así como los que violan el número leptónico, con especial interés aquellos que lo violan en dos unidades ($\Delta L = 2$), al ser relevantes en procesos como la desintegración doble beta sin emisión de neutrinos ($0\nu\beta\beta$ decay).

Esta recopilación exhaustiva de operadores sienta las bases para los dos bloques de trabajo originales de la tesis: la descomposición UV de estos términos efectivos en interacciones renormalizables con nuevos mediadores, y su aplicación fenomenológica al estudio de señales de partículas de vida media larga (LLPs) en el LHC y en detectores especializados en LLPs.

2. DESCOMPOSICIÓN UV A NIVEL ÁRBOL DE OPERADORES DE N_RSMEFT

Una de las contribuciones principales de esta tesis consiste en establecer una conexión sistemática entre los operadores de N_RSMEFT y posibles modelos de nueva física en el régimen ultravioleta. Para ello, se realiza la descomposición (a nivel árbol) de los operadores efectivos en interacciones renormalizables. Este procedimiento permite identificar qué partículas mediadoras (caracterizadas por su *spin* y números cuánticos del grupo de simetría gauge) pueden originar una determinada interacción efectiva a bajas energía, y qué tipo de interacciones deben existir en el UV.

El análisis de las distintas descomposiciones se lleva a cabo siguiendo un método diagramático, que se puede resumir en los siguientes pasos:

1. **Construcción de topologías**. Se generan las posibles topologías a nivel árbol que pueden originar cada tipo de operador con un número dado de campos. Una topología se define como un grafo con un conjunto de patas externas conectadas por líneas internas utilizando interacciones renormalizables.

2. **Obtención de diagramas**. Al asignar los campos del operador a las patas externas de cada topología, se impone la invariancia de Lorentz en cada vértice para determinar la naturaleza o *spin* de los campos internos (escalares, vectores o fermiones). De este modo, se obtienen distintas clases de diagramas compatibles con la estructura del operador, donde todas las líneas tienen el spin fijado.

3. **Identificación de los modelos**. Finalmente, se impone la invariancia gauge bajo $SU(3)_C \times SU(2)_L \times U(1)_Y$ para determinar los números cuánticos de las partículas mediadoras, identificando así los posibles modelos UV subyacentes.

Este procedimiento se implementa de forma automatizada mediante un paquete desarrollado en `Mathematica`, que permite generar los diagramas, imponer las simetrías de Lorentz y gauge, y eliminar redundancias. Además, se emplean herramientas como `Sym2Int` y `MatchMakerEFT` para escribir las interacciones renormalizables de los modelos en el UV y realizar el *matching* entre los operadores efectivos y los modelos obtenidos.

Esta sección también aborda de forma detallada la violación del número leptónico (*lepton number violation*, LNV) en el marco de N_RSMEFT y su conexión con la la observación de procesos LNV en el LHC y con la generación de masas de Majorana para los neutrinos del SM. En particular, se demuestra que la presencia simultánea de operadores de dimensión 6 y 7 de N_RSMEFT conduce de manera inevitable a la violación del número leptónico. Esta conexión implica una contribución directa de dichos operadores a la masa de los neutrinos del SM, lo cual permite derivar restricciones sobre los modelos UV que los generan. Se analizan distintos casos concretos de modelos para operadores de dimensión 7 y se extraen cotas utilizando las relaciones de *matching* establecidas.

Los resultados principales de esta sección incluyen:

- La identificación de todas las extensiones con una o dos partículas mediadoras capaces de generar operadores de N_RSMEFT hasta dimensión 7 a nivel árbol.
- La observación de que un mismo operador puede ser generado por múltiples modelos UV, y que, a su vez, algunos mediadores pueden inducir simultáneamente varios operadores, estableciendo correlaciones entre procesos observables a bajas energías.
- La demostración de que la conexión entre la violación del número leptónico en N_RSMEFT y la generación de masas de Majorana para neutrinos del SM no excluye la posibilidad de que ciertos operadores de dimensión 7 produzcan efectos observables en los experimentos actuales o futuros.

Estos resultados fueron sistematizados en una clasificación exhaustiva y tabulada, lo que constituye una herramienta útil para guiar la construcción de modelos UV, explorar nuevas señales fenomenológicas, y conectar la EFT con mecanismos concretos de generación de masa de neutrinos.

El trabajo presentado en esta sección, correspondiente al Capítulo 5, constituye una contribución original de la tesis y fue desarrollado en colaboración con otros autores. Los resultados completos fueron publicados en el artículo "Tree-level UV completions for N_RSMEFT $d = 6$ and $d = 7$ operators" [156].

3. Aplicación fenomenológica de operadores de N_RSMEFT

La tercera línea de trabajo de esta tesis está dedicada al estudio fenomenológico de los leptones neutros pesados (HNLs) como partículas de vida media larga (LLPs) en colisionadores y experimentos asociados al LHC. En este contexto, se realizan análisis de sensibilidad de búsquedas de señales de LLPs para investigar la presencia de HNLs en los marcos efectivos descritos en la Parte II, concretamente N_RSMEFT y N_RLEFT.

Este enfoque extiende el escenario más minimalista de los HNLs, en el que éstos interactúan únicamente a través de su mezcla con los neutrinos del SM, al considerar interacciones adicionales representadas por operadores no renormalizables de N_RSMEFT. De este modo, se abarca una clase amplia de procesos potencialmente relevantes en colisionadores y experimentos de baja energía. En los escenarios considerados, los HNLs se producen y/o desintegran mediante operadores efectivos de dimensión 5 o 6, cuyas estructuras permiten explorar acoplamientos superdébiles asociados a escalas de nueva física por encima del TeV.

En tales contextos, los HNLs presentan tiempos de vida lo suficientemente largos como para recorrer distancias macroscópicas antes de desintegrarse dentro o fuera del detector, generando señales caracterísitcas como:

- Vértices desplazados en los detectores principales del LHC, como ATLAS o CMS.
- Señales con fotones que no apuntan al vértice primario.
- Desintegraciones en detectores lejanos situados a decenas o cientos de metros del punto de colisión (por ejemplo, MATHUSLA, FASER, ANUBIS, CODEX-b, MOEDAL-MAPP).

Este régimen es particularmente atractivo desde el punto de vista experimental, ya que las señales asociadas a LLPs suelen presentar eventos de fondo prácticamente nulos, permitiendo alcanzar sensibilidades incluso cuando las tasas de producción de las LLPs son muy bajas.

La metodología seguida consiste en seleccionar operadores de N_RSMEFT (o N_RLEFT) con potencial para producir HNLs que generen señales de LLPs. Se identifican dos clases de escenarios donde los operadores juegan un papel relevante:

- Escenarios donde los HNLs se producen en desintegraciones de mesones.
- Escenarios donde los HNLs se producen en directamente en las colisiones de partones en el LHC.

A continuación se detallan los estudios principales desarrollados en esta tesis que exploran los dos escenarios mencionados, los cuales cubren distintos rangos de masa, mecanismos de producción y canales de desintegración de los HNLs.

a) Producción de HNLs en desintegraciones de mesones.
Uno de los canales más prometedores para la búsqueda de HNLs de baja masa (hasta unos pocos GeV) es su producción en desintegraciones de mesones pesados, como los mesones pseudoescalares B y D. Estos mesones se producen abundantemente en el LHC, lo que permite investigar canales de desintegración de mesones extremadamente raros. Además, estos procesos también son relevantes en experimentos dedicados a la física de sabor o a la búsqueda de partículas exóticas, tales como NA62, SHiP o Belle II. El presente estudio investiga cómo las búsquedas de LLPs en el LHC pueden aportar información complementaria a la de estos experimentos.

Las desintegraciones de mesones pueden estudiarse en el marco teórico de N_RLEFT, donde las interacciones entre HNLs y quarks se describen mediante operadores de cuatro fermiones. Estos operadores pueden conservar o violar número leptónico (LNC o LNV, respectivamente). Por ejemplo, destacamos

$$\begin{aligned}
\text{LNC:}\quad & \mathcal{O}_{dN,ij}^{V,RR} = (\overline{d_R^i}\gamma^\mu d_R^j)(\overline{N_R}\gamma_\mu N_R)\,, \quad \mathcal{O}_{d\nu N,ij}^{S,RR} = (\overline{d_L^i} d_R^j)(\overline{\nu_L} N_R)\,, \\
\text{LNV:}\quad & \mathcal{O}_{uN,ij}^{S,RR} = (\overline{u_L^i} u_R^j)(\overline{N_R^c} N_R)\,, \quad \mathcal{O}_{uN,ij}^{V,RR} = (\overline{u_R^i}\gamma^\mu u_R^j)(\overline{\nu_L^c}\gamma_\mu N_R)\,.
\end{aligned}$$

Dependiendo de los índices de sabor (i, j) de los quarks involucrados, se abren diferentes canales de desintegración de mesones con HNLs y otras partículas en el estado final. Este estudio se centra particularmente en los operadores con dos quarks y dos leptones neutros (ya sea dos HNLs, o un HNL y un neutrino del SM), los cuales producen la desintegración de mesones mediante corrientes neutras. En el caso de los operadores con dos HNLs, la desintegración de los HNLs ocurre a través de la mezcla con neutrinos del SM, por lo que los HNLs son potenciales LLPs si dicha mezcla es suficientemente pequeña.

Para determinar la sensibilidad de los detectores lejanos del LHC a los HNLs, interactuando a través de su mezcla con neutrinos y de los operadores efectivos seleccionados, se realiza un análisis en dos etapas:

1. **Cálculo de la tasa de producción de HNLs**: En el marco de N_RLEFT, se calculan las tasas de desintegración de mesones B y D en HNLs, incorporando factores de forma y constantes de desintegración extraídas de la literatura. Se exploran varios operadores con distintas combinaciones de sabor de los quarks, que dan lugar a múltiples escenarios de producción de HNLs.

2. **Simulación de propagación y desintegración**: Para cada escenario, se realizan simulaciones del tiempo de vida medio de los HNLs como función de su masa y acoplamiento (mezcla con neutrinos), que puede variar desde unos pocos centímetros hasta cientos de metros. Se evalúa la probabilidad de desintegración dentro del volumen de los detectores lejanos del LHC (como FASER, ANUBIS o MATHUSLA).

Este estudio permite:

- Cuantificar la producción de HNLs en desintegraciones de mesones como función de su masa y los coeficientes efectivos relevantes.
- Determinar las regiones de sensibilidad de múltiples experimentos, evaluando la probabilidad de detección.
- Establecer proyecciones futuras para estos detectores en el espacio de parámetros definido por las masas, mezclas y coeficientes de los operadores.

Los resultados muestran que, para masas de HNL entre 500 MeV y 3 GeV, los experimentos mencionados tienen una sensibilidad significativa a canales dominados por operadores de dimensión 6 de N_RLEFT, mejorando los límites actuales en varios órdenes de magnitud. Este trabajo, correspondiente al Capítulo 6, fue presentado en el artículo "Long-lived heavy neutral leptons from mesons in effective field theory" [175].

b) Momentos magnéticos de HNLs.

Un escenario particularmente interesante ocurre cuando los HNLs poseen momentos magnéticos de transición que conectan 1) neutrinos estériles con neutrinos activos o 2) diferentes generaciones de neutrinos estériles. Estas interacciones magnéticas pueden describirse mediante los operadores de dimensión 5 de N_RLEFT,

$$\mathcal{O}_{NN\gamma} = (\overline{N_R^c}\sigma_{\mu\nu}N_R)F^{\mu\nu}\,, \quad \mathcal{O}_{\nu N\gamma} = (\overline{\nu_L^c}\sigma_{\mu\nu}N_R)F^{\mu\nu}$$

Asumiendo que N_RLEFT proviene de N_RSMEFT, los operadores anteriores se generan, a su vez, a partir de los operadores de N_RSMEFT siguientes:

$$\begin{aligned}
&\mathcal{O}_{NNB} = (\overline{N_R^c}\sigma_{\mu\nu}N_R)B^{\mu\nu}\,, \\
&\mathcal{O}_{NHB} = (\overline{L}\sigma_{\mu\nu}N_R)\tilde{H}B^{\mu\nu}\,, \quad \mathcal{O}_{NHW} = (\overline{L}\sigma_{\mu\nu}N_R)\tau^I\tilde{H}W^{I\mu\nu}
\end{aligned}$$

Estos operadores generan nuevas interacciones entre los HNLs los bosones Z y W y el fotón a la escala electrodébil, abriendo nuevos modos de producción de HNLs en el

LHC. Además, desencadenan desintegraciones radiativas como $N_2 \to N_1\gamma$ o $N_i \to \nu\gamma$, que pueden dar lugar a señales exóticas si el HNL que se desintegra es una LLP.

El origen de estos momentos magnéticos puede justificarse en modelos UV. En este trabajo se presenta un modelo sencillo con solo dos nuevas partículas cargadas: un escalar $\phi \sim (\mathbf{1}, \mathbf{1}, -1)$ y un fermión $E \sim (\mathbf{1}, \mathbf{1}, -1)$. El Lagrangiano del modelo viene descrito por

$$\begin{aligned}\mathcal{L} \supset\ & \bar{E}\left(i\not{D} - m_E\right)E + (D_\mu\phi)^*(D^\mu\phi) - m_\phi^2|\phi|^2 - \lambda_{\phi\phi}|\phi|^4 - \lambda_{\phi H}|\phi|^2(H^\dagger H) \\ & - \Big[\bar{N}_R h E_L \phi^* + \bar{N}_R^c h' E_R \phi^* \\ & \quad + \bar{L} Y_E H E_R + \bar{E}_L m_{eE} e_R + \bar{L} f \tilde{L} \phi + \bar{N}_R^c f' e_R \phi^* + \text{h.c.}\Big] .\end{aligned}$$

Estas interacciones generan momentos magnéticos de los neutrinos estériles mediante diagramas de 1-loop. Además, estas interacciones también contribuyen a distintos observables en la fenomenología de sabor, fuertemente restringidos por datos experimentales, lo cual impone cotas sobra las masas y acoplamientos de E y ϕ. Estas restricciones se incorporan al análisis para estimar el orden de magnitud esperable del momento magnético en función de los parámetros del modelo.

Este estudio tiene como objetivo determinar la sensibilidad del experimento ATLAS para detectar HNLs con momentos magnéticos. Para ello, se utiliza el marco de N_RSMEFT para describir las interacciones correspondientes a la escala de energías del LHC. Se consideran dos HNLs con masas diferentes, interactuando entre si y con los leptones del SM mediante los operadores $\mathcal{O}_{NNB}$, $\mathcal{O}_{NHB}$ y $\mathcal{O}_{NHW}$ y mediante el acoplamiento de mezcla con los neutrinos del SM. Dependiendo de qué interacción domine la producción y/o desintegración de los HNLs se identifican nueve escenarios teóricamente posibles, de los cuales se seleccionan los más prometedores para búsquedas de LLPs. Se realizan simulaciones numéricas de los escenarios seleccionados que tienen como señal característica fotones que no apuntan al vértice primario (*non-pointing photons*).

La metodología consiste en simular, para cada escenario, la producción de HNLs en el LHC seguida de su desintegración en el detector ATLAS. Para ello, se utilizan herramientas de simulación como:

- `MadGraph5`, para la generación de eventos a partir de los operadores efectivos.
- `Pythia8` para la hadronización y la desintegración de los HNLs, así como para la simulación de la respuesta del detector en la reconstrucción de los fotones *non-pointing*.

Los principales resultados de este estudio son:

- Los fotones *non-pointing* provenientes de HNLs con masas por encima del GeV presentan prácticamente cero eventos de fondo del SM, lo que permite establecer límites muy competitivos sobre el momento magnético de neutrinos estériles pesados.
- Se construyen curvas de exclusión para el momento magnético en función de la masa del HNL, mostrando que las búsquedas de señales de LLPs en detectores como ATLAS pueden extender significativamente la cobertura del espacio de parámetros.
- Estas curvas se traducen también al espacio de parámetros del modelo UV considerado, en particular, en el plano de masa vs. acoplamiento del nuevo escalar ϕ y fermión E.

Este estudio, presentando en el Capítulo 7, representa una de las primeras evaluaciones sistemáticas del potencial del LHC para estudiar momentos magnéticos de neutrinos estériles con masas por encima del GeV mediante búsquedas de LLPs. Los resultados fueron publicados en el artículo "Probing Heavy Neutrino Magnetic Moments at the LHC using Long-lived Particle Searches" [206].

c) Producción de HNLs a partir de quarks ligeros y quark top.

Una tercera línea de análisis fenomenológico explora la posibilidad de producir HNLs con masas por encima del GeV directamente en colisiones protón-protón o a partir de desintegraciones del quark top. Esta segunda idea resulta atractiva por varias razones:

- El top es la partícula más pesada del SM, lo que permite acceder a un rango más amplio de masas de HNLs (hasta 100 GeV o más).
- En el LHC, el quark top se produce de manera abundante y está bien estudiado, lo que permite implementar búsquedas dedicadas con buenas estadísticas.

En el contexto del LHC, los operadores efectivos relevantes en N_RSMEFT son, por ejemplo

$$
\begin{aligned}
\mathcal{O}_{uN}^{ij} &= (\overline{u_R^i}\gamma_\mu u_R^j)(\overline{N_R}\gamma^\mu N_R)\,,\\
\mathcal{O}_{duNe}^{ij} &= (\overline{d_R^i}\gamma_\mu u_R^j)(\overline{N_R}\gamma^\mu e_R)\,,\\
\mathcal{O}_{QuNL}^{ij} &= (\overline{Q^i}u_R^j)(\overline{N_R}L)\,,
\end{aligned}
$$

Los índices de sabor $(i, j = 1, 2, 3)$ de los operadores determinan con qué generaciones de quarks interactúan los HNLs. En este línea se realizaron dos estudios independientes: uno centrado en operadores con quarks únicamente de la primera y segunda generación, presentado en el Capítulo 8, y otro en operadores que involucran al menos un quark top (es decir, un quark up de tercera generación), presentado en el Capítulo 9.

En ambos casos se distingue entre operadores que contienen un único HNL y aquellos que contienen dos. Los primeros contribuyen tanto a la producción como a la desintegración del HNL, mientras que los segundos solo contribuyen a la producción; en este último caso, se asume que el HNL se desintegra mediante su mezcla con los neutrinos del SM. Ambos escenarios conducen a HNLs de vida media larga, por lo que se realiza un análisis de las búsquedas de LLPs en el LHC que sean sensibles a sus señales.

La señal característica en estos escenarios es la aparición de vértices desplazados, producto de la desintegración del HNL a distancias alejadas del vértice primario de colisión. El análisis se centra en la búsqueda de esta señal, simulando el proceso $pp \to N\ell\,, (\ell = e, \mu, \tau)$, en el caso del estudio del Capítulo 8 (o, por ejemplo, $pp \to t\bar{t}, t \to qN\bar{N}$ en el caso del Capítulo 9), seguido de la desintegración del HNL dentro del volumen de ATLAS, generando un vértice desplazado con leptones o jets. Se estudia la cinemática de estos procesos, la eficiencia de reconstrucción de los vértices, y las regiones del espacio de parámetros que podrían explorarse en la fase de alta luminosidad del LHC. Para el estudio con quarks top (Capítulo 9) se considera además la posibilidad de que los HNLs escapen del detector principal y se desintegren en los detectores lejanos del LHC, como MATHUSLA, ANUBIS, CODEX-b o MOEDAL-MAPP, obteniéndose su sensibilidad esperada.

Los principales resultados muestran que:

- Para masas de HNL entre 10 y 100 GeV, las búsquedas en el sector top permiten explorar escalas de nueva física del orden de varios TeV.
- Los canales de producción considerados son complementarios a los canales de producción desde mesones, ya que son sensibles a regiones diferentes masas y tiempos de vida.
- Las búsquedas de vértices desplazados con leptones o jets en ATLAS tienen potencial para descubrir señales con muy pocos eventos de fondo.

Estos estudio fueron desarrollados a partir de los trabajos presentados en los artículos “Heavy neutral leptons and top quarks in effective field theory” [284] y “Long-lived heavy neutral leptons at the LHC: four-fermion single-N_R operators” [267].

En resumen, los cuatro estudios descritos en la Parte III de la tesis muestran cómo los operadores efectivos de N_RSMEFT (y su límite a baja energía N_RLEFT) pueden originar una gran variedad de señales experimentales para HNLs, muchas de ellas no contempladas en los modelos simplificados considerados generalmente en los análisis experimentales. La consideración explícita de estos operadores permite:

- Identificar nuevas señales experimentales asociadas a HNLs, viables en los detectores actuales del LHC y en la próxima generación de detectores dedicados a LLPs.
- Establecer límites competitivos sobre acoplamientos efectivos poco explorados, como momentos magnéticos o interacciones con quarks pesados.
- Comparar distintos escenarios de nueva física sin necesidad de especificar un modelo UV en particular.

Estas contribuciones amplían significativamente el rango de escenarios teóricos y observables experimentales asociados a neutrinos estériles, posicionando al enfoque efectivo como una herramienta versátil en la búsqueda de nueva física más allá del SM.

CONCLUSIONES

A lo largo de esta tesis doctoral se ha abordado el estudio de partículas débilmente acopladas, en particular, leptones neutros pesados (HNLs), como una ventana hacia nueva física más allá del Modelo Estándar (SM). Este trabajo se ha estructurado en torno a una idea central: la combinación de teorías efectivas y búsquedas de partículas de vida media larga (LLPs) constituye una estrategia poderosa y flexible para explorar escenarios motivados por el problema del origen de las masas de los neutrinos.

En la primera parte de la tesis se contextualizó el papel de los neutrinos como una pista clave hacia nueva física. Tras repasar las posibles extensiones del SM que incorporan neutrinos estériles, se hizo énfasis en la necesidad de ir más allá del enfoque minimalista de mezcla activa-estéril. En este marco, se introdujo el uso de teorías efectivas, específicamente N_RSMEFT y su límite a baja energía, N_RLEFT, como herramientas que permiten describir interacciones generales entre los HNLs y el contenido del SM sin necesidad de especificar una teoría UV.

La segunda parte se centró en la formulación y clasificación sistemática de los operadores efectivos relevantes, hasta dimensión 6 y 7. Si bien el N_RSMEFT se ha presentado en unos pocos artículos, se ofreció una presentación detallada y completa de sus operadores hasta dimensión 7, poniendo especial atención en su estructura y posibles aplicaciones fenomenológicas. Asimismo, se analizó el paso al límite de baja energía, en el cual se manifiestan procesos como las desintegraciones de mesones.

En la tercera parte se aplicó este marco teórico a estudios fenomenológicos originales. Se exploraron distintos escenarios experimentales en los cuales los HNLs podrían producirse y desintegrarse, dando lugar a señales características de partículas de vida media larga. Entre los principales resultados se destacan: (i) el análisis de producción de HNLs en desintegraciones de mesones, con especial relevancia para los detectores lejanos; (ii) el estudio del momento magnético de HNLs y su impacto en búsquedas de fotones *non-pointing* en ATLAS; y (iii) la producción de HNLs desde el sector top del LHC, como una vía complementaria para acceder a masas más elevadas. En todos los casos se obtuvieron nuevas proyecciones de sensibilidad y se delimitaron regiones del espacio de parámetros que podrían ser exploradas en futurs programas experimentales.

En conjunto, esta tesis contribuye al desarrollo de un enfoque más general, sistemático y realista para el estudio de neutrinos estériles, teniendo en cuenta tanto los desafíos teóricos como las oportunidades experimentales. Los resultados obtenidos resaltan el valor de adoptar una perspectiva basada en EFTs y búsquedas de LLPs para maximizar la sensibilidad a nueva física débilmente acoplada.

Finalmente, esta línea de investigación permanece abierta a múltiples extensiones, incluyendo el estudio de procesos con violación de número leptónico, así como la conexión con un sector oscuro y los mecanismos específicos de generación de masa de neutrinos. Los métodos y resultados aquí desarrollados sientan las bases para avanzar en esas direcciones futuras.

APPENDIX

Appendix A

UV Lagrangian for N_RSMEFT

This appendix, which complements Chapter 5, is based on the appendix of Ref. [156]. The UV Lagrangian describing renormalizable interactions among the SM fields, the singlet N_R, and the new BSM fields introduced in Tables 5.1 - 5.3, can be expressed as

$$\mathcal{L}_{\text{UV}} = \mathcal{L}_{\text{light}} + \mathcal{L}_{\text{mixed}} + \mathcal{L}_{\text{heavy}} .$$

The first term includes interactions involving only the SM fields and the N_R, $\mathcal{L}_{\text{mixed}}$ describes the interactions between the light fields and the heavy BSM fields, while the last term contains the interactions of the heavy fields among themselves.

In this appendix, we write down all renormalizable terms in which the light singlet N_R is involved. Additionally, we provide the Lagrangian terms that include the new vector field $\mathcal{U}_1$ and new interactions for the vector $\mathcal{L}_1$ not considered in Ref. [157]. Finally, we present the interaction terms belonging to $\mathcal{L}_{\text{heavy}}$ that contribute to the model diagrams leading to N_RSMEFT operators at $d = 7$.

The Lagrangian $\mathcal{L}_{\text{light}}$ comprises the renormalizable SM Lagrangian, the mass term for N_R,[1] and the allowed Yukawa interaction for the singlet. It is expressed as

$$\mathcal{L}_{\text{light}} = \mathcal{L}_{\text{SM}} - \frac{1}{2}\overline{N_R^c} M_R N_R - \overline{L}\tilde{H} Y_\nu N_R + \text{h.c.} \tag{A.1}$$

The interactions involving N_R in $\mathcal{L}_{\text{mixed}}$ can be classified into two categories: fermion-fermion-scalar (*FFS*) and fermion-fermion-vector (*FFV*) interactions. Each category includes two types of terms: A) those with one light field (N_R) and two heavy fields,

[1] Notice we only write down a Majorana mass for N_R. We further discuss this in Section 5.3.

and B) those with two light fields (either one or two N_R) and one heavy field. We gather all these interactions in $\mathcal{L}^{N_R}_{\text{mixed}}$, which is given by [2]

$$\mathcal{L}^{N_R}_{\text{mixed}} = \mathcal{L}^{N_R}_{FFS,(A)} + \mathcal{L}^{N_R}_{FFS,(B)} + \mathcal{L}^{N_R}_{FFV,(A)} + \mathcal{L}^{N_R}_{FFV,(B)}\,, \tag{A.2}$$

where

$$\begin{aligned}
\mathcal{L}^{N_R}_{FFS,(A)} = {} & y^{\mathcal{S}}_{N\mathcal{N}_R}\left(\overline{N^c_R}\mathcal{N}_R\right)\mathcal{S} + y^{\mathcal{S}}_{N\mathcal{N}_L}\left(\overline{N_R}\mathcal{N}_L\right)\mathcal{S} \\
& + y^{\mathcal{S}_1}_{NE_R}\left(\overline{N^c_R}E_R\right)\mathcal{S}_1 + y^{\mathcal{S}_1}_{NE_L}\left(\overline{N_R}E_L\right)\mathcal{S}_1 \\
& + y^{\varphi}_{N\Delta_{1R}}\left(\overline{N^c_R}\Delta_{1R}\right)\varphi + y^{\varphi}_{N\Delta_{1L}}\left(\overline{N_R}\Delta_{1L}\right)\varphi \\
& + y^{\Xi}_{N\Sigma_R}\left(\overline{N^c_R}\Sigma_R\right)\Xi + y^{\Xi}_{N\Sigma_L}\left(\overline{N_R}\Sigma_L\right)\Xi \\
& + y^{\Xi_1}_{N\Sigma_{1R}}\left(\overline{N^c_R}\Sigma_{1R}\right)\Xi_1 + y^{\Xi_1}_{N\Sigma_{1L}}\left(\overline{N_R}\Sigma_{1L}\right)\Xi_1 \\
& + y^{\omega_1}_{ND_R}\left(\overline{N^c_R}D_R\right)\omega_1^\dagger + y^{\omega_1}_{ND_L}\left(\overline{N_R}D_L\right)\omega_1^\dagger \\
& + y^{\omega_2}_{NU_R}\left(\overline{N^c_R}U_R\right)\omega_2^\dagger + y^{\omega_2}_{NU_L}\left(\overline{N_R}U_L\right)\omega_2^\dagger \\
& + y^{\Pi_1}_{NQ_{1R}}\left(\overline{N^c_R}Q_{1R}\right)\Pi_1^\dagger + y^{\Pi_1}_{NQ_{1L}}\left(\overline{N_R}Q_{1L}\right)\Pi_1^\dagger \\
& + y^{\Pi_7}_{NQ_{7R}}\left(\overline{N^c_R}Q_{7R}\right)\Pi_7^\dagger + y^{\Pi_7}_{NQ_{7L}}\left(\overline{N_R}Q_{7L}\right)\Pi_7^\dagger \\
& + y^{\zeta}_{NT_{1R}}\left(\overline{N^c_R}T_{1R}\right)\zeta^\dagger + y^{\zeta}_{NT_{1L}}\left(\overline{N_R}T_{1L}\right)\zeta^\dagger + \text{h.c.}\,,
\end{aligned} \tag{A.3}$$

$$\begin{aligned}
\mathcal{L}^{N_R}_{FFS,(B)} = {} & y^{\mathcal{S}}_{NN}\left(\overline{N^c_R}N_R\right)\mathcal{S} + y^{\mathcal{S}_1}_{Ne}\left(\overline{N^c_R}e_R\right)\mathcal{S}_1 + y^{\varphi}_{NL}\left(\overline{N_R}L\right)\varphi \\
& + y^{\omega_1}_{Nd}\left(\overline{N^c_R}d_R\right)\omega_1^\dagger + y^{\omega_2}_{Nu}\left(\overline{N^c_R}u_R\right)\omega_2^\dagger + y^{\Pi_1}_{QN}\left(\overline{Q}N_R\right)\Pi_1 \\
& + y_{N\Delta_{1R}}\left(\overline{N^c_R}\Delta_{1R}\right)H + y_{N\Delta_{1L}}\left(\overline{N_R}\Delta_{1L}\right)H + \text{h.c.}\,,
\end{aligned} \tag{A.4}$$

$$\begin{aligned}
\mathcal{L}^{N_R}_{FFV,(A)} = {} & g^{\mathcal{B}}_{N\mathcal{N}_R}\left(\overline{N_R}\gamma_\mu\mathcal{N}_R\right)\mathcal{B}^\mu + g^{\mathcal{B}}_{N\mathcal{N}_L}\left(\overline{N^c_R}\gamma_\mu\mathcal{N}_L\right)\mathcal{B}^\mu \\
& + g^{\mathcal{B}_1}_{NE_R}\left(\overline{N_R}\gamma_\mu E_R\right)\mathcal{B}_1^\mu + g^{\mathcal{B}_1}_{NE_L}\left(\overline{N^c_R}\gamma_\mu E_L\right)\mathcal{B}_1^\mu \\
& + g^{\mathcal{L}_1}_{N\Delta_{1R}}\left(\overline{N_R}\gamma_\mu\Delta_{1R}\right)\mathcal{L}_1^\mu + g^{\mathcal{L}_1}_{N\Delta_{1L}}\left(\overline{N^c_R}\gamma_\mu\Delta_{1L}\right)\mathcal{L}_1^\mu \\
& + g^{\mathcal{L}_3}_{N\Delta_{3R}}\left(\overline{N_R}\gamma_\mu\Delta_{3R}\right)\mathcal{L}_3^{\mu\dagger} + g^{\mathcal{L}_3}_{N\Delta_{3L}}\left(\overline{N^c_R}\gamma_\mu\Delta_{3L}\right)\mathcal{L}_3^{\mu\dagger} \\
& + g^{\mathcal{W}}_{N\Sigma_R}\left(\overline{N_R}\gamma_\mu\Sigma_R\right)\mathcal{W}^\mu + g^{\mathcal{W}}_{N\Sigma_L}\left(\overline{N^c_R}\gamma_\mu\Sigma_L\right)\mathcal{W}^\mu \\
& + g^{\mathcal{W}_1}_{N\Sigma_{1R}}\left(\overline{N_R}\gamma_\mu\Sigma_{1R}\right)\mathcal{W}_1^\mu + g^{\mathcal{W}_1}_{N\Sigma_{1L}}\left(\overline{N^c_R}\gamma_\mu\Sigma_{1L}\right)\mathcal{W}_1^\mu \\
& + g^{\mathcal{U}_1}_{ND_R}\left(\overline{N_R}\gamma_\mu D_R\right)\mathcal{U}_1^{\mu\dagger} + g^{\mathcal{U}_1}_{ND_L}\left(\overline{N^c_R}\gamma_\mu D_L\right)\mathcal{U}_1^{\mu\dagger} \\
& + g^{\mathcal{U}_2}_{NU_R}\left(\overline{N_R}\gamma_\mu U_R\right)\mathcal{U}_2^{\mu\dagger} + g^{\mathcal{U}_2}_{NU_L}\left(\overline{N^c_R}\gamma_\mu U_L\right)\mathcal{U}_2^{\mu\dagger} \\
& + g^{\mathcal{Q}_1}_{NQ_{1R}}\left(\overline{N_R}\gamma_\mu Q_{1R}\right)\mathcal{Q}_1^{\mu\dagger} + g^{\mathcal{Q}_1}_{NQ_{1L}}\left(\overline{N^c_R}\gamma_\mu Q_{1L}\right)\mathcal{Q}_1^{\mu\dagger} \\
& + g^{\mathcal{Q}_5}_{NQ_{5R}}\left(\overline{N_R}\gamma_\mu Q_{5R}\right)\mathcal{Q}_5^{\mu\dagger} + g^{\mathcal{Q}_5}_{NQ_{5L}}\left(\overline{N^c_R}\gamma_\mu Q_{5L}\right)\mathcal{Q}_5^{\mu\dagger} \\
& + g^{\chi}_{NT_{2R}}\left(\overline{N_R}\gamma_\mu T_{2R}\right)\chi^{\mu\dagger} + g^{\chi}_{NT_{2L}}\left(\overline{N^c_R}\gamma_\mu T_{2L}\right)\chi^{\mu\dagger} + \text{h.c.}\,,
\end{aligned} \tag{A.5}$$

[2]Explicit $SU(2)$ and $SU(3)$ index contractions have been omitted in the Lagrangians of this appendix.

$$
\begin{aligned}
\mathcal{L}^{N_R}_{FFV,(B)} = {} & g^{\mathcal{B}}_{NN}\left(\overline{N_R}\gamma_\mu N_R\right)\mathcal{B}^\mu + g^{\mathcal{B}_1}_{Ne}\left(\overline{N_R}\gamma_\mu e_R\right)\mathcal{B}_1^\mu + g^{\mathcal{L}_1}_{NL}\left(\overline{N^c_R}\gamma_\mu L\right)\mathcal{L}_1^\mu \\
& + g^{\mathcal{U}_1}_{Nd}\left(\overline{N_R}\gamma_\mu d_R\right)\mathcal{U}_1^{\mu\dagger} + g^{\mathcal{U}_2}_{Nu}\left(\overline{N_R}\gamma_\mu u_R\right)\mathcal{U}_2^{\mu\dagger} + g^{\mathcal{Q}_1}_{QN}\left(\overline{N^c_R}\gamma_\mu Q\right)\mathcal{Q}_1^{\mu\dagger} + \text{h.c.}
\end{aligned}
\tag{A.6}
$$

In the previous Lagrangian, we assumed all new heavy fermions are Dirac spinors, although there are two cases, $\mathcal{N}$ and Σ, which could be Majorana fermions. In the case of those fields being Majorana, one can replace one of the Weyl fermions by its charged conjugated counterpart, since $\psi_L \equiv \psi_R^c$ (and $\psi_R \equiv \psi_L^c$). In fact, in one particular model discussed in Section 5.3, the Majorana nature of $\mathcal{N}$ was required to draw one model diagram. Nevertheless, in this appendix we keep the notation of two distinct chiral components for each fermion.

The Lagrangian terms that involve the new vector $\mathcal{U}_1$ and contain at least one light field are

$$
\begin{aligned}
\mathcal{L}^{\mathcal{U}_1}_{\text{mixed}} = {} & g^{\mathcal{U}_1}_{ND_L}\left(\overline{N^c_R}\gamma_\mu D_L\right)\mathcal{U}_1^{\mu\dagger} + g^{\mathcal{U}_1}_{ND_R}\left(\overline{N_R}\gamma_\mu D_R\right)\mathcal{U}_1^{\mu\dagger} + g^{\mathcal{U}_1}_{Nd}\left(\overline{N_R}\gamma_\mu d_R\right)\mathcal{U}_1^{\mu\dagger} \\
& + g^{\mathcal{U}_1}_{eU}\left(\overline{e^c_R}\gamma_\mu U_L\right)\mathcal{U}_1^{\mu\dagger} + g^{\mathcal{U}_1}_{LQ_1}\left(\overline{L^c}\gamma_\mu Q_{1R}\right)\mathcal{U}_1^{\mu\dagger} + g^{\mathcal{U}_1}_{LQ_5}\left(\overline{L}\gamma_\mu Q_{5L}\right)\mathcal{U}_1^{\mu\dagger} \\
& + g^{\mathcal{U}_1}_{uE}\left(\overline{u^c_R}\gamma_\mu E_L\right)\mathcal{U}_1^{\mu\dagger} + g^{\mathcal{U}_1}_{Q\Delta_1}\left(\overline{Q^c}\gamma_\mu \Delta_{1R}\right)\mathcal{U}_1^{\mu\dagger} \\
& + g^{\mathcal{U}_1}_{uD}\left(\overline{u^c_R}\gamma_\mu D_L\right)\mathcal{U}_1^{\mu} + g^{\mathcal{U}_1}_{dU}\left(\overline{d^c_R}\gamma_\mu U_L\right)\mathcal{U}_1^{\mu} + g^{\mathcal{U}_1}_{QQ_1}\left(\overline{Q^c}\gamma_\mu Q_{1R}\right)\mathcal{U}_1^{\mu} \\
& + g^{\mathcal{U}_1}_{d\mathcal{N}_L}\left(\overline{d^c_R}\gamma_\mu \mathcal{N}_L\right)\mathcal{U}_1^{\mu\dagger} + g^{\mathcal{U}_1}_{d\mathcal{N}_R}\left(\overline{d_R}\gamma_\mu \mathcal{N}_R\right)\mathcal{U}_1^{\mu} + \text{h.c.}
\end{aligned}
\tag{A.7}
$$

For completeness, we have written in the first line the interaction terms containing N_R, which were already introduced in $\mathcal{L}^{N_R}_{FFV}$.

The renormalizable interactions of the vector $\mathcal{L}_1$ with the light fields are given by

$$
\begin{aligned}
\mathcal{L}^{\mathcal{L}_1}_{\text{mixed}} = {} & g^{\mathcal{L}_1}_{N\Delta_{1R}}\left(\overline{N_R}\gamma_\mu \Delta_{1R}\right)\mathcal{L}_1^\mu + g^{\mathcal{L}_1}_{N\Delta_{1L}}\left(\overline{N^c_R}\gamma_\mu \Delta_{1L}\right)\mathcal{L}_1^\mu + g^{\mathcal{L}_1}_{NL}\left(\overline{N^c_R}\gamma_\mu L\right)\mathcal{L}_1^\mu \\
& + g^{\mathcal{L}_1}_{e\Delta_1}\left(\overline{\Delta_{1R}}\gamma_\mu e_R\right)\mathcal{L}_1^\mu + g^{\mathcal{L}_1}_{L\mathcal{N}_L}\left(\overline{\mathcal{N}_L}\gamma_\mu L\right) + g^{\mathcal{L}_1}_{L\mathcal{N}_R}\left(\overline{\mathcal{N}^c_R}\gamma_\mu L\right)\mathcal{L}_1^\mu \\
& + g^{\mathcal{L}_1}_{e\Delta_3}\left(\overline{e_R}\gamma_\mu \Delta_{3R}\right)\mathcal{L}_1^\mu + g^{\mathcal{L}_1}_{L\Sigma_L}\left(\overline{\Sigma_L}\gamma_\mu L\right)\mathcal{L}_1^\mu + g^{\mathcal{L}_1}_{L\Sigma_R}\left(\overline{\Sigma^c_R}\gamma_\mu L\right)\mathcal{L}_1^\mu \\
& + g^{\mathcal{L}_1}_{LE}\left(\overline{L}\gamma_\mu E_L\right)\mathcal{L}_1^\mu + g^{\mathcal{L}_1}_{L\Sigma_1}\left(\overline{L}\gamma_\mu \Sigma_{1L}\right)\mathcal{L}_1^\mu \\
& + g^{\mathcal{L}_1}_{QT_2}\left(\overline{T_{2L}}\gamma_\mu Q\right)\mathcal{L}_1^\mu + g^{\mathcal{L}_1}_{uQ_7}\left(\overline{Q_{7R}}\gamma_\mu u_R\right)\mathcal{L}_1^\mu + g^{\mathcal{L}_1}_{dQ_1}\left(\overline{Q_{1R}}\gamma_\mu d_R\right)\mathcal{L}_1^\mu \\
& + g^{\mathcal{L}_1}_{QU}\left(\overline{U_L}\gamma_\mu Q\right)\mathcal{L}_1^\mu + g^{\mathcal{L}_1}_{QD}\left(\overline{Q}\gamma_\mu D_L\right)\mathcal{L}_1^\mu + g^{\mathcal{L}_1}_{QT_1}\left(\overline{Q}\gamma_\mu T_{1L}\right)\mathcal{L}_1^\mu \\
& + g^{\mathcal{L}_1}_{dQ_5}\left(\overline{d_R}\gamma_\mu Q_{5R}\right)\mathcal{L}_1^\mu + g^{\mathcal{L}_1}_{uQ_1}\left(\overline{u_R}\gamma_\mu Q_{1R}\right)\mathcal{L}_1^\mu + \text{h.c.}
\end{aligned}
\tag{A.8}
$$

Again, we have included in the first line the three interactions with N_R, which we already presented in $\mathcal{L}^{N_R}_{FFV}$. The remaining terms involve at least one SM field.

Finally, we write down the 3-point interaction terms among heavy BSM fields that are needed in different opening diagrams of the operator $\mathcal{O}_{NH^4}$. These are

$$\begin{aligned}
\mathcal{L}_{\text{heavy}}^{\text{diag}} = &\Big\{ y_{\Delta_1}^{\mathcal{S}} \left(\overline{\Delta_{1L}}\Delta_{1R}\right) \mathcal{S} + y_{\Delta_1}^{\Xi} \left(\overline{\Delta_{1L}}\Delta_{1R}\right) \Xi \\
&+ y_{\Delta_{1L}}^{\Xi_1} \left(\overline{\Delta_{1L}^c}\Delta_{1L}\right) \Xi_1 + y_{\Delta_{1R}}^{\Xi_1} \left(\overline{\Delta_{1R}^c}\Delta_{1R}\right) \Xi_1 \Big\} + \text{ h.c.} \\
&+ \mu_{\mathcal{S}\Xi_1} \left(\mathcal{S}\Xi_1^\dagger \Xi_1\right) + \mu_{\mathcal{S}\Xi} \left(\mathcal{S}\Xi\Xi\right) + \mu_{\mathcal{S}} \left(\mathcal{S}\mathcal{S}\mathcal{S}\right) \, .
\end{aligned} \tag{A.9}$$

Appendix B

Meson decays: analytical computations

This appendix is based on the appendices of Ref. [175]. It complements Chapter 6 and includes technical details of the computations of meson and HNL decay widths in the N_RLEFT. Section B.1 contains the derivation of two-body and three-body pseudoscalar meson decays into (i) two HNLs and (ii) one HNL and one SM neutrino. In Section B.2, we show the branching ratios of the decay channels including a SM neutrino and an HNL in the final state as a function of the HNL mass, which were not displayed in Chapter 6. Finally, in Section B.3, we provide the partial decay width formulas for HNLs decaying into mesons via the single-N_R operators of interest.

B.1 Pseudoscalar meson decays into HNLs

The four-fermion operators in the N_RLEFT contained in Tables 6.1 and 6.2 lead to two-body and three-body meson decays, if the HNL mass is small enough. The former involve two neutral leptons in the final state, whereas the latter correspond to semileptonic decays with an additional lighter meson within the final products. This appendix gathers the necessary formulae to determine meson decay rates into HNLs, assuming a pseudoscalar meson (of mass m_P and momentum p) in the initial state.

In pure leptonic decays we define the meson decay constants through the transition matrix elements (see e.g. Ref. [172])

$$\langle 0|\overline{q_i}\gamma^\mu\gamma_5 q_j|P(p)\rangle = i f_P p^\mu \,,$$

$$\langle 0|\overline{q_i}\gamma_5 q_j|P(p)\rangle = i\frac{m_P^2}{m_{q_i}+m_{q_j}} f_P \equiv i f_P^S\,, \tag{B.1}$$

where i, j denote quark flavor indices, and $|P(p)\rangle$ is the decaying pseudoscalar meson.

In semileptonic meson decays, the hadronic matrix elements are described by the corresponding form factors. We distinguish two scenarios depending on the nature of the outgoing meson. If it is a pseudoscalar (of mass m and momentum p'), the nonvanishing matrix elements are

$$\begin{aligned}
\langle P'(p')|\overline{q_i}\gamma^\mu q_j|P(p)\rangle &= f_+(q^2)\left[(p+p')^\mu - \frac{m_P^2-m^2}{q^2}q^\mu\right] + f_0(q^2)\frac{m_P^2-m^2}{q^2}q^\mu\,,\\
\langle P'(p')|\overline{q_i}q_j|P(p)\rangle &= f_S(q^2)\,,\\
\langle P'(p')|\overline{q_i}\sigma^{\mu\nu}q_j|P(p)\rangle &= \frac{2i}{m_P+m}\left[p^\mu p'^\nu - p^\nu p'^\mu\right] f_T(q^2)\,,
\end{aligned} \tag{B.2}$$

where $q^\mu \equiv p^\mu - p'^\mu$. Of the four form factors (f_+, f_0, f_S and f_T), the scalar one can be related to the others using the equations of motion, through

$$f_S(q^2) = \frac{m_P^2-m^2}{m_{q_j}-m_{q_i}} f_0(q^2)\,. \tag{B.3}$$

When the final meson is a vector (of mass m, outgoing momentum p' and polarization vector ϵ), the nonzero matrix elements are

$$\begin{aligned}
\langle V(p',\epsilon)|\overline{q_i}\gamma^\mu q_j|P(p)\rangle &= ig(q^2)\epsilon^{\mu\nu\alpha\beta}\epsilon^*_\nu P_\alpha q_\beta\,,\\
\langle V(p',\epsilon)|\overline{q_i}\gamma^\mu\gamma_5 q_j|P(p)\rangle &= f(q^2)\epsilon^{*\mu} + a_+(q^2)P^\mu\epsilon^*\cdot p + a_-(q^2)q^\mu\epsilon^*\cdot p\,,\\
\langle V(p',\epsilon)|\overline{q_i}\sigma^{\mu\nu}q_j|P(p)\rangle &= \epsilon^{\mu\nu\alpha\beta}\left(g_+(q^2)\epsilon^*_\alpha P_\beta + g_-(q^2)\epsilon^*_\alpha q_\beta + g_0(q^2)p_\alpha p'_\beta\,\epsilon^*\cdot p\right)\,,\\
\langle V(p',\epsilon)|\overline{q_i}\gamma_5 q_j|P(p)\rangle &= f_{PS}(q^2)\,\epsilon^*\cdot p\,,
\end{aligned} \tag{B.4}$$

where we defined $P^\mu \equiv p^\mu + p'^\mu$. These transitions, denoted by $P\to V$, are parametrized by eight functions of q^2: g, f, a_+, a_-, g_+, g_-, g_0 and f_{PS}. Equations of motion relate the pseudoscalar form factor with the rest through the following expression

$$f_{PS}(q^2) = \frac{1}{m_{q_i}+m_{q_j}}\left[f(q^2) + a_+(q^2)\left(m_P^2-m^2\right) + a_-(q^2)q^2\right]. \tag{B.5}$$

Two-body decays

In the rest frame of a particle of mass M, the two-body decay width reads

$$\Gamma = \frac{\lambda^{1/2}\left(M^2, m_a^2, m_b^2\right)}{64\pi^2 M^3} \int \mathrm{d}\Omega_{\mathrm{cm}} \sum_{\mathrm{spins}} |\mathcal{M}|^2 \ , \tag{B.6}$$

where $\lambda\left(x,y,z\right) \equiv (x-y-z)^2 - 4yz$, and m_a, m_b denote the masses of the decay products. Note that for identical particles in the final state one has $\int \mathrm{d}\Omega_{\mathrm{cm}} = 2\pi$.

In this section, we list the amplitudes and corresponding partial decay widths of a neutral pseudoscalar meson $P \sim \overline{q_i} q_j$ decaying into (i) a pair of HNLs, and (ii) one HNL plus one active neutrino. For a Dirac HNL (and Dirac ν), these decays occur via the LNC pair-N_R operators in Table 6.1 and the LNC single-N_R operators in Table 6.2. In the Majorana scenario (where the HNL and ν are Majorana), the decays receive contributions from both the LNC and LNV operators. The amplitudes for Dirac neutrinos read

$$\mathcal{M}\left(P \to N\overline{N}\right) = i\frac{f_P}{2}\left(c_{qN,\,ij}^{V,RR} - c_{qN,\,ij}^{V,LR}\right)\overline{u_N}\not{p}P_R v_{N'}\ , \tag{B.7}$$

$$\mathcal{M}\left(P \to \nu_\alpha\overline{N}\right) = i\frac{f_P^S}{2}\left(c_{q\nu N,\,ij\alpha}^{S,RR} - c_{q\nu N,\,ij\alpha}^{S,LR}\right)\overline{u_\nu}P_R v_N\ , \tag{B.8}$$

where u_N (u_ν) and v_N are the spinors corresponding to N (ν) and $\overline{N}$, respectively. A prime is added when there are two HNLs in the final state. For Majorana neutrinos, we recall that the full Majorana HNL field is $N = N_R^c + N_R$, such that $N^c = N$. The amplitude for $P \to NN$ has to be anti-symmetrized in N and N', since there are two identical particles in the final state[1]

$$\begin{aligned}\mathcal{M}(P \to NN) = {} & i\frac{f_P}{2}\left(c_{qN,\,ij}^{V,RR} - c_{qN,\,ij}^{V,LR}\right)\overline{u_N}\not{p}\gamma_5 v_{N'} \\ & + i f_P^S\left[\left(c_{qN,\,ij}^{S,RR} - c_{qN,\,ij}^{S,LR}\right)\overline{u_N}P_R v_{N'} - \left(c_{qN,\,ji}^{S,RR*} - c_{qN,\,ji}^{S,LR*}\right)\overline{u_N}P_L v_{N'}\right],\end{aligned} \tag{B.9}$$

$$\begin{aligned}\mathcal{M}\left(P \to \nu_\alpha N\right) = {} & i\frac{f_P^S}{2}\left[\left(c_{q\nu N,\,ij\alpha}^{S,RR} - c_{q\nu N,\,ij\alpha}^{S,LR}\right)\overline{u_\nu}P_R v_N - \left(c_{q\nu N,\,ji\alpha}^{S,RR*} - c_{q\nu N,\,ji\alpha}^{S,LR*}\right)\overline{u_\nu}P_L v_N\right] \\ & + i\frac{f_P}{2}\left[\left(c_{q\nu N,\,ij\alpha}^{V,RR} - c_{q\nu N,\,ij\alpha}^{V,LR}\right)\overline{u_\nu}\not{p}P_R v_N - \left(c_{q\nu N,\,ji\alpha}^{V,RR*} - c_{q\nu N,\,ji\alpha}^{V,LR*}\right)\overline{u_\nu}\not{p}P_L v_N\right].\end{aligned} \tag{B.10}$$

[1]The convention for associating a u or v spinor to a Majorana particle is arbitrary. Our is such that there is one $\overline{u}$ spinor and one v spinor in each process. In this way, we recover the usual Dirac relations for the sums over spins. Nonetheless, the physical result does not depend on the convention's choice.

The decay rates of these two processes in the Dirac scenario are given by

$$\Gamma\left(P \to N\overline{N}\right) = \frac{|f_P|^2}{32\pi} \left|c^{V,RR}_{qN,\,ij} - c^{V,LR}_{qN,\,ij}\right|^2 m_P\, m_N^2 \sqrt{1 - \frac{4m_N^2}{m_P^2}}\,, \tag{B.11}$$

$$\Gamma\left(P \to \nu_\alpha\overline{N}\right) = \frac{|f_P^S|^2}{64\pi} \left|c^{S,RR}_{q\nu N,\,ij\alpha} - c^{S,LR}_{q\nu N,\,ij\alpha}\right|^2 m_P \left(1 - \frac{m_N^2}{m_P^2}\right)^2\,, \tag{B.12}$$

and in the Majorana case by

$$\begin{aligned}\Gamma\left(P \to NN\right) = \frac{m_P}{32\pi}\sqrt{1 - \frac{4m_N^2}{m_P^2}} \Bigg[& 2\,|f_P|^2 \left|c^{V,RR}_{qN,\,ij} - c^{V,LR}_{qN,\,ij}\right|^2 m_N^2 \\ &+ |f_P^S|^2 \Bigg\{ \left(\left|c^{S,RR}_{qN,\,ij} - c^{S,LR}_{qN,\,ij}\right|^2 + \left|c^{S,RR}_{qN,\,ji} - c^{S,LR}_{qN,\,ji}\right|^2\right)\left(1 - \frac{2m_N^2}{m_P^2}\right) \\ &\qquad + 2\left[\left(c^{S,RR}_{qN,\,ij} - c^{S,LR}_{qN,\,ij}\right)\left(c^{S,RR}_{qN,\,ji} - c^{S,LR}_{qN,\,ji}\right) + \text{h.c.}\right]\frac{m_N^2}{m_P^2}\Bigg\} \\ &+ f_P f_P^S \Bigg\{ \left(c^{V,RR}_{qN,\,ij} - c^{V,LR}_{qN,\,ij}\right)\left(c^{S,RR*}_{qN,\,ij} - c^{S,LR*}_{qN,\,ij} + c^{S,RR}_{qN,\,ji} - c^{S,LR}_{qN,\,ji}\right) m_N + \text{h.c.}\Bigg\}\Bigg]\,,\end{aligned} \tag{B.13}$$

$$\begin{aligned}\Gamma\left(P \to \nu_\alpha N\right) = \frac{m_P}{64\pi}\left(1 - \frac{m_N^2}{m_P^2}\right)^2 \Bigg[& |f_P^S|^2 \left(\left|c^{S,RR}_{q\nu N,\,ij\alpha} - c^{S,LR}_{q\nu N,\,ij\alpha}\right|^2 + \left|c^{S,RR}_{q\nu N,\,ji\alpha} - c^{S,LR}_{q\nu N,\,ji\alpha}\right|^2\right) \\ &+ |f_P|^2 \left(\left|c^{V,RR}_{q\nu N,\,ij\alpha} - c^{V,LR}_{q\nu N,\,ij\alpha}\right|^2 + \left|c^{V,RR}_{q\nu N,\,ji\alpha} - c^{V,LR}_{q\nu N,\,ji\alpha}\right|^2\right) m_N^2 \\ &+ f_P f_P^S \Bigg\{\Bigg[\left(c^{S,RR}_{q\nu N,\,ij\alpha} - c^{S,LR}_{q\nu N,\,ij\alpha}\right)\left(c^{V,RR}_{q\nu N,\,ji\alpha} - c^{V,LR}_{q\nu N,\,ji\alpha}\right) \\ &\qquad + \left(c^{S,RR*}_{q\nu N,\,ji\alpha} - c^{S,LR*}_{q\nu N,\,ji\alpha}\right)\left(c^{V,RR*}_{q\nu N,\,ij\alpha} - c^{V,LR*}_{q\nu N,\,ij\alpha}\right)\Bigg] m_N + \text{h.c.}\Bigg\}\Bigg]\,.\end{aligned} \tag{B.14}$$

Three-body decays

For the three-body phase space integral calculations we follow the procedure described in Ref. [172, Appendix B.1]. However, we adopt general labels for the leptonic products. In the rest frame of the decaying pseudoscalar meson, the decay rate reads

$$\begin{aligned}\Gamma = \frac{1}{2m_P}\frac{1}{(2\pi)^5}\int \mathrm{d}^4p' \int \mathrm{d}^4p_a \int \mathrm{d}^4p_b\, \delta(p'^2 - m^2)\delta(p_a^2 - m_a^2)\delta(p_b^2 - m_b^2) \\ \times \sum_{\text{spins}} |\mathcal{M}|^2\, \delta^{(4)}(p - p' - p_a - p_b)\,,\end{aligned} \tag{B.15}$$

where p (p') is the momentum of the decaying (outgoing) meson and p_a and p_b denote the momenta of the produced leptons.[2] The summed over spins squared matrix element can be written in terms of four-momentum invariant scalar products and the hadronic form factors, which are functions of $q^2 = (p - p')^2$. After performing the integral over the four-momentum p_b, it is convenient to introduce the variable a via a factor of $1 = \int \mathrm{d}a\, \delta(a - q^2)$. Then, the spin-summed matrix element squared can be written as

$$\sum_{\text{spins}} |\mathcal{M}|^2 \bigg|_{p_b = q - p_a} = \sum_{n=0}^{K} c_n(a)(p_a \cdot p)^n \,, \tag{B.16}$$

where $c_n(a)$ are functions of a, particle masses and the hadronic form factors. For the decays under study we have $K \leq 2$. After performing the remaining momentum integrals, one arrives at the final decay rate expression[3]

$$\Gamma = \frac{1}{2m_P} \frac{1}{(2\pi)^5} \int_{(m_a+m_b)^2}^{(m_P-m)^2} \mathrm{d}a\, I_P \sum_{n=0}^{K} c_n(a) I_n \,, \tag{B.17}$$

where the integrals I_P and I_n (for $n = 0, 1, 2$) are given by

$$\begin{aligned}
I_P &= \frac{\pi}{2m_P^2} \lambda^{1/2}\left(a, m^2, m_P^2\right) , \\
I_0 &= \frac{\pi}{2a} \lambda^{1/2}\left(a, m_a^2, m_b^2\right) , \qquad I_1 = \frac{(p_a \cdot q)(p \cdot q)}{a} I_0 \,, \\
I_2 &= \frac{I_0}{a^2} \left((p_a \cdot q)^2 (p \cdot q)^2 + \frac{1}{48} \lambda(a, m^2, m_P^2) \lambda(a, m_a^2, m_b^2) \right) .
\end{aligned} \tag{B.18}$$

The scalar products above have to be replaced by

$$p_a \cdot q = \frac{1}{2}\left(a + m_a^2 - m_b^2\right) , \qquad p \cdot q = \frac{1}{2}\left(m_P^2 + a - m^2\right) . \tag{B.19}$$

In summary, after computing the spin-summed matrix element squared with standard techniques and arranging it in the form of Eq. (B.16), one replaces $(p_a \cdot p)^n$ by the corresponding integral result I_n, substitutes the form factor expressions, and evaluates the integral in Eq. (B.17) numerically.

In the rest of this section, we give the amplitudes of the relevant three-body decays for producing the HNLs via the N_RLEFT operators. For Dirac HNLs, these are

[2] The labels a and b will refer to (i) N' and N, and (ii) ν and N.

[3] When the outgoing leptons are two Majorana HNLs an extra factor of $1/2$ appears in the final expression.

$$\mathcal{M}\left(P \to P' N\overline{N}\right) = \frac{1}{2}\left(c^{V,RR}_{qN,\,ij} + c^{V,LR}_{qN,\,ij}\right)\left(f_+ P_\mu + (f_0 - f_+)\,\frac{m_P^2 - m^2}{q^2} q_\mu\right)\left[\overline{u_N}\gamma^\mu P_R v_{N'}\right] , \tag{B.20}$$

$$\begin{aligned}\mathcal{M}\left(P \to V N\overline{N}\right) = &\Bigg\{ \left(c^{V,RR}_{qN,\,ij} + c^{V,LR}_{qN,\,ij}\right)\left(ig\epsilon_{\mu\nu\alpha\beta}\epsilon^{*\nu}p'^\alpha p^\beta\right) \\ &+ \frac{1}{2}\left(c^{V,RR}_{qN,\,ij} - c^{V,LR}_{qN,\,ij}\right)\left(f\epsilon^*_\mu + a_+ P_\mu \epsilon^*\cdot p + a_- q_\mu \epsilon^*\cdot p\right)\Bigg\}\left[\overline{u_N}\gamma^\mu P_R v_{N'}\right] ,\end{aligned} \tag{B.21}$$

$$\begin{aligned}\mathcal{M}\left(P \to P'\nu_\alpha\overline{N}\right) = &\frac{f_S}{2}\left(c^{S,RR}_{q\nu N,\,ij\alpha} + c^{S,LR}_{q\nu N,\,ij\alpha}\right)\left[\overline{u_\nu}P_R v_N\right] \\ &+ c^{T,RR}_{q\nu N,\,ij\alpha}\frac{2if_T}{m_P + m}\left(p_\mu p'_\nu + \frac{i}{2}\epsilon_{\mu\nu\rho\sigma}p^\rho p'^\sigma\right)\left[\overline{u_\nu}\sigma^{\mu\nu}P_R v_N\right] ,\end{aligned} \tag{B.22}$$

$$\begin{aligned}\mathcal{M}\left(P \to V\nu_\alpha\overline{N}\right) = &\frac{f_{PS}}{2}\left(c^{S,RR}_{q\nu N,\,ij\alpha} - c^{S,LR}_{q\nu N,\,ij\alpha}\right)(\epsilon^*\cdot p)\left[\overline{u_\nu}P_R v_N\right] \\ &+ c^{T,RR}_{q\nu N,\,ij\alpha}\Bigg\{\frac{1}{2}\epsilon_{\mu\nu\alpha\beta}\left[g_+\epsilon^{*\alpha}(p+p')^\beta + g_-\epsilon^{*\alpha}q^\beta + g_0 p^\alpha p'^\beta\epsilon^*\cdot p\right] \\ &- i\left[g_+\epsilon^*_\mu(p+p')_\nu + g_-\epsilon^*_\mu q_\nu + g_0 p_\mu p'_\nu\epsilon^*\cdot p\right]\Bigg\}\left[\overline{u_\nu}\sigma^{\mu\nu}P_R v_N\right] .\end{aligned} \tag{B.23}$$

The corresponding amplitudes for Majorana HNLs read

$$\begin{aligned}\mathcal{M}(P \to P' NN) = &\frac{1}{2}\left(c^{V,RR}_{qN,\,ij} + c^{V,LR}_{qN,\,ij}\right)\left(f_+ P_\mu + (f_0 - f_+)\,\frac{m_P^2 - m^2}{q^2}q_\mu\right)\left[\overline{u_N}\gamma^\mu\gamma^5 v_{N'}\right] \\ &+ f_S\left(c^{S,RR}_{qN,\,ij} + c^{S,LR}_{qN,\,ij}\right)\left[\overline{u_N}P_R v_{N'}\right] + f_S\left(c^{S,RR*}_{qN,\,ji} + c^{S,LR*}_{qN,\,ji}\right)\left[\overline{u_N}P_L v_{N'}\right] ,\end{aligned} \tag{B.24}$$

$$\begin{aligned}\mathcal{M}(P \to VNN) = &\Bigg\{ \left(c^{V,RR}_{qN,\,ij} + c^{V,LR}_{qN,\,ij}\right)\left(ig\epsilon_{\mu\nu\alpha\beta}\epsilon^{*\nu}p'^\alpha p^\beta\right) \\ &+ \frac{1}{2}\left(c^{V,RR}_{qN,\,ij} - c^{V,LR}_{qN,\,ij}\right)\left(f\epsilon^*_\mu + a_+ P_\mu\epsilon^*\cdot p + a_- q_\mu\epsilon^*\cdot p\right)\Bigg\}\left[\overline{u_N}\gamma^\mu\gamma^5 v_{N'}\right] \\ &+ f_{PS}\Bigg\{\left(c^{S,RR}_{q\nu N,\,ij} - c^{S,LR}_{q\nu N,\,ij}\right)(\epsilon^*\cdot p)\left[\overline{u_N}P_R v_{N'}\right] \\ &- \left(c^{S,RR*}_{q\nu N,\,ji} - c^{S,LR*}_{q\nu N,\,ji}\right)(\epsilon^*\cdot p)\left[\overline{u_N}P_L v_{N'}\right]\Bigg\} ,\end{aligned} \tag{B.25}$$

$$\begin{aligned}\mathcal{M}(P \to P'\nu_\alpha N) = &\frac{f_S}{2}\Bigg\{\left(c^{S,RR}_{q\nu N,\,ij\alpha} + c^{S,LR}_{q\nu N,\,ij\alpha}\right)\left[\overline{u_\nu}P_R v_N\right] + \left(c^{S,RR*}_{q\nu N,\,ji\alpha} + c^{S,LR*}_{q\nu N,\,ji\alpha}\right)\left[\overline{u_\nu}P_L v_N\right]\Bigg\} \\ &+ \frac{if_T}{M+m}\Bigg\{c^{T,RR}_{q\nu N,\,ij\alpha}\left(2p_\mu p'_\nu + i\epsilon_{\mu\nu\rho\sigma}p^\rho p'^\sigma\right)\left[\overline{u_\nu}\sigma^{\mu\nu}P_R v_N\right] \\ &- c^{T,RR*}_{q\nu N,\,ji\alpha}\left(2p_\mu p'_\nu - i\epsilon_{\mu\nu\rho\sigma}p^\rho p'^\sigma\right)\left[\overline{u_\nu}\sigma^{\mu\nu}P_L v_N\right]\Bigg\}\end{aligned}$$

$$
\begin{aligned}
&+ \left\{ \left(c^{V,RR}_{q\nu N,\,ij\alpha} + c^{V,LR}_{q\nu N,\,ij\alpha}\right) \left[\overline{u_\nu}\gamma^\mu P_R v_N\right] - \left(c^{V,RR*}_{q\nu N,\,ji\alpha} + c^{V,LR*}_{q\nu N,\,ji\alpha}\right) \left[\overline{u_\nu}\gamma^\mu P_L v_N\right] \right\} \\
&\times \frac{1}{2}\left(f_+ P_\mu + (f_0 - f_+)\,\frac{m_P^2 - m^2}{q^2} q_\mu \right) , \qquad \text{(B.26)}
\end{aligned}
$$

$$
\begin{aligned}
\mathcal{M}\left(P \to V\nu_\alpha N\right) = \frac{f_{PS}}{2} &\left\{ \left(c^{S,RR}_{q\nu N,\,ij\alpha} - c^{S,LR}_{q\nu N,\,ij\alpha}\right) (\epsilon^* \cdot p) \left[\overline{u_\nu} P_R v_N\right] \right. \\
&\left. - \left(c^{S,RR*}_{q\nu N,\,ji\alpha} - c^{S,LR*}_{q\nu N,\,ji\alpha}\right) (\epsilon^* \cdot p) \left[\overline{u_\nu} P_L v_N\right] \right\} \\
&+ c^{T,RR}_{q\nu N,\,ij\alpha} \left(\frac{1}{2}\epsilon_{\mu\nu\alpha\beta} T^{\alpha\beta} - i T_{\mu\nu} \right) \left[\overline{u_\nu}\sigma^{\mu\nu} P_R v_N\right] \\
&- c^{T,RR*}_{q\nu N,\,ji\alpha} \left(\frac{1}{2}\epsilon_{\mu\nu\alpha\beta} T^{\alpha\beta} + i T_{\mu\nu} \right) \left[\overline{u_\nu}\sigma^{\mu\nu} P_L v_N\right] \\
&+ \frac{1}{2}\left\{ \left(c^{V,RR}_{q\nu N,\,ij\alpha} + c^{V,LR}_{q\nu N,\,ij\alpha}\right) V_\mu + \left(c^{V,RR}_{q\nu N,\,ij\alpha} - c^{V,LR}_{q\nu N,\,ij\alpha}\right) A_\mu \right\} \left[\overline{u_\nu}\gamma^\mu P_R v_N\right] \\
&- \frac{1}{2}\left\{ \left(c^{V,RR*}_{q\nu N,\,ji\alpha} + c^{V,LR*}_{q\nu N,\,ji\alpha}\right) V_\mu + \left(c^{V,RR*}_{q\nu N,\,ji\alpha} - c^{V,LR*}_{q\nu N,\,ji\alpha}\right) A_\mu \right\} \left[\overline{u_\nu}\gamma^\mu P_L v_N\right] ,
\end{aligned}
\qquad \text{(B.27)}
$$

where we have introduced:

$$
\begin{aligned}
T^{\alpha\beta} &\equiv g_+ \epsilon^{*\,\alpha} (p+p')^\beta + g_- \epsilon^{*\,\alpha} q^\beta + g_0 p^\alpha p'^\beta (\epsilon^* \cdot p) , \\
V_\mu &\equiv 2ig\epsilon_{\mu\nu\alpha\beta}\epsilon^{*\nu} p'^\alpha p^\beta , \\
A_\mu &\equiv f\epsilon^*_\mu + a_+ (p+p')_\mu (\epsilon^* \cdot p) + a_- q_\mu (\epsilon^* \cdot p) .
\end{aligned}
$$

Specific software, such as `FeynCalc` [303, 304], automatizes the computation of the summed over spins squared matrix elements. Finally, to simplify notation in the previous expressions, we have omitted the q^2 dependence of the form factors.

Decay constants and form factors

The masses of all mesons involved in the decays are taken from Ref. [168]. In addition, we use the light quark masses at a renormalization scale of $\mu = 2$ GeV in $\overline{\text{MS}}$, whereas for m_c and m_b we employ the $\overline{\text{MS}}$ masses at $\mu = m_c$ and $\mu = m_b$, respectively, as in Ref. [168]:

$$
m_u = 2.2\,\text{MeV}, \quad m_d = 4.7\,\text{MeV}, \quad m_s = 93\,\text{MeV}, \quad m_c = 1.27\,\text{GeV}, \quad m_b = 4.18\,\text{GeV}.
$$

We provide the decay constants of the heavy neutral pseudoscalar mesons in Table B.1.

Meson P	Decay constant f_P [MeV]
D^0	212.0 (0.7)
B^0	190.0 (1.3)
B_s^0	230.3 (1.3)

TABLE B.1: Decay constants of heavy neutral pseudoscalar mesons [305].

We use the isospin-averaged results[4] for $N_f = 2+1+1$ dynamical quark flavors from Ref. [305]. As regards hadronic form factors, several parametrizations exist in the literature for describing their dependence on q^2. One of the most used is the BCL method [307], and we try to stick to it as long as there is available data. In all other cases, we use the so-called double-pole parametrization. In Table B.2, we show all hadronic transitions mediated by the selected N_RLEFT operators and the references studying the associated form factors. We indicate the equation where the explicit q^2 parametrization appears and the tables where the best-fit parameter values are given.[5]

B.2 Branching ratios of meson decays triggered by single-N_R operators

We have also computed the branching ratios for two- and three-body pseudoscalar meson decays including in the final state a SM neutrino and an HNL. These decays are triggered by the single-N_R operators given in Table 6.2. As an example, we show in Fig. B.1 the corresponding branching ratios in the case of $b \to d$ transitions triggered by three single-N_R operators, namely, $\mathcal{O}^{S,RR}_{d\nu N,31\alpha}$, $\mathcal{O}^{T,RR}_{d\nu N,31\alpha}$, and $\mathcal{O}^{V,RR}_{d\nu N,31\alpha}$. The scalar and tensor operators are LNC, whereas the operator of the vector type is LNV.

As can be seen from Eq. (B.14), the tensor operator does not contribute to the two-body decay width. This is why there is no solid blue line in the corresponding plot in Fig. B.1. The tensor form factors for the $B \to \pi$ transitions have been taken from Table 50 in Ref. [305]. For $B^0 \to \eta,\ \eta'$ and $B_s^0 \to \overline{K^0}$, we have used Eq. (27) from Ref. [310], which relates f_T to f_+ and f_0. Finally, for the $B_{(s)} \to V$ transitions, we have

[4] In other words, we assume the isospin symmetry, *i.e.* the (approximate) symmetry between the u and d quarks. In this limit, the decay constants for D^0 and D^+ are the same, f_D. Similarly, B^0 and B^+ mesons are characterised by one constant, f_B. The difference $|f_{P^+} - f_P|$ is estimated to be $\simeq 0.5$ MeV for both $P = D$ and $P = B$ [305, 306].

[5] Notice that there are several conventions in the literature for writing hadronic matrix elements in terms of form factors. The basis presented in Eqs. (B.2) and (B.4) must be converted to the new basis in each reference before using their q^2 parametrization.

<table>
<tr><th colspan="2">Meson transitions</th><th>Form factor parametrization</th><th>Fitted parameters</th></tr>
<tr><td rowspan="2">D-mesons</td><td>$D^0 \to \pi^0$
$D^+ \to \pi^+$</td><td>BCL [308, Eqs. (A1)–(A2)]</td><td>[308, Tab. VI]</td></tr>
<tr><td>$D^0 \to \eta,\, \eta',\, \rho^0,\, \omega$
$D^+ \to \rho^+$
$D_s^+ \to K^+,\, K^{*+}$</td><td>Double-pole [309, Eq. (63)]</td><td>[309, Tab. VI]</td></tr>
<tr><td rowspan="3">B-mesons</td><td>$B^0 \to \pi^0,\, K^0$
$B^+ \to \pi^+,\, K^+$
$B_s^0 \to \overline{K^0}$</td><td>BCL [305, Eqs. (529)–(530)]</td><td>[305, Tabs. 46, 48, 50, 51]</td></tr>
<tr><td>$B^0 \to \eta,\, \eta'$
$B_s^0 \to \eta,\, \eta'$</td><td>Double-pole [310, Eq. (36)]</td><td>[310, Tab. 4]</td></tr>
<tr><td>$B^0 \to \rho^0,\, \omega,\, K^{*0}$
$B^+ \to \rho^+,\, K^{*+}$
$B_s^0 \to \phi,\, \overline{K^{*0}}$</td><td>BCL [311, Eq. (2.16)]</td><td>[311, Tab. 14]</td></tr>
</table>

TABLE B.2: Relevant meson transitions for the decays studied in Section 6.2. The two last columns show the references to the form factor parametrizations and the best-fit parameter values. Isospin symmetry is assumed so that identical form factors are taken for $P^0 \to M^0$ and $P^+ \to M^+$ transitions, where M can be a pseudoscalar or vector meson.

used the results of Ref. [311]. In Table B.2 we include these references and the ones for all other form factors.

We note that the branching ratios in Fig. B.1 are very similar to those for the meson decays induced by the single-N_R operators with a charged lepton, which have been studied in detail in Ref. [172], cf. Fig. 2 therein. Thus, the constraints on the neutral current single-N_R operators from the far detectors are expected to be very similar to those derived in Ref. [172] for the charged current single-N_R operators. For this reason, we do not study the neutral current single-N_R operators in more detail.

B.3 HNL two-body decays via single-N_R operators

Single-N_R operators contribute to both HNL production and decay. In fact, depending on the Wilson coefficient and the value of active-heavy mixing, they can even dominate the HNL decay width. The LNC and LNV operators in Table 6.2 make HNLs undergo two- and three-body semileptonic decays. The dominant channels are two-body decays, mediated by just one insertion of an effective operator, with one light neutral meson and one active neutrino in the final state. If the HNL mass is large enough, then multimeson final states could also be important in the computation of the total decay

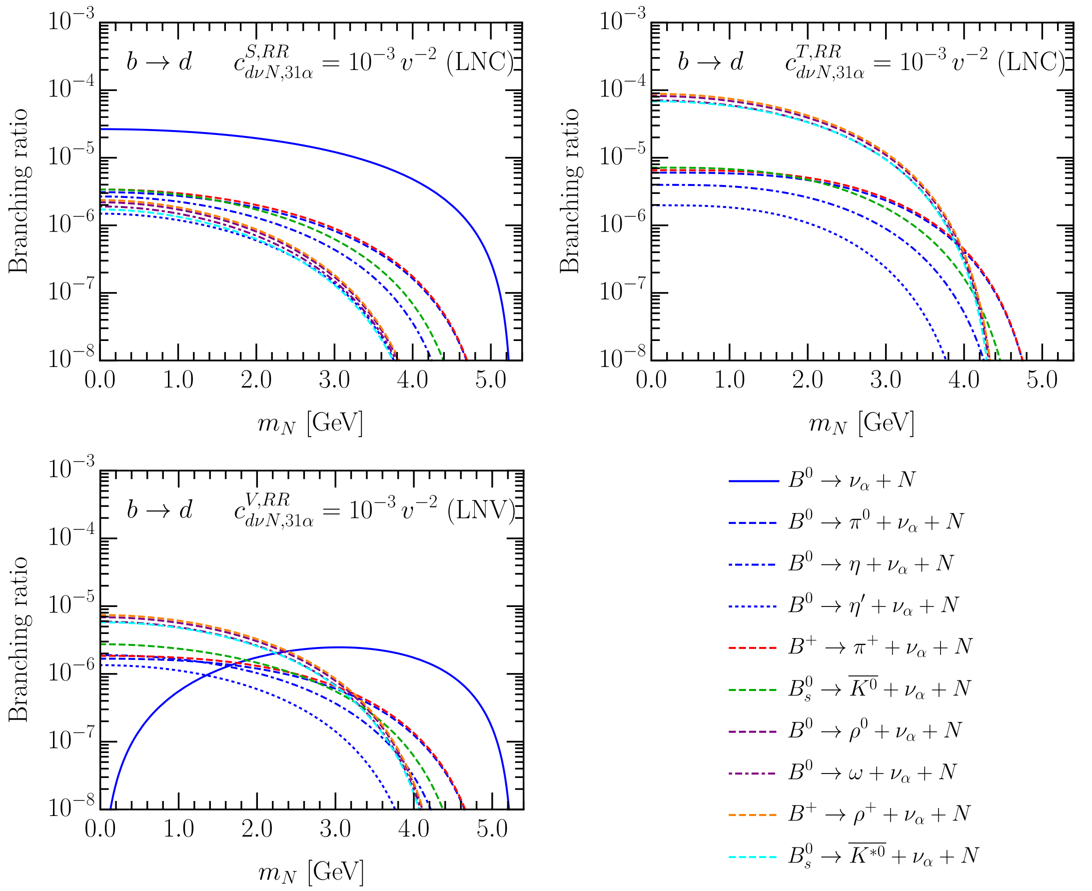

FIGURE B.1: Branching ratios of B-meson decays triggered by the single-N_R operators $\mathcal{O}^{S,RR}_{d\nu N,31\alpha}$, $\mathcal{O}^{T,RR}_{d\nu N,31\alpha}$ and $\mathcal{O}^{V,RR}_{d\nu N,32\alpha}$. In each case, the corresponding Wilson coefficient has been set to $10^{-3}v^{-2}$.

width. We do not compute this contribution, though. The single-N_R operators with light quarks can mediate the two-body decay processes mentioned above at tree level. The contribution from operators with heavy quarks, which control B- and D-meson decays into HNLs, is loop-suppressed, and we do not compute it. The interference between active-heavy mixing and single-N_R operators is also not treated here.

In this appendix, we list the HNL partial decay rates into a neutral meson and a SM neutrino mediated by the effective operators containing two light quarks. We leave, however, the flavor indices of the Wilson coefficients unspecified. We consider the scenarios where both N and ν are either Dirac or Majorana particles. In each case, we distinguish between a pseudoscalar and a vector meson in the final state. The latter requires the introduction of the following form factors:

$$\langle 0|\overline{q_i}\gamma^\mu q_j|V(p,\epsilon)\rangle = i f_V m_V \epsilon^\mu \,,$$

$$\langle 0|\overline{q_i}\sigma^{\mu\nu}q_j|V(p,\epsilon)\rangle = -f_V^T(p^\mu\epsilon^\nu - p^\nu\epsilon^\mu)\,, \tag{B.28}$$

where $|V(p,\epsilon)\rangle$ denotes a vector meson with mass m_V, momentum p, and polarization vector ϵ. For Dirac N and ν, the decay rate into a SM neutrino and a pseudoscalar (vector) meson P $(V) \sim \overline{q_i}q_j$ of mass m_P (m_V) reads

$$\Gamma(N\to\nu_\alpha P) = \frac{\left|f_P^S\right|^2}{128\pi}\left|c^{S,RR}_{q\nu N,\,ji\alpha} - c^{S,LR}_{q\nu N,\,ji\alpha}\right|^2 m_N\left(1-\frac{m_P^2}{m_N^2}\right)^2\,, \tag{B.29}$$

$$\Gamma(N\to\nu_\alpha V) = \frac{\left|f_V^T\right|^2}{4\pi}\left|c^{T,RR}_{q\nu N,\,ji\alpha}\right|^2 m_N^3\left(1-\frac{m_V^2}{m_N^2}\right)^2\left(1+\frac{m_V^2}{2m_N^2}\right)\,. \tag{B.30}$$

In the Majorana scenario, the decay rates receive contributions from both the LNC and LNV single-N_R operators and are given by

$$\begin{aligned}\Gamma(N\to\nu_\alpha P) = \frac{m_N}{128\pi}\left(1-\frac{m_P^2}{m_N^2}\right)^2 \Bigg\{ &\left|f_P^S\right|^2\left(\left|c^{S,RR}_{q\nu N,\,ji\alpha} - c^{S,LR}_{q\nu N,\,ji\alpha}\right|^2 + \left|c^{S,RR}_{q\nu N,\,ij\alpha} - c^{S,LR}_{q\nu N,\,ij\alpha}\right|^2\right)\\
&+ |f_P|^2\left(\left|c^{V,RR}_{q\nu N,\,ji\alpha} - c^{V,LR}_{q\nu N,\,ji\alpha}\right|^2 + \left|c^{V,RR}_{q\nu N,\,ij\alpha} - c^{V,LR}_{q\nu N,\,ij\alpha}\right|^2\right) m_N^2\\
&- f_P f_P^S\Big[\left(c^{S,RR}_{q\nu N,\,ji\alpha} - c^{S,LR}_{q\nu N,\,ji\alpha}\right)\left(c^{V,RR}_{q\nu N,\,ij\alpha} - c^{V,LR}_{q\nu N,\,ij\alpha}\right)\\
&\quad + \left(c^{S,RR}_{q\nu N,\,ij\alpha} - c^{S,LR}_{q\nu N,\,ij\alpha}\right)\left(c^{V,RR}_{q\nu N,\,ji\alpha} - c^{V,LR}_{q\nu N,\,ji\alpha}\right) + \text{h.c.}\Big] m_N\Bigg\}\,,\end{aligned} \tag{B.31}$$

$$\begin{aligned}\Gamma(N\to\nu_\alpha V) = \frac{m_N^3}{128\pi}\left(1-\frac{m_V^2}{m_N^2}\right)^2 \Bigg\{ &32\left|f_V^T\right|^2\left(\left|c^{T,RR}_{q\nu N,\,ij\alpha}\right|^2 + \left|c^{T,RR}_{q\nu N,\,ji\alpha}\right|^2\right)\left(1+\frac{m_V^2}{2m_N^2}\right)\\
&+ |f_V|^2\left(\left|c^{V,RR}_{q\nu N,\,ji\alpha} + c^{V,LR}_{q\nu N,\,ji\alpha}\right|^2 + \left|c^{V,RR}_{q\nu N,\,ij\alpha} + c^{V,LR}_{q\nu N,\,ij\alpha}\right|^2\right)\left(1+\frac{2m_V^2}{m_N^2}\right)\\
&- 12 f_V^T f_V\Big[c^{T,RR}_{q\nu N,\,ji\alpha}\left(c^{V,RR}_{q\nu N,\,ij\alpha} + c^{V,LR}_{q\nu N,\,ij\alpha}\right)\\
&\quad + c^{T,RR}_{q\nu N,\,ij\alpha}\left(c^{V,RR}_{q\nu N,\,ji\alpha} + c^{V,LR}_{q\nu N,\,ji\alpha}\right) + \text{h.c.}\Big]\frac{m_V}{m_N}\Bigg\}\,.\end{aligned} \tag{B.32}$$

Bibliography

[1] R. N. Mohapatra and P. B. Pal. *Massive Neutrinos in Physics and Astrophysics*. 3rd. WORLD SCIENTIFIC, 2004. DOI: 10.1142/5024.

[2] Particle Data Group. “Review of particle physics”. *Phys. Rev. D* 110.3 (2024), p. 030001. DOI: 10.1103/PhysRevD.110.030001.

[3] P. F. De Salas et al. “Neutrino Mass Ordering from Oscillations and Beyond: 2018 Status and Future Prospects”. *Front. Astron. Space Sci.* 5 (2018), p. 36. DOI: 10.3389/fspas.2018.00036. arXiv: 1806.11051 [hep-ph].

[4] P. F. de Salas et al. “2020 global reassessment of the neutrino oscillation picture”. *JHEP* 02 (2021), p. 071. DOI: 10.1007/JHEP02(2021)071. arXiv: 2006.11237 [hep-ph].

[5] JUNO Collaboration. “Sub-percent precision measurement of neutrino oscillation parameters with JUNO”. *Chin. Phys. C* 46.12 (2022), p. 123001. DOI: 10.1088/1674-1137/ac8bc9. arXiv: 2204.13249 [hep-ex].

[6] Hyper-Kamiokande Collaboration. “Hyper-Kamiokande Design Report” (May 2018). arXiv: 1805.04163 [physics.ins-det].

[7] I. Esteban et al. “NuFit-6.0: updated global analysis of three-flavor neutrino oscillations”. *JHEP* 12 (2024), p. 216. DOI: 10.1007/JHEP12(2024)216. arXiv: 2410.05380 [hep-ph].

[8] KATRIN Collaboration. “Direct neutrino-mass measurement based on 259 days of KATRIN data” (June 2024). arXiv: 2406.13516 [nucl-ex].

[9] Planck Collaboration. “Planck 2018 results. VI. Cosmological parameters”. *Astron. Astrophys.* 641 (2020). [Erratum: Astron.Astrophys. 652, C4 (2021)], A6. DOI: 10.1051/0004-6361/201833910. arXiv: 1807.06209 [astro-ph.CO].

[10] J. W. F. Valle and J. C. Romao. *Neutrinos in high energy and astroparticle physics*. Physics textbook. Weinheim: Wiley-VCH, 2015. ISBN: 978-3-527-41197-9, 978-3-527-67102-1.

[11] S. Centelles Chuliá, R. Srivastava, and J. W. F. Valle. "Seesaw roadmap to neutrino mass and dark matter". *Phys. Lett. B* 781 (2018), pp. 122–128. DOI: 10.1016/j.physletb.2018.03.046. arXiv: 1802.05722 [hep-ph].

[12] J. Calle et al. "Minimal radiative Dirac neutrino mass models". *Phys. Rev. D* 99.7 (2019), p. 075008. DOI: 10.1103/PhysRevD.99.075008. arXiv: 1812.05523 [hep-ph].

[13] S. Centelles Chuliá et al. "Dirac Neutrinos and Dark Matter Stability from Lepton Quarticity". *Phys. Lett. B* 767 (2017), pp. 209–213. DOI: 10.1016/j.physletb.2017.01.070. arXiv: 1606.04543 [hep-ph].

[14] E. Ma and O. Popov. "Pathways to Naturally Small Dirac Neutrino Masses". *Phys. Lett. B* 764 (2017), pp. 142–144. DOI: 10.1016/j.physletb.2016.11.027. arXiv: 1609.02538 [hep-ph].

[15] S. Weinberg. "Baryon and Lepton Nonconserving Processes". *Phys. Rev. Lett.* 43 (1979), pp. 1566–1570. DOI: 10.1103/PhysRevLett.43.1566.

[16] P. Minkowski. "$\mu \to e\gamma$ at a Rate of One Out of 10^9 Muon Decays?" *Phys. Lett. B* 67 (1977), pp. 421–428. DOI: 10.1016/0370-2693(77)90435-X.

[17] R. N. Mohapatra and G. Senjanovic. "Neutrino Mass and Spontaneous Parity Nonconservation". *Phys. Rev. Lett.* 44 (1980), p. 912. DOI: 10.1103/PhysRevLett.44.912.

[18] J. Schechter and J. W. F. Valle. "Neutrino Masses in SU(2) x U(1) Theories". *Phys. Rev. D* 22 (1980), p. 2227. DOI: 10.1103/PhysRevD.22.2227.

[19] M. Magg and C. Wetterich. "Neutrino Mass Problem and Gauge Hierarchy". *Phys. Lett. B* 94 (1980), pp. 61–64. DOI: 10.1016/0370-2693(80)90825-4.

[20] T. P. Cheng and L.F. Li. "Neutrino Masses, Mixings and Oscillations in $SU(2) \times U(1)$ Models of Electroweak Interactions". *Phys. Rev. D* 22 (1980), p. 2860. DOI: 10.1103/PhysRevD.22.2860.

[21] R. Foot et al. "Seesaw Neutrino Masses Induced by a Triplet of Leptons". *Z. Phys. C* 44 (1989), p. 441. DOI: 10.1007/BF01415558.

[22] J. C. Pati and A. Salam. "Lepton Number as the Fourth Color". *Phys. Rev. D* 10 (1974). [Erratum: Phys.Rev.D 11, 703–703 (1975)], pp. 275–289. DOI: 10.1103/PhysRevD.10.275.

[23] R. N. Mohapatra and J. C. Pati. "A Natural Left-Right Symmetry". *Phys. Rev. D* 11 (1975), p. 2558. DOI: 10.1103/PhysRevD.11.2558.

[24] A. Zee. "A Theory of Lepton Number Violation, Neutrino Majorana Mass, and Oscillation". *Phys. Lett. B* 93 (1980). [Erratum: Phys.Lett.B 95, 461 (1980)], p. 389. DOI: 10.1016/0370-2693(80)90349-4.

[25] E. Ma. "Verifiable radiative seesaw mechanism of neutrino mass and dark matter". *Phys. Rev. D* 73 (2006), p. 077301. DOI: 10.1103/PhysRevD.73.077301. arXiv: hep-ph/0601225.

[26] K. S. Babu and C. N. Leung. "Classification of effective neutrino mass operators". *Nucl. Phys. B* 619 (2001), pp. 667–689. DOI: 10.1016/S0550-3213(01)00504-1. arXiv: hep-ph/0106054.

[27] F. Bonnet et al. "Systematic study of the d=5 Weinberg operator at one-loop order". *JHEP* 07 (2012), p. 153. DOI: 10.1007/JHEP07(2012)153. arXiv: 1204.5862 [hep-ph].

[28] D. Aristizabal Sierra et al. "Systematic classification of two-loop realizations of the Weinberg operator". *JHEP* 03 (2015), p. 040. DOI: 10.1007/JHEP03(2015)040. arXiv: 1411.7038 [hep-ph].

[29] R. Cepedello, M. Hirsch, and J. C. Helo. "Loop neutrino masses from $d = 7$ operator". *JHEP* 07 (2017), p. 079. DOI: 10.1007/JHEP07(2017)079. arXiv: 1705.01489 [hep-ph].

[30] R. Cepedello, R. M. Fonseca, and M. Hirsch. "Systematic classification of three-loop realizations of the Weinberg operator". *JHEP* 10 (2018). [Erratum: JHEP 06, 034 (2019)], p. 197. DOI: 10.1007/JHEP10(2018)197. arXiv: 1807.00629 [hep-ph].

[31] C. Arbeláez et al. "How many 1-loop neutrino mass models are there?" *JHEP* 08 (2022), p. 023. DOI: 10.1007/JHEP08(2022)023. arXiv: 2205.13063 [hep-ph].

[32] K. Fridell et al. "Radiative neutrino masses from dim-7 SMEFT: a simplified multi-scale approach" (Dec. 2024). arXiv: 2412.14268 [hep-ph].

[33] J. Schechter and J. W. F. Valle. "Neutrinoless Double beta Decay in SU(2) x U(1) Theories". *Phys. Rev. D* 25 (1982), p. 2951. DOI: 10.1103/PhysRevD.25.2951.

[34] Michael Duerr, Manfred Lindner, and Alexander Merle. "On the Quantitative Impact of the Schechter-Valle Theorem". *JHEP* 06 (2011), p. 091. DOI: 10.1007/JHEP06(2011)091. arXiv: 1105.0901 [hep-ph].

[35] C. Giunti and C. W. Kim. *Fundamentals of Neutrino Physics and Astrophysics*. 2007. ISBN: 978-0-19-850871-7. DOI: 10.1093/acprof:oso/9780198508717.001.0001.

[36] GERDA Collaboration. "Probing Majorana neutrinos with double-β decay". *Science* 365 (2019), p. 1445. DOI: 10.1126/science.aav8613. arXiv: 1909.02726 [hep-ex].

[37] KamLAND-Zen Collaboration. "Search for Majorana Neutrinos near the Inverted Mass Hierarchy Region with KamLAND-Zen". *Phys. Rev. Lett.* 117.8

(2016). [Addendum: Phys.Rev.Lett. 117, 109903 (2016)], p. 082503. DOI: 10.1103/PhysRevLett.117.082503. arXiv: 1605.02889 [hep-ex].

[38] CUORE Collaboration. "Improved Limit on Neutrinoless Double-Beta Decay in ^{130}Te with CUORE". *Phys. Rev. Lett.* 124.12 (2020), p. 122501. DOI: 10.1103/PhysRevLett.124.122501. arXiv: 1912.10966 [nucl-ex].

[39] nEXO Collaboration. "nEXO: neutrinoless double beta decay search beyond 10^{28} year half-life sensitivity". *J. Phys. G* 49.1 (2022), p. 015104. DOI: 10.1088/1361-6471/ac3631. arXiv: 2106.16243 [nucl-ex].

[40] DARWIN Collaboration. "Sensitivity of the DARWIN observatory to the neutrinoless double beta decay of ^{136}Xe". *Eur. Phys. J. C* 80.9 (2020). [Erratum: Eur.Phys.J.C 83, 996 (2023)], p. 808. DOI: 10.1140/epjc/s10052-020-8196-z. arXiv: 2003.13407 [physics.ins-det].

[41] LEGEND Collaboration. "The Large Enriched Germanium Experiment for Neutrinoless $\beta\beta$ Decay: LEGEND-1000 Preconceptual Design Report" (July 2021). arXiv: 2107.11462 [physics.ins-det].

[42] H. Pas, M. Hirsch, and H. V. Klapdor-Kleingrothaus. "Improved bounds on SUSY accompanied neutrinoless double beta decay". *Phys. Lett. B* 459 (1999), pp. 450–454. DOI: 10.1016/S0370-2693(99)00711-X. arXiv: hep-ph/9810382.

[43] P. D. Bolton, F. F. Deppisch, and P. S. B. Dev. "Neutrinoless double beta decay via light neutralinos in R-parity violating supersymmetry". *JHEP* 03 (2022), p. 152. DOI: 10.1007/JHEP03(2022)152. arXiv: 2112.12658 [hep-ph].

[44] M. Hirsch, H. V. Klapdor-Kleingrothaus, and S. G. Kovalenko. "New leptoquark mechanism of neutrinoless double beta decay". *Phys. Rev. D* 54 (1996), R4207–R4210. DOI: 10.1103/PhysRevD.54.R4207. arXiv: hep-ph/9603213.

[45] P. S. B. Dev et al. "Neutrinoless double beta decay from scalar leptoquarks: interplay with neutrino mass and flavor physics". *JHEP* 01 (2025), p. 004. DOI: 10.1007/JHEP01(2025)004. arXiv: 2407.04670 [hep-ph].

[46] F. F. Deppisch et al. "Neutrinoless double beta decay in left-right symmetric models with a universal seesaw mechanism". *Phys. Rev. D* 97.3 (2018), p. 035005. DOI: 10.1103/PhysRevD.97.035005. arXiv: 1701.02107 [hep-ph].

[47] H. Pas et al. "Towards a superformula for neutrinoless double beta decay". *Phys. Lett. B* 453 (1999), pp. 194–198. DOI: 10.1016/S0370-2693(99)00330-5.

[48] H. Pas et al. "A Superformula for neutrinoless double beta decay. 2. The Short range part". *Phys. Lett. B* 498 (2001), pp. 35–39. DOI: 10.1016/S0370-2693(00)01359-9. arXiv: hep-ph/0008182.

[49] K. Fujikawa and R. E. Shrock. "Magnetic Moment of a Massive Neutrino and Neutrino-Spin Rotation". *Phys. Rev. Lett.* 45 (12 1980), pp. 963–966. DOI: 10.1103/PhysRevLett.45.963.

[50] A. G. Beda et al. "The results of search for the neutrino magnetic moment in GEMMA experiment". *Adv. High Energy Phys.* 2012 (2012), p. 350150. DOI: 10.1155/2012/350150.

[51] F. Capozzi and G. Raffelt. "Axion and neutrino bounds improved with new calibrations of the tip of the red-giant branch using geometric distance determinations". *Phys. Rev. D* 102.8 (2020), p. 083007. DOI: 10.1103/PhysRevD.102.083007. arXiv: 2007.03694 [astro-ph.SR].

[52] H. T. Wong et al. "Research program towards observation of neutrino-nucleus coherent scattering". *J. Phys. Conf. Ser.* 39 (2006). Ed. by Alexey Sissakian, Gennady Kozlov, and Elena Kolganova, pp. 266–268. DOI: 10.1088/1742-6596/39/1/064. arXiv: hep-ex/0511001.

[53] T. S. Kosmas et al. "Sensitivities to neutrino electromagnetic properties at the TEXONO experiment". *Phys. Lett. B* 750 (2015), pp. 459–465. DOI: 10.1016/j.physletb.2015.09.054. arXiv: 1506.08377 [hep-ph].

[54] O. G. Miranda et al. "Low-energy probes of sterile neutrino transition magnetic moments". *JHEP* 12 (2021), p. 191. DOI: 10.1007/JHEP12(2021)191. arXiv: 2109.09545 [hep-ph].

[55] M. Atkinson et al. "Heavy Neutrino Searches through Double-Bang Events at Super-Kamiokande, DUNE, and Hyper-Kamiokande". *JHEP* 04 (2022), p. 174. DOI: 10.1007/JHEP04(2022)174. arXiv: 2105.09357 [hep-ph].

[56] G. Huang et al. "Probing heavy sterile neutrinos at neutrino telescopes via the dipole portal". *Phys. Lett. B* 840 (2023), p. 137842. DOI: 10.1016/j.physletb.2023.137842. arXiv: 2204.10347 [hep-ph].

[57] V. Brdar et al. "The Neutrino Magnetic Moment Portal: Cosmology, Astrophysics, and Direct Detection". *JCAP* 01 (2021), p. 039. DOI: 10.1088/1475-7516/2021/01/039. arXiv: 2007.15563 [hep-ph].

[58] G. Chauhan et al. "Probing the sterile neutrino dipole portal with SN1987A and low-energy supernovae". *Phys. Rev. D* 110.1 (2024), p. 015007. DOI: 10.1103/PhysRevD.110.015007. arXiv: 2402.01624 [hep-ph].

[59] S. T. Petcov. "The Processes $\mu \to e + \gamma, \mu \to e + e + \overline{e}, \nu' \to \nu + \gamma$ in the Weinberg-Salam Model with Neutrino Mixing". *Sov. J. Nucl. Phys.* 25 (1977).

[Erratum: Sov.J.Nucl.Phys. 25, 698 (1977), Erratum: Yad.Fiz. 25, 1336 (1977)], p. 340.

[60] E. Arganda and M. J. Herrero. "Testing supersymmetry with lepton flavor violating tau and mu decays". *Phys. Rev. D* 73 (2006), p. 055003. DOI: 10.1103/PhysRevD.73.055003. arXiv: hep-ph/0510405.

[61] S. Davidson. "$\mu \to e\gamma$ in the 2HDM: an exercise in EFT". *Eur. Phys. J. C* 76.5 (2016), p. 258. DOI: 10.1140/epjc/s10052-016-4076-y. arXiv: 1601.01949 [hep-ph].

[62] R. A. Diaz, R. Martinez, and J. A. Rodriguez. "Phenomenology of lepton flavor violation in 2HDM(3) from $(g-2)(\mu)$ and leptonic decays". *Phys. Rev. D* 67 (2003), p. 075011. DOI: 10.1103/PhysRevD.67.075011. arXiv: hep-ph/0208117.

[63] A. Abada et al. "Low energy effects of neutrino masses". *JHEP* 12 (2007), p. 061. DOI: 10.1088/1126-6708/2007/12/061. arXiv: 0707.4058 [hep-ph].

[64] T. Toma and A. Vicente. "Lepton Flavor Violation in the Scotogenic Model". *JHEP* 01 (2014), p. 160. DOI: 10.1007/JHEP01(2014)160. arXiv: 1312.2840 [hep-ph].

[65] A. Abada, V. De Romeri, and A. M. Teixeira. "Impact of sterile neutrinos on nuclear-assisted cLFV processes". *JHEP* 02 (2016), p. 083. DOI: 10.1007/JHEP02(2016)083. arXiv: 1510.06657 [hep-ph].

[66] MEG Collaboration. "Search for the lepton flavour violating decay $\mu^+ \to \mathrm{e}^+\gamma$ with the full dataset of the MEG experiment". *Eur. Phys. J. C* 76.8 (2016), p. 434. DOI: 10.1140/epjc/s10052-016-4271-x. arXiv: 1605.05081 [hep-ex].

[67] MEG II Collaboration. "The Search for $\mu^+e^+\gamma$ with 10^{-14} Sensitivity: The Upgrade of the MEG Experiment". *Symmetry* 13.9 (2021), p. 1591. DOI: 10.3390/sym13091591. arXiv: 2107.10767 [hep-ex].

[68] BaBar Collaboration. "Searches for Lepton Flavor Violation in the Decays $\tau^\pm \to e^\pm\gamma$ and $\tau^\pm \to \mu^\pm\gamma$". *Phys. Rev. Lett.* 104 (2010), p. 021802. DOI: 10.1103/PhysRevLett.104.021802. arXiv: 0908.2381 [hep-ex].

[69] Belle-II Collaboration. "The Belle II Physics Book". *PTEP* 2019.12 (2019). Ed. by E. Kou and P. Urquijo. [Erratum: PTEP 2020, 029201 (2020)], p. 123C01. DOI: 10.1093/ptep/ptz106. arXiv: 1808.10567 [hep-ex].

[70] Belle Collaboration. "Search for lepton-flavor-violating tau-lepton decays to $\ell\gamma$ at Belle". *JHEP* 10 (2021), p. 19. DOI: 10.1007/JHEP10(2021)019. arXiv: 2103.12994 [hep-ex].

[71] SINDRUM Collaboration. "Search for the Decay $\mu^+ \to e^+e^+e^-$". *Nucl. Phys. B* 299 (1988), pp. 1–6. DOI: 10.1016/0550-3213(88)90462-2.

[72] Mu3e Collaboration. "Technical design of the phase I Mu3e experiment". *Nucl. Instrum. Meth. A* 1014 (2021), p. 165679. DOI: 10.1016/j.nima.2021.165679. arXiv: 2009.11690 [physics.ins-det].

[73] K. Hayasaka et al. "Search for Lepton Flavor Violating τ Decays into Three Leptons with 719 Million Produced $\tau^+\tau^-$ Pairs". *Phys. Lett. B* 687 (2010), pp. 139–143. DOI: 10.1016/j.physletb.2010.03.037. arXiv: 1001.3221 [hep-ex].

[74] Belle-II Collaboration. "Search for lepton-flavor-violating $\tau^- \to \mu^-\mu^+\mu^-$ decays at Belle II". *JHEP* 09 (2024), p. 062. DOI: 10.1007/JHEP09(2024)062. arXiv: 2405.07386 [hep-ex].

[75] D. Wyler and L. Wolfenstein. "Massless Neutrinos in Left-Right Symmetric Models". *Nucl. Phys. B* 218 (1983), pp. 205–214. DOI: 10.1016/0550-3213(83)90482-0.

[76] R.N. Mohapatra and J.W.F. Valle. "Neutrino Mass and Baryon Number Nonconservation in Superstring Models". *Phys. Rev.* D34 (1986), p. 1642. DOI: 10.1103/PhysRevD.34.1642.

[77] M. C. Gonzalez-Garcia and J. W. F. Valle. "Fast Decaying Neutrinos and Observable Flavor Violation in a New Class of Majoron Models". *Phys. Lett. B* 216 (1989), pp. 360–366. DOI: 10.1016/0370-2693(89)91131-3.

[78] E. K. Akhmedov et al. "Dynamical left-right symmetry breaking". *Phys.Rev.* D53 (1996), pp. 2752–2780. DOI: 10.1103/PhysRevD.53.2752. arXiv: hep-ph/9509255 [hep-ph].

[79] E. K. Akhmedov et al. "Left-right symmetry breaking in NJL approach". *Phys.Lett.* B368 (1996), pp. 270–280. DOI: 10.1016/0370-2693(95)01504-3. arXiv: hep-ph/9507275 [hep-ph].

[80] M. Malinsky, J. C. Romao, and J. W. F. Valle. "Novel supersymmetric SO(10) seesaw mechanism". *Phys. Rev. Lett.* 95 (2005), p. 161801. DOI: 10.1103/PhysRevLett.95.161801. arXiv: hep-ph/0506296.

[81] M. B. Gavela et al. "Minimal Flavour Seesaw Models". *JHEP* 09 (2009), p. 038. DOI: 10.1088/1126-6708/2009/09/038. arXiv: 0906.1461 [hep-ph].

[82] Gerard 't Hooft. "Naturalness, chiral symmetry, and spontaneous chiral symmetry breaking". *NATO Sci. Ser. B* 59 (1980). Ed. by Gerard 't Hooft et al., pp. 135–157. DOI: 10.1007/978-1-4684-7571-5_9.

[83] J. Lopez-Pavon, S. Pascoli, and C. Wong. "Can heavy neutrinos dominate neutrinoless double beta decay?" *Phys. Rev. D* 87.9 (2013), p. 093007. DOI: 10.1103/PhysRevD.87.093007. arXiv: 1209.5342 [hep-ph].

[84] L. Wolfenstein. "Different Varieties of Massive Dirac Neutrinos". *Nucl. Phys. B* 186 (1981), pp. 147–152. DOI: 10.1016/0550-3213(81)90096-1.

[85] J. W. F. Valle and M. Singer. "Lepton Number Violation With Quasi Dirac Neutrinos". *Phys. Rev. D* 28 (1983), p. 540. DOI: 10.1103/PhysRevD.28.540.

[86] Z. J. Tao. "Radiative seesaw mechanism at weak scale". *Phys. Rev. D* 54 (1996), pp. 5693–5697. DOI: 10.1103/PhysRevD.54.5693. arXiv: hep-ph/9603309.

[87] Y. Cai et al. "From the trees to the forest: a review of radiative neutrino mass models". *Front. in Phys.* 5 (2017), p. 63. DOI: 10.3389/fphy.2017.00063. arXiv: 1706.08524 [hep-ph].

[88] T. Asaka, S. Blanchet, and M. Shaposhnikov. "The nuMSM, dark matter and neutrino masses". *Phys. Lett. B* 631 (2005), pp. 151–156. DOI: 10.1016/j.physletb.2005.09.070. arXiv: hep-ph/0503065.

[89] R. Barbier et al. "R-parity violating supersymmetry". *Phys. Rept.* 420 (2005), pp. 1–202. DOI: 10.1016/j.physrep.2005.08.006. arXiv: hep-ph/0406039.

[90] M. Fabbrichesi, E. Gabrielli, and G. Lanfranchi. "The Dark Photon" (May 2020). DOI: 10.1007/978-3-030-62519-1. arXiv: 2005.01515 [hep-ph].

[91] L. J. Hall et al. "Freeze-In Production of FIMP Dark Matter". *JHEP* 03 (2010), p. 080. DOI: 10.1007/JHEP03(2010)080. arXiv: 0911.1120 [hep-ph].

[92] T. Tantau. *TikZ and PGF: Manual for Version 3.0.0*. https://ctan.org/pkg/pgf. PGF/TikZ Development Team. 2013.

[93] R. M. Bianchi and ATLAS Collaboration. "ATLAS experiment schematic or layout illustration". General Photo. 2022. URL: https://cds.cern.ch/record/2837191.

[94] CMS Collaboration. "Search for low-mass long-lived particles decaying to displaced jets in proton-proton collisions at $\sqrt{s} = 13.6$ TeV" (2024).

[95] ATLAS Collaboration. "Search for neutral long-lived particles that decay into displaced jets in the ATLAS calorimeter in association with leptons or jets using pp collisions at $\sqrt{\mathrm{s}}$ = 13 TeV". *JHEP* 11 (2024), p. 036. DOI: 10.1007/JHEP11(2024)036. arXiv: 2407.09183 [hep-ex].

[96] ATLAS Collaboration. "Search for events with one displaced vertex from long-lived neutral particles decaying into hadronic jets in the ATLAS muon spectrometer in pp collisions at $\sqrt{s} = 13$ TeV" (Mar. 2025). arXiv: 2503.20445 [hep-ex].

[97] ATLAS Collaboration. "The new ATLAS triggers for long-lived particles that leave unconventional signatures in the tracking detectors". *PoS* LHCP2022 (2023), p. 300. DOI: 10.22323/1.422.0300.

[98] CMS Collaboration. "Long-Lived Particle Triggering with the CMS Hadron Calorimeter". *PoS* ICHEP2024 (2025), p. 895. DOI: 10.22323/1.476.0895.

[99] LHCb Collaboration. "Long-lived particle reconstruction downstream of the LHCb magnet". *Eur. Phys. J. C* 85.1 (2025). [Erratum: Eur.Phys.J.C 85, 310 (2025)], p. 7. DOI: 10.1140/epjc/s10052-024-13686-6. arXiv: 2211.10920 [hep-ex].

[100] J. Alimena et al. "Searching for long-lived particles beyond the Standard Model at the Large Hadron Collider". *J. Phys. G* 47.9 (2020), p. 090501. DOI: 10.1088/1361-6471/ab4574. arXiv: 1903.04497 [hep-ex].

[101] CERN. *The Large Hadron Collider*. Accessed: 2025-04-30. 2024. URL: https://home.cern/science/accelerators/large-hadron-collider.

[102] D. Curtin et al. "Long-Lived Particles at the Energy Frontier: The MATHUSLA Physics Case". *Rept. Prog. Phys.* 82.11 (2019), p. 116201. DOI: 10.1088/1361-6633/ab28d6. arXiv: 1806.07396 [hep-ph].

[103] MATHUSLA Collaboration. "An Update to the Letter of Intent for MATHUSLA: Search for Long-Lived Particles at the HL-LHC" (Sept. 2020). arXiv: 2009.01693 [physics.ins-det].

[104] MATHUSLA Collaboration. "Conceptual Design Report for the MATHUSLA Long-Lived Particle Detector near CMS" (Mar. 2025). arXiv: 2503.20893 [physics.ins-det].

[105] M. Bauer et al. "ANUBIS: Proposal to search for long-lived neutral particles in CERN service shafts" (Sept. 2019). arXiv: 1909.13022 [physics.ins-det].

[106] J. L. Pinfold. "The MoEDAL Experiment at the LHC—A Progress Report". *Universe* 5.2 (2019), p. 47. DOI: 10.3390/universe5020047.

[107] James L. Pinfold. "The MoEDAL experiment: a new light on the high-energy frontier". *Phil. Trans. Roy. Soc. Lond. A* 377.2161 (2019). Ed. by John Dainton, p. 20190382. DOI: 10.1098/rsta.2019.0382.

[108] V. V. Gligorov et al. "Searching for Long-lived Particles: A Compact Detector for Exotics at LHCb". *Phys. Rev. D* 97.1 (2018), p. 015023. DOI: 10.1103/PhysRevD.97.015023. arXiv: 1708.09395 [hep-ph].

[109] J. L. Feng et al. "ForwArd Search ExpeRiment at the LHC". *Phys. Rev. D* 97.3 (2018), p. 035001. DOI: 10.1103/PhysRevD.97.035001. arXiv: 1708.09389 [hep-ph].

[110] FASER Collaboration. "FASER's physics reach for long-lived particles". *Phys. Rev. D* 99.9 (2019), p. 095011. DOI: 10.1103/PhysRevD.99.095011. arXiv: 1811.12522 [hep-ph].

[111] S. Cerci et al. "FACET: A new long-lived particle detector in the very forward region of the CMS experiment". *JHEP* 06 (2022), p. 110. DOI: 10.1007/JHEP06(2022)110. arXiv: 2201.00019 [hep-ex].

[112] T. P. Satterthwaite. "Sensitivity of the ANUBIS and ATLAS Detectors to Neutral Long-Lived Particles Produced in pp Collisions at the Large Hadron Collider". Presented 08 Sep 2022. MA thesis. 2022. URL: http://cds.cern.ch/record/2839063.

[113] J. L. Feng et al. "The Forward Physics Facility at the High-Luminosity LHC". *J. Phys. G* 50.3 (2023), p. 030501. DOI: 10.1088/1361-6471/ac865e. arXiv: 2203.05090 [hep-ex].

[114] SHiP Collaboration. "A facility to Search for Hidden Particles (SHiP) at the CERN SPS" (Apr. 2015). arXiv: 1504.04956 [physics.ins-det].

[115] S. Alekhin et al. "A facility to Search for Hidden Particles at the CERN SPS: the SHiP physics case". *Rept. Prog. Phys.* 79.12 (2016), p. 124201. DOI: 10.1088/0034-4885/79/12/124201. arXiv: 1504.04855 [hep-ph].

[116] SHiP Collaboration. "The SHiP experiment at the proposed CERN SPS Beam Dump Facility". *Eur. Phys. J. C* 82.5 (2022), p. 486. DOI: 10.1140/epjc/s10052-022-10346-5. arXiv: 2112.01487 [physics.ins-det].

[117] DUNE Collaboration. "Long-baseline neutrino oscillation physics potential of the DUNE experiment". *Eur. Phys. J. C* 80.10 (2020), p. 978. DOI: 10.1140/epjc/s10052-020-08456-z. arXiv: 2006.16043 [hep-ex].

[118] DUNE Collaboration. "Experiment Simulation Configurations Approximating DUNE TDR" (Mar. 2021). arXiv: 2103.04797 [hep-ex].

[119] DUNE Collaboration. "Low exposure long-baseline neutrino oscillation sensitivity of the DUNE experiment". *Phys. Rev. D* 105.7 (2022), p. 072006. DOI: 10.1103/PhysRevD.105.072006. arXiv: 2109.01304 [hep-ex].

[120] DUNE Collaboration. "Deep Underground Neutrino Experiment (DUNE) Near Detector Conceptual Design Report". *Instruments* 5.4 (2021), p. 31. DOI: 10.3390/instruments5040031. arXiv: 2103.13910 [physics.ins-det].

[121] A. Atre et al. "The Search for Heavy Majorana Neutrinos". *JHEP* 05 (2009), p. 030. DOI: 10.1088/1126-6708/2009/05/030. arXiv: 0901.3589 [hep-ph].

[122] K. Bondarenko et al. "Phenomenology of GeV-scale Heavy Neutral Leptons". *JHEP* 11 (2018), p. 032. DOI: 10.1007/JHEP11(2018)032. arXiv: 1805.08567 [hep-ph].

[123] E. Fernández-Martínez et al. "Effective portals to heavy neutral leptons". *JHEP* 09 (2023), p. 001. DOI: 10.1007/JHEP09(2023)001. arXiv: 2304.06772 [hep-ph].

[124] ATLAS Collaboration. "Search for Heavy Neutral Leptons in Decays of W Bosons Using a Dilepton Displaced Vertex in $\sqrt{s} = 13$ TeV pp Collisions with

the ATLAS Detector". *Phys. Rev. Lett.* 131.6 (2023), p. 061803. DOI: 10.1103/PhysRevLett.131.061803. arXiv: 2204.11988 [hep-ex].

[125] CMS Collaboration. "Search for heavy neutral leptons in final states with electrons, muons, and hadronically decaying tau leptons in proton-proton collisions at $\sqrt{s}$ = 13 TeV". *JHEP* 06 (2024), p. 123. DOI: 10.1007/JHEP06(2024)123. arXiv: 2403.00100 [hep-ex].

[126] CHARM Collaboration. "A Search for Decays of Heavy Neutrinos in the Mass Range 0.5-GeV to 2.8-GeV". *Phys. Lett. B* 166 (1986), pp. 473–478. DOI: 10.1016/0370-2693(86)91601-1.

[127] R. Barouki, G. Marocco, and S. Sarkar. "Blast from the past II: Constraints on heavy neutral leptons from the BEBC WA66 beam dump experiment". *SciPost Phys.* 13 (2022), p. 118. DOI: 10.21468/SciPostPhys.13.5.118. arXiv: 2208.00416 [hep-ph].

[128] T2K Collaboration. "Search for heavy neutrinos with the T2K near detector ND280". *Phys. Rev. D* 100.5 (2019), p. 052006. DOI: 10.1103/PhysRevD.100.052006. arXiv: 1902.07598 [hep-ex].

[129] NA62 Collaboration. "Search for heavy neutral lepton production in K+ decays to positrons". *Phys. Lett. B* 807 (2020), p. 135599. DOI: 10.1016/j.physletb.2020.135599. arXiv: 2005.09575 [hep-ex].

[130] N. Sabti, A. Magalich, and A. Filimonova. "An Extended Analysis of Heavy Neutral Leptons during Big Bang Nucleosynthesis". *JCAP* 11 (2020), p. 056. DOI: 10.1088/1475-7516/2020/11/056. arXiv: 2006.07387 [hep-ph].

[131] M. Blennow et al. "Bounds on lepton non-unitarity and heavy neutrino mixing". *JHEP* 08 (2023), p. 030. DOI: 10.1007/JHEP08(2023)030. arXiv: 2306.01040 [hep-ph].

[132] A. Abada et al. "Collider searches for heavy neutral leptons: beyond simplified scenarios". *Eur. Phys. J. C* 82.11 (2022), p. 1030. DOI: 10.1140/epjc/s10052-022-11011-7. arXiv: 2208.13882 [hep-ph].

[133] A. V. Manohar. "Introduction to Effective Field Theories" (Apr. 2018). Ed. by Sacha Davidson et al. DOI: 10.1093/oso/9780198855743.003.0002. arXiv: 1804.05863 [hep-ph].

[134] I. Brivio and M. Trott. "The Standard Model as an Effective Field Theory". *Phys. Rept.* 793 (2019), pp. 1–98. DOI: 10.1016/j.physrep.2018.11.002. arXiv: 1706.08945 [hep-ph].

[135] F. Wilczek and A. Zee. "Operator Analysis of Nucleon Decay". *Phys. Rev. Lett.* 43 (1979), pp. 1571–1573. DOI: 10.1103/PhysRevLett.43.1571.

[136] W. Buchmuller and D. Wyler. "Effective Lagrangian Analysis of New Interactions and Flavor Conservation". *Nucl. Phys. B* 268 (1986), pp. 621–653. DOI: 10.1016/0550-3213(86)90262-2.

[137] B. Grzadkowski et al. "Dimension-Six Terms in the Standard Model Lagrangian". *JHEP* 10 (2010), p. 085. DOI: 10.1007/JHEP10(2010)085. arXiv: 1008.4884 [hep-ph].

[138] L. Lehman. "Extending the Standard Model Effective Field Theory with the Complete Set of Dimension-7 Operators". *Phys. Rev. D* 90.12 (2014), p. 125023. DOI: 10.1103/PhysRevD.90.125023. arXiv: 1410.4193 [hep-ph].

[139] L. Lehman and A. Martin. "Hilbert Series for Constructing Lagrangians: expanding the phenomenologist's toolbox". *Phys. Rev. D* 91 (2015), p. 105014. DOI: 10.1103/PhysRevD.91.105014. arXiv: 1503.07537 [hep-ph].

[140] L. Lehman and A. Martin. "Low-derivative operators of the Standard Model effective field theory via Hilbert series methods". *JHEP* 02 (2016), p. 081. DOI: 10.1007/JHEP02(2016)081. arXiv: 1510.00372 [hep-ph].

[141] B. Henning et al. "2, 84, 30, 993, 560, 15456, 11962, 261485, ...: Higher dimension operators in the SM EFT". *JHEP* 08 (2017). [Erratum: JHEP 09, 019 (2019)], p. 016. DOI: 10.1007/JHEP08(2017)016. arXiv: 1512.03433 [hep-ph].

[142] R. M. Fonseca. "The Sym2Int program: going from symmetries to interactions". *J. Phys. Conf. Ser.* 873.1 (2017). Ed. by Bohdan Grzadkowski, Jan Kalinowski, and Maria Krawczyk, p. 012045. DOI: 10.1088/1742-6596/873/1/012045. arXiv: 1703.05221 [hep-ph].

[143] R. M. Fonseca. "Enumerating the operators of an effective field theory". *Phys. Rev. D* 101.3 (2020), p. 035040. DOI: 10.1103/PhysRevD.101.035040. arXiv: 1907.12584 [hep-ph].

[144] A. Carmona et al. "Matchmakereft: automated tree-level and one-loop matching". *SciPost Phys.* 12.6 (2022), p. 198. DOI: 10.21468/SciPostPhys.12.6.198. arXiv: 2112.10787 [hep-ph].

[145] J. Fuentes-Martín et al. "A proof of concept for matchete: an automated tool for matching effective theories". *Eur. Phys. J. C* 83.7 (2023), p. 662. DOI: 10.1140/epjc/s10052-023-11726-1. arXiv: 2212.04510 [hep-ph].

[146] J. Aebischer, J. Kumar, and D. M. Straub. "Wilson: a Python package for the running and matching of Wilson coefficients above and below the electroweak scale". *Eur. Phys. J. C* 78.12 (2018), p. 1026. DOI: 10.1140/epjc/s10052-018-6492-7. arXiv: 1804.05033 [hep-ph].

[147] D. M. Straub. "flavio: a Python package for flavour and precision phenomenology in the Standard Model and beyond" (Oct. 2018). arXiv: 1810.08132 [hep-ph].

[148] Y. Liao and X. D. Ma. "Operators up to Dimension Seven in Standard Model Effective Field Theory Extended with Sterile Neutrinos". *Phys. Rev. D* 96.1 (2017), p. 015012. DOI: 10.1103/PhysRevD.96.015012. arXiv: 1612.04527 [hep-ph].

[149] H. Li et al. "Operator bases in effective field theories with sterile neutrinos: d $\leq$ 9". *JHEP* 11 (2021), p. 003. DOI: 10.1007/JHEP11(2021)003. arXiv: 2105.09329 [hep-ph].

[150] F. del Aguila et al. "Heavy Majorana Neutrinos in the Effective Lagrangian Description: Application to Hadron Colliders". *Phys. Lett. B* 670 (2009), pp. 399–402. DOI: 10.1016/j.physletb.2008.11.031. arXiv: 0806.0876 [hep-ph].

[151] A. Aparici et al. "Right-handed neutrino magnetic moments". *Phys. Rev. D* 80 (2009), p. 013010. DOI: 10.1103/PhysRevD.80.013010. arXiv: 0904.3244 [hep-ph].

[152] Y. Liao and X. D. Ma. "Renormalization Group Evolution of Dimension-seven Baryon- and Lepton-number-violating Operators". *JHEP* 11 (2016), p. 043. DOI: 10.1007/JHEP11(2016)043. arXiv: 1607.07309 [hep-ph].

[153] E. E. Jenkins, A. V. Manohar, and P. Stoffer. "Low-Energy Effective Field Theory below the Electroweak Scale: Operators and Matching". *JHEP* 03 (2018), p. 016. DOI: 10.1007/JHEP03(2018)016. arXiv: 1709.04486 [hep-ph].

[154] T. Li, X. D. Ma, and M. A. Schmidt. "General neutrino interactions with sterile neutrinos in light of coherent neutrino-nucleus scattering and meson invisible decays". *JHEP* 07 (2020), p. 152. DOI: 10.1007/JHEP07(2020)152. arXiv: 2005.01543 [hep-ph].

[155] M. Chala and A. Titov. "One-loop matching in the SMEFT extended with a sterile neutrino". *JHEP* 05 (2020), p. 139. DOI: 10.1007/JHEP05(2020)139. arXiv: 2001.07732 [hep-ph].

[156] R. Beltrán, R. Cepedello, and M. Hirsch. "Tree-level UV completions for N_RSMEFT $d = 6$ and $d = 7$ operators". *JHEP* 08 (2023), p. 166. DOI: 10.1007/JHEP08(2023)166. arXiv: 2306.12578 [hep-ph].

[157] J. de Blas et al. "Effective description of general extensions of the Standard Model: the complete tree-level dictionary". *JHEP* 03 (2018), p. 109. DOI: 10.1007/JHEP03(2018)109. arXiv: 1711.10391 [hep-ph].

[158] R. Cepedello, R. Fonseca, and M. Hirsch. "Neutrino masses beyond the minimal seesaw". *J. Phys. Conf. Ser.* 1468.1 (2020). Ed. by Masayuki Nakahata, p. 012171. DOI: 10.1088/1742-6596/1468/1/012171. arXiv: 1911.01125 [hep-ph].

[159] Ricardo Cepedello et al. "Mapping the SMEFT to discoverable models". *JHEP* 09 (2022), p. 229. DOI: 10.1007/JHEP09(2022)229. arXiv: 2207.13714 [hep-ph].

[160] Ricardo Cepedello et al. "SMEFT goes dark: Dark Matter models for four-fermion operators". *JHEP* 09 (2023), p. 081. DOI: 10.1007/JHEP09(2023)081. arXiv: 2302.03485 [hep-ph].

[161] I. Bischer and W. Rodejohann. "General neutrino interactions from an effective field theory perspective". *Nucl. Phys. B* 947 (2019), p. 114746. DOI: 10.1016/j.nuclphysb.2019.114746. arXiv: 1905.08699 [hep-ph].

[162] C. Arzt, M. B. Einhorn, and J. Wudka. "Patterns of deviation from the standard model". *Nucl. Phys. B* 433 (1995), pp. 41–66. DOI: 10.1016/0550-3213(94)00336-D. arXiv: hep-ph/9405214.

[163] M. Singer, J. W. F. Valle, and J. Schechter. "Canonical Neutral Current Predictions From the Weak Electromagnetic Gauge Group $SU(3) \times U(1)$". *Phys. Rev. D* 22 (1980), p. 738. DOI: 10.1103/PhysRevD.22.738.

[164] F. Pisano and V. Pleitez. "An $SU(3) \times U(1)$ model for electroweak interactions". *Phys. Rev. D* 46 (1992), pp. 410–417. DOI: 10.1103/PhysRevD.46.410. arXiv: hep-ph/9206242.

[165] R. M. Fonseca and M. Hirsch. "Lepton number violation in 331 models". *Phys. Rev. D* 94.11 (2016), p. 115003. DOI: 10.1103/PhysRevD.94.115003. arXiv: 1607.06328 [hep-ph].

[166] ATLAS Collaboration. "Observation of a new particle in the search for the Standard Model Higgs boson with the ATLAS detector at the LHC". *Phys. Lett. B* 716 (2012), pp. 1–29. DOI: 10.1016/j.physletb.2012.08.020. arXiv: 1207.7214 [hep-ex].

[167] CMS Collaboration. "Observation of a New Boson at a Mass of 125 GeV with the CMS Experiment at the LHC". *Phys. Lett. B* 716 (2012), pp. 30–61. DOI: 10.1016/j.physletb.2012.08.021. arXiv: 1207.7235 [hep-ex].

[168] Particle Data Group. "Review of Particle Physics". *PTEP* 2022 (2022), p. 083C01. DOI: 10.1093/ptep/ptac097.

[169] F. Bonnet et al. "Systematic decomposition of the neutrinoless double beta decay operator". *JHEP* 03 (2013). [Erratum: JHEP 04, 090 (2014)], p. 055. DOI: 10.1007/JHEP03(2013)055. arXiv: 1212.3045 [hep-ph].

[170] J. C. Helo et al. "Double beta decay and neutrino mass models". *JHEP* 05 (2015), p. 092. DOI: 10.1007/JHEP05(2015)092. arXiv: 1502.05188 [hep-ph].

[171] I. Cordero-Carrión, M. Hirsch, and A. Vicente. "General parametrization of Majorana neutrino mass models". *Phys. Rev. D* 101.7 (2020), p. 075032. DOI: 10.1103/PhysRevD.101.075032. arXiv: 1912.08858 [hep-ph].

[172] J. De Vries et al. "Long-lived Sterile Neutrinos at the LHC in Effective Field Theory". *JHEP* 03 (2021), p. 148. DOI: 10.1007/JHEP03(2021)148. arXiv: 2010.07305 [hep-ph].

[173] G. Zhou et al. "Long-lived sterile neutrinos at Belle II in effective field theory". *JHEP* 04 (2022), p. 057. DOI: 10.1007/JHEP04(2022)057. arXiv: 2111.04403 [hep-ph].

[174] T. Han et al. "Right-handed Dirac and Majorana neutrinos at Belle II". *JHEP* 04 (2023). [Erratum: JHEP 09, 016 (2023)], p. 013. DOI: 10.1007/JHEP04(2023)013. arXiv: 2207.07029 [hep-ph].

[175] R. Beltrán et al. "Long-lived heavy neutral leptons from mesons in effective field theory". *JHEP* 01 (2023), p. 015. DOI: 10.1007/JHEP01(2023)015. arXiv: 2210.02461 [hep-ph].

[176] W. Dekens et al. "Sterile neutrinos and neutrinoless double beta decay in effective field theory". *JHEP* 06 (2020), p. 097. DOI: 10.1007/JHEP06(2020)097. arXiv: 2002.07182 [hep-ph].

[177] W. Dekens, J. de Vries, and T. Tong. "Sterile neutrinos with non-standard interactions in β- and $0\nu\beta\beta$-decay experiments". *JHEP* 08 (2021), p. 128. DOI: 10.1007/JHEP08(2021)128. arXiv: 2104.00140 [hep-ph].

[178] J. de Vries et al. "Light sterile neutrinos, left-right symmetry, and $0\nu\beta\beta$ decay". *JHEP* 11 (2022), p. 056. DOI: 10.1007/JHEP11(2022)056. arXiv: 2209.03031 [hep-ph].

[179] V. Cirigliano et al. "Neutrinoless Double-Beta Decay: A Roadmap for Matching Theory to Experiment" (Mar. 2022). arXiv: 2203.12169 [hep-ph].

[180] E. E. Jenkins, A. V. Manohar, and P. Stoffer. "Low-Energy Effective Field Theory below the Electroweak Scale: Anomalous Dimensions". *JHEP* 01 (2018). [Erratum: JHEP 12, 042 (2023)], p. 084. DOI: 10.1007/JHEP01(2018)084. arXiv: 1711.05270 [hep-ph].

[181] M. Chala and A. Titov. "One-loop running of dimension-six Higgs-neutrino operators and implications of a large neutrino dipole moment". *JHEP* 09 (2020), p. 188. DOI: 10.1007/JHEP09(2020)188. arXiv: 2006.14596 [hep-ph].

[182] A. Datta et al. "Anomalous dimensions from gauge couplings in SMEFT with right-handed neutrinos". *JHEP* 02 (2021), p. 015. DOI: 10.1007/JHEP02(2021)015. arXiv: 2010.12109 [hep-ph].

[183] A. Datta et al. "Anomalous dimensions from Yukawa couplings in SMNEFT: four-fermion operators". *JHEP* 05 (2021), p. 037. DOI: 10.1007/JHEP05(2021)037. arXiv: 2103.04441 [hep-ph].

[184] M. Hirsch, H. V. Klapdor-Kleingrothaus, and S. G. Kovalenko. "New low-energy leptoquark interactions". *Phys. Lett. B* 378 (1996), pp. 17–22. DOI: 10.1016/0370-2693(96)00419-4. arXiv: hep-ph/9602305.

[185] P. Ballett, T. Boschi, and S. Pascoli. "Heavy Neutral Leptons from low-scale seesaws at the DUNE Near Detector". *JHEP* 03 (2020), p. 111. DOI: 10.1007/JHEP03(2020)111. arXiv: 1905.00284 [hep-ph].

[186] P. Coloma et al. "GeV-scale neutrinos: interactions with mesons and DUNE sensitivity". *Eur. Phys. J. C* 81.1 (2021), p. 78. DOI: 10.1140/epjc/s10052-021-08861-y. arXiv: 2007.03701 [hep-ph].

[187] R. Beltrán et al. "Heavy neutral leptons from kaons in effective field theory". *Phys. Rev. D* 109.11 (2024), p. 115014. DOI: 10.1103/PhysRevD.109.115014. arXiv: 2309.11546 [hep-ph].

[188] LHCb. "Measurement of the B_c^- meson production fraction and asymmetry in 7 and 13 TeV pp collisions". *Phys. Rev. D* 100.11 (2019), p. 112006. DOI: 10.1103/PhysRevD.100.112006. arXiv: 1910.13404 [hep-ex].

[189] T. Sjöstrand et al. "An introduction to PYTHIA 8.2". *Comput. Phys. Commun.* 191 (2015), pp. 159–177. DOI: 10.1016/j.cpc.2015.01.024. arXiv: 1410.3012 [hep-ph].

[190] C. Bierlich et al. "A comprehensive guide to the physics and usage of PYTHIA 8.3". *SciPost Phys. Codeb.* 2022 (2022), p. 8. DOI: 10.21468/SciPostPhysCodeb.8. arXiv: 2203.11601 [hep-ph].

[191] *Forward Physics in PYTHIA 8*. https://pythia.org/download/talks/SjostrandForward20.pdf.

[192] V. V. Gligorov et al. "Leveraging the ALICE/L3 cavern for long-lived particle searches". *Phys. Rev. D* 99.1 (2019), p. 015023. DOI: 10.1103/PhysRevD.99.015023. arXiv: 1810.03636 [hep-ph].

[193] J. P. Chou, D. Curtin, and H. J. Lubatti. "New Detectors to Explore the Lifetime Frontier". *Phys. Lett. B* 767 (2017), pp. 29–36. DOI: 10.1016/j.physletb.2017.01.043. arXiv: 1606.06298 [hep-ph].

[194] M. Cacciari, M. Greco, and P. Nason. "The p_T spectrum in heavy-flavour hadroproduction." *JHEP* 05 (1998), p. 007. DOI: 10.1088/1126-6708/1998/05/007. arXiv: hep-ph/9803400.

[195] M. Cacciari, S. Frixione, and P. Nason. "The p_T spectrum in heavy flavor photoproduction". *JHEP* 03 (2001), p. 006. DOI: 10.1088/1126-6708/2001/03/006. arXiv: hep-ph/0102134.

[196] M. Hirsch and Z. S. Wang. "Heavy neutral leptons at ANUBIS". *Phys. Rev. D* 101.5 (2020), p. 055034. DOI: 10.1103/PhysRevD.101.055034. arXiv: 2001.04750 [hep-ph].

[197] G. Magill et al. “Dipole Portal to Heavy Neutral Leptons”. *Phys. Rev. D* 98.11 (2018), p. 115015. DOI: 10.1103/PhysRevD.98.115015. arXiv: 1803.03262 [hep-ph].

[198] T. Schwetz, A. Zhou, and J. Zhu. “Constraining active-sterile neutrino transition magnetic moments at DUNE near and far detectors”. *JHEP* 21 (2020), p. 200. DOI: 10.1007/JHEP07(2021)200. arXiv: 2105.09699 [hep-ph].

[199] P. D. Bolton et al. “Probing active-sterile neutrino transition magnetic moments with photon emission from CEνNS”. *Phys. Rev. D* 106.3 (2022), p. 035036. DOI: 10.1103/PhysRevD.106.035036. arXiv: 2110.02233 [hep-ph].

[200] D. Barducci et al. “Probing right-handed neutrinos dipole operators”. *JHEP* 03 (2023), p. 239. DOI: 10.1007/JHEP03(2023)239. arXiv: 2209.13469 [hep-ph].

[201] D. Barducci et al. “Probing the dipole portal to heavy neutral leptons via meson decays at the high-luminosity LHC”. *Phys. Rev. D* 108.11 (2023), p. 115009. DOI: 10.1103/PhysRevD.108.115009. arXiv: 2308.16608 [hep-ph].

[202] J. Y. Günther et al. “Long-lived neutral fermions at the DUNE near detector”. *JHEP* 01 (2024), p. 108. DOI: 10.1007/JHEP01(2024)108. arXiv: 2310.12392 [hep-ph].

[203] W. Liu and Y. Zhang. “Testing neutrino dipole portal by long-lived particle detectors at the LHC”. *Eur. Phys. J. C* 83.7 (2023), p. 568. DOI: 10.1140/epjc/s10052-023-11751-0. arXiv: 2302.02081 [hep-ph].

[204] E. J. Chun, S. Mandal, and R. Padhan. “Collider imprints of a right handed neutrino magnetic moment operator”. *Phys. Rev. D* 109.11 (2024), p. 115002. DOI: 10.1103/PhysRevD.109.115002. arXiv: 2401.05174 [hep-ph].

[205] L. Duarte, J. Jones-Pérez, and C. Manrique-Chavil. “Bounding the Dimension-5 Seesaw Portal with non-pointing photon searches”. *JHEP* 04 (2024), p. 133. DOI: 10.1007/JHEP04(2024)133. arXiv: 2311.17989 [hep-ph].

[206] R. Beltrán et al. “Probing heavy neutrino magnetic moments at the LHC using long-lived particle searches”. *JHEP* 07 (2024), p. 153. DOI: 10.1007/JHEP07(2024)153. arXiv: 2405.08877 [hep-ph].

[207] A. Aparici, A. Santamaria, and J. Wudka. “A model for right-handed neutrino magnetic moments”. *J. Phys. G* 37 (2010), p. 075012. DOI: 10.1088/0954-3899/37/7/075012. arXiv: 0911.4103 [hep-ph].

[208] K. Fridell et al. “Probing lepton number violation: a comprehensive survey of dimension-7 SMEFT”. *JHEP* 05 (2024), p. 154. DOI: 10.1007/JHEP05(2024)154. arXiv: 2306.08709 [hep-ph].

[209] J. M. Alves et al. "Vector-like singlet quarks: A roadmap". *Phys. Rept.* 1057 (2024), pp. 1–69. DOI: 10.1016/j.physrep.2023.12.004. arXiv: 2304.10561 [hep-ph].

[210] F. del Aguila, J. de Blas, and M. Perez-Victoria. "Effects of new leptons in Electroweak Precision Data". *Phys. Rev. D* 78 (2008), p. 013010. DOI: 10.1103/PhysRevD.78.013010. arXiv: 0803.4008 [hep-ph].

[211] A. Crivellin et al. "Global Electroweak Fit and Vector-Like Leptons in Light of the Cabibbo Angle Anomaly". *JHEP* 12 (2020), p. 166. DOI: 10.1007/JHEP12(2020)166. arXiv: 2008.01113 [hep-ph].

[212] J. de Blas et al. "Observable Effects of General New Scalar Particles". *JHEP* 04 (2015), p. 078. DOI: 10.1007/JHEP04(2015)078. arXiv: 1412.8480 [hep-ph].

[213] A. Crivellin et al. "Searching for lepton flavor universality violation and collider signals from a singly charged scalar singlet". *Phys. Rev. D* 103.7 (2021), p. 073002. DOI: 10.1103/PhysRevD.103.073002. arXiv: 2012.09845 [hep-ph].

[214] T. Felkl, J. Herrero-Garcia, and M. A. Schmidt. "The Singly-Charged Scalar Singlet as the Origin of Neutrino Masses". *JHEP* 05 (2021). [Erratum: JHEP 05, 073 (2022)], p. 122. DOI: 10.1007/JHEP05(2021)122. arXiv: 2102.09898 [hep-ph].

[215] D. Zhang and S. Zhou. "Complete one-loop matching of the type-I seesaw model onto the Standard Model effective field theory". *JHEP* 09 (2021), p. 163. DOI: 10.1007/JHEP09(2021)163. arXiv: 2107.12133 [hep-ph].

[216] J. A. Casas and A. Ibarra. "Oscillating neutrinos and $\mu \to e, \gamma$". *Nucl. Phys. B* 618 (2001), pp. 171–204. DOI: 10.1016/S0550-3213(01)00475-8. arXiv: hep-ph/0103065.

[217] TEXONO Collaboration. "A Search of Neutrino Magnetic Moments with a High-Purity Germanium Detector at the Kuo-Sheng Nuclear Power Station". *Phys. Rev. D* 75 (2007), p. 012001. DOI: 10.1103/PhysRevD.75.012001. arXiv: hep-ex/0605006.

[218] A. G. Beda et al. "First Result for Neutrino Magnetic Moment from Measurements with the GEMMA Spectrometer". *Phys. Atom. Nucl.* 70 (2007), pp. 1873–1884. DOI: 10.1134/S1063778807110063. arXiv: 0705.4576 [hep-ex].

[219] LSND Collaboration. "Measurement of electron - neutrino - electron elastic scattering". *Phys. Rev. D* 63 (2001), p. 112001. DOI: 10.1103/PhysRevD.63.112001. arXiv: hep-ex/0101039.

[220] Borexino Collaboration. "Direct Measurement of the Be-7 Solar Neutrino Flux with 192 Days of Borexino Data". *Phys. Rev. Lett.* 101 (2008), p. 091302. DOI: 10.1103/PhysRevLett.101.091302. arXiv: 0805.3843 [astro-ph].

[221] Q. Cao et al. "Searching for Weak Singlet Charged Scalar at the Large Hadron Collider". *Phys. Rev. D* 97.11 (2018), p. 115036. DOI: 10.1103/PhysRevD.97.115036. arXiv: 1711.02113 [hep-ph].

[222] J. Alcaide, M. Chala, and A. Santamaria. "LHC signals of radiatively-induced neutrino masses and implications for the Zee–Babu model". *Phys. Lett. B* 779 (2018), pp. 107–116. DOI: 10.1016/j.physletb.2018.02.001. arXiv: 1710.05885 [hep-ph].

[223] J. Alcaide and N. I. Mileo. "LHC sensitivity to singly-charged scalars decaying into electrons and muons". *Phys. Rev. D* 102.7 (2020), p. 075030. DOI: 10.1103/PhysRevD.102.075030. arXiv: 1906.08685 [hep-ph].

[224] ATLAS Collaboration. "Search for electroweak production of charginos and sleptons decaying into final states with two leptons and missing transverse momentum in $\sqrt{s} = 13$ TeV pp collisions using the ATLAS detector". *Eur. Phys. J. C* 80.2 (2020), p. 123. DOI: 10.1140/epjc/s10052-019-7594-6. arXiv: 1908.08215 [hep-ex].

[225] DELPHI Collaboration. "Photon events with missing energy in e^+e^- collisions at $\sqrt{s}$ = 130 GeV to 209 GeV". *Eur. Phys. J. C* 38 (2005), pp. 395–411. DOI: 10.1140/epjc/s2004-02051-8. arXiv: hep-ex/0406019.

[226] P. J. Fox et al. "LEP Shines Light on Dark Matter". *Phys. Rev. D* 84 (2011), p. 014028. DOI: 10.1103/PhysRevD.84.014028. arXiv: 1103.0240 [hep-ph].

[227] L3 Collaboration. "Search for heavy neutral and charged leptons in e^+e^- annihilation at LEP". *Phys. Lett. B* 517 (2001), pp. 75–85. DOI: 10.1016/S0370-2693(01)01005-X. arXiv: hep-ex/0107015.

[228] ATLAS Collaboration. "Search for heavy lepton resonances decaying to a Z boson and a lepton in pp collisions at $\sqrt{s} = 8$ TeV with the ATLAS detector". *JHEP* 09 (2015), p. 108. DOI: 10.1007/JHEP09(2015)108. arXiv: 1506.01291 [hep-ex].

[229] N. Kumar and S. P. Martin. "Vectorlike Leptons at the Large Hadron Collider". *Phys. Rev. D* 92.11 (2015), p. 115018. DOI: 10.1103/PhysRevD.92.115018. arXiv: 1510.03456 [hep-ph].

[230] J. de Blas. "Electroweak limits on physics beyond the Standard Model". *EPJ Web Conf.* 60 (2013). Ed. by M. Bosman et al., p. 19008. DOI: 10.1051/epjconf/20136019008. arXiv: 1307.6173 [hep-ph].

[231] A. Falkowski, D. M. Straub, and A. Vicente. "Vector-like leptons: Higgs decays and collider phenomenology". *JHEP* 05 (2014), p. 092. DOI: 10.1007/JHEP05(2014)092. arXiv: 1312.5329 [hep-ph].

[232] A. Crivellin et al. "Renormalisation-group improved analysis of $\mu \to e$ processes in a systematic effective-field-theory approach". *JHEP* 05 (2017), p. 117. DOI: 10.1007/JHEP05(2017)117. arXiv: 1702.03020 [hep-ph].

[233] Z. Poh and S. Raby. "Vectorlike leptons: Muon g-2 anomaly, lepton flavor violation, Higgs boson decays, and lepton nonuniversality". *Phys. Rev. D* 96.1 (2017), p. 015032. DOI: 10.1103/PhysRevD.96.015032. arXiv: 1705.07007 [hep-ph].

[234] A. E. Cárcamo Hernández, S. F. King, and H. Lee. "Z mediated flavor changing neutral currents with a fourth vectorlike family". *Phys. Rev. D* 105.1 (2022), p. 015021. DOI: 10.1103/PhysRevD.105.015021. arXiv: 2110.07630 [hep-ph].

[235] K. Hamaguchi et al. "Probing new physics in the vector-like lepton model by lepton electric dipole moments". *JHEP* 01 (2023), p. 100. DOI: 10.1007/JHEP01(2023)100. arXiv: 2211.16800 [hep-ph].

[236] W. Altmannshofer et al. "Charged Lepton Flavour Violation in Heavy Particle Decays". *Snowmass 2021*. May 2022. arXiv: 2205.10576 [hep-ph].

[237] R. Alonso et al. "Muon conversion to electron in nuclei in type-I seesaw models". *JHEP* 01 (2013), p. 118. DOI: 10.1007/JHEP01(2013)118. arXiv: 1209.2679 [hep-ph].

[238] L. Allwicher, G. Isidori, and N. Selimovic. "LFU violations in leptonic τ decays and B-physics anomalies". *Phys. Lett. B* 826 (2022), p. 136903. DOI: 10.1016/j.physletb.2022.136903. arXiv: 2109.03833 [hep-ph].

[239] A. Pich. "Precision Tau Physics". *Prog. Part. Nucl. Phys.* 75 (2014), pp. 41–85. DOI: 10.1016/j.ppnp.2013.11.002. arXiv: 1310.7922 [hep-ph].

[240] HFLAV Collaboration. "Averages of b-hadron, c-hadron, and τ-lepton properties as of 2021". *Phys. Rev. D* 107.5 (2023), p. 052008. DOI: 10.1103/PhysRevD.107.052008. arXiv: 2206.07501 [hep-ex].

[241] Y. Kuno and Y. Okada. "Muon decay and physics beyond the standard model". *Rev. Mod. Phys.* 73 (2001), pp. 151–202. DOI: 10.1103/RevModPhys.73.151. arXiv: hep-ph/9909265.

[242] A. Crivellin, S. Najjari, and J. Rosiek. "Lepton Flavor Violation in the Standard Model with general Dimension-Six Operators". *JHEP* 04 (2014), p. 167. DOI: 10.1007/JHEP04(2014)167. arXiv: 1312.0634 [hep-ph].

[243] S. Banerjee et al. "Snowmass 2021 White Paper: Charged lepton flavor violation in the tau sector" (Mar. 2022). arXiv: 2203.14919 [hep-ph].

[244] R. Kitano, M. Koike, and Y. Okada. "Detailed calculation of lepton flavor violating muon electron conversion rate for various nuclei". *Phys. Rev. D* 66 (2002). [Erratum: Phys.Rev.D 76, 059902 (2007)], p. 096002. DOI: 10.1103/PhysRevD.76.059902. arXiv: hep-ph/0203110.

[245] S. Davidson, Y. Kuno, and M. Yamanaka. "Selecting $\mu \to e$ conversion targets to distinguish lepton flavour-changing operators". *Phys. Lett. B* 790 (2019), pp. 380–388. DOI: 10.1016/j.physletb.2019.01.042. arXiv: 1810.01884 [hep-ph].

[246] SINDRUM II Collaboration. "A Search for muon to electron conversion in muonic gold". *Eur. Phys. J. C* 47 (2006), pp. 337–346. DOI: 10.1140/epjc/s2006-02582-x.

[247] G. M. Pruna and A. Signer. "The $\mu \to e\gamma$ decay in a systematic effective field theory approach with dimension 6 operators". *JHEP* 10 (2014), p. 014. DOI: 10.1007/JHEP10(2014)014. arXiv: 1408.3565 [hep-ph].

[248] S. Davidson. "$\mu \to e\gamma$ and matching at m_W". *Eur. Phys. J. C* 76.7 (2016), p. 370. DOI: 10.1140/epjc/s10052-016-4207-5. arXiv: 1601.07166 [hep-ph].

[249] R. Harnik, J. Kopp, and J. Zupan. "Flavor Violating Higgs Decays". *JHEP* 03 (2013), p. 026. DOI: 10.1007/JHEP03(2013)026. arXiv: 1209.1397 [hep-ph].

[250] G. Blankenburg, J. Ellis, and G. Isidori. "Flavour-Changing Decays of a 125 GeV Higgs-like Particle". *Phys. Lett. B* 712 (2012), pp. 386–390. DOI: 10.1016/j.physletb.2012.05.007. arXiv: 1202.5704 [hep-ph].

[251] OPAL Collaboration. "A Search for lepton flavor violating Z^0 decays". *Z. Phys. C* 67 (1995), pp. 555–564. DOI: 10.1007/BF01553981.

[252] ATLAS Collaboration. "Search for the lepton flavor violating decay $Z \to e\mu$ in pp collisions at $\sqrt{s} = 8$ TeV with the ATLAS detector". *Phys. Rev. D* 90.7 (2014), p. 072010. DOI: 10.1103/PhysRevD.90.072010. arXiv: 1408.5774 [hep-ex].

[253] ATLAS Collaboration. "Searches for lepton-flavour-violating decays of the Higgs boson in $\sqrt{s} = 13$ TeV pp collisions with the ATLAS detector". *Phys. Lett. B* 800 (2020), p. 135069. DOI: 10.1016/j.physletb.2019.135069. arXiv: 1907.06131 [hep-ex].

[254] CMS Collaboration. "Search for lepton-flavor violating decays of the Higgs boson in the $\mu\tau$ and eτ final states in proton-proton collisions at $\sqrt{s}$ = 13 TeV". *Phys. Rev. D* 104.3 (2021), p. 032013. DOI: 10.1103/PhysRevD.104.032013. arXiv: 2105.03007 [hep-ex].

[255] N. D. Christensen and C. Duhr. "FeynRules - Feynman rules made easy". *Comput. Phys. Commun.* 180 (2009), pp. 1614–1641. DOI: 10.1016/j.cpc.2009.02.018. arXiv: 0806.4194 [hep-ph].

[256] A. Alloul et al. "FeynRules 2.0 - A complete toolbox for tree-level phenomenology". *Comput. Phys. Commun.* 185 (2014), pp. 2250–2300. DOI: 10.1016/j.cpc.2014.04.012. arXiv: 1310.1921 [hep-ph].

[257] C. Degrande et al. "UFO - The Universal FeynRules Output". *Comput. Phys. Commun.* 183 (2012), pp. 1201–1214. DOI: 10.1016/j.cpc.2012.01.022. arXiv: 1108.2040 [hep-ph].

[258] J. Alwall et al. "The automated computation of tree-level and next-to-leading order differential cross sections, and their matching to parton shower simulations". *JHEP* 07 (2014), p. 079. DOI: 10.1007/JHEP07(2014)079. arXiv: 1405.0301 [hep-ph].

[259] P. Artoisenet et al. "Automatic spin-entangled decays of heavy resonances in Monte Carlo simulations". *JHEP* 03 (2013), p. 015. DOI: 10.1007/JHEP03(2013)015. arXiv: 1212.3460 [hep-ph].

[260] ATLAS Collaboration. "Search for displaced photons produced in exotic decays of the Higgs boson using 13 TeV pp collisions with the ATLAS detector". *Phys. Rev. D* 108.3 (2023), p. 032016. DOI: 10.1103/PhysRevD.108.032016. arXiv: 2209.01029 [hep-ex].

[261] F. Delgado et al. "Assessment of the dimension-5 seesaw portal and impact of exotic Higgs decays on non-pointing photon searches". *JHEP* 09 (2022), p. 079. DOI: 10.1007/JHEP09(2022)079. arXiv: 2205.13550 [hep-ph].

[262] CMS Collaboration. "Search for New Physics with Long-Lived Particles Decaying to Photons and Missing Energy in pp Collisions at $\sqrt{s} = 7$ TeV". *JHEP* 11 (2012), p. 172. DOI: 10.1007/JHEP11(2012)172. arXiv: 1207.0627 [hep-ex].

[263] CMS. "Search for long-lived heavy neutral leptons with displaced vertices in proton-proton collisions at $\sqrt{\mathrm{s}}$ =13 TeV". *JHEP* 07 (2022), p. 081. DOI: 10.1007/JHEP07(2022)081. arXiv: 2201.05578 [hep-ex].

[264] G. Cottin et al. "Heavy neutral leptons in effective field theory and the high-luminosity LHC". *JHEP* 09 (2021), p. 039. DOI: 10.1007/JHEP09(2021)039. arXiv: 2105.13851 [hep-ph].

[265] M. Drewes and J. Hajer. "Heavy Neutrinos in displaced vertex searches at the LHC and HL-LHC". *JHEP* 02 (2020), p. 070. DOI: 10.1007/JHEP02(2020)070. arXiv: 1903.06100 [hep-ph].

[266] G. Cottin, J. C. Helo, and M. Hirsch. "Displaced vertices as probes of sterile neutrino mixing at the LHC". *Phys. Rev. D* 98.3 (2018), p. 035012. DOI: 10.1103/PhysRevD.98.035012. arXiv: 1806.05191 [hep-ph].

[267] R. Beltrán et al. "Long-lived heavy neutral leptons at the LHC: four-fermion single-N_R operators". *JHEP* 01 (2022), p. 044. DOI: 10.1007/JHEP01(2022)044. arXiv: 2110.15096 [hep-ph].

[268] J. Alwall et al. "MadGraph 5 : Going Beyond". *JHEP* 06 (2011), p. 128. DOI: 10.1007/JHEP06(2011)128. arXiv: 1106.0522 [hep-ph].

[269] ATLAS Collaboration. "Search for massive, long-lived particles using multi-track displaced vertices or displaced lepton pairs in pp collisions at $\sqrt{s}$ = 8 TeV with the ATLAS detector". *Phys. Rev. D* 92.7 (2015), p. 072004. DOI: 10.1103/PhysRevD.92.072004. arXiv: 1504.05162 [hep-ex].

[270] ATLAS Collaboration. "Search for long-lived, massive particles in events with displaced vertices and missing transverse momentum in $\sqrt{s}$ = 13 TeV pp collisions with the ATLAS detector". *Phys. Rev. D* 97.5 (2018), p. 052012. DOI: 10.1103/PhysRevD.97.052012. arXiv: 1710.04901 [hep-ex].

[271] M. Cacciari, G. P. Salam, and G. Soyez. "FastJet User Manual". *Eur. Phys. J. C* 72 (2012), p. 1896. DOI: 10.1140/epjc/s10052-012-1896-2. arXiv: 1111.6097 [hep-ph].

[272] G. Cottin, J. C. Helo, and M. Hirsch. "Searches for light sterile neutrinos with multitrack displaced vertices". *Phys. Rev. D* 97.5 (2018), p. 055025. DOI: 10.1103/PhysRevD.97.055025. arXiv: 1801.02734 [hep-ph].

[273] S. Davidson, D. C. Bailey, and B. A. Campbell. "Model independent constraints on leptoquarks from rare processes". *Z. Phys. C* 61 (1994), pp. 613–644. DOI: 10.1007/BF01552629. arXiv: hep-ph/9309310.

[274] CMS Collaboration. "Search for pair production of first-generation scalar leptoquarks at $\sqrt{s} = 13$ TeV". *Phys. Rev. D* 99.5 (2019), p. 052002. DOI: 10.1103/PhysRevD.99.052002. arXiv: 1811.01197 [hep-ex].

[275] CMS Collaboration. "Search for dark matter in events with a leptoquark and missing transverse momentum in proton-proton collisions at 13 TeV". *Phys. Lett. B* 795 (2019), pp. 76–99. DOI: 10.1016/j.physletb.2019.05.046. arXiv: 1811.10151 [hep-ex].

[276] CMS Collaboration. "Searches for physics beyond the standard model with the M_{T2} variable in hadronic final states with and without disappearing tracks in proton-proton collisions at $\sqrt{s} = 13$ TeV". *Eur. Phys. J. C* 80.1 (2020), p. 3. DOI: 10.1140/epjc/s10052-019-7493-x. arXiv: 1909.03460 [hep-ex].

[277] ATLAS Collaboration. “Search for scalar leptoquarks in pp collisions at $\sqrt{s}$ = 13 TeV with the ATLAS experiment”. *New J. Phys.* 18.9 (2016), p. 093016. DOI: 10.1088/1367-2630/18/9/093016. arXiv: 1605.06035 [hep-ex].

[278] ATLAS Collaboration. “Search for pairs of scalar leptoquarks decaying into quarks and electrons or muons in $\sqrt{s}$ = 13 TeV pp collisions with the ATLAS detector”. *JHEP* 10 (2020), p. 112. DOI: 10.1007/JHEP10(2020)112. arXiv: 2006.05872 [hep-ex].

[279] CMS Collaboration. “Search for long-lived particles that decay into final states containing two electrons or two muons in proton-proton collisions at $\sqrt{s}$ = 8 TeV”. *Phys. Rev. D* 91.5 (2015), p. 052012. DOI: 10.1103/PhysRevD.91.052012. arXiv: 1411.6977 [hep-ex].

[280] CMS Collaboration. “Search for long-lived particles decaying to leptons with large impact parameter in proton-proton collisions at $\sqrt{s} = 13$ TeV”. *Eur. Phys. J. C* 82.2 (2022), p. 153. DOI: 10.1140/epjc/s10052-022-10027-3. arXiv: 2110.04809 [hep-ex].

[281] CMS Collaboration. “Search for long-lived heavy neutral leptons with displaced vertices in pp collisions at $\sqrt{s} = 13$ TeV with the CMS detector” (2021).

[282] J. Alcaide et al. “Probes of the Standard Model effective field theory extended with a right-handed neutrino”. *JHEP* 08 (2019), p. 031. DOI: 10.1007/JHEP08(2019)031. arXiv: 1905.11375 [hep-ph].

[283] H. Bahl, S. Koren, and L. Wang. “Topportunities at the LHC: rare top decays with light singlets”. *Eur. Phys. J. C* 84.10 (2024), p. 1100. DOI: 10.1140/epjc/s10052-024-13411-3. arXiv: 2307.11154 [hep-ph].

[284] R. Beltrán et al. “Heavy neutral leptons and top quarks in effective field theory” (Jan. 2025). arXiv: 2501.09065 [hep-ph].

[285] F. Garosi et al. “Indirect constraints on top quark operators from a global SMEFT analysis”. *JHEP* 12 (2023), p. 129. DOI: 10.1007/JHEP12(2023)129. arXiv: 2310.00047 [hep-ph].

[286] ATLAS Collaboration. “Measurement of the $t\bar{t}$ production cross-section in the lepton+jets channel at $\sqrt{s} = 13$ TeV with the ATLAS experiment”. *Phys. Lett. B* 810 (2020), p. 135797. DOI: 10.1016/j.physletb.2020.135797. arXiv: 2006.13076 [hep-ex].

[287] ATLAS Collaboration. “Measurement of t-channel production of single top quarks and antiquarks in pp collisions at 13 TeV using the full ATLAS Run 2 data sample”. *JHEP* 05 (2024), p. 305. DOI: 10.1007/JHEP05(2024)305. arXiv: 2403.02126 [hep-ex].

[288] M. Czakon and A. Mitov. “Top++: A Program for the Calculation of the Top-Pair Cross-Section at Hadron Colliders”. *Comput. Phys. Commun.* 185 (2014),

p. 2930. DOI: 10.1016/j.cpc.2014.06.021. arXiv: 1112.5675 [hep-ph].

[289] A. Biswas et al. “Phenomenology of Dirac neutrino EFTs up to dimension six” (Nov. 2024). arXiv: 2411.17414 [hep-ph].

[290] T. Hahn. “Generating Feynman diagrams and amplitudes with FeynArts 3”. *Comput. Phys. Commun.* 140 (2001), pp. 418–431. DOI: 10.1016/S0010-4655(01)00290-9. arXiv: hep-ph/0012260.

[291] T. Hahn and M. Perez-Victoria. “Automatized one loop calculations in four-dimensions and D-dimensions”. *Comput. Phys. Commun.* 118 (1999), pp. 153–165. DOI: 10.1016/S0010-4655(98)00173-8. arXiv: hep-ph/9807565.

[292] ATLAS Collaboration. “Search for long-lived, massive particles in events with displaced vertices and multiple jets in pp collisions at $\sqrt{s}$ = 13 TeV with the ATLAS detector”. *JHEP* 06 (2023), p. 200. DOI: 10.1007/JHEP06(2023)200. arXiv: 2301.13866 [hep-ex].

[293] K. Cheung et al. “Quark flavor violation and axion-like particles from top-quark decays at the LHC”. *JHEP* 07 (2024), p. 209. DOI: 10.1007/JHEP07(2024)209. arXiv: 2404.06126 [hep-ph].

[294] NNPDF Collaboration. “Parton distributions from high-precision collider data”. *Eur. Phys. J. C* 77.10 (2017), p. 663. DOI: 10.1140/epjc/s10052-017-5199-5. arXiv: 1706.00428 [hep-ph].

[295] B. C. Allanach et al. “Prompt Signals and Displaced Vertices in Sparticle Searches for Next-to-Minimal Gauge Mediated Supersymmetric Models”. *Eur. Phys. J. C* 76.9 (2016), p. 482. DOI: 10.1140/epjc/s10052-016-4330-3. arXiv: 1606.03099 [hep-ph].

[296] CMS Collaboration. “Enriching the physics program of the CMS experiment via data scouting and data parking”. *Phys. Rept.* 1115 (2025), pp. 678–772. DOI: 10.1016/j.physrep.2024.09.006. arXiv: 2403.16134 [hep-ex].

[297] CMS Collaboration. “Search for long-lived heavy neutrinos in the decays of B mesons produced in proton-proton collisions at $\sqrt{s}$ = 13 TeV”. *JHEP* 06 (2024), p. 183. DOI: 10.1007/JHEP06(2024)183. arXiv: 2403.04584 [hep-ex].

[298] ATLAS Collaboration. “Commissioning of the ATLAS high-performance b-tagging algorithms in the 7 TeV collision data” (July 2011).

[299] J. Alwall et al. “A Standard format for Les Houches event files”. *Comput. Phys. Commun.* 176 (2007), pp. 300–304. DOI: 10.1016/j.cpc.2006.11.010. arXiv: hep-ph/0609017.

[300] Erez Etzion. “MATHUSLA: https://indico.cern.ch/event/1381368/contributions/5963280/attachments/2887173/5061292/LLP2024-MATHUSLA-Etzion.pdf”. 2024.

[301] Louie D. Corpe. "Update on (pro)ANUBIS detector proposal: https://indico.cern.ch/event/1216822/contributions/5449255/attachments/2671754/4631593/LCORPE_LLPWorkshop2023_ANUBIS_June2023.pdf". 2023.

[302] MATHUSLA Collaboration. "An Update to the Letter of Intent for MATHUSLA: Search for Long-Lived Particles at the HL-LHC" (Sept. 2020). arXiv: 2009.01693 [physics.ins-det].

[303] V. Shtabovenko, R. Mertig, and F. Orellana. "New Developments in FeynCalc 9.0". *Comput. Phys. Commun.* 207 (2016), pp. 432–444. DOI: 10.1016/j.cpc.2016.06.008. arXiv: 1601.01167 [hep-ph].

[304] V. Shtabovenko, R. Mertig, and F. Orellana. "FeynCalc 9.3: New features and improvements". *Comput. Phys. Commun.* 256 (2020), p. 107478. DOI: 10.1016/j.cpc.2020.107478. arXiv: 2001.04407 [hep-ph].

[305] Flavour Lattice Averaging Group (FLAG). "FLAG Review 2021". *Eur. Phys. J. C* 82.10 (2022), p. 869. DOI: 10.1140/epjc/s10052-022-10536-1. arXiv: 2111.09849 [hep-lat].

[306] J. L. Rosner, S. Stone, and R. S. Van de Water. "Leptonic Decays of Charged Pseudoscalar Mesons". *Review of Particle Physics 2021 update* (2021).

[307] C. Bourrely, I. Caprini, and L. Lellouch. "Model-independent description of $B \to \pi\ell\nu$ decays and a determination of $|V_{ub}|$". *Phys. Rev. D* 79 (2009). [Erratum: Phys.Rev.D 82, 099902 (2010)], p. 013008. DOI: 10.1103/PhysRevD.82.099902. arXiv: 0807.2722 [hep-ph].

[308] ETM Collaboration. "Scalar and vector form factors of $D \to \pi(K)\ell\nu$ decays with $N_f = 2+1+1$ twisted fermions". *Phys. Rev. D* 96.5 (2017). [Erratum: Phys.Rev.D 99, 099902 (2019), Erratum: Phys.Rev.D 100, 079901 (2019)], p. 054514. DOI: 10.1103/PhysRevD.96.054514. arXiv: 1706.03017 [hep-lat].

[309] M. A. Ivanov et al. "Exclusive semileptonic decays of D and D_s mesons in the covariant confining quark model". *Front. Phys. (Beijing)* 14.6 (2019), p. 64401. DOI: 10.1007/s11467-019-0908-1. arXiv: 1904.07740 [hep-ph].

[310] Y. Wu, M. Zhong, and Y. Zuo. "$B_{(s)}$, $D_{(s)} \to \pi, K, \eta, \rho, K^*, \omega, \phi$ Transition Form Factors and Decay Rates with Extraction of the CKM parameters $|V_{ub}|$, $|V_{cs}|$, $V_{cd}|$". *Int. J. Mod. Phys. A* 21 (2006), pp. 6125–6172. DOI: 10.1142/S0217751X06033209. arXiv: hep-ph/0604007.

[311] A. Bharucha, D. M. Straub, and R. Zwicky. "$B \to V\ell^+\ell^-$ in the Standard Model from light-cone sum rules". *JHEP* 08 (2016), p. 098. DOI: 10.1007/JHEP08(2016)098. arXiv: 1503.05534 [hep-ph].